ANALYSIS OF CERTAIN INVISCID FLOWS ON THE BETA PLANE

by

Boris Moro

SUBMITTED IN PARTIAL FULFILLMENT

OF THE REQUIREMENTS OF THE

DEGREE OF

DOCTOR OF PHILOSOPHY

at the

MASSACHUSETTS INSTITUTE OF TECHNOLOGY

and the

WOODS HOLE OCEANOGRAPHIC INSTITUTION

January 1986

@ Massachusetts Institute of Technology 1986

Signature of Author_____

Joint Program in Oceanography
Massachusetts Institute of Technology - Woods Hole Oceanographic Institution

Certified by_____

Steven A. Orszag
Thesis Supervisor

Accepted by_____

Joseph Pedlosky
Chairman, Joint Committee for Physical Oceanography
Massachusetts Institute of Technology - Woods Hole Oceanographic Institution

WITHDRAWN
FROM
MIT LIBRARIES
MASS. INST. TECH.
MAY 1986
LIBRARIES

ANALYSIS OF CERTAIN INVISCID FLOWS ON THE BETA-PLANE

by

BORIS MORO

Submitted to the Department of
Earth,Atmospheric and Planetary Sciences
on January 22, 1986 in partial fulfillment of the requirements
for the Degree of Doctor of Philosophy

ABSTRACT

An investigation of properties of the solutions of the steady state inviscid quasigeostrophic vorticity equation in a rectangular basin, was performed for various assumed functional relationships between potential vorticity and the streamfunction. All solutions that were found, which have slow interior flow and satisfy the Arnol'd-Blumen condition, are qualitatively similar to Fofonoff's inertial gyre. A new class of solutions with a small vortex near the boundary current is described. Such solutions are not stable under finite amplitude perturbations, but the vortices have lifetime much longer than their characteristic time. The relationship between bottom friction and wind forcing and the westward motion of vortices is established. It is shown that friction may act as a mechanism for conversion of kinetic energy of rotation into kinetic energy of translation. It is argued that friction may be among the causes of westward motion of the mesoscale eddies. It is also shown that the inertial boundary current may be much wider than in Fofonoff's model, due to the appearance of a countercurrent on its seaward side.

Several solutions describing steady general circulation in two layer model are found. We discuss strongly baroclinic long living vortices and a pure baroclinic mode of general circulation.

A simple approach to the numerical solution of some systems of nonlinear elliptic partial differential equations, depending on several parameters is also described.

Thesis Supervisor: Dr. Steven A. Orszag
Title: Professor of Applied and Computational Mathematics
Princeton University
Formerly Professor of Applied Mathematics, MIT

ACKNOWLEDGEMENTS

Author is indebted to Drs. N.P. Fofonoff and J. Pedlosky for useful suggestions, and to Prof. S.A. Orszag for support and encouragement. Computations were performed on computers of the National Center for Atmospheric Research*. I should also like to acknowledge support under ONR contract 150F090 and NSF grant ATM 84-14410.

* The National Center for Atmospheric Research is supported by the National Science Foundation.

CONTENTS

I Introduction 5

II Barotropic Flows

1 Steady State Solutions 17

2 Perturbation Experiments 33

3 Influence of Friction 48

4 Influence of the Wind Stress 68

III Two Layer Flows

1 Numerical Method 88

2 Mixed Modes 96

3 Evolution Experiments 110

4 Pure Baroclinic Mode 126

IV Conclusions 137

V Appendix

Numerical Solution of the Quasigeostrophic Vorticity Equation in Two-Layer Model 142

REFERENCES 145

I INTRODUCTION

The thesis is concerned with some problems of general circulation and its relation to mesoscale flows. We shall first review previous theories. New results are presented in Chapter II, which deals with barotropic flows, and Chapter III where baroclinic flows are discussed. Some suggestions about possible generalizations and future work are given in Chapter IV.

The earliest models of steady, homogeneous, large scale circulation, developed by Stommel and Munk, succeeded in explaining some of the basic features of the oceanic circulation, in particular showing that the reason for the existence of the intense western boundary current is the variation of the Coriolis parameter with latitude. In both Stommel's and Munk's models steady state solutions were obtained assuming linear dynamics in which the energy of the wind stress is absorbed in the basin and dissipated in the western boundary current. Advection terms were neglected, which is a good approximation in the interior of the basin. However in the region of the boundary current, these terms can be neglected only if the friction is assumed to be unrealistically large. Although, the solutions included strong western boundary current, the dynamics of the intensification remained unclear. Pedlosky (1965) gave a simple explanation in terms of Rossby waves which display strong anisotropy in east-west energy transmission, caused by the β-effect. From the dispersion relation for Rossby waves, it can be shown that energy associated with large scales must be transmitted to the west, and will be reflected with reduced wavelength, thus making the western boundary a source of small scale

energy which is then dissipated in the viscous boundary layer. As in the models of Stommel and Munk, this theory is limited to the small amplitude motions (note that one plane Rossby wave is the finite amplitude solution of the vorticity equation, but a wave packet is not). This poses the question whether there are low frequency but large amplitude motions which will show similar behavior.

In large scale circulation (e.g. in the North Atlantic subtropical gyre (Fig 1.)), the observed boundary current transport is several times larger than the transport of the interior, wind-forced flow. This shows that for a more accurate description of the general circulation nonlinear effects must be taken into account.

While Stommel and Munk obtained solutions of the equations of motion by neglecting nonlinear terms, Fofonoff (1954) considered steady flow without forcing and friction, i.e. when the flow is described only by the advection of potential vorticity. In this case the barotropic vorticity equation reduces to the functional relationship between potential vorticity and the streamfunction. By assuming the dependence to be linear, Fofonoff was able to find an analytic solution which consists of slow interior westward flow and a fast eastward current at northern and/or southern boundary (Fig. 2). From the form the simplified equation of motion, it is clear that such solutions must have east-west symmetry, which is broken either by friction, or by variations in the bottom topography.

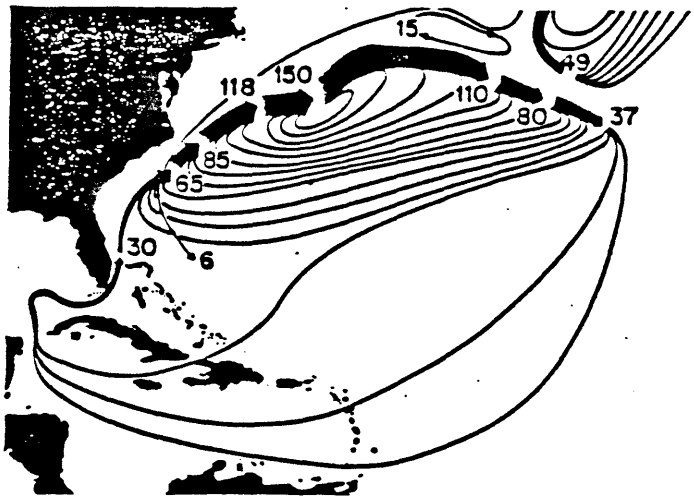


Figure 1. The North Atlantic Subtropical Gyre
(Worthington, 1976)

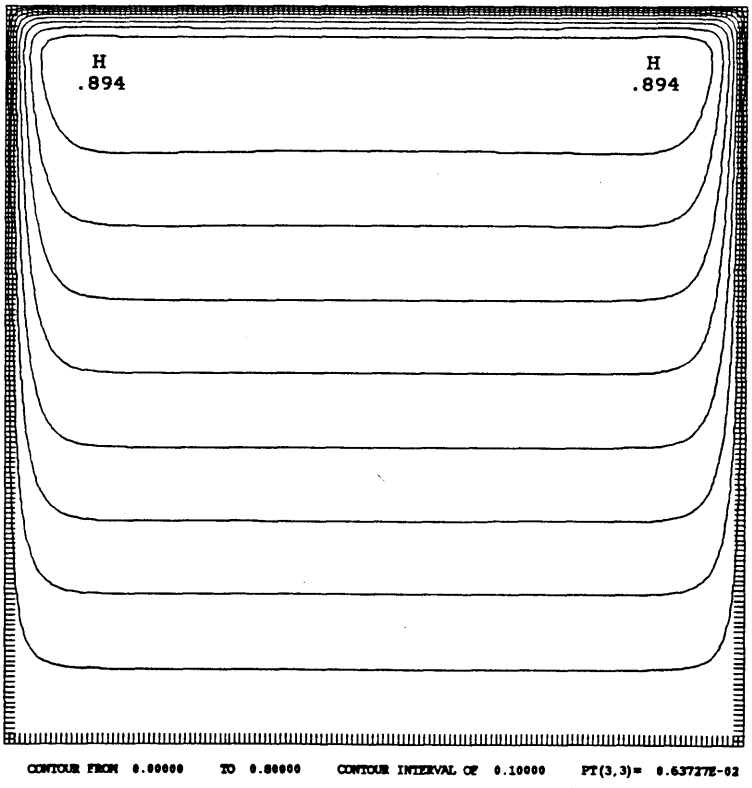


Figure 2. Fofonoff's solution ($\beta = 2000$)

Merkine et al. (1985) argued that such a "linear" model is barotropically unstable, although it can be shown that it satisfies the sufficient condition for stability in inviscid fluid under small but finite amplitude perturbations due to Arnol'd (1965) and Blumen (1968). This flow pattern is often regarded as a peculiarity of the linear relation between the potential vorticity and the streamfunction. Pierrehumbert and Malguzzi (1985) considered an essentially inertial ocean with forcing and dissipation included as higher order effects. By making an expansion of the streamfunction in terms of a small parameter which determined the size of the sources and sinks of energy, they derived a system of nonlinear integro-differential equations, one of which, in principle, could be used to determine an unknown functional for a given wind stress. Such a system is of limited usefulness, since in general it will have to be solved numerically, and in this case straightforward solution of the full steady state barotropic vorticity equation is likely to be easier. Moreover, although it imposes a constraint on the functional, it still does not guarantee its uniqueness. There remains the question how the relationship between potential vorticity and the streamfunction affects the nature of the solution describing the inertial flow.

The complexity of the vorticity equation, when both advection and friction are included makes analytical calculations difficult, and use of numerical techniques becomes necessary. Bryan (1963), has solved the barotropic vorticity equation with lateral friction for various values of Reynolds number ranging from 10 to 120. Spin up of initially motionless

fluid, was achieved by applying a wind stress where curl had a single gyre profile. He showed that there exist steady solutions with fast western boundary current, provided that the Reynolds number is sufficiently small (Re $<$ 60). With smaller lateral friction the solutions became unsteady. Veronis (1966), found steady solutions with wind forcing and bottom friction. Some of his solutions with sufficiently small friction bear closer resemblance to Fofonoff's result; we shall return to this point later.

In steady, linear, general circulation models, small scale motions are included through parametrization (e.g. eddy viscosity) and it cannot describe the mesoscale flows.

During the past three decades a number of oceanographic field measurements have shown that in various parts of the world ocean, and in particular in the vicinity of the western boundary currents, there are intense mesoscale vortices with energy density much larger than that of the mean flow. The amount of data about such motions increased greatly since the introduction of the expendable bathytermograph (XBT) and more recently by use of satellite infrared imaging. Ring observations were reported in the North Pacific in the vicinity of Kuroshio current (Cheney and Richardson, 1977), in the Tasman sea off the coast of Australia, and in the South Atlantic in the region of the Brazilian and Falkland currents, but the most extensively studied are the Gulf Stream Rings.

After leaving the continental shelf north-east of Cape Hatteras, the Gulf Stream develops large amplitude meanders. Detaching southward meanders enclose the slope water and thus form cyclonic eddies known as

the Gulf Stream rings (Fuglister and Worthington, 1951). Similar (anticyclonic) eddies are formed from northward meanders of the Gulf Stream. The core of the ring contains water of lower salinity and temperature than the surrounding ocean, with the thermocline raised by as much as 500 m. The diameter of the ring is typically 100-250 km (based on the extent of 15 C water at the depth of 500 m). Its decay rate is small - some rings were observed for up to two years before disappearing after collision with the Gulf Stream (Lai and Richardson, 1977). The motion of the ring is slow: 1 to 8 km/day; generally in the west-southwest direction (this is somewhat larger than the speed of the mean ocean flow in the Sargasso sea).The particle velocity is relatively large (0.8 - 1.0 m/s; as in the Gulf Stream) and since the length scale is not large, the motion in the ring must be considered strongly nonlinear.

In modeling mesoscale eddies, two approaches have been commonly considered. In one, vortices are treated as soliton like isolated objects in the channel or on the infinite β-plane, and in another, they are regarded as a part of the general circulation. Until now studies of the second type were limited to evolution experiments, and no steady state solutions were found. Studies of the isolated eddies (the definition of "isolated" will be given below) are more numerous. They began with theories of long living atmospheric vortices (Long (1964) and Larsen (1965)), and the Great Red Spot of Jupiter (Maxworthy and Redekopp (1976)).

Stern (1975) obtained the first, exact, isolated solution of the steady state barotropic vorticity equation on the infinite β-plane. The modon is a

stationary dipole embedded in motionless fluid. Larichev and Reznik (1976) showed that modons have a steadily translating analog in which the streamfunction that vanishes exponentially as $r \rightarrow \infty$. More complicated versions of these results were found by Berestov (1979) for a dipole in continuously stratified fluid with constant Brunt-Väisälä frequency, and by Flierl et al. (1980), who derived an exact nonlinear solution of the two layer inviscid quasigeostrophic vorticity equation representing a solitary eddy which has baroclinic component and dipolar character. A radially symmetric component of arbitrary amplitude can be added to their solution, which masks the original dipole.

Flierl et al. (1983) showed that, on an infinite β-plane, solutions of the equations of motion describing an isolated vortex must satisfy the condition:

$$\beta \int \int \psi(x,y)\, dx\, dy = 0 \qquad \text{(I-1)}$$

which implies that the total angular momentum of the vortex must be zero. They define the vortex as "isolated" if its streamfunction vanishes at least as fast as $1/r^2$ as $r \rightarrow \infty$, where r is distance from the center of the vortex. A dipole (e.g. modon) is obviously the simplest structure satisfying condition (I-1). As a model for a Gulf Stream Ring, a modon has several shortcomings. Observed mesoscale vortices are nearly radially symmetric and usually move to the west (Lai and Richardson (1976)), while modons can move to the east or west but with velocity which for typical parameters is excessively large ($>$ 10 m/s). Monopoles cannot exist on the infinite β-plane unless the fluid is stratified and there is a countervortex in

the lower layer, or the eddy consists of a monopole and counterrotating outer "ring" which cancels its angular momentum.

It appears that the removal of boundaries of the oceanic basin represents an oversimplification of the problem, and that in search of solutions which could be used as models for mesoscale eddies one has to consider a basin of finite size.

Numerical evolution experiments have, in the past, typically dealt with statistical properties of the eddy field rather than behavior of specific vortices, In order to asses the importance of eddies in general circulation, Robinson et. al. (1977) made simulations of stratified flow in a basin on the β-plane using a five-layer model. In their work as well as in the paper of Holland (1978), nearly radially symmetric vortices were generated from the instability of the eastward, wind driven jet.

In the more recent work of Davey and Killworth (1984), the generation of a long living vortices and their behavior is described, but without reference to the large scale flow, so that this study is closer to the solitary wave-type works discussed before.

An analysis of vortex behavior (which is not of statistical character) in a closed basin is still lacking. Here we shall present new steady state solutions describing large scale flow in the basin with one or two vortices near the boundary current. Properties of vortices and their behavior under the influence of the friction and wind stress will be studied using evolution experiments.

We have already mentioned the problem of westward intensification and its formulation in terms of Rossby wave dynamics. We shall show that the friction, which when coupled with the β-effect is the cause of intensification in Stommel's and Munk's model, has a similar influence on the mesoscale vortices. Besides qualitative comparisons, we shall use numerical experiments to establish a quantitative relationship between the friction and a westward force acting on the vortex. This result is rather unexpected: friction is typically a mechanism that slows down the motion while here it accelerates the vortex through conversion of its energy of rotation into the kinetic energy of translation.

Homogeneous fluid is an useful approximation in modeling of the large scale flows. It does exhibit some basic features of the general circulation, but more realistic models must take into account stratification. Steady state quasigeostrophic vorticity equation for fully stratified fluid is three-dimensional and its solution is beyond capacity of computers at present. As an approximation to the continuously stratified ocean, one can consider fluid consisting of two layers with constant density. For oceanic motions this approximation is very good since in midlatitudes, top 600-700 meters of the ocean consist of water with typical density of 1.024-1.025 g/cm^3 which is influenced by atmospheric motion. At about 700 m (thermocline), density increases to 1.027-1.028 g/cm^3 and then remains nearly constant. This simplification will allow us to solve the problem of inertial stratified circulation.

Fofonoff's model, can be easily generalized to the two layer model, yielding a system of two linear or nonlinear Helmholtz-type equations. The first attempt to solve such a system was made by Fofonoff in his original paper, and later by several other investigators. Analytical solution of such a system is not easy to obtain and only recently Marshall et al. (1985) solved two-layer equations with linear relationship between potential vorticity and streamfunction. However, they had to make some additional assumptions on the flow e.g. that the layers have the same thickness and that they overlay a layer of much greater depth. In their work forcing and dissipation were treated as higher order effects and used to determine constants which in original Fofonoff's work were arbitrary. Here we shall consider stratified inertial flow with assumed relationships between the potential vorticity and the streamfunction which can be either linear or nonlinear. This poses a much more difficult technical problem than the homogeneous flow due to the limits of computer memory, and required computing time.

In a recent work by Keffer (1985), maps of the potential vorticity (q) in the oceanic basins were presented. He found that in the midthermocline, potential vorticity is essentially homogeneous, suggesting strongly nonlinear circulation. At greater depth, isolines of q are closer to the lines of constant $f_0 + \beta y$ due to weaker driving. Pure inertial two-layer model cannot produce accurate agreement with the observed flows. Some obvious reasons are poor vertical resolution and exclusion of friction and forcing. Also, a closed basin model of e.g. the North Atlantic subtropical gyre, can-

not account for intrusion of water from other parts of the world ocean. However, such a model may give flow with the patterns of q which is similar to the observed ones, in the midthermocline and lower thermocline. One of our solutions will show that this is the case. In the surface layer, which is under strong influence of the atmospheric disturbances, inertial model cannot apply.

We have already listed several questions which arise in studies of the large and meso-scale flows. The aim of this thesis was to answer some of them and to provide a model of steady circulation which will incorporate both of these phenomena. Although the results were obtained numerically, this work should be regarded as a study of *qualitative* properties of the steady state inviscid quasigeostrophic vorticity equation. Consequently, no attempt was made to fix coefficients in various functionals to adjust the transport, width of the boundary current, or some other property of the flow to be in agreement with observations. Rather, the parameters were varied across ranges to show how the flow changes with them. There are no analytical results, and all solutions are presented graphically. In some cases several similar plots will be shown. The reason for their inclusion was our desire to show that some different physical processes (eg. wind stress and dissipation) may produce very similar effects.

We could consider only some of the possible functional relationships and moreover our procedures do not guarantee that all solutions for a given nonlinear functional will be found. Consequently, conclusions drawn about general properties of inertial flows are tentative, but, keeping in

mind the number of solutions we obtained, it is very likely that they hold and we hope will be proved rigorously by some analytical technique.

The effects of bottom topography will be ignored in all computations. It is known that straightforward inclusion of bottom topography in the vorticity equation overestimates its influence on the flow, so that in steady general circulation models the variations in the shape of the sea floor can be neglected. In studies of the evolution of the flow, its importance may be greater as a triggering mechanism for development of instability (e.g. of eastward jet). It was argued by Warren (1963) that the seamounts in the path of the Gulf Stream may be the cause of its meandering. Such an orographically induced instability may produce some of the flows which will be discussed below.

II BAROTROPIC FLOWS

1 STEADY STATE SOLUTIONS

We shall consider a homogeneous incompressible fluid of constant depth in a rectangular basin on the β-plane, and neglect effects of friction, forcing and the exchange of heat. Vertical motions will also be neglected so that the pressure is given by the hydrostatic equation. It is well known that under these assumptions the steady state barotropic vorticity equation takes the simple form:

$$\nabla^2 \psi + \beta (y - y_0) + F (\delta , \gamma , \psi) = 0 \qquad \text{(II-1)}$$

with the boundary condition:

$$\psi = \text{constant} \ \ (= 0)$$

i.e. normal velocity on the boundary vanishes. The domain is the unit square, $\beta = \dfrac{\beta_0 L^2}{U}$ is the scaled northward gradient of the Coriolis parameter and y_0 is a constant, usually chosen in the interval [0,1]. For large scale motions, the length, L, must be at least 1000 km, the velocity of the interior flow ,U, is in the range between 1 and 5 cm/s and $\beta_0 = 10^{-11}$ m^{-1} s^{-1}, so that β will be O(10^3). F (δ , γ , ψ) is an arbitrary function of the streamfunction ψ, δ is a free parameter and γ will measure the size of nonlinear terms in F. We shall for simplicity, consider only single valued analytic functionals. Vorticity, the eastward and northward velocity components are related to the streamfunction ψ by:

$$\varsigma = \nabla^2 \psi$$

$$u = -\frac{\partial \psi}{\partial y}$$

$$v = \frac{\partial \psi}{\partial x}$$

Equation (II-1) was solved numerically using a fourth order ("compact") finite difference approximation with nine point molecule on the grids 25x25, 37x37 and 49x49. The resulting system of nonlinear equations was solved by pseudoarclength continuation (Keller (1977)) and Newton's iteration, which will be described in Chapter III. For large β the solutions have sharp boundary layers, which are difficult to resolve in evolution experiments, but, for the steady state solutions, the problem is simpler, since only one discretization point in the layer is necessary (in our experiments there will be typically 3 to 5). Consequently, there will be no difficulties with resolving the flow for all physically relevant values of β (100 - 4000). By comparing solutions on the different grids we have found that the maximum error on the finest grid is less than 0.5%. For some of the continuation curves, computations were repeated with the streamfunction approximated by truncated double Chebyshev series, confirming the correctness of above error estimate.

Fofonoff solved (II-1) with

$$F(\delta, \psi) = \delta \psi \qquad \text{(II-2)}$$

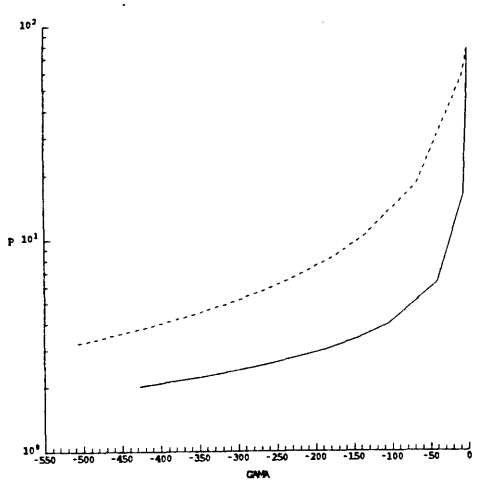
where $\delta = -\beta$, so that the velocity is negative (westward) and its magnitude is equal to the scale velocity, U. In that case, an exact analytic solution in terms of Fourier series can be obtained, but since β is large, the boundary layer method gives a good approximation (Fig. 2):

$$\psi = -\frac{\beta}{\delta}\left[(y-y_0)\left(1-e^{-x\sqrt{\beta}}-e^{-(1-x)\sqrt{\beta}}\right)-(1-y_0)\,e^{-(1-y)\sqrt{\beta}}+y_0\,e^{-y\sqrt{\beta}}\right]$$

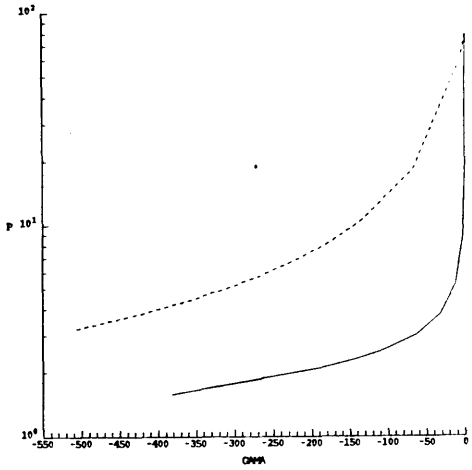
This solution is known to be stable under small but finite amplitude perturbations, since it satisfies the sufficient condition for stability (Arnol'd (1965); Blumen (1968)) which can be written as:

$$0 < -\frac{\partial F(\psi)}{\partial \psi} < \infty \qquad \text{(II-3)}$$

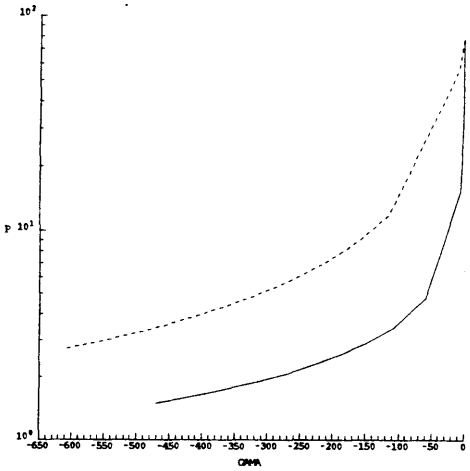
We shall consider (II-1) with various nonlinear functionals. In a search for solutions which resemble large scale circulation, we shall be primarily interested in those which have slow interior flow and are stable. We cannot show streamfunctions of all solutions that were found, but observing the relationship between the $|\psi|_{max}$ and the parameter γ is instructive. Figure 3 shows the continuation curves for some nonlinear functionals (solid lines), compared to the curve for the linear one ($\beta = 2000$, $y_0 = 0$). The maximum of the streamfunction decreases with γ, so that for polynomial or rational function solution reduces to the linear (this holds for variety of other functionals e.g. $\gamma \sinh(\psi)$, $\gamma'(e^{\psi}-1)$ etc.). All of these solutions are stable as long as $\gamma < 0$. For $F(\psi) = \gamma\,\psi^n$, situation is more complicated. First, we note that these solutions do not satisfy (II-3) (it is violated at $\psi = 0$), and may be unstable. Nevertheless, since ψ_{max} decreases with γ, we expect that the pattern for $|\gamma| >> 1$ will be similar to the Fofonoff's gyre. Indeed, single gyre flow with $y_0 = 0$, is almost the same as the linear one, except for appearance of a weak *westward* boundary current at y_0. If n is odd, and $y_0 > 0$ this current will occur at the latitude y_0.



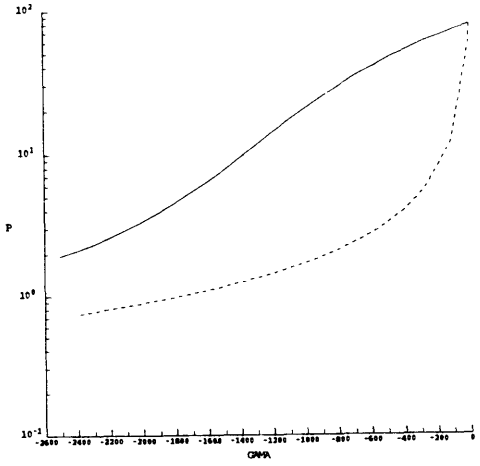
a) $F(\gamma,\psi) = \gamma\psi^2$



b) $F(\gamma,\psi) = \gamma\psi^3$



c) $F(\gamma,\psi) = \gamma\psi(1+\psi)$



d) $F(\gamma,\psi) = \dfrac{\gamma\psi}{1+\psi}$

Figure 3. The continuation curves: $|\psi|_{max}$ vs. γ, for various nonlinear functionals (solid lines), and a linear functional (dashed lines); $\beta = 2000$; $y_0 = 0$.

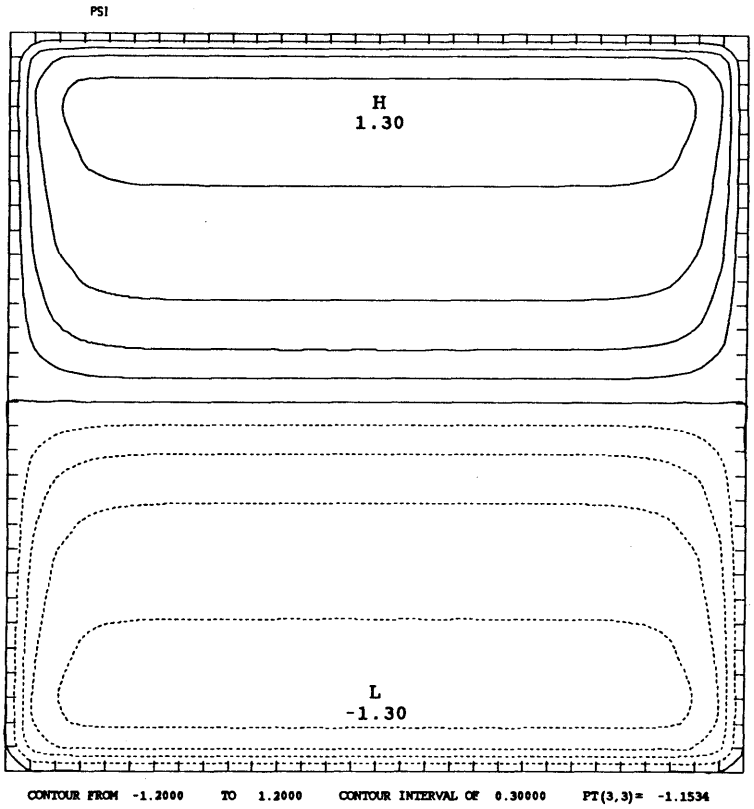


Figure 4a. The streamfunction for $F(\psi) = \gamma\psi^3$
$\gamma = -338.67$; $\beta = 2000$; $y_0 = 1/2$

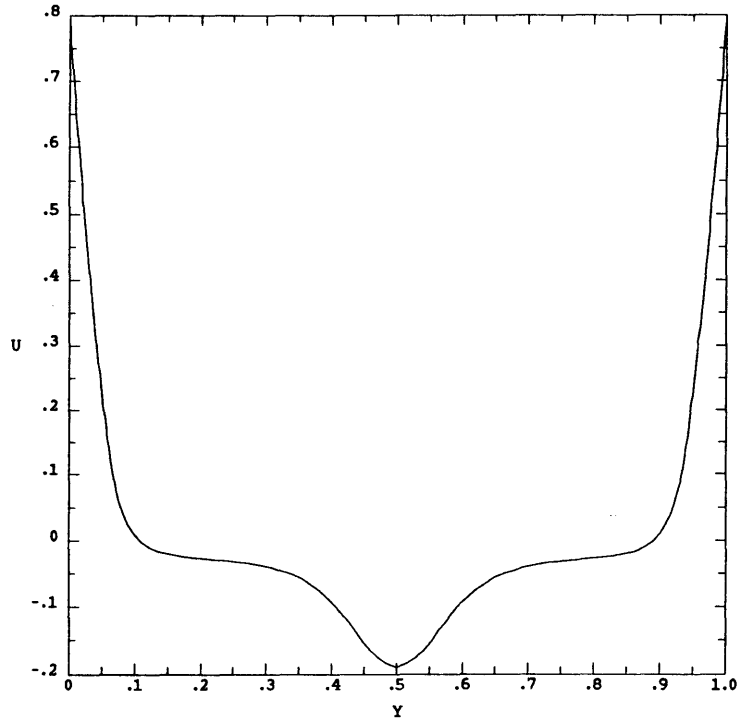


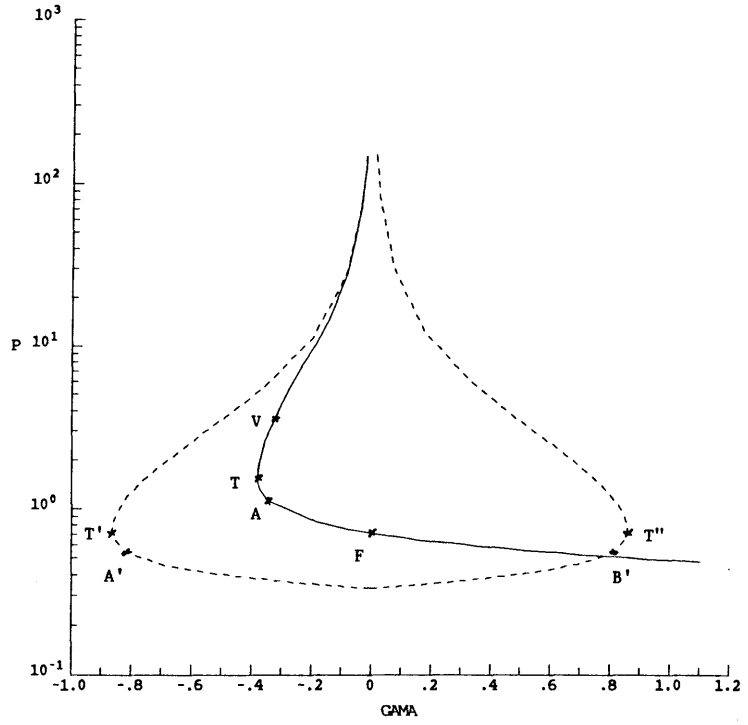
Figure 4b. Profile of the east-west velocity, u(y), at x=1/2 (m/s)

It is much wider and slower than the boundary currents, but faster than the return flow (Fig. 4). For n even and $y_0 \neq 0,1$, it is clear from parity considerations, that there will be a region in the basin (other than the boundary layer) where $F(\psi)$ cannot balance the β-term, so that the relative vorticity must be large. This will in general produce a very strong large vortex. In the next example, a similar vortex will appear, but with more interesting properties.

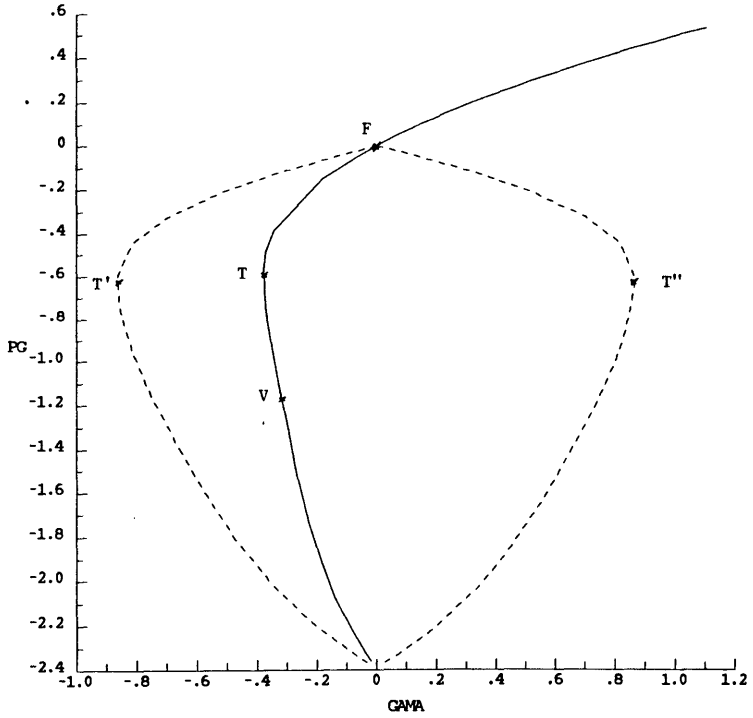
Let

$$F(\delta, \gamma, \psi) = \delta \psi (1 + \gamma \psi) \qquad \text{(II-4)}$$

Equation (II-1), with (II-4) has two solutions for $\gamma \in [T', 0)$ and $\gamma \in (0, T'']$, where T' and T" are left and right turning points. This will hold provided that $0 < y_0 < 1$, and β is sufficiently large (e.g. for small β say $\beta=50$ only one solution was found in the interval $-700 < \gamma < 700$). A typical continuation curve of the dependence of the maximum of the absolute value of the streamfunction on γ is shown in Figure 5 ($\beta = 2000$; $\delta = -1.25\beta$). The dashed curve is symmetric with respect to the axis $\gamma = 0$, since $y_0 = 1/2$; as $y_0 \to 0$ the right turning point will shift to $+\infty$ and for $y_0 = 0$ only one solution was found in the right half of the $(\gamma, |\psi|_{max})$ plane (solid curve). Analogously, the shift $y_0 \to 1$ causes $T' \to -\infty$. To the right of the turning point T, the pattern of the flows is essentially the same as the linear one (Fig. 2). However, due to the nonlinear term, the boundary current may be wider and interior velocity cannot be constant, but slowly varies.

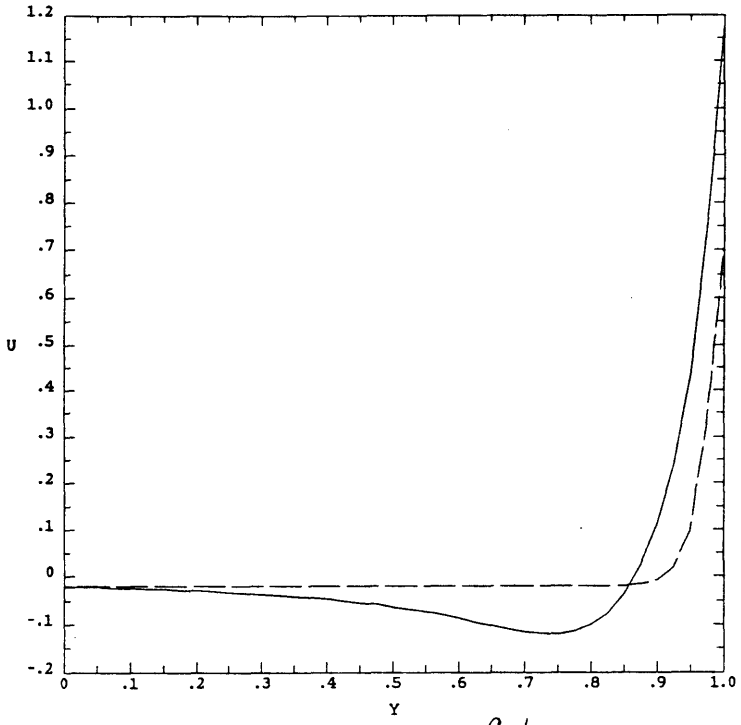


a) $|\psi(\gamma)|_{max}$; T,T',T" are the turning points.
V denotes the solution shown in the Figures 7.
F denotes Fofonoff's solution (Fig. 2)

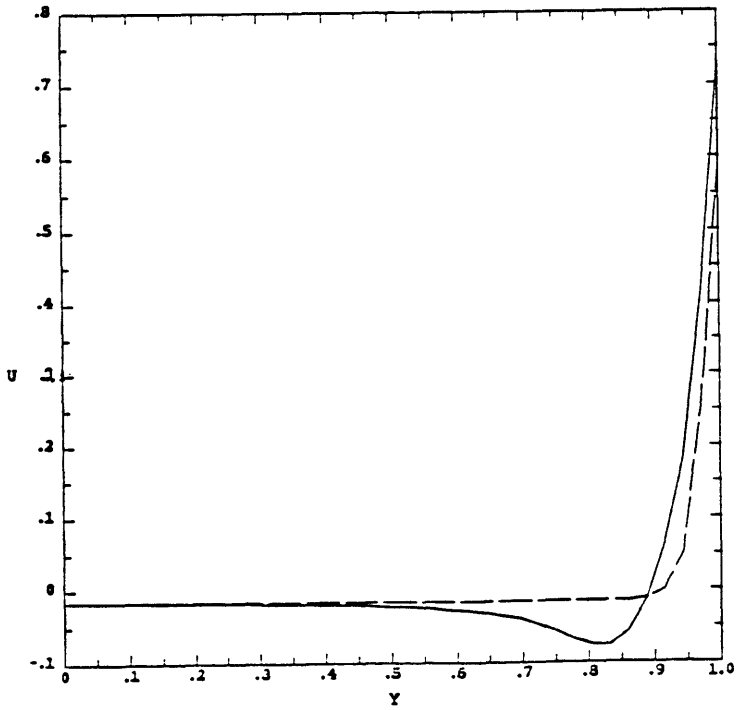


b) $\gamma\,|\psi(\gamma)|_{max}$ (i.e. relative size of the maximum of the nonlinear term)

Figure 5. The continuation curves for the functional (II-4) with $\beta = 2000$; $\delta = -2500$; $y_0 = 0$ (solid curve); $y_0 = 1/2$ (dashed curve)



a) $F(\psi) = -\dfrac{\beta\,\psi}{1 + 0.85\psi}$



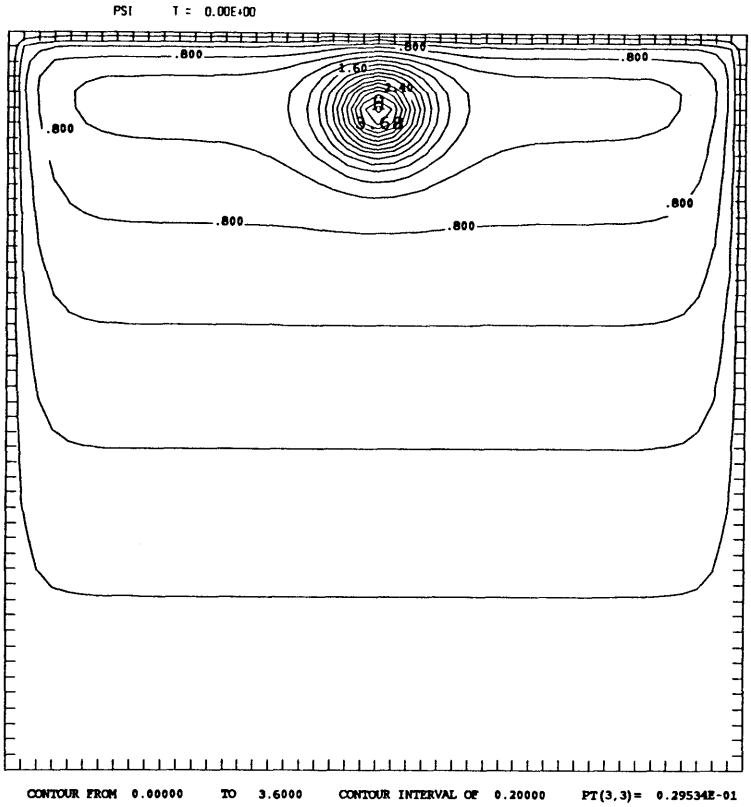
b) $F(\psi) = -\,2500\;\psi\,(\,1 - 0.32\;\psi^3\,)$

Figure 6. Profile of the east-west velocity, u(y), at x = 1/2 for two nonlinear functionals (solid curves), and a linear functional (dashed curves). $\beta = 2000$; $y_0 = 0$

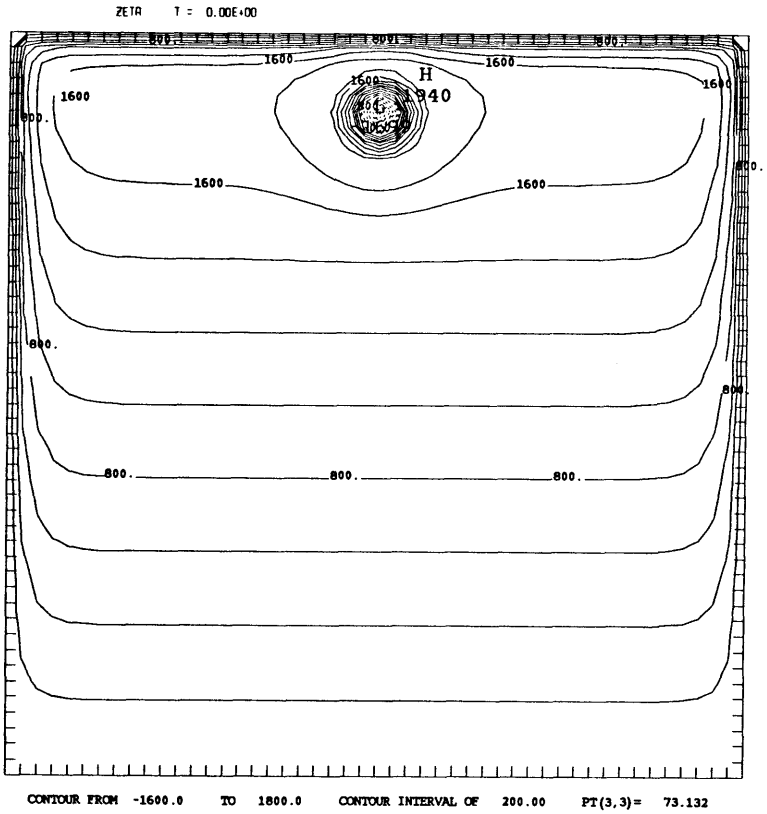
Estimates of the width of the inertial boundary layer (Pedlosky (1979)) are usually given with the assumption that the streamfunction has small amplitude, i.e. it is effectively reduced to Fofonoff's model. In midlatitudes with $\beta = 2000$, the interior velocity is U = 2 cm/s and scale length L = 2000 km, so the dimensional width is $\delta_I = (\frac{U}{\beta_0})^{1/2} \approx 45$ km . For nonlinear F, the width may be substantially larger. In Fig. 6 profiles of the east-west velocity at x = 0.5 (1000km) for two nonlinear functionals (solid curves) are compared with the profile of the linear one (dashed curves). Increase of the eastward transport is compensated by the appearance of the counterflow on the seaward side of the boundary current. This phenomenon is observed in nature and is usually described as a consequence of friction (see e.g. Pedlosky (1979)). As our result shows, it may well be regarded as a purely inertial effect.

By solving (II-1) with (II-4) for various values of γ, it can be shown that the condition (II-3) holds for all solutions on the continuation curve to the right of the point A (solid curve), and between points A' and B' (dashed curve in Fig. 5). Solutions with the velocity profiles given in Fig. 6 are also stable.

Above the turning point T (Fig. 5) solution changes character. If β is relatively small (e.g. 200), when γ increases there develops a strong large eddy which covers more than half of the inertial gyre. Such a flow is not relevant for oceanic circulation since the particle speed in the interior is too large.

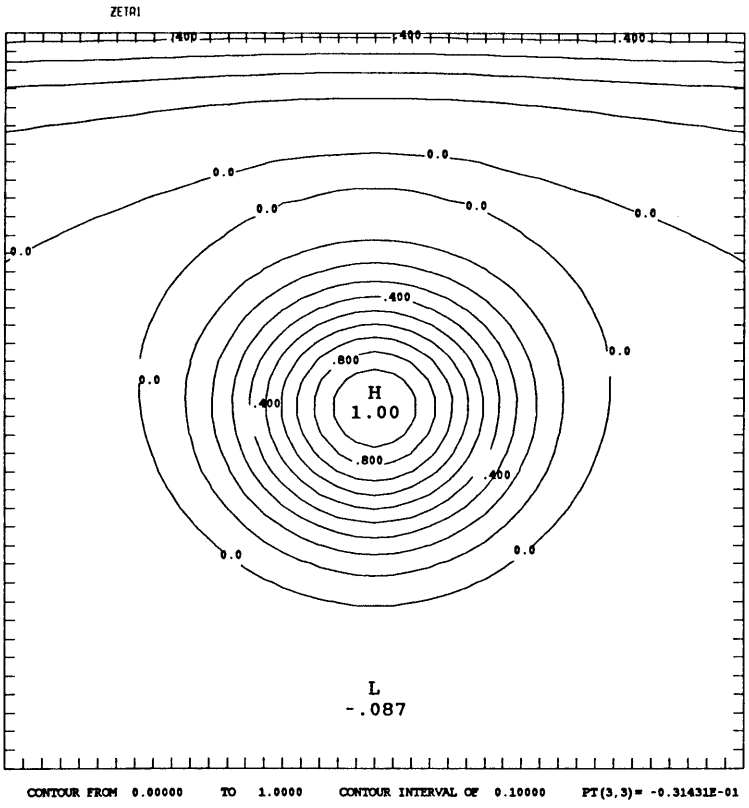


a) ψ

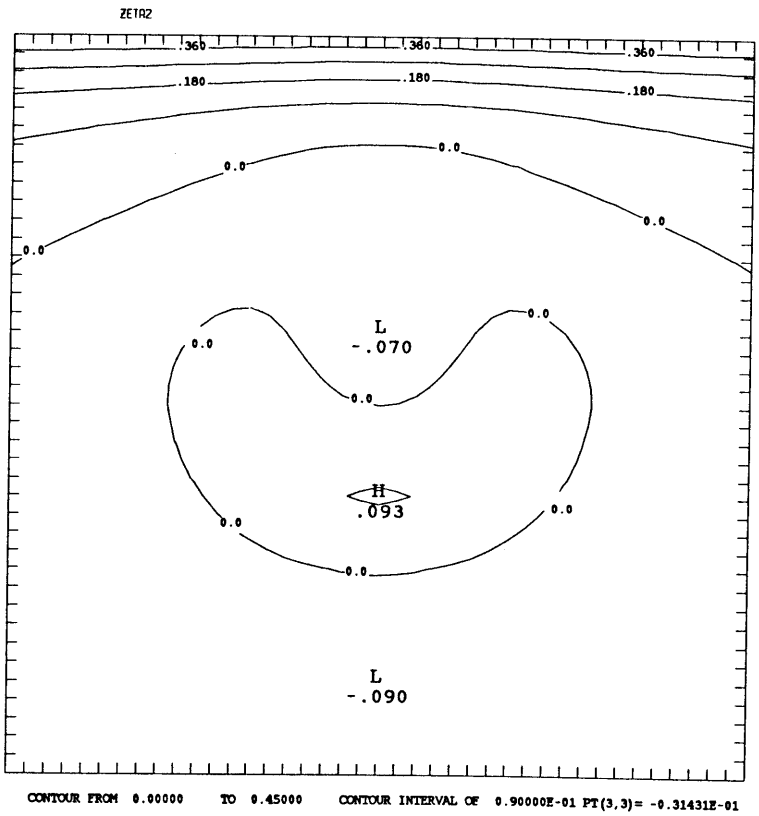


b) q

Figure 7. The streamfunction (a) and the potential vorticity (b) for the functional $F(\psi) = -2500\,\psi\,(1 - 0.322\psi)$;$\beta = 2000$; $y_0 = 0$.



a) ς



b) $[\varsigma - e^{-(\frac{r-r_0}{0.032})^2}]/\varsigma_{max}$

Figure 8. The enlarged area of the vortex [0.40,0.60]x[0.79,0.99] showing normalized vorticity (a) and the vorticity after subtracting the radially symmetric part (b)

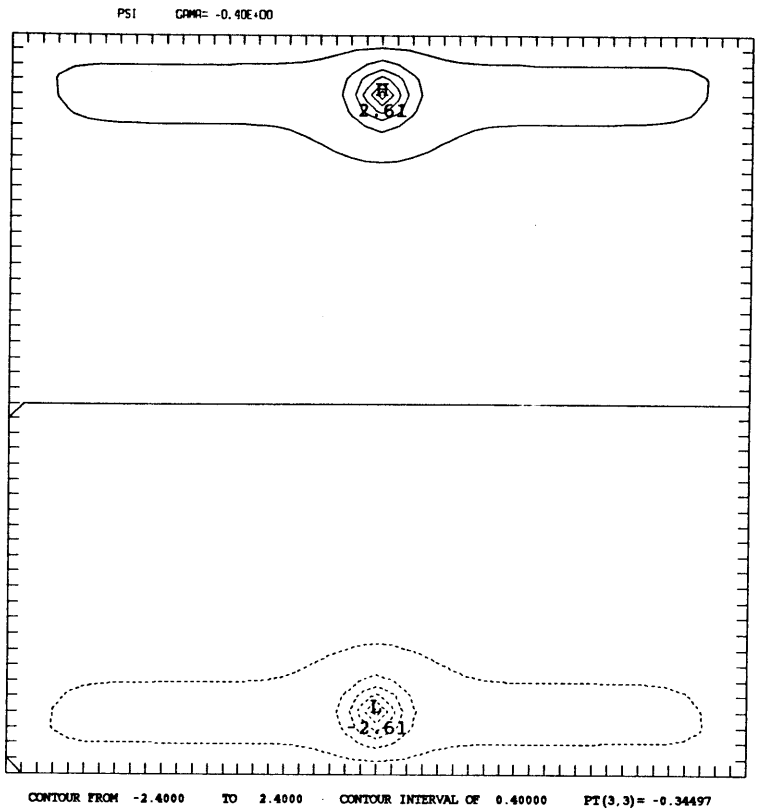
However, as β increases the flow becomes slower, and the eddy becomes smaller eventually (at $\beta = 2000$) degenerating into a vortex of the size of mesoscale eddy near the boundary current (Fig. 7). In Figure 5. the point V denotes this solution on the continuation curve.

In the vortex core, the nonlinear term in F (γ , ψ) is larger than the linear (Fig. 5b) and F has the same sign and nearly the same magnitude as the β-term. In the interior, the nonlinear correction is small but not negligible, so that the velocity varies from 1.7 cm/s at the southern boundary to 3 cm/s in the northern part. Boundary current and the vortex have particle velocities of 0.5-0.8 m/s, and contain almost all energy of the flow. The eddy is nearly radially symmetric. Taking for the edge of the vortex point where the streamfunction is a half of its maximum value, we find an east-west diameter of 270 km and a north-south diameter of 240 km. The structure of the flow becomes clearer after subtracting the radially symmetric part. Let

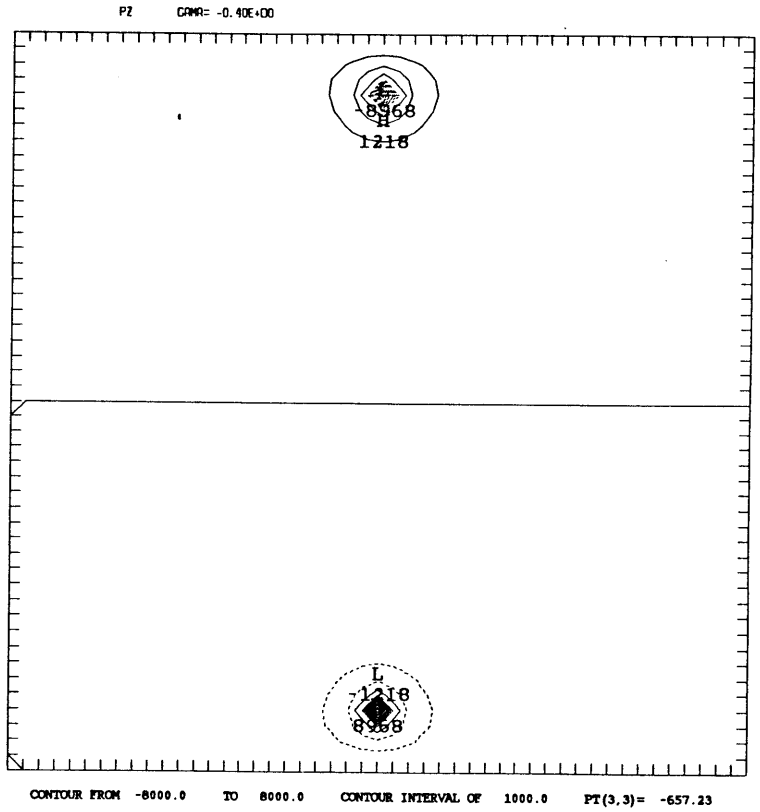
$$\varsigma_1 = (\varsigma - \exp (- R^2))/\varsigma_{max}$$

where ς is the relative vorticity of the flow, $R = (r - r_0)/\alpha$, r_0 is the center of the vortex and α is small number which depends on properties of the vortex (which in turn are determined by β and γ) here $\alpha = 0.032$. ς_1 (Fig. 8) contains a weak asymmetric dipole. Its southern (stronger) part is less than 10% of ς_{max}.

The above described solution holds for $y_0 = 0$. On the other hand, if $y_0 = 1$ and $\gamma > 0$ one obtains a solution in the form of gyre with the cyclonic vortex near the southern boundary.



a) ψ



b) q

Figure 9. The streamfunction (a) and the potential vorticity (b) for the functional $F(\psi) = -\beta\,\psi\,(1 - 0.4\psi^2)$; $\beta = 2000$; $y_0 = 1/2$.

Note that the vortex has always the same sign of the vorticity as the gyre in which it is embedded.

As in Fofonoff's solution (see e.g. Pedlosky (1979) p. 289), when $0 < y_0 < 1$, the pattern will consist of two gyres, which between the turning points T' and T'' (dashed curve in the Figure 5) is similar to the linear one, except that the northern boundary current is wider if $\gamma < 0$ while the southern one remains in the linear regime. The opposite happens when $\gamma > 0$. Above the left turning point T', the northern gyre will develop a small anticyclonic vortex like the single gyre solution, while the southern one will remain unchanged. Similarly, above the right turning point T'', the southern gyre will contain a cyclonic vortex.

For higher order correction,

$$F (\delta , \gamma , \psi) = \delta \psi (1 + \gamma \psi^n) \qquad \text{(II-5)}$$

the solution for $y_0 = 0{,}1$ is similar to that of Fig. 7, except that the vortex is smaller and more intense. If n is even, F is odd function of ψ and when $y_0 \neq 0{,}1$, there will be two vortices near both the northern and southern boundary current (Fig. 9). We have solved (II-1) with (II-5) for n =2,3,4, but we expect that the same conclusions would hold for higher powers. In contrast with previous solutions describing small vortices which exist only for certain functional and moreover only for certain parameter values (those which satisfy some "dispersion relation"), our solution apparently exists for an entire class of functionals and for parameter values which may change continuously.

In the recent work of Malguzzi and Rizzoli (1984), equation (II-1) was solved in a channel with F as in (II-5) with n=2. They obtained a dipole superimposed on a shearing flow with cubic profile. However, their result is fundamentally different from ours, because their solution exists only if the nonlinear term $\gamma\psi^2$ is small compared to unity (though not infinitesimal, this is a "weakly nonlinear problem"). Our solution with vortices can exist only if the nonlinear term is *sufficiently large.* More specifically, it exists only above the turning point when $| \gamma \psi |_{max} > 1/2$. At this point the vortex is extremely weak (see Fig. 10b), and for the strong vortex of Fig. 7 $| \gamma \psi |_{max} \approx 1.2$, i.e. it dominates the linear term. Figure 5b shows how the product $| \gamma\psi |_{max}$ changes with γ for the same data as in the Figure 5a. As $\gamma \rightarrow 0$, the product reaches the asymptotic value of -2.4. This limit is associated with the second singular point of the partial differential operator in (II-1), the first one being the turning point T. In the next section we shall examine the stability properties of such solutions.

Our procedure does not guarantee that all solutions of equation (II-1) for given F will be found. There may be additional solutions on disjoint branches, which could be found if the number of variable parameters is increased. One such example will be described in the Chapter III in the context of two-layer flow.

For a single layer, we found no physically relevant bifurcation points, although in some cases, e.g. $F = \gamma \sin (\psi)$ with $| \gamma | >> 1$, several numerical bifurcations were observed, but they disappeared upon refining

the mesh.

There is no physical reason why, for inertial flows, any one particular relationship between potential vorticity and streamfunction which satisfies the conditions of having a slow interior flow and being stable should be favored over another. We have examined solutions for a number of functionals to see how the flow pattern changes. Only functionals such that $F(0) = 0$ were considered (this is not restrictive because if the first term in the Taylor expansion of F is a constant it can be absorbed in y_0).

For *all solutions that we computed, which satisfy the above stated conditions the basic pattern is qualitatively the same as Fofonoff's*, only in some instances the boundary current was wider.

2 PERTURBATION EXPERIMENTS

Solutions with vortices do not satisfy the Arnol'd-Blumen condition and may be unstable. It is possible to investigate the stability of such flows numerically by solving the normal mode problem. This approach is cumbersome and if no growing modes are found it would still be inconclusive. Instead, we shall solve the time dependent problem with the initial condition in the form

$$\varsigma = \varsigma_0 + \varsigma_p$$

where ς_0 is vorticity of the steady solution, and ς_p is the perturbation:

$$\varsigma_p = P \mid \varsigma_0 \mid \frac{\sum_{i=ML}^{i=MU} \sum_{j=ML}^{j=MU} \alpha_{i,j} \cos(\pi x+\omega_i) \cos(\pi y+\omega_j)}{\left| \sum_{i=ML}^{i=MU} \sum_{j=ML}^{j=MU} \alpha_{i,j} \cos(\pi x+\omega_i) \cos(\pi y+\omega_j) \right|} \qquad \text{(II-6)}$$

where $\alpha_{i,j}$ are random numbers from the interval [-1/2,1/2], while ω_i and ω_j are random numbers from the interval $[0,\pi]$. P measures relative size of the vorticity of the perturbation and $|\cdot|$ denotes L_2 norm:

$$\mid \varsigma_0 \mid = \left(\int_0^1 \int_0^1 \varsigma_0^2(x,y)\, dxdy \right)^{1/2}$$

The barotropic vorticity equation

$$\frac{\partial \varsigma}{\partial t} + \frac{\partial \psi}{\partial x} \frac{\partial \varsigma}{\partial y} - \frac{\partial \psi}{\partial y} \frac{\partial \varsigma}{\partial x} + \beta \frac{\partial \psi}{\partial x} = 0 \qquad \text{(II-7)}$$

was solved numerically with free slip boundary conditions ($\varsigma = 0$). The timestepping scheme was leapfrog and the space discretization scheme was second order centered finite differences with the Arakawa formulation of the Jacobian. The experiments with low frequency perturbations were

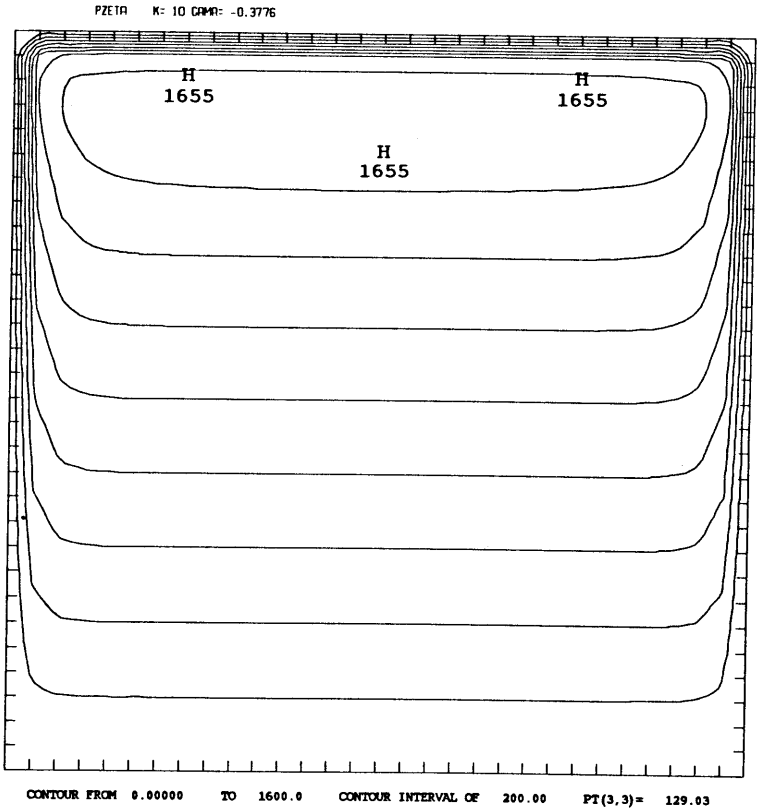
done on a grid 145x145, and those with high frequency on a grid 257x257.

Before we proceed with description of the perturbation experiments we shall examine in which region of the basin the condition (II-3) is violated and how the solution changes in the vicinity of the turning point (Fig. 5). We have examined solutions just to the right, and to the left of the point A (both on the lower branch). Although one of the solutions ("right") satisfies the Arnol'd-Blumen condition and the other does not, there were no qualitative differences. Thus, it is possible that all flows between points A and T are still stable (remember that the Arnol'd-Blumen condition is *sufficient*, but not necessary for the stability). Near the turning point T, there is a sudden change. Figure 10 shows the potential vorticity of the flow below T (upper plot) and above T (lower plot). Note the appearance of the "hole" in the potential vorticity surface in the place where the vortex will develop. The rest of the pattern is almost unchanged. This suggests that the instability will be confined (at least for sufficiently short time) to the area of the vortex. We plotted potential vorticity instead of the streamfunction, because it is much more sensitive to the changes of the parameter γ.

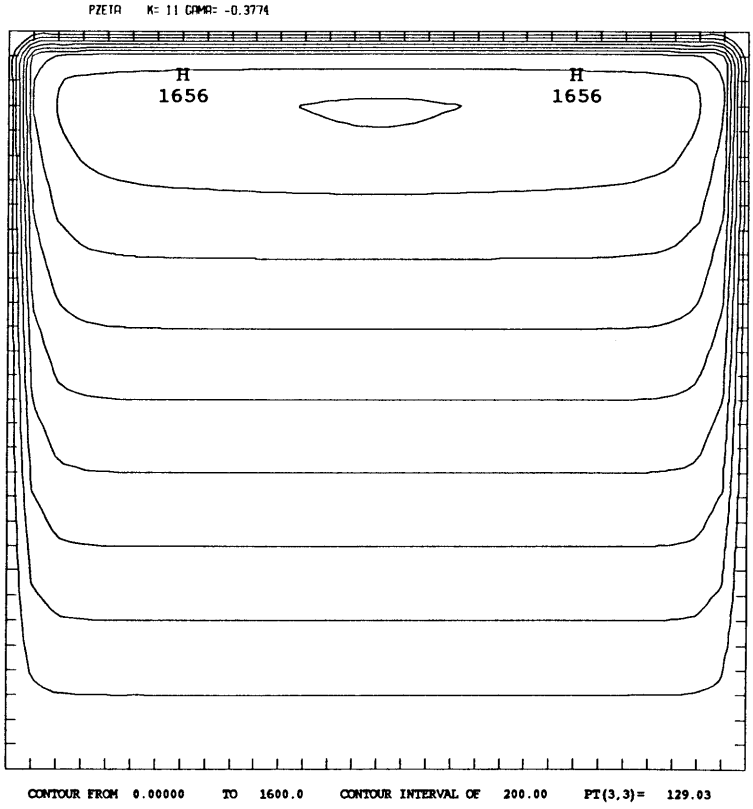
Equation (II-1) with (II-4), was solved with assumption that the Rossby radius is infinite.[1]

---

[1] The Rossby radius is defined as $R = \frac{(gD)^{1/2}}{f_0}$ where g is gravitational acceleration, D is the depth of the ocean and f_0 is Coriolis parameter.) For typical parameter values: $g = 10 ms^{-2}$, $f_0 = 10^{-4}\ s^{-1}$ and $D = 4000$ m, we have $R = 2000$ km, which equals the size of the basin, so the scaled Rossby radius is 1.



a) $\gamma = -0.3776$



b) $\gamma = -0.3774$

Figure 10. Potential vorticity of the solution below (a) and above (b) the turning point T in Figure 5a.

It is easily seen that our solution (Fig. 7) is also the solution of the vorticity equation with the effects of surface deformation included:

$$(\nabla^2 - (\frac{L}{R})^2) \psi + \beta (y - y_0) + G(\gamma,\delta,\psi) = 0 \qquad \text{(II-8)}$$

where $G(\gamma,\delta,\psi) = \delta \psi (1 + \frac{L^2}{\delta R^2} + \gamma \psi)$. Note that $| \frac{L^2}{\delta R^2} | \ll 1$.

Recently, Benzi et al. (1982) found that for the barotropic vorticity equation with finite Rossby radius, there are two sufficient conditions for for the stability under small but finite amplitude perturbations: first,

$$\text{a)} \qquad 0 < - \frac{\partial G}{\partial \psi} < \infty \qquad \text{(II-9)}$$

which is a generalization of (II-3), or, second,

$$\text{b)} \qquad - \infty < - \frac{\partial G}{\partial \psi} \leq - (\frac{R}{L})^2$$

We applied these inequalities to the vortex solution. The basin can be divided into three parts: outside the solid curve (Fig. 11) inequality a) holds, while b) holds within. Actually, these two regions are separated by a gap which is very narrow, because $| \frac{R^2}{2\gamma\delta L^2} | \ll 1$, and in which neither a) nor b) hold. Both conditions (II-9), as well as (II-3), were derived from integral inequalities and they cannot show how the local instability will occur. Nevertheless, we may expect that the vortex where b) is satisfied, will be robust, and that instability may occur in the annulus that separates it from the surrounding flow.

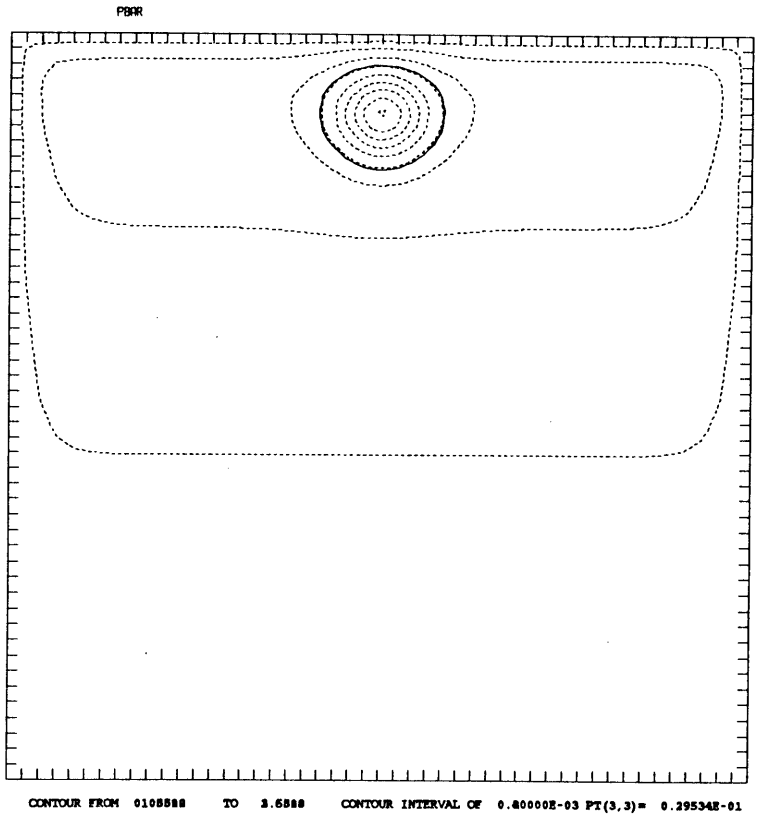


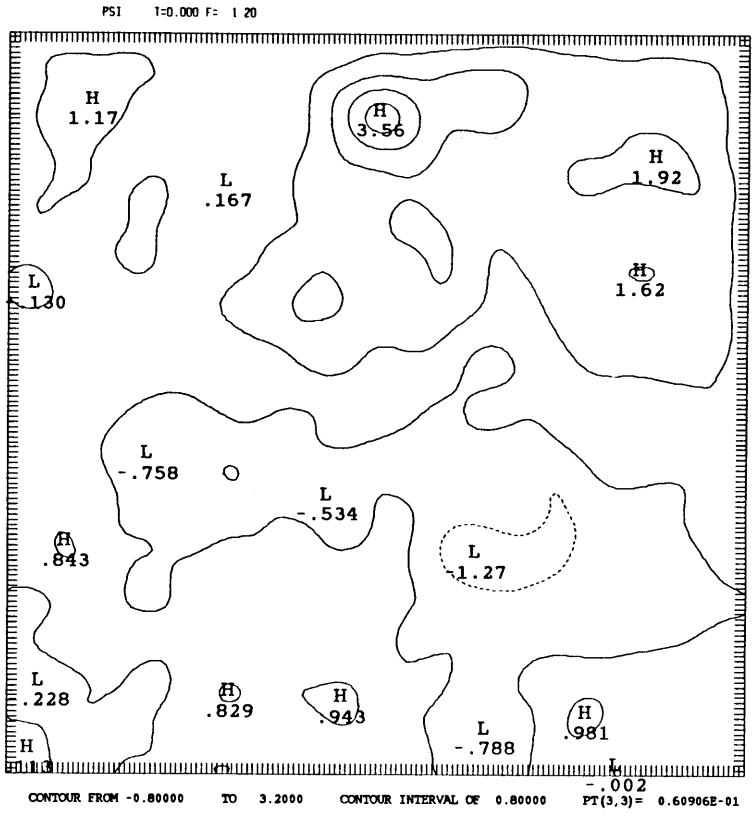
Figure 11. Streamfunction of the solution from Fig. 7 (dashed lines). Solid line separates regions satisfying Arnol'd-Blumen condition (outside) and BVPS condition (inside).

To examine the response of the vortex to the perturbations we performed a number of perturbation experiments for various magnitudes and frequencies of perturbations. Here we shall show results of three of them.

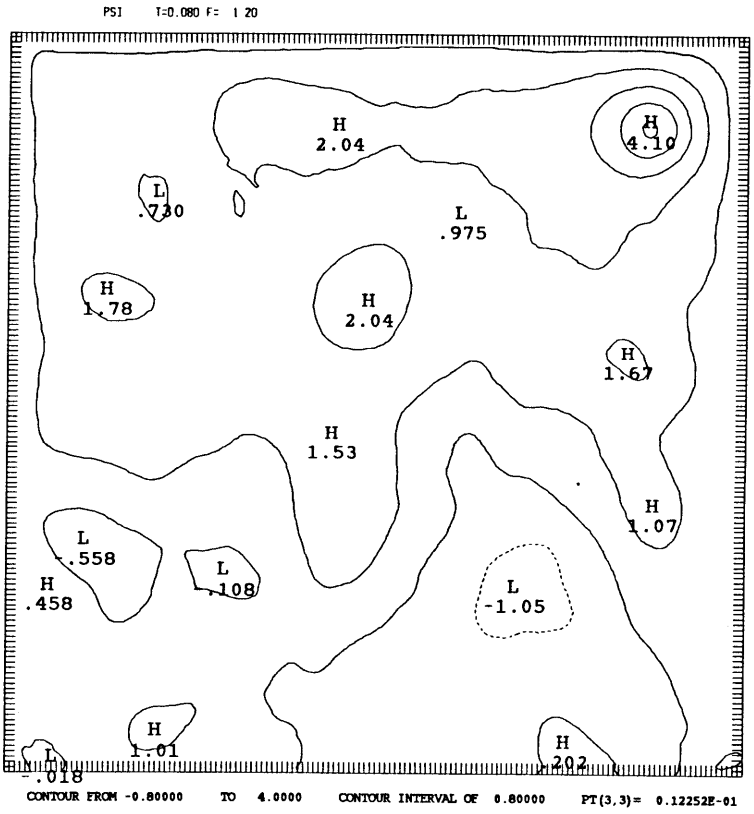
EXPERIMENT II-1

We shall first consider only low frequency perturbations, i.e. in which the wavelength is of the order the diameter of the vortex or larger. Thus let ML=1 and MU=20 and P = 1 (so the RMS vorticity of the perturbation equals that of the basic flow). Figure 12a shows the streamfunction of the initial condition. The integration time will be relatively short since the characteristic time of the large scale flow is 10^8s or 1157 days, which is long compared to the characteristic time of the vortex ($O(10^5$s)). Under the influence of perturbations, the vortex moves to the east with nearly uniform velocity ($\approx$ 8.5 km/day) and after the time 0.08 (dimensionally 93 days) reaches the boundary. The vortex was not carried by the boundary current since its velocity of translation is much smaller. There is no dispersion prior to the collision (Fig 12b).

There is some ambiguity in determination of the time of collision. One possibility the time when the maximum of the streamfunction of the vortex is closest to the boundary. However, the vortex "feels" the boundary earlier, so that it is more appropriate to choose the time when its amplitude starts rapidly decreasing. In this set of experiments another uncertainty is induced by perturbations passing through the vortex, masking the position of its center.

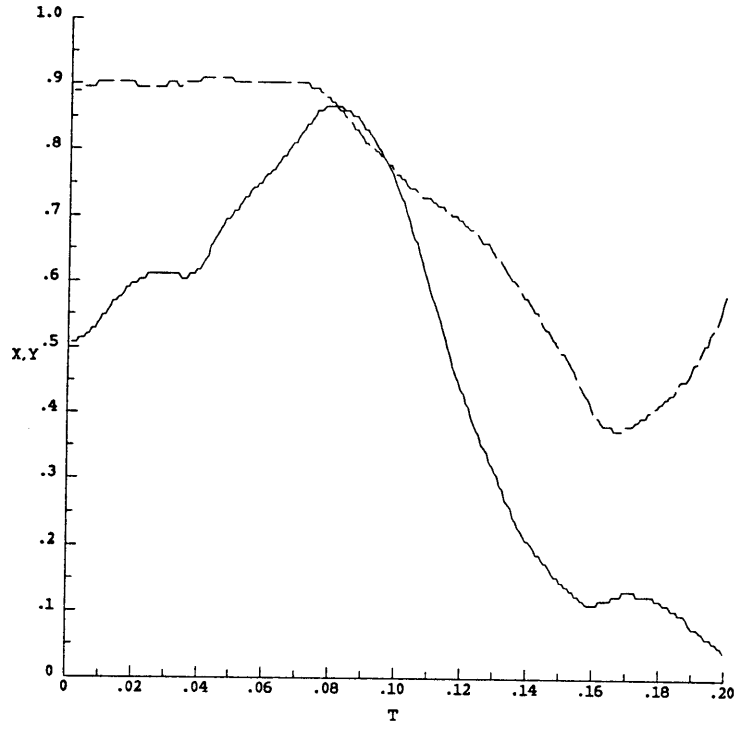


a) Initial condition; ML=1, MU=20, P=1, τ_0=0, r=0

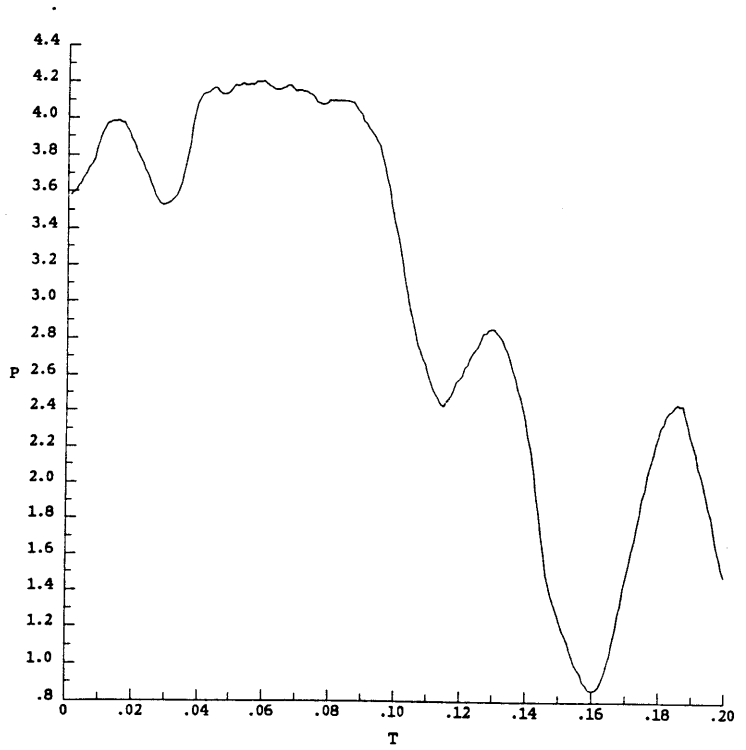


b) Streamfunction after t=0.08 (93 days).

Figure 12. EXPERIMENT II-1



c) Coordinates of the center of the vortex; x - solid curve; y - dashed curve.



d) Magnitude of the streamfunction in the center of the vortex.

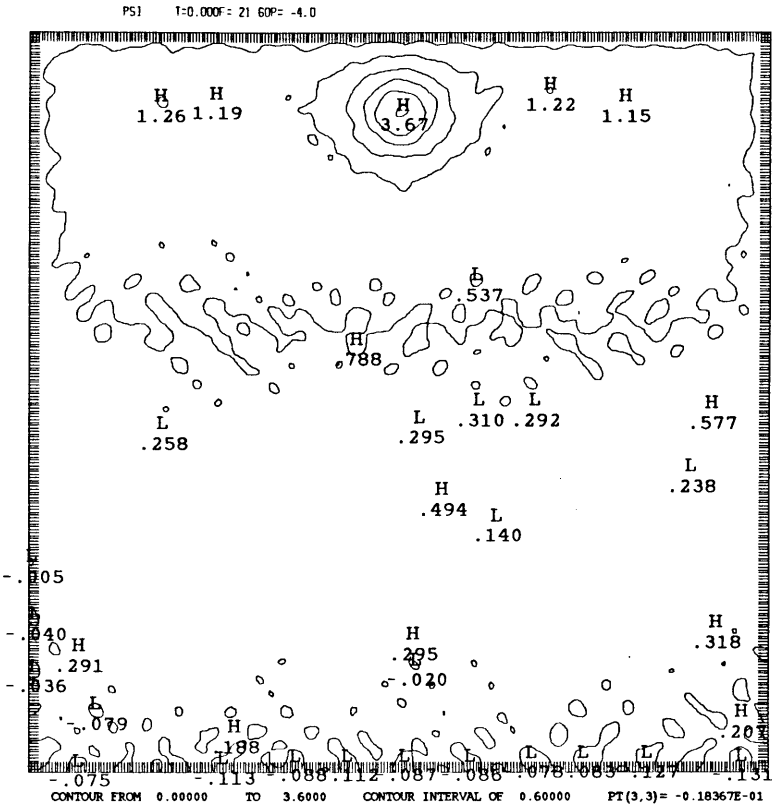
Figure 12. EXPERIMENT II-1

Thus, the above estimate of collision time has an error which is less than D/U, where D is the length of its east-west semiaxis and U is the speed of translation just before collision (a good estimate being the average speed of translation). Note that the amplitude of the vortex has slightly increased showing that the vortex may gain strength at the expense of the perturbations. After the collision, the vortex moves to the southwest with rapidly decreasing amplitude and after the time 0.20 (232 days) disappears. This experiment was repeated with the same ML,MU and P and only the sign of the perturbation changed. As a result the vortex moved to the west with the same speed as in the original experiment.

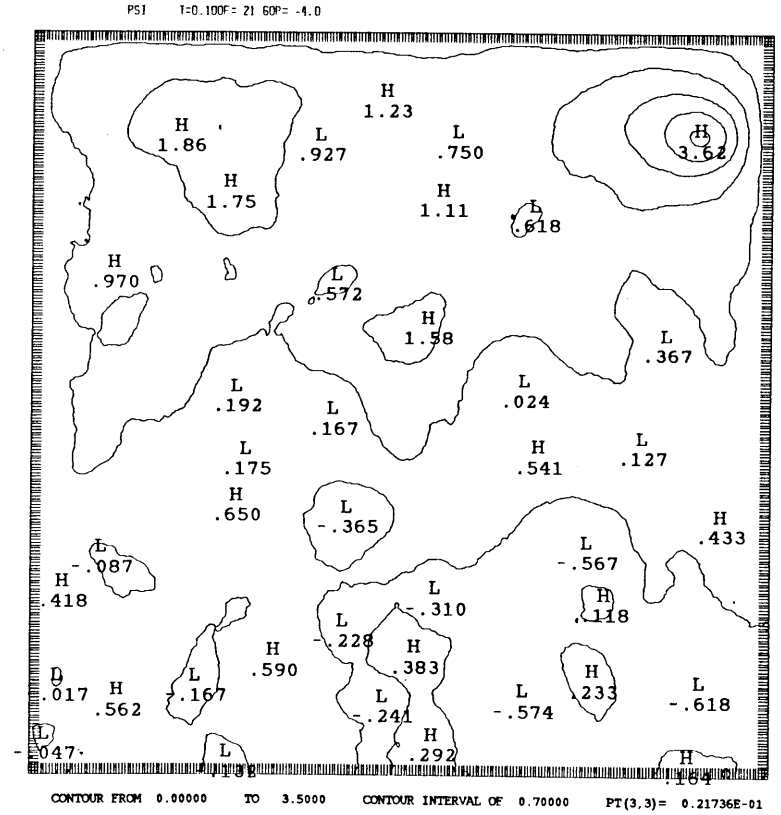
This experiment was repeated with the perturbations of the same frequency and sign, but larger amplitude (P=4). The perturbed vortex moved very rapidly to the east and collided with the boundary after time 0.01 (only 16 days). In this period, there was no decrease of its amplitude and dispersion was not observed.

EXPERIMENT II-2

In this experiment we observed the behavior of the vortex under the influence of the high frequency perturbations. Let P = 4, ML = 21, MU = 60 so that the highest frequency perturbation has wavelength less than 1/4 of the vortex diameter. The vortex slowly drifted to the east (Fig. 13ab), and after the time 0.10 (106 days) collided with the boundary. There was no dispersion and the vortex decayed only after the collision (Fig. 13cd).

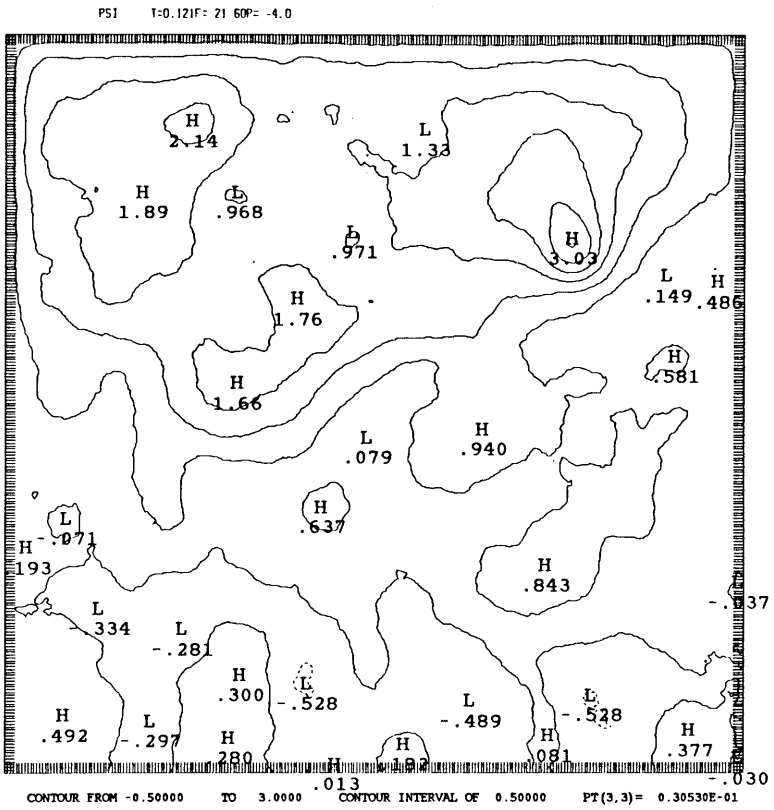


a) Initial condition; ML=21, MU=60, P=4, τ_0=0, r=0

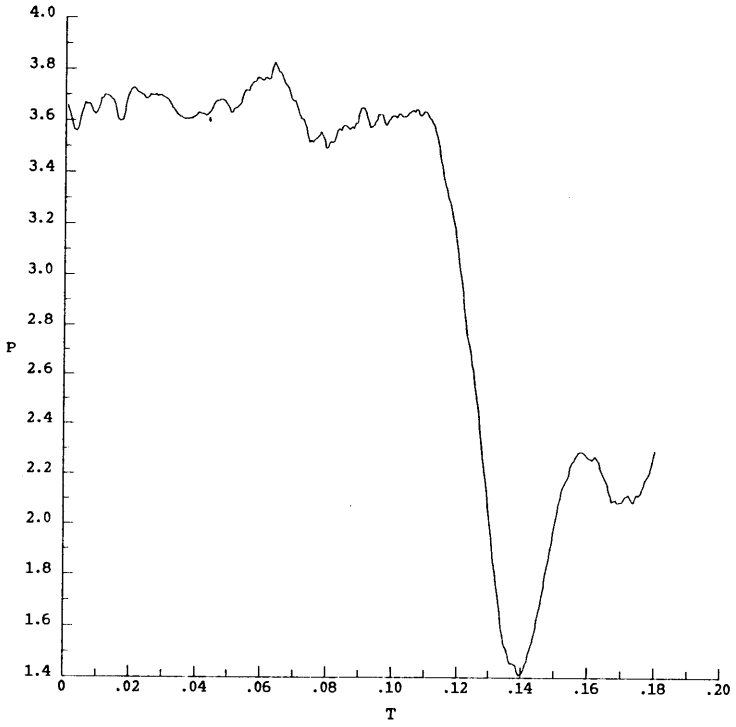


b) Streamfunction after t=0.10 (116 days).

Figure 13. EXPERIMENT II-2



c) Streamfunction after t=0.12 (139 days).



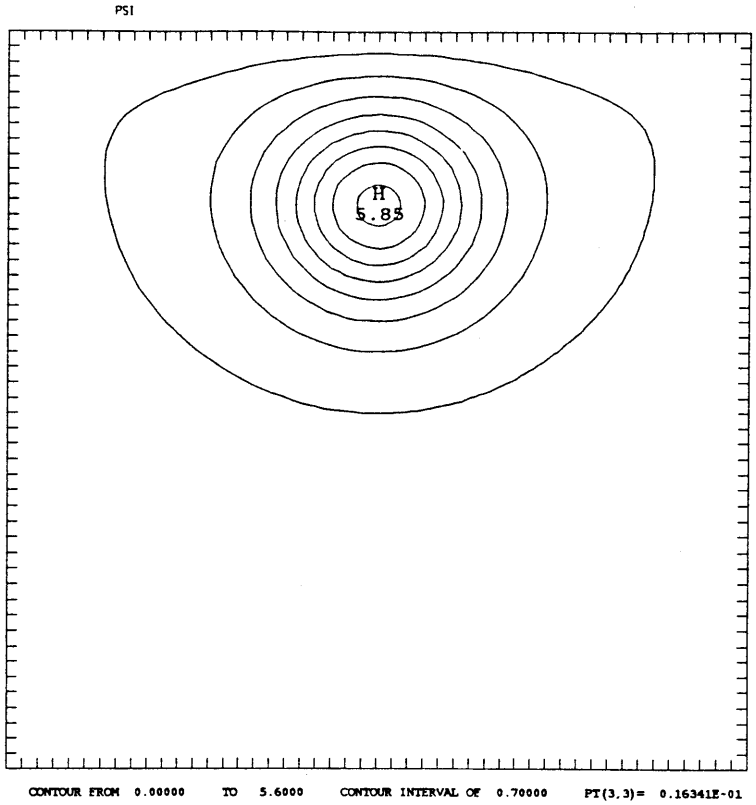
d) Magnitude of the streamfunction in the center of the vortex.

Figure 13. EXPERIMENT II-2

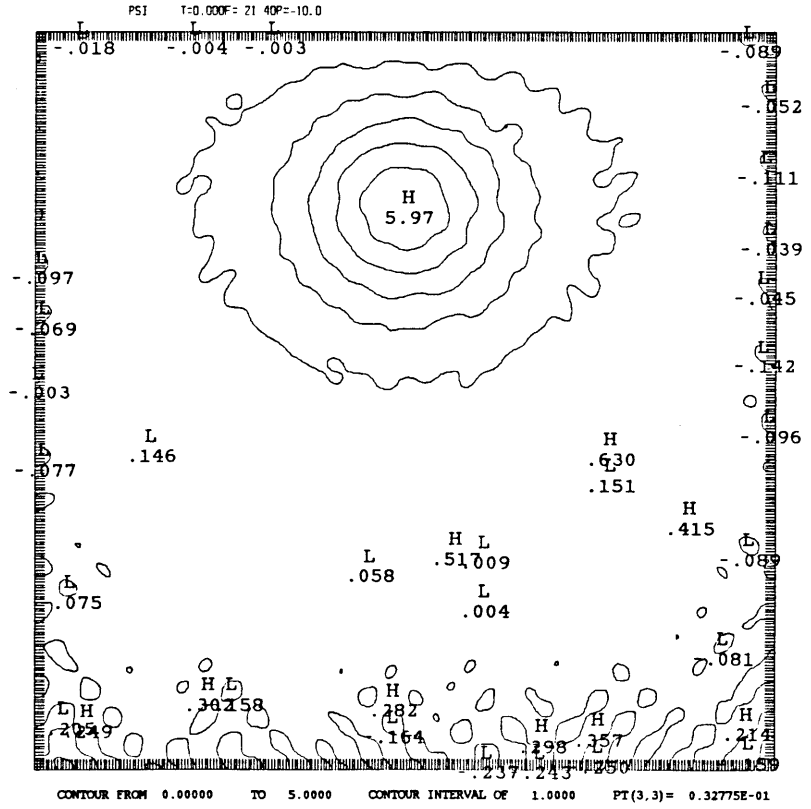
EXPERIMENT II-3

The highest frequency of the perturbations is limited by the resolution of the numerical scheme, so in the previous experiments the smallest wavelength of ζ_p was approximately one third of the diameter of the vortex. To reduce the relative wavelength of the perturbation, we consider a vortex from the same class of solutions only with $\beta = 200$. As we mentioned in the previous section, in flows with relatively small β, the eddy size will be much larger (this is clear from the scaling: β L^2). In Figure 14a, we plot the streamfunction ($\gamma = -0.29$) of the solution. We shall add perturbations with high frequency (ML=21,MU=40) with RMS vorticity 10 times larger than the RMS vorticity of the basic flow (Fig. 14b). After the time 0.10 (23 days) the vortex collided with the boundary, but unlike the previous cases, it did not disperse afterwards, but its amplitude increased (Fig. 14cd). This is apparently a consequence of the two-dimensional infrared cascade of energy. In the next Chapter we shall give an example of the large vortex which is destroyed by more energetic high frequency perturbations.

Thus, the steady flow of Figure 5 is unstable under finite amplitude perturbations with the instability manifested by the drift of the vortex. The speed of translation increases with the magnitude of the perturbations and the direction of movement depends only on the nature of perturbations. The vortex is very robust and does not disperse until the collision with the boundary or under the influence of very strong perturbations.

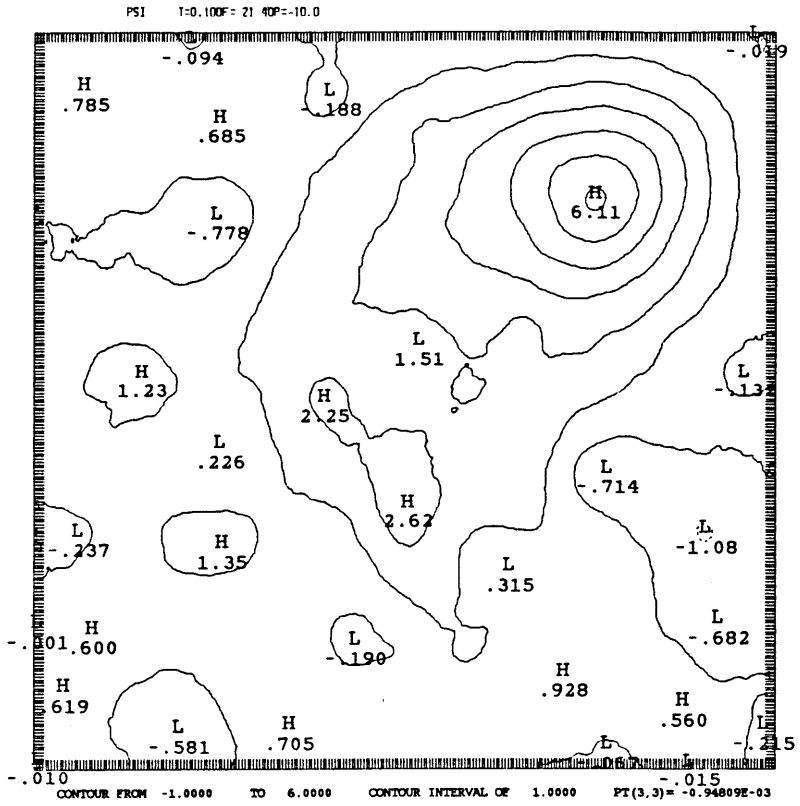


a) The streamfunction: $F(\psi) = -250\psi\ (\ 1 - 0.29\psi\ )$; $y_0 = 0$; $\beta = 200$.

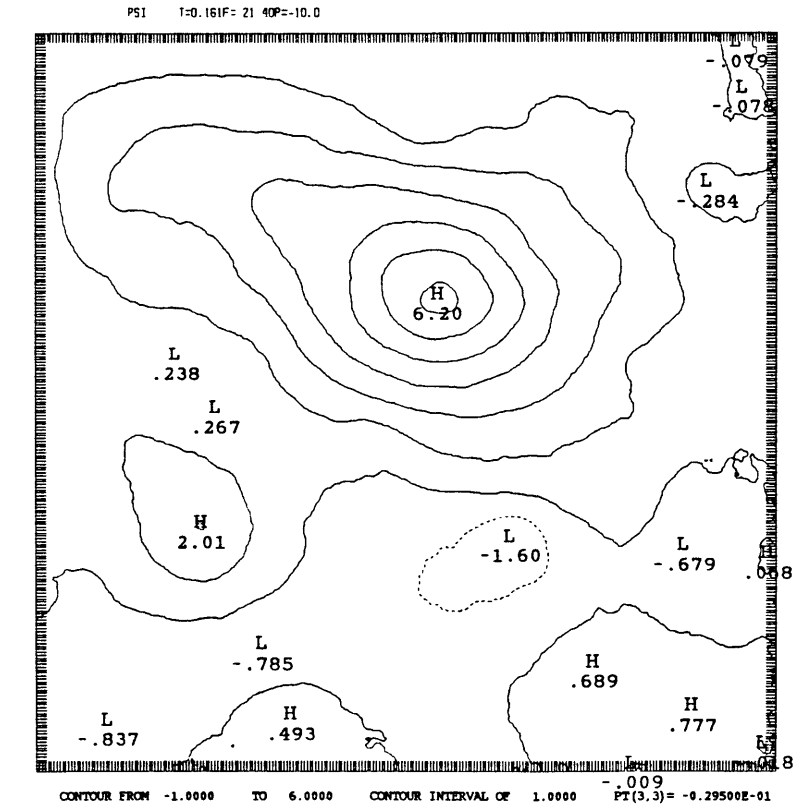


b) The initial condition; ML=21, MU=40, P=10

Figure 14. EXPERIMENT II-3



c) ψ after t=0.10 (23 days)



d) ψ after t=0.16 (37 days)

Figure 14. EXPERIMENT II-3

Shearing flow may support a strong vortex (see e.g. Flierl (1979)). Here, there is weak shear of the basic flow surrounding the vortex. However, since the vortex survives in the perturbed flow with rapidly varying magnitude and direction of velocity, it is unlikely that the shear has an important influence on its motion.

3 INFLUENCE OF FRICTION

In the next set of experiments we shall analyze motion of the anticyclonic vortex induced by the bottom friction without perturbations or forcing.

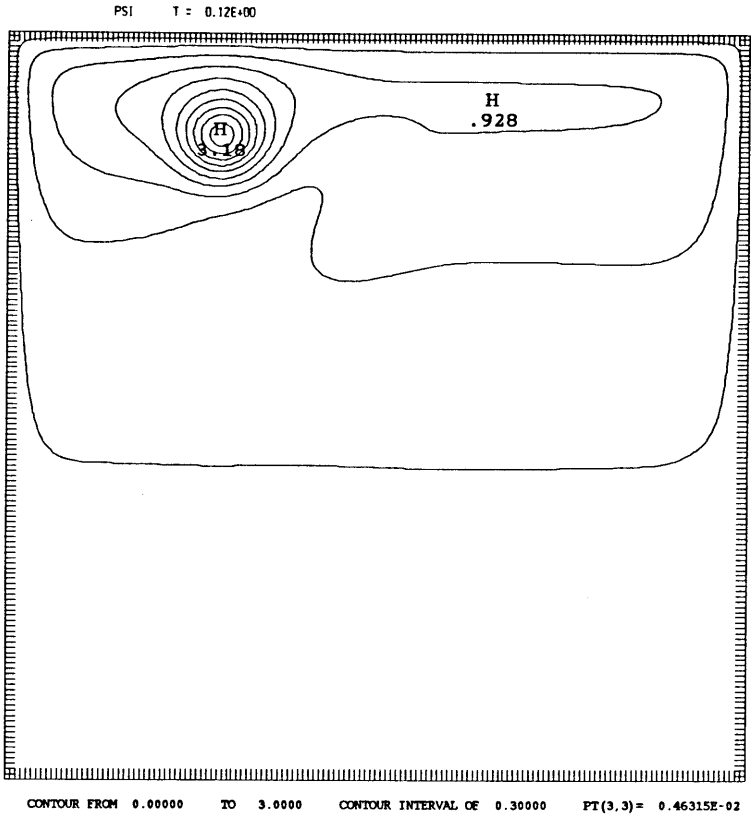
EXPERIMENT II-4

The steady solution of Fig. 7 was used as an initial condition for the barotropic vorticity equation:

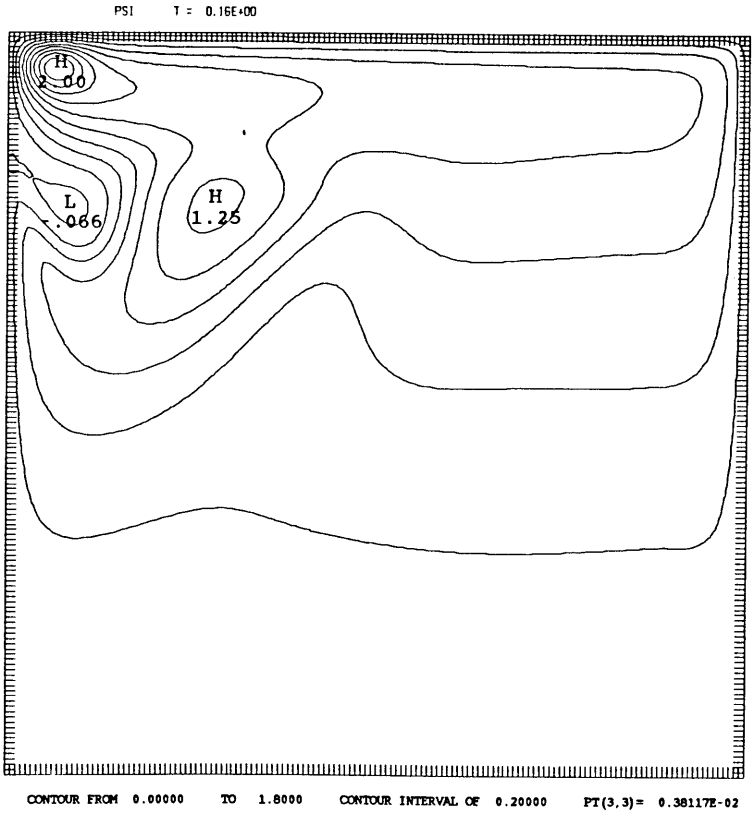
$$\frac{\partial \varsigma}{\partial t} + J (\psi , \varsigma + \beta y) = - r\varsigma \qquad \text{(II-10)}$$

The bottom friction coefficient, r, will chosen to be 1 (spindown time equals characteristic time of the large scale flow). Figure 15 shows the evolution of the flow. The vortex translates to the west with increasing velocity and collides with the boundary at the time 0.14 (162 days). The average speed is approximately 5 km/day. Before it is deformed in the collision with the western boundary, the dispersion is extremely small, as can be seen from Fig. 15d (upper curve). Dependence of the distance the vortex travels was found by repeating the first experiment with a larger bottom friction coefficient (r = 2,3 - spindown time is now 579 and 386 days respectively). From Fig. 15f it is clear that the acceleration of the vortex is proportional to the bottom friction coefficient and increases nearly linearly with time. The distance traveled depends on the time and bottom friction coefficient as:

$$d (t) = C_0 \, r \, t^3 \qquad \text{(II-11)}$$

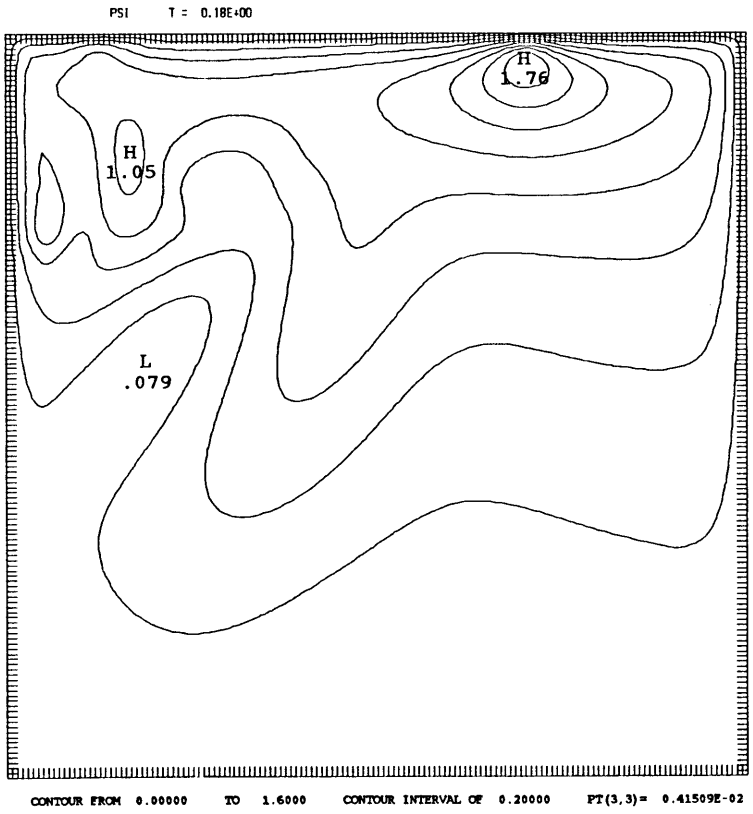


a) ψ after t=0.12 (139 days); r=1

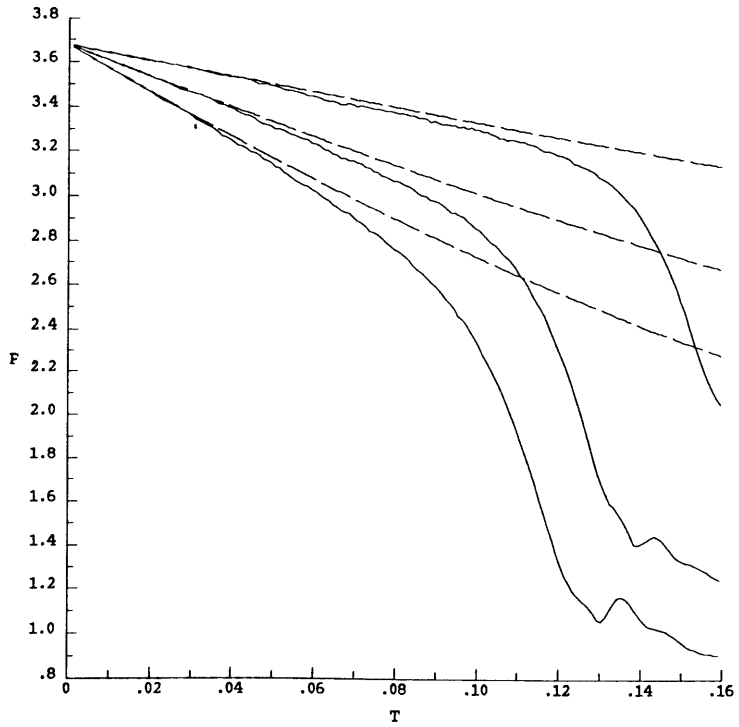


b) ψ after t=0.16 (185 days); r=1

Figure 15. EXPERIMENT II-4

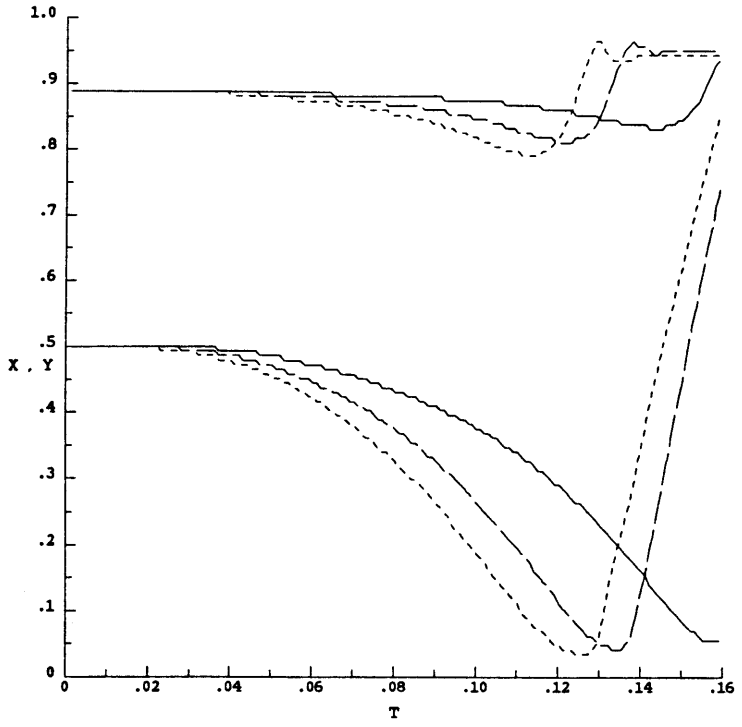


c) ψ after t=0.18 (208 days); r=1

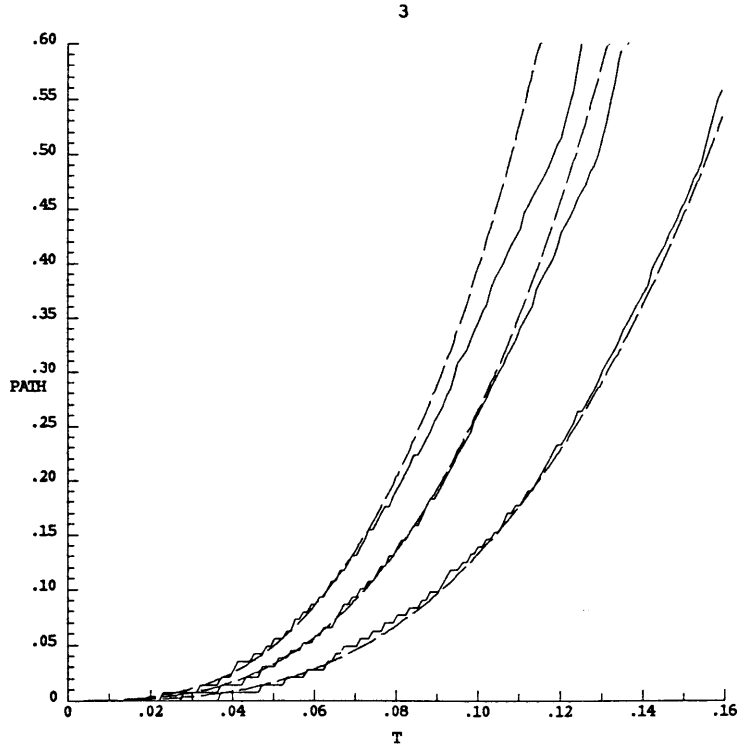


d) Magnitude of the streamfunction in the center of the vortex
upper curve r=1; middle r=2; lower r=3;
Dashed curves show the fit (II-12)

Figure 15. EXPERIMENT II-4



e) Coordinates of the center of the vortex (x-lower curves; y-upper)
solid curves r=1; dashed r=2; dotted r=3



f) Distance traveled by the vortex
lower curve r=1; middle r=2; upper r=3;
Dashed curves show the fit (II-11)

Figure 15. EXPERIMENT II-4

where C_0 is a constant depending on the vortex (i.e. β and γ), but independent of friction. The dashed curve in Fig. 15f represents the fit (II-11). The vortex translates as a solid body under the influence of the force which is proportional to the bottom friction coefficient. Total energy of the flow slowly decreases. A part of the energy of rotation is, through the influence of bottom friction and the β-effect, converted into the kinetic energy of translation. It is easy to give a crude estimate of the distribution of the spent energy of rotation between dissipation and energy of translation.

By assuming that the vortex behaves as a uniformly rotating cylinder, its initial energy is entirely contained in rotation:

$$E_r(0) = \frac{I\,\omega}{2}$$

where $I = \frac{mR^2}{2} = \frac{\rho D R^4 \pi}{2}$ is the moment of inertia (D is depth of the ocean, R is radius of the vortex and ρ is density), and ω is angular velocity $\omega = \frac{v_r}{R}$, (v_r is tangential velocity).

We shall assume for simplicity that the vortex retains its shape and only its angular velocity decreases with time. Then after the time t_0, total energy is

$$E = E_r(t_0) + E_t(t_0)$$

where energy of translation is:

$$E_t = \frac{m v_t^2}{2} = \frac{\rho D R^2 \pi v_t^2}{2}$$

and total kinetic energy at the time t_0 expressed in terms of the initial energy is:

$$E_k(t) = [\,(\frac{v_r(t_0)}{v_r(0)})^2 + 2\,(\frac{v_t(t_0)}{v_r(0)})^2\,]\,E_r(0)$$

where the first term in the bracket is the remaining energy of rotation and the second is acquired energy of translation. From the slope of the streamfunction in the vortex the tangential velocity can be estimated, initially $v_r(0) \approx 80$cm/s and after the time $t_0 = 0.12$, $v_r(t_0) \approx 65$cm/s and $v_t(t_0) = 10$cm/s, then we have:

$$E_r(t_0) \approx 0.65\ E_r(0)$$

$$E_t(t_0) \approx 0.03\ E_r(0)$$

Thus, of 35% of energy of rotation lost, 32% was dissipated and only 3% was converted to kinetic energy of translation. This "engine" is apparently very inefficient, but may be enough so to make difference in distribution of eddies in the basin. By the assumption that the vortex does not change shape, it follows that the change in angular velocity is proportional to the change of the streamfunction, which changes as $\psi(0)(1-rt)$ where r is the bottom friction coefficient. We shall also assume that $t \ll 1$ and r is at most O(1). Since v_t is proportional to rt^2, it follows that the ratio of the energy of translation to the dissipated energy after the time t is

$$\frac{E_t}{E_r(0)-E_k(t)} \approx \frac{C_1 r^2 t^4}{1-(1-rt)^2} \approx Crt^3$$

where C_1 and C are constants and we used the fact that $E_t(t) \ll E_r(t)$. Thus the efficiency of the "engine" increases with r.

Warren (1967) suggested that the reason for westward movement of the radially symmetric eddies is the β-effect. More recently it was argued

that the Gulf Stream Rings are advected by the interior flow, although their average speed is larger that of the mean flow (Lai and Richardson (1977)). In our experiments, β-effect alone cannot account for westward motion. Indeed, when the vortex was perturbed in the inviscid flow, the direction of motion was dependent only on the nature of the perturbation. This also shows that for our vortex the advection by the mean flow cannot provide a mechanism for the westward movement either. We shall return to the question of westward motion later.

The decrease of the maximum of the streamfunction is slightly faster than linear, which for the time before collision agrees with the fit:

$$\psi (x_0 (t) , y_0 (t)) = \psi (x_0 (0) , y_0 (0)) \exp (- r t) \qquad \text{(II-12)}$$

where x_0 and y_0 are the coordinates of the center of the vortex. From the above relation, it follows that the basic balance in the equation of motion in the region of the largest vorticity is:

$$\frac{\partial}{\partial t} \nabla^2 \psi \approx - r \nabla^2 \psi$$

Fig. 15e shows the x and y coordinates of the center of the vortex. Note that the southward shift of the vortex increases with the bottom friction. This is usually explained as a consequence of the "form drag instability". This is manifested in the appearance of a countervortex to the south of the main vortex. It cannot be seen in our figures since it is very weak.

In the previous experiment, the bottom friction was turned on abruptly, so it is possible that it just "pushed" the vortex from its (unstable) equilibrium near the boundary current and it later accelerated

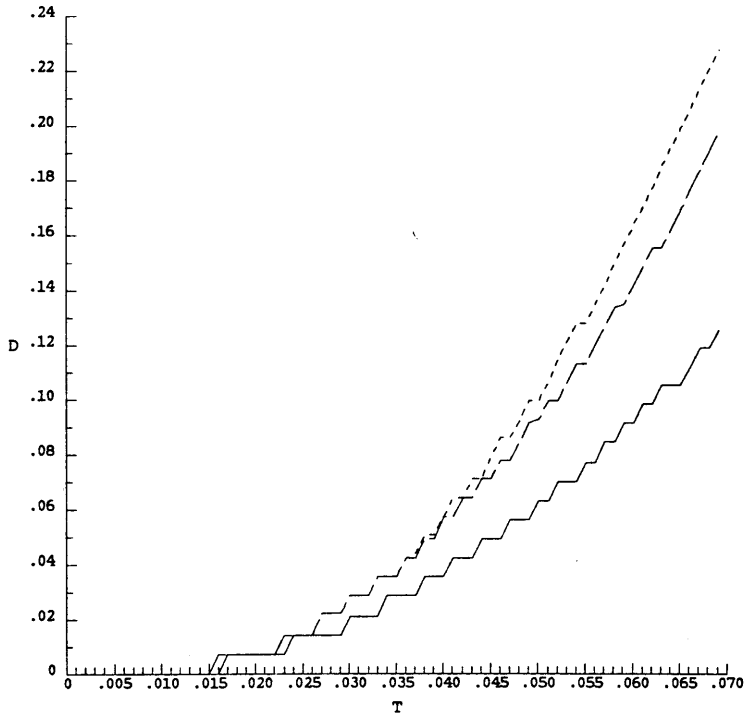
only by the influence of the β-effect. Recall that in the experiment (II-4) the coefficient of the bottom friction assumed values of 1,2,3. to which this "push" would be proportional. In the next experiment we shall show motion of the vortex under the influence of the bottom friction with the same coefficient, only it will act for different period of time.

EXPERIMENT II-5

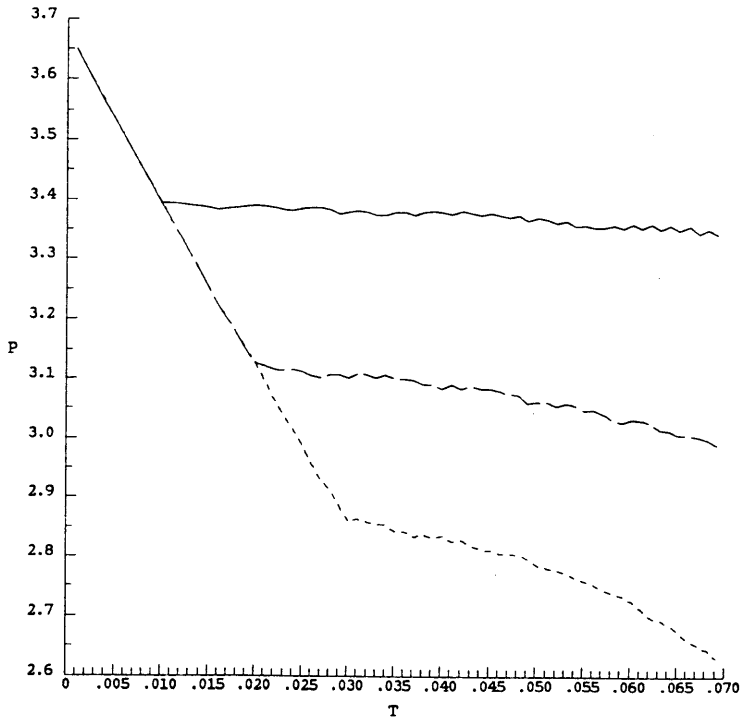
There will be three runs with r=8, but in the first run the friction was turned off after the time 0.01 (12 days), in the second after 0.02 (23 days), and 0.03 (35 days) in the third one. Figure 16b shows how the maximum of the streamfunction and coordinates of the center of the vortex depend on time. It is interesting that in the first run after the friction was turned off, the streamfunction remained constant until the vortex reached the western boundary. In the second and third run (lower curves) the dispersion is more appreciable, what could be expected since the streamfunction decreased more and the vortex approached the linear regime. The distance traveled by the vortex (Fig 16a) increases proportionately to t^2 after the friction is turned off, so that the acceleration is constant. Apparently, the friction has changed the vortex so that now β-effect alone produces a net westward force.

The Rossby wave packet propagates to the west and accelerates if its east-west scale increases relative to the north-south one. This can be seen from the expression for the dimensional group velocity

$$C_{gx} = \beta_0 \frac{k^2 - l^2 - R^{-2}}{(k^2 + l^2 + R^{-2})^2}$$



a) Distance traveled by the vortex, r=8;
solid curve t_0=0.01; dashed t_0=0.02; dotted t_0=0.03.



b) Magnitude of the streamfunction in the center of the vortex, r=8;
solid curve t_0=0.01; dashed t_0=0.02; dotted t_0=0.03.

Figure 16. EXPERIMENT II-5

where k and l are the wavevectors in x and y direction respectively and R is the Rossby radius (= 2000km). If the friction acts to "flatten" out the vortex in such a way that k decreases relative to l (i.e. the east-west length increases relative to the north-south), then the vortex would accelerate. However, inspection of the plots shows that no such deformation occurs. The explanation in terms of Rossby wave packet is inadequate because it applies to the small amplitude motions.

It looks that the friction makes a small modification in the shape of the vortex in such a way that the resulting force due to the β-effect is to the west. This mechanism is still obscure and an analytical study seems necessary to find an explanation.

As the perturbation experiments show, the vortex has some similarity with solitary waves. The speed of such a wave depends on its amplitude. To see how the speed of our vortices change with their intensity, we have repeated the above experiment with a different vortex in the initial condition and bottom friction coefficient $r = 1$. The functional F was also quadratic but γ was increased to - 0.307 (the maximum of the streamfunction increased from 3.68 to 4.18). As expected, the velocity increased (the constant C_0 in (II-11) increased by nearly 25%).

In the first section of this chapter, we showed that vortices similar to the one investigated in the above experiments, exist for several nonlinear functionals and they do not have to be anticyclonic.

In the next

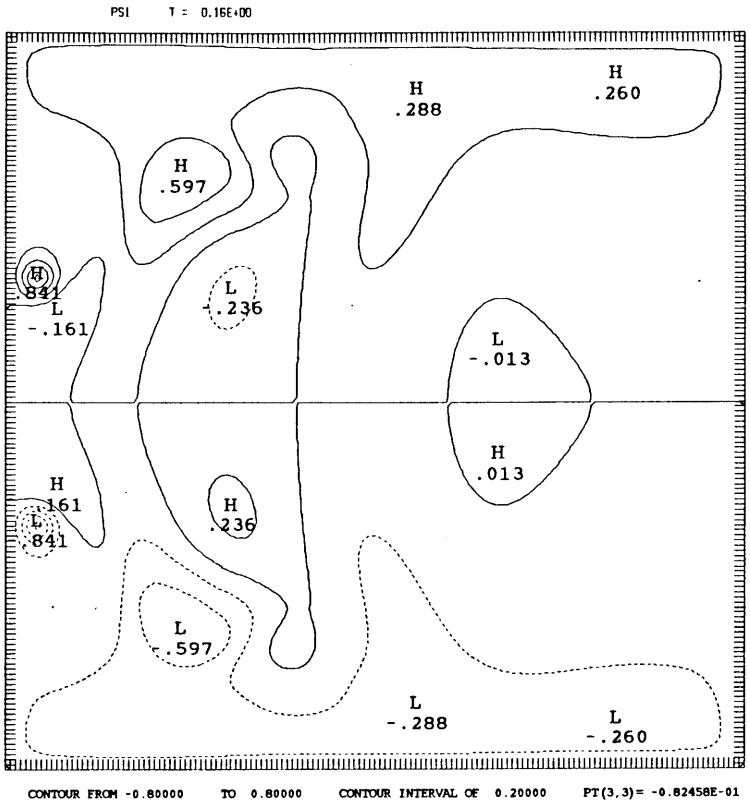
EXPERIMENT II-6

we shall show the behavior of the pair of vortices (Fig. 9) which are solutions of (II-1) with $F(\gamma,\psi) = \delta\psi\,(\,1 + \gamma\psi^2\,)$. The experiment will also show how the friction influences the *cyclonic* vortex.

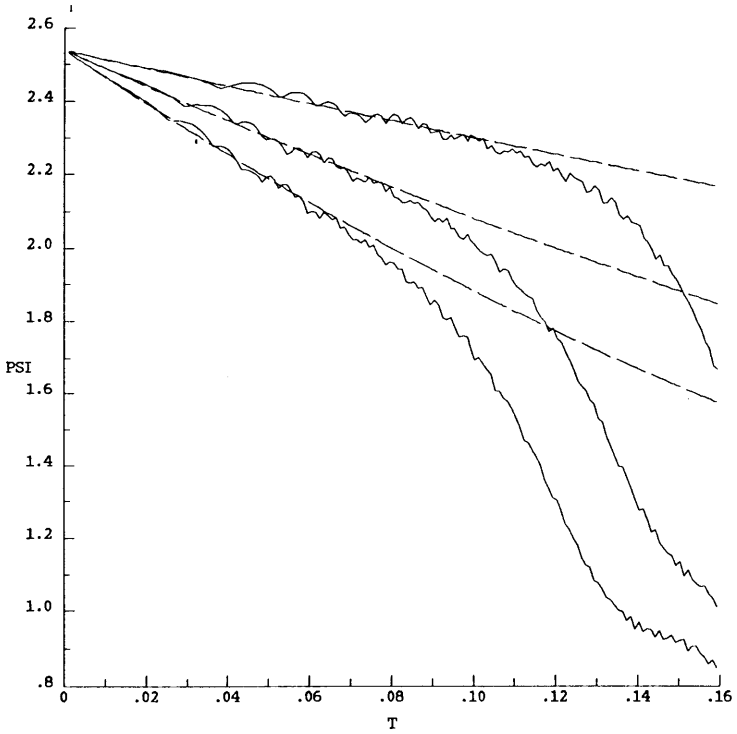
The solution plotted in Figure 9 was chosen to be the initial condition for equation (II-10). We consider three values of the bottom friction coefficient: r=1,2,3. Figure 17a shows the flow with r=3 after the time 0.16 (185 days). The cyclonic vortex behaves as a mirror image of the anticyclonic one. Their east-west velocity is smaller than in EXPERIMENT II-4, and the cubic fit (II-11) is less accurate (Fig. 17d). The shift away from the boundary is greater (Fig. 17c), but the dispersion prior to the collision is weak, especially for small r (Fig 17b).

The EXPERIMENT II-4 was repeated with the cyclonic vortex in the initial condition. As expected it moved to the west (with small northward drift) with the velocity of the same magnitude as the anticyclonic vortex.

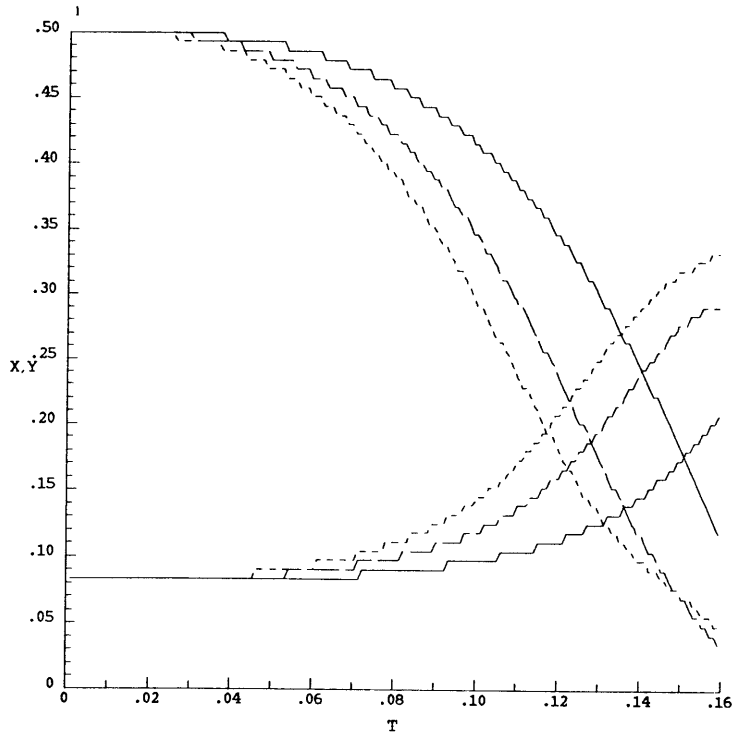
It is well known that, in Stommel's model, the westward intensification of the large scale flow arises as a consequence of bottom friction and a β-effect. Since we have shown that the westward drift of the vortex of our solution may have similar origin, it would be instructive to see how the entire inertial gyre behaves when bottom friction is included.



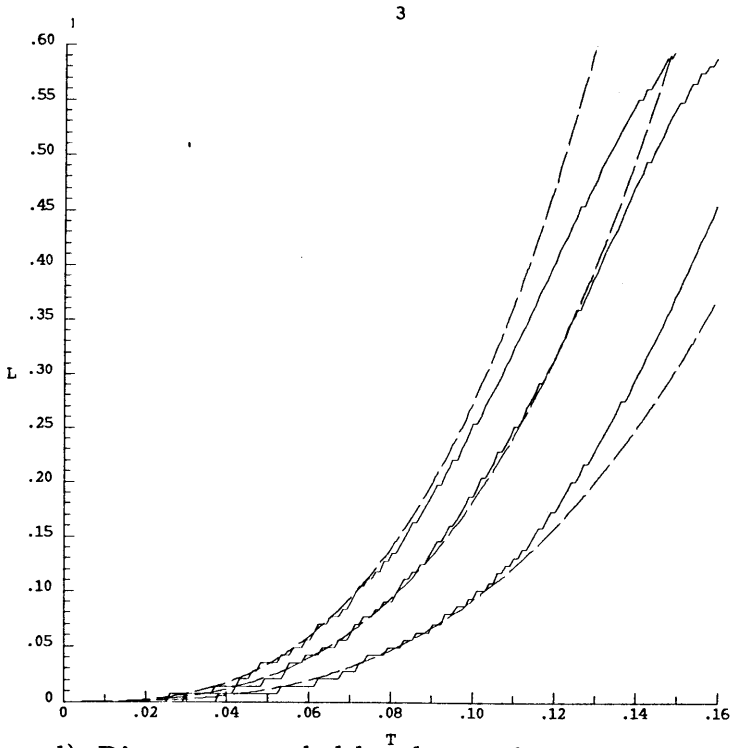
a) ψ after t=0.16 (185 days); r=3; initial condition is shown in Fig. 9



b) Magnitude of the streamfunction in the center of the vortices
upper curve r=1; middle r=2; lower r=3;
Dashed lines show the fit (II-12).
Figure 17. EXPERIMENT II-6



c) Coordinates of the center of the cyclonic vortex (x - upper; y - lower)
solid curves r=1; dashed r=2; dotted r=3;



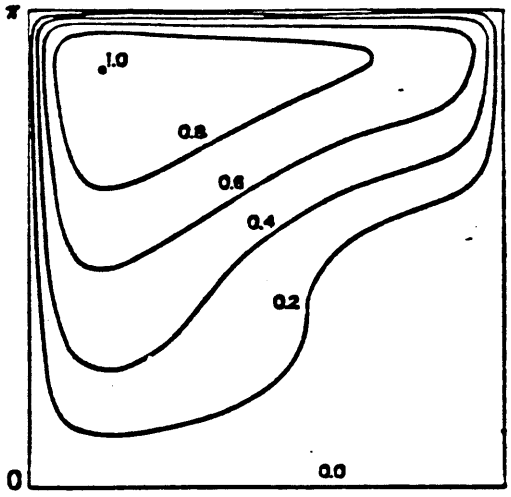
d) Distance traveled by the vortices
upper curve r=3; middle r=2; lower r=1;
Dashed curves show the fit (II-11)

Figure 17. EXPERIMENT II-6

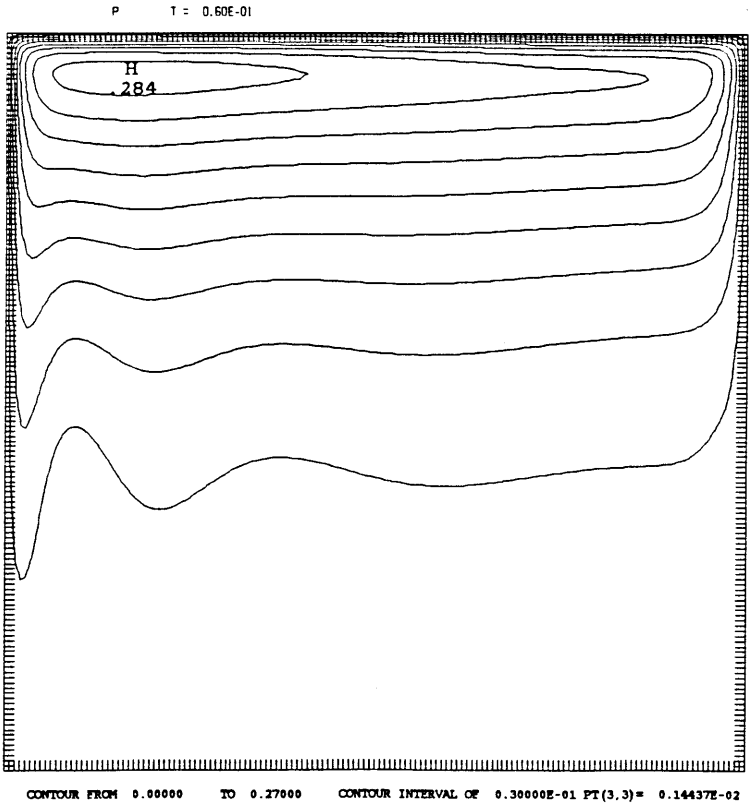
EXPERIMENT II-7

We shall use Fofonoff's solution consisting of an anticyclonic gyre (Fig. 2) as an initial condition for the barotropic vorticity equation. To isolate the effect of bottom friction, we shall not include wind stress or lateral friction. Obviously, the total energy of the flow will decrease with time. However, our aim is to show how the bottom friction influences the distribution of the energy in the basin. The motion of the gyre could not be observed in the previous experiment since the time of integration was too short. In this experiment we shall not extend the period of integration but increase the bottom friction coefficient to $r = 20$ (spindown time 55 days) which will produce the same result: the center of the gyre moves to the west and the northern boundary current slowly becomes the "northwestern" current (Fig 18b). This pattern resembles that found by Veronis (1966) (Fig 18a), which was obtained by the spinup of fluid from rest by the wind stress. The interior flow in our solution is nearly zonal because β was much larger than in Veronis' experiment.

Although the specific relationship between the acceleration of the vorticity extremum (eddy) and the time (II-11) may vary from one solution to another, it is likely that for any steady or slowly varying vortex on the β-plane, the acceleration will be proportional to the bottom friction coefficient and that the induced motion will be westward. A laboratory experiment could be used to verify this result.



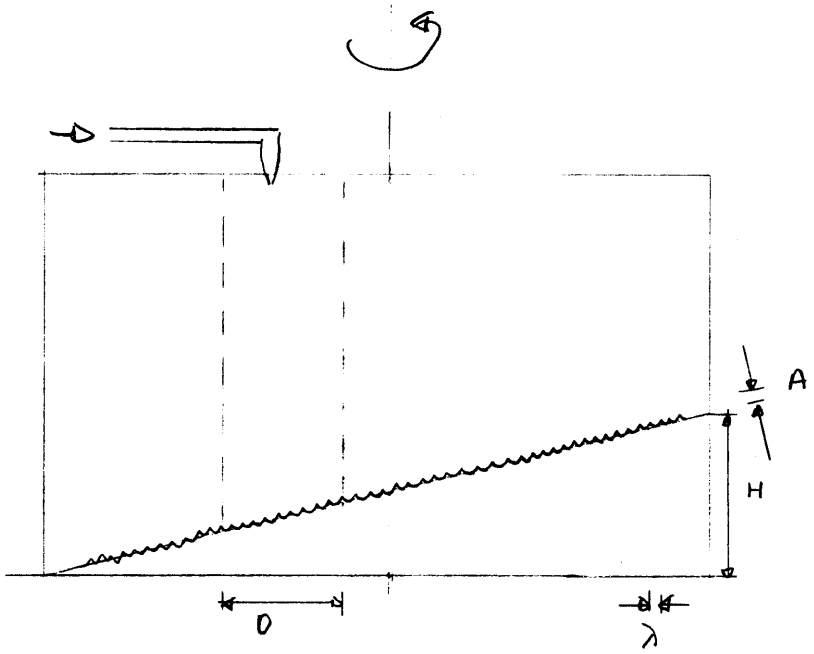
a) Steady forced flow with bottom friction obtained by the spinup from the rest; Veronis (1966).



b) Evolution of the Fofonoff gyre (Fig. 2); t=0.06 (70 days); r=20.

Figure 18. EXPERIMENT II-7

In a rotating tank filled with homogeneous fluid and an inclined bottom to simulate the β-effect (Pedlosky and Greenspan (1967)), a strong, slowly varying vortex can be mechanically generated. The bottom surface can be made of irregularly corrugated plastic sheet.



The amplitude, A, and the "wavelength" ,λ, must be much smaller than the height, H, of the elevated side of the tank, and diameter of the vortex, D, respectively. By injecting a small amount of the polymer solution, the drag (i.e. the bottom friction coefficient) can be either increased or decreased (Lumley, 1969) and the influence of the bottom friction on the motion of the vortex can be determined.

Bottom friction is believed to be the main dissipation mechanism on scales of 100km and larger (Holland (1978)). Lateral friction is important for dissipation of small scale motions, and we expect that its influence on

the motion of mesoscale eddies will be smaller. This applies to the barotropic model, but if the fluid is stratified, and the vortex is in the upper layer, contribution of the lateral friction to the vortex motion may be significant. However, its influence is more difficult to assess. The reason involves the nature of our steady state solution, which has a sharp extremum of both vorticity and east-west velocity at the northern boundary. The vorticity equation is now fourth order and apart from no normal flow, requires an additional boundary condition which may may be free slip: $\varsigma = 0$, or no slip: $u_{|} = 0$. In either case, at time t=0, a strong wave will be generated at the northern boundary and then propagate into the interior. Clearly, it may have dominant influence on the motion of the vortex. Another possibility would be to replace the Dirichlet boundary condition at three sides where $\varsigma \neq 0$ by the Neumann condition $\frac{\partial \varsigma}{\partial n} = 0$, and leave the Dirichlet condition only at southern boundary. This, however would supply energy through the boundaries which would, at least initially, overshadow dissipation.

In

EXPERIMENT II-8

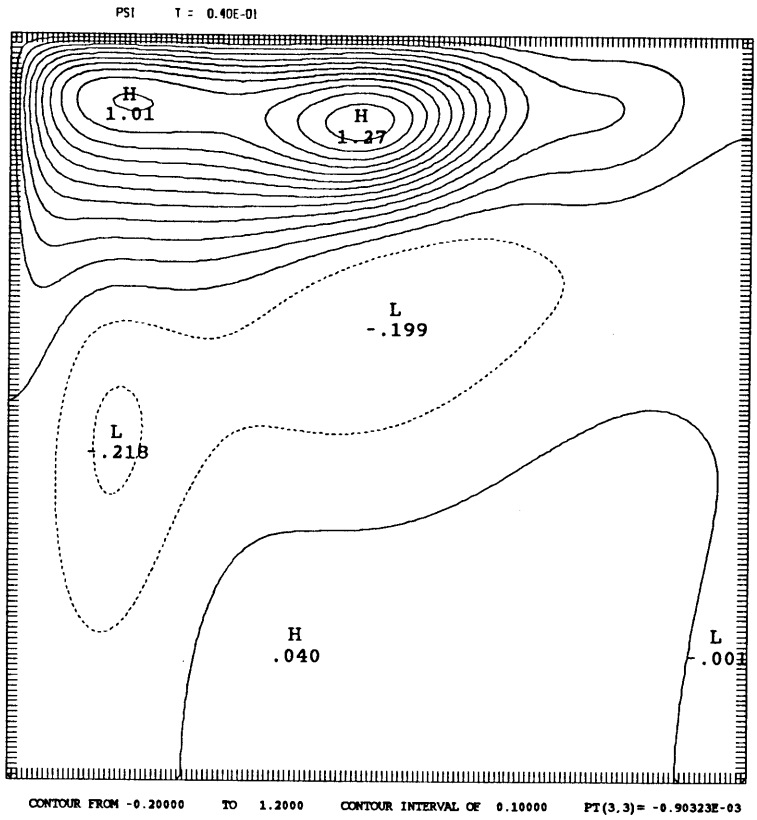
we shall demonstrate the influence of lateral friction on the motion of the vortex.

The equation

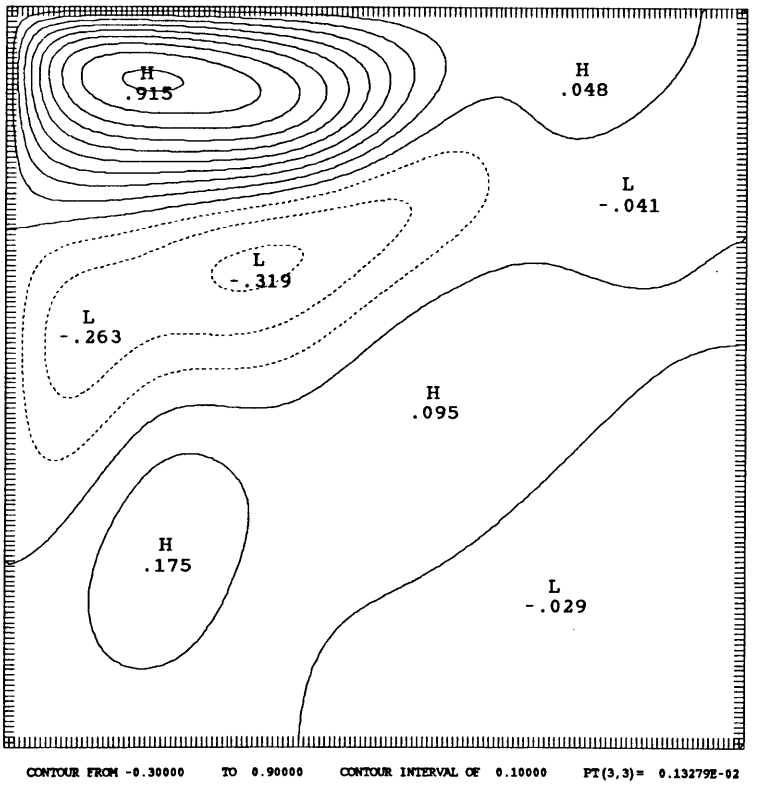
$$\frac{\partial \varsigma}{\partial t} + J (\psi , \varsigma + \beta y) = \frac{1}{Re} \nabla^2 \varsigma \qquad (II\text{-}13)$$

is solved with the initial condition given by the flow plotted in Fig. 7. Boundary conditions are $\psi = 0$, $\varsigma = 0$. The friction was turned on instantaneously with a small Reynolds number (Re=20), so that the waves will be strongly damped. Unfortunately, this had a negative side effect of a very fast damping of the vortex since its length scale is small. Initially the wave from the northern boundary caused slight shift to the east, but soon after the vortex turned to the west (Fig 19a). Its amplitude decreased much faster than with the bottom friction.

We could not establish a quantitative relationship between the Reynolds number and the westward acceleration, but this experiment has shown at least its qualitative nature.



a) ψ after t=0.04 (46 days); Re=20
Initial condition is shown in Fig. 7a.



b) ψ after t=0.06 (70 days); Re=20

Figure 19. EXPERIMENT II-8

There is a clear parallel between the westward motion of the vortices and the westward intensification of the large scale flow, induced by the friction.

In the Rossby wave interpretation of the westward intensification, friction contributes to the intensification only by trapping the short wavelength Rossby waves reflected from the western boundary. Our experiments suggest that the friction may play direct role in inducing the motion of the (non)linear waves towards the western boundary and in this way make it the most energetic region in the oceanic circulation.

4 INFLUENCE OF THE WIND STRESS

In the previous section we have shown that the westward motion of the vortices is associated with dissipation. Now we shall investigate how the wind stress affects the behavior of the vortices. In another set of experiments we shall show how vortices similar to our steady state solutions may be generated.

Consider the barotropic vorticity equation with forcing but without dissipation:

$$\frac{\partial \varsigma}{\partial t} + J(\psi, \varsigma + \beta y) = \tau_0 (\nabla \times \tau)_z \qquad \text{(II-14)}$$

where the curl of the wind stress has the standard sinusoidal profile with one or two gyres:

$$(\nabla \times \tau)_z = -\sin(m\pi y) \qquad m = 1,2$$

and τ_0 is the constant. We shall perform two experiments which are similar to the EXPERIMENT II-4, where we compared the flows evolving with different bottom friction coefficient.

EXPERIMENT II-9

There will be three runs with the coefficient τ_0 assuming three values: 500, 1000 and 1500. This corresponds to the dimensional wind stress of 5,10 and 15 dynes cm^{-2} respectively, for the ocean with depth of 5000m. These values are too large for comparison with the observed flows, but we need strong forcing to emphasize the effects.

The initial condition is again the solution plotted in Fig. 7. The forcing is turned on instantaneously. Figure 20 shows the evolution of the flow

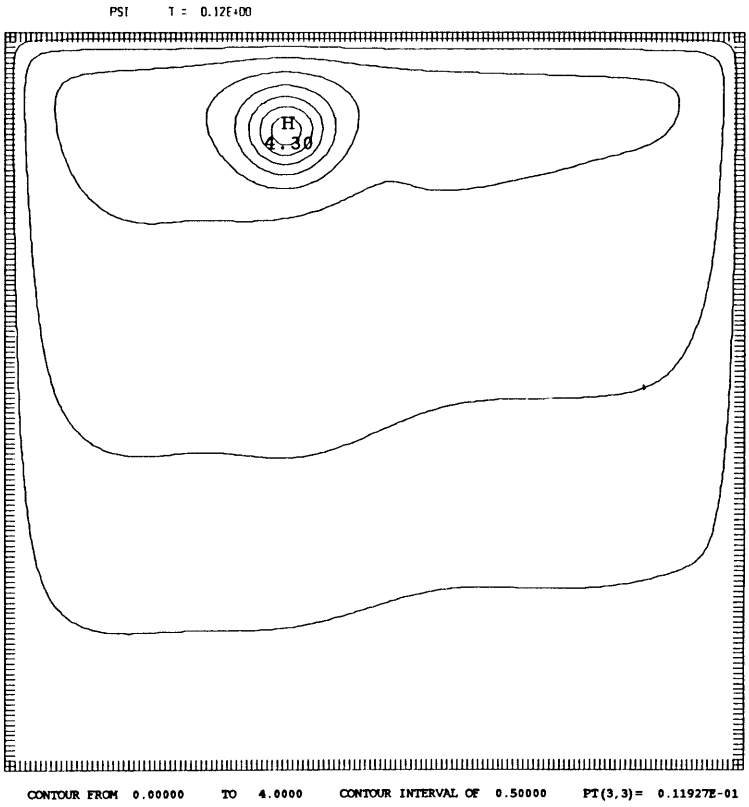
in the first run ($\tau_0 = 500$) after the time 0.12 (139 days). This picture is very similar to the one obtained in EXPERIMENT II-4 (Fig. 15a), with the exception that the magnitude of the streamfunction has increased. The similarity between forcing and friction in their influence on the motion of the vortex is even more striking if we compare the plots showing the coordinates of the center of the vortex (Figures 20c and 15e). The streamfunction in the center of the vortex does not increase uniformly. The reason for is the small amplitude Rossby waves which are generated by the instantaneous application of the wind stress. These waves also cause small initial eastward shift. The dashed curves (Fig. 20d) were obtained from the fit:

$$\psi_{max} = \psi_{max}(0)\, e^{\alpha\tau_0 t} \qquad \text{(II-15)}$$

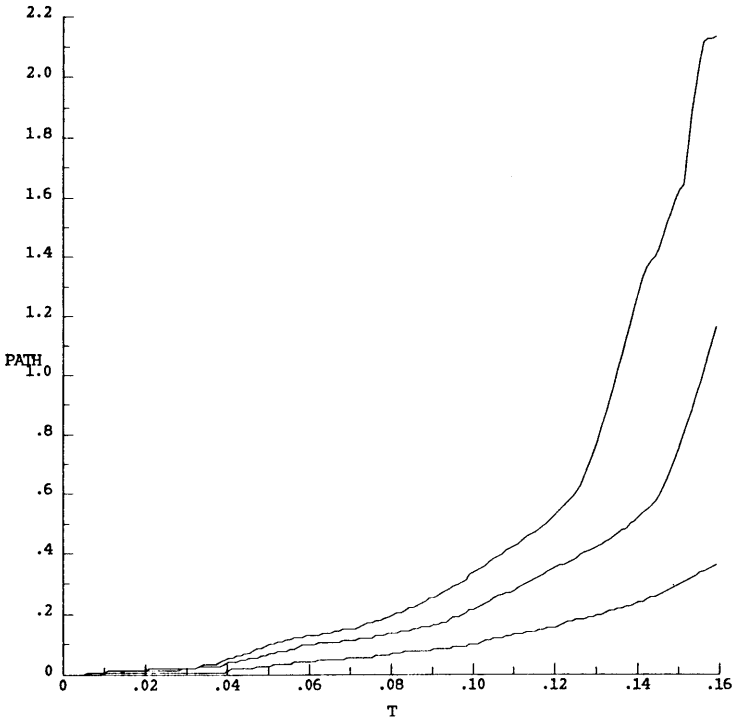
where $\alpha > 0$ is a constant independent of the coefficient of the wind stress.

The quantitative relationship between the acceleration and the time is more difficult to establish, but it is clear (Fig. 20b) that the acceleration is proportional to the wind stress coefficient.

Thus, the wind stress may produce the westward force on the vortex. Note that the curl of the wind stress had the same sign as the vorticity of the inertial gyre and the vortex (the stress *supplied* energy to the flow). In the next experiment we shall show what happens when the cyclonic wind stress acts on the anticyclonic ocean flow.

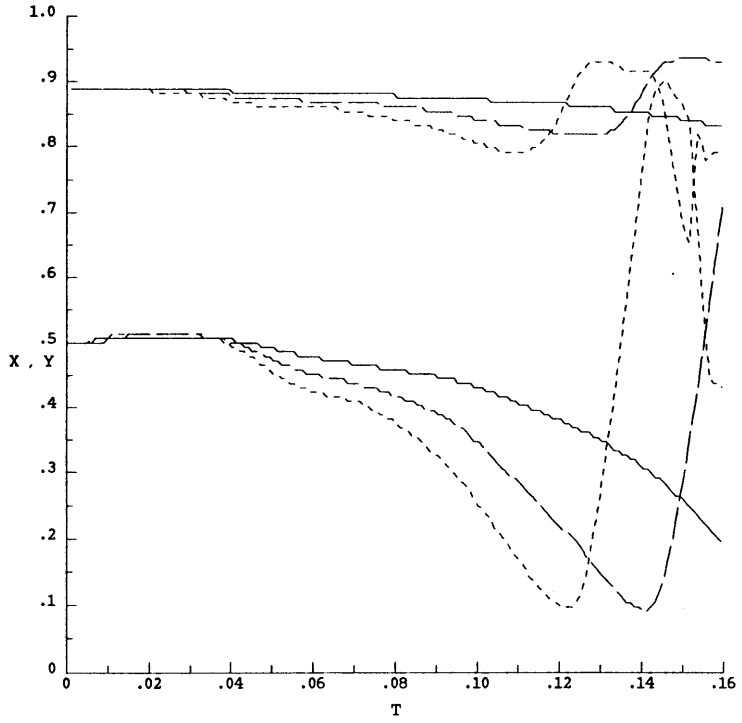


a) ψ after t=0.12 (139 days); $\tau_0 = 500$
Initial condition is shown in Fig. 7a.

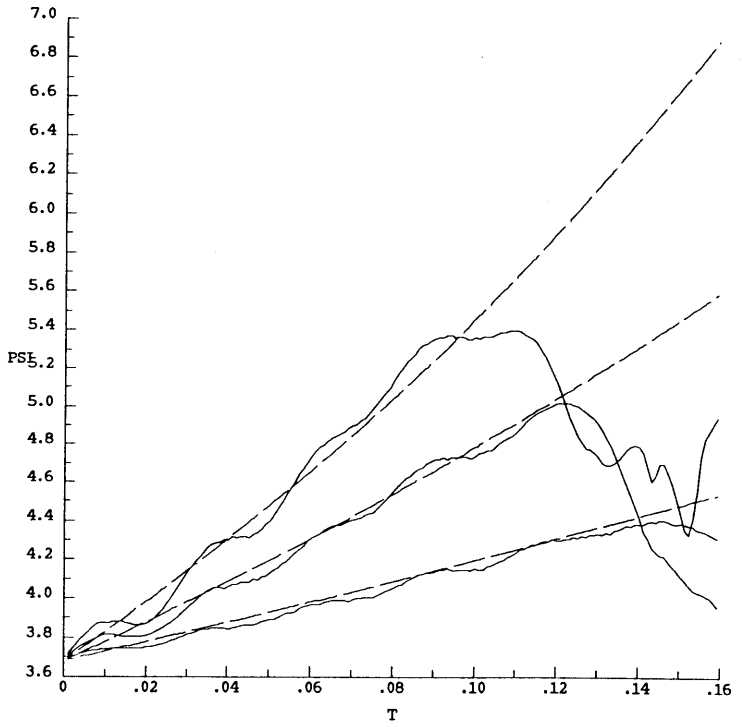


b) Distance traveled by the vortex
lower curve τ_0=500; middle τ_0=1000; upper τ_0=1500;

Figure 20. EXPERIMENT II-9



c) Coordinates of the center of the vortex (x-lower curves; y-upper) solid curve τ_0=500; dashed τ_0=1000; dotted τ_0=1500;



d) Magnitude of the streamfunction in the center of the vortex lower curve τ_0=500; middle τ_0=1000; upper τ_0=1500; Dashed curves show the fit (II-15)

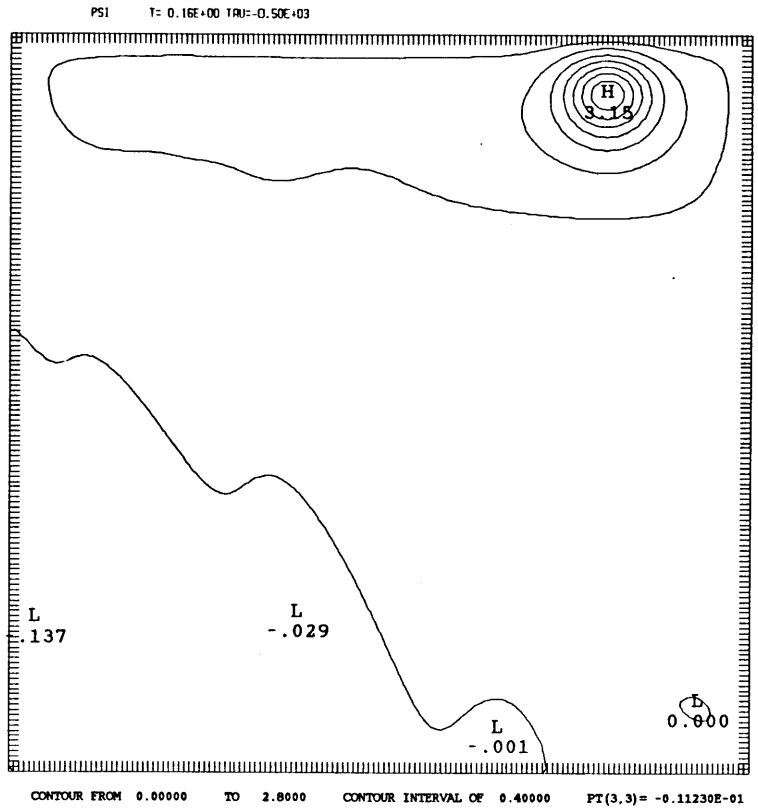
Figure 20. EXPERIMENT II-9

EXPERIMENT II-10

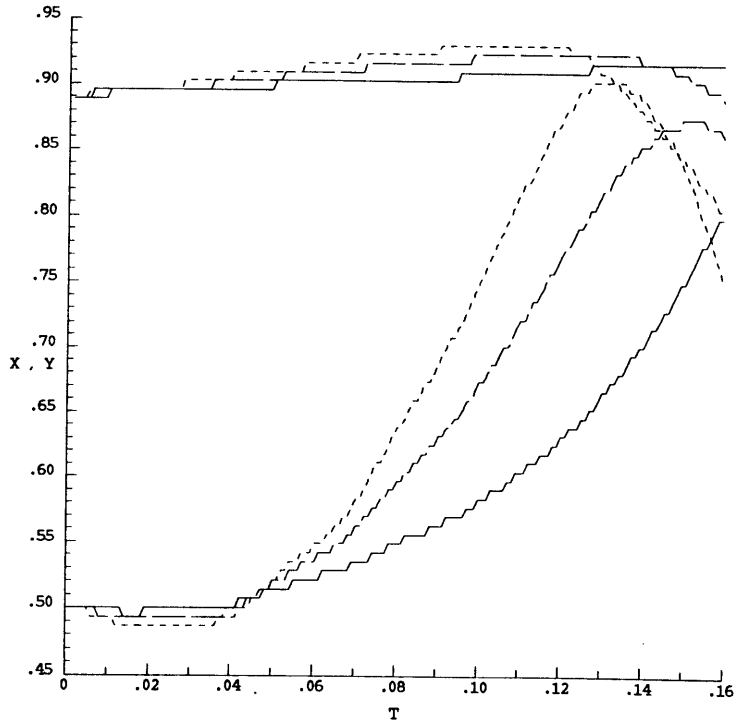
is identical to the EXPERIMENT II-9, with only the sign of the wind stress changed. Figure 21a shows the flow after the time 0.16 (185 days). The amplitude of the vortex decreases and is given approximately by the fit (II-15) with the change $\alpha \rightarrow 0.6\ \alpha$ (Fig. 21d). Figure 21b shows that the vortex was drawn closer to the boundary current. This is the reason why the absolute value of the slope, α, is smaller than before. The distance traveled by the vortex is proportional to τ_0 and increases slightly slowlier than t^3.

The result of this experiment may be important for understanding of the forces acting on a mesoscale eddy in a realistic viscous forced flow. An anticyclonic eddy under cyclonic wind stress will be under the influence of two competing forces: friction which will drive it to the west and wind stress which would drive it to the east. The friction could be expected to dominate because the relatively small scale of the eddies (which diminishes the importance of the wind stress) and large vorticity (which increases the importance of the friction).

We have repeated this experiment with a cyclonic vortex near the southern boundary with the expected result: under the cyclonic wind stress its amplitude increased and it moved to the west, and under anticyclonic stress the opposite happened. By the same argument as given above, this would imply that cyclonic eddies embedded into the anticyclonic gyre (e.g. Gulf Stream Rings) must move to the west with decreasing amplitude.

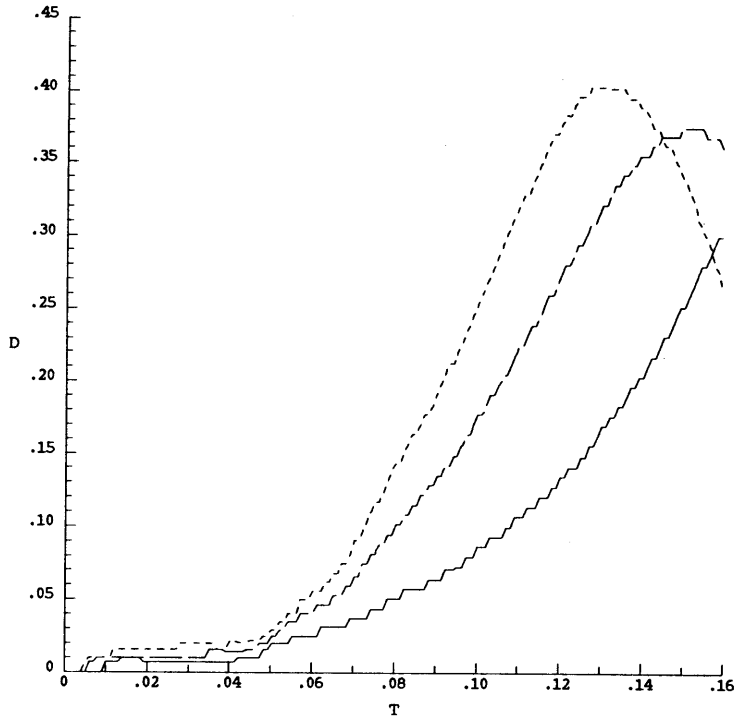


a) ψ after t=0.16 (185 days); $\tau_0 = -500$
Initial condition is shown in Fig. 7a.

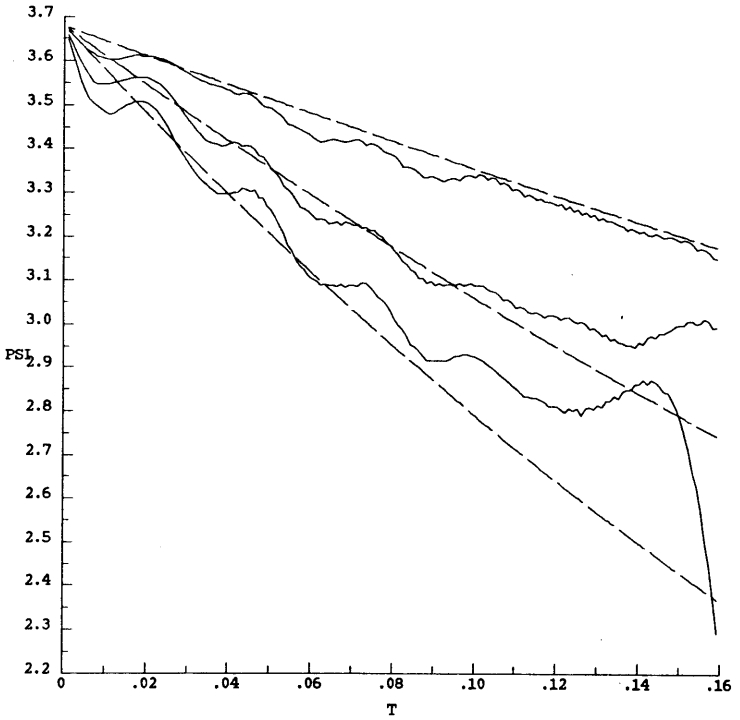


b) Coordinates of the center of the vortex (x-lower curves; y-upper) solid curve τ_0=–500; dashed τ_0=–1000; dotted τ_0=–1500;

Figure 21. EXPERIMENT II-10



c) Distance traveled by the vortex
solid curve τ_0=–500; dashed τ_0=–1000; dotted τ_0=–1500;



d) Magnitude of the streamfunction in the center of the vortex
upper curve τ_0=–500; middle τ_0=–1000; lower τ_0=–1500;
Dashed curves show the fit (II-15)

Figure 21. EXPERIMENT II-10

It would be useful to perform laboratory experiments similar to those suggested in the previous section. Instead of changing the bottom friction coefficient, one would change the forcing of the flow which contains a slowly varying vortex. The wind forcing may be simulated by a rotating plate (or system of concentric plates) at the surface.

The last two numerical experiments we wanted to isolate the effect of the wind stress and to show what is its (small) direct contribution to the motion of the eddies. As in the previous section, this raises the question of possible direct influence of the wind stress on the westward intensification of the large scale flow. This will be discussed in some detail below.

In Sverdrup's theory the north-south velocity of the interior flow is equal to the curl of the wind stress

$$v = (\nabla \times \tau)_z$$

From the incompressibility condition:

$$\frac{\partial u}{\partial x} + \frac{\partial v}{\partial y} = 0$$

it follows that the east-west velocity is:

$$u = (C - x) \frac{\partial}{\partial y}(\nabla \times \tau)_z$$

which must satisfy the no normal flow condition on either the east or west boundary (which specifies the constant C). By conservation of mass there must be a fast boundary current at the opposite side of the basin. There is complete symmetry between the east and west side of the basin and the boundary current may be at either the east or west side. Inclusion of friction removes the degeneracy of such a flow and a *western* boundary

current is shown to be necessary to close the flow. This is the usual argument (see e.g. Pedlosky (1979) pp 245-270) in both Stommel's and Munk's model, but it may be misleading. It implies that it is friction that makes the western boundary current and the wind stress is needed only to supply the energy to allow for steady state solution. In the next two experiments we shall observe evolution of the flow under the influence of the wind stress and without friction. This flow obviously cannot be steady and its energy must increase, however we want to observe how *distribution* of energy changes with time. In both experiments we shall use a two gyre wind stress

$$(\nabla \times \tau)_z = - \tau_0 \sin(2\pi y)$$

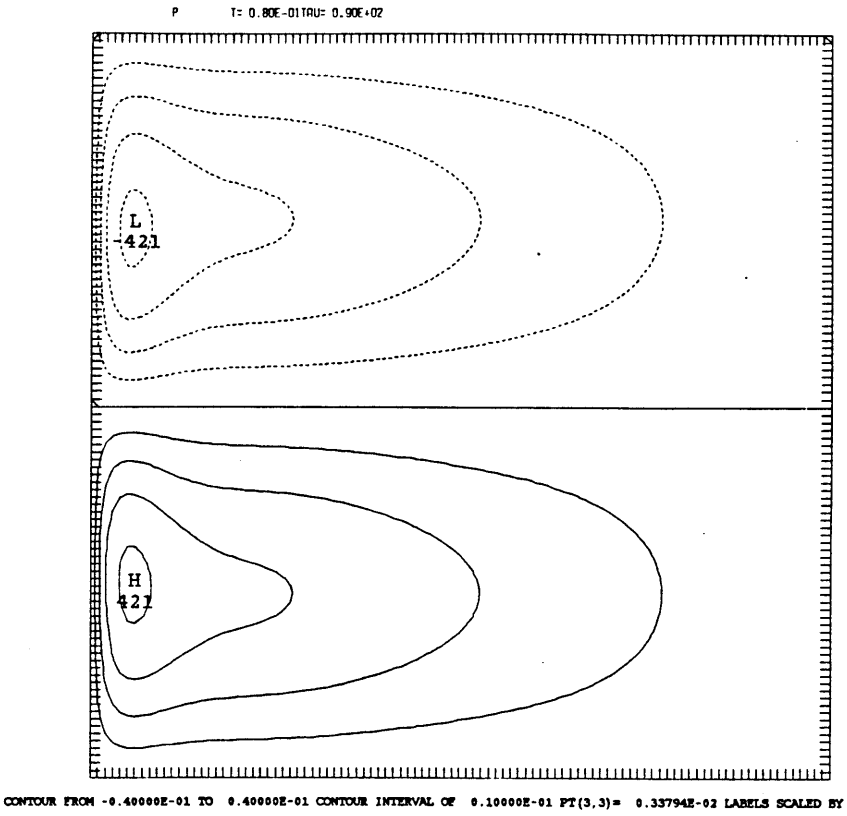
acting on an initially motionless fluid with $\beta = 2000$.

EXPERIMENT II-11

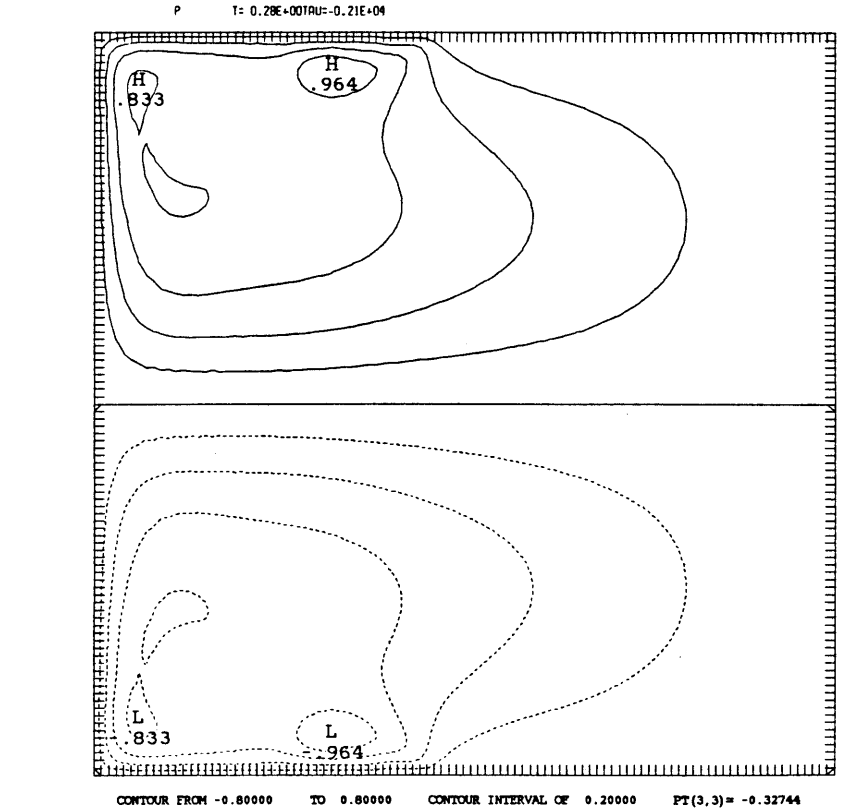
In this experiment forcing will be turned on smoothly as

$$\tau_0 (t) = \tau_{max} \frac{t^2}{t_0^2} \left(3 - 2 \frac{t}{t_0} \right)$$

Note that in the initial period, $t < \frac{3}{2} t_0$, $\tau_0 > 0$ and after that $\tau_0 < 0$ ($t_0 = 0.10$, $\tau_{max} = 100$). In the next experiment we shall use forcing which does not change the sign. Figure 22a shows the pattern after the time 0.08 (93 days). Note the westward intensification in *both* the northern and southern gyre. After the stress changes sign, the large scale flow again shows westward intensification (Fig. 22b).



a) ψ after t=0.08 (93 days); $\tau_0(0.08) = +90$; $\beta = 2000$; r=0
Initial condition is $\psi \equiv 0$;



b) ψ after t=0.28 (324 days); $\tau_0(0.28) = -2100$
Note the change of the sign of the wind stress.
Figure 22. EXPERIMENT II-11

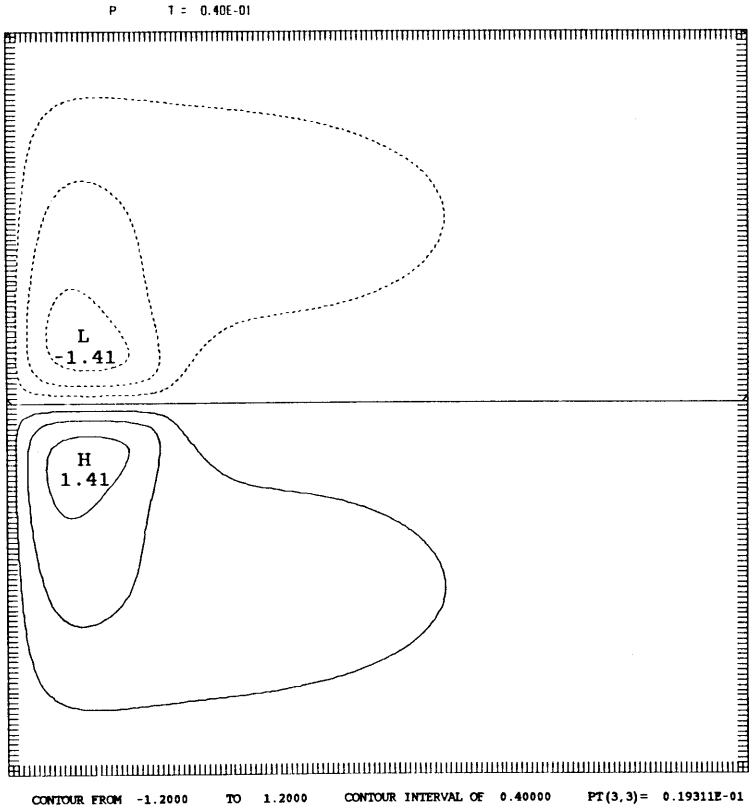
This experiment is important for another detail: near the northern and southern boundary there are vortices moving eastward with the boundary current, which are similar to the pair from Figure 9. It shows that a variable wind stress may generate weak vortices analogous to our steady solutions.

EXPERIMENT II-12

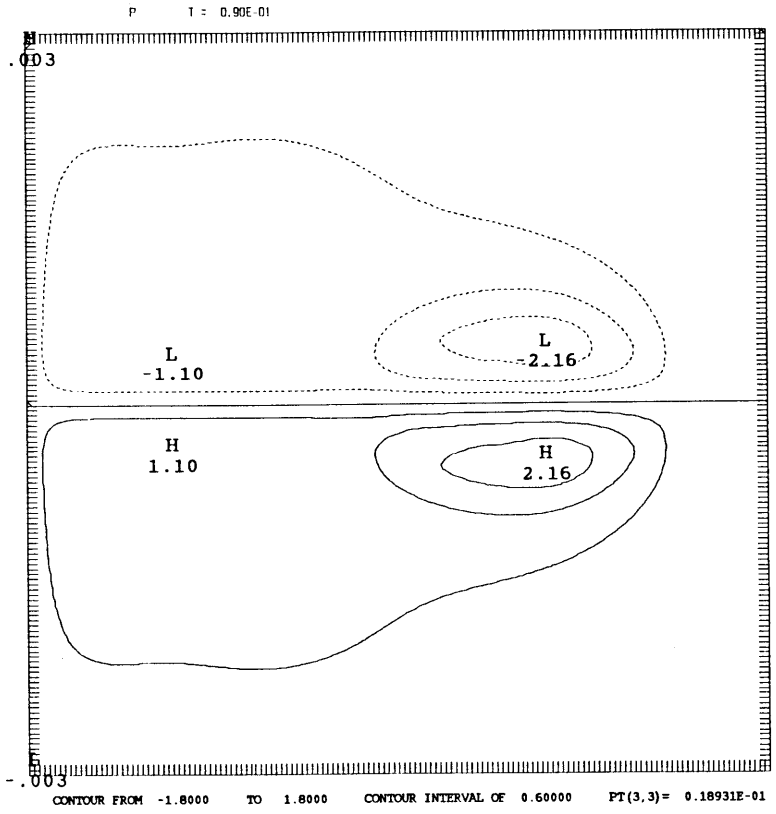
In this experiment, the coefficient of the wind stress will be constant in time $\tau_0 = 2000$ (β is again 2000). This corresponds to a wind stress of 20 dyne cm^{-2} acting on the layer of the depth of 5000m. Figure 23a shows the flow after the time 0.04 (46 days). Again, the westward intensification occurred in both gyres. At the time 0.09 (104 days), a modon like structure develops along the central jet. A similar picture may be obtained from Fig. 9 by "folding over" the surface.

It is easy to see that after sufficiently long time, the pattern will become almost inertial since the wind stress does not increase while the vorticity (and advection terms) do, so that eventually forcing becomes a small term in the vorticity equation. Westward intensification occurs only in the initial period in which advection terms are not much larger than the forcing itself.

We have made several other experiments with one and two gyre wind stress and we conclude that a *wind driven* inviscid ocean flow cannot have the pattern shown in Figure 24 (Stommel 1965). The reason for this is that it was derived on the false assumption that the flow is forced, frictionless *and steady.*



a) ψ after t=0.04 (46 days); $\tau_0 = 2000$; $\beta = 2000$; r=0
Initial condition is $\psi \equiv 0$;



b) ψ after t=0.09 (104 days); $\tau_0 = 2000$

Figure 23. EXPERIMENT II-12

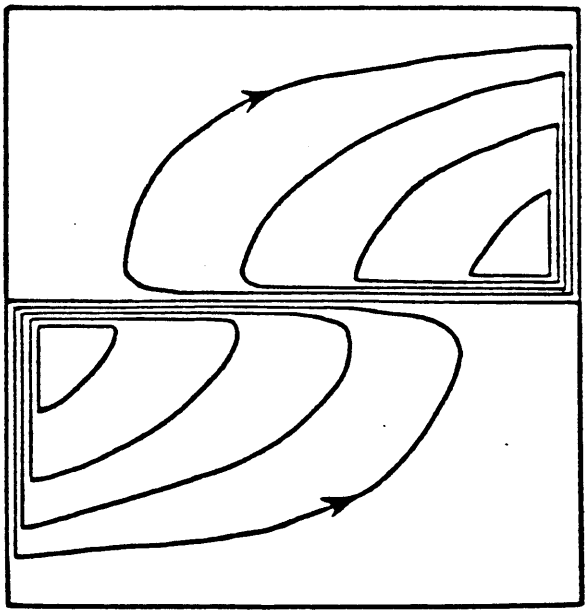


Figure 24. Large scale inviscid circulation induced by the wind stress, as shown in "The Gulf Stream" p. 203 (Stommel, 1965)
Compare with Figures 22 and 23a.

In the next

EXPERIMENT II-13

we shall observe behavior of the vortex in perturbed viscous and forced flow, which will more closely simulate realistic conditions. The equation (II-14) will be solved with added bottom friction (r=1); the curl of the wind stress will be a sinusoidal single gyre with $\tau_0 = 200$ (dimensionally: 2 dyne/cm^2 in the ocean of the depth 5000m). The vorticity of the perturbation is given by (II-6) with ML=1, MU=8 and P=0.2 (Fig. 25a).

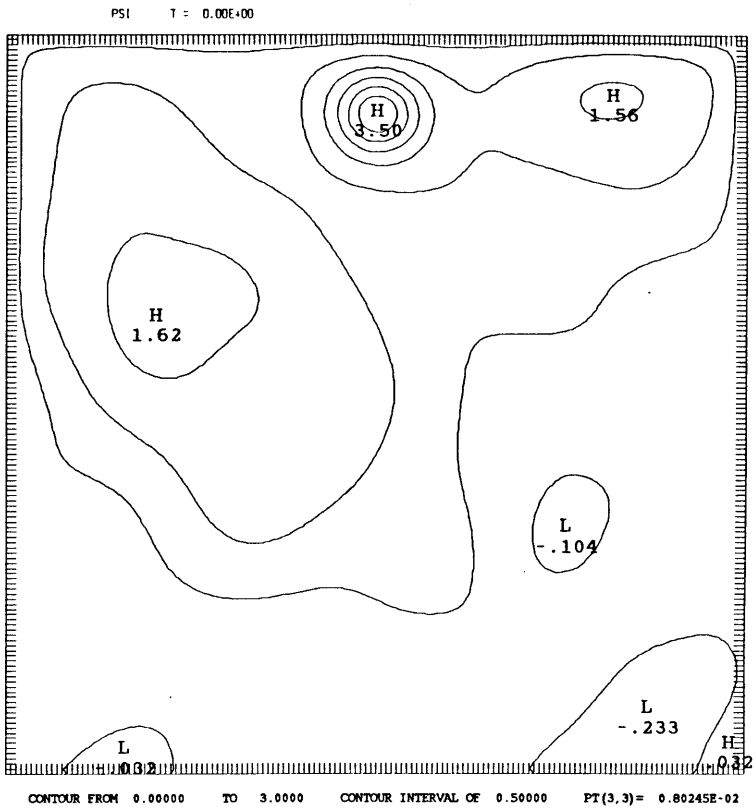
Initially, under the influence of the perturbations vortex moves to the east for approximately 300km. After the time 0.08 (92 days) it stops and starts drifting to the west. Its velocity is uneven, although it generally increases until the collision with the western boundary (after t=0.18 - 208 days; Fig. 25b). In the area of the collision several smaller vortices are formed while the body of the original eddy is absorbed into the boundary current and carried to the east with rapidly decreasing amplitude. After the time 0.30 (347 days) it disappears. Note the very small decrease of the mean amplitude of the vortex prior to the collision (the waves in the Fig. 25d are passing perturbations). From the mean slope of the curve we can estimate its lifetime to be nearly 6 years.

We repeated this experiment with the same initial data except the coefficient of the wind stress was chosen such that the following relation is satisfied:

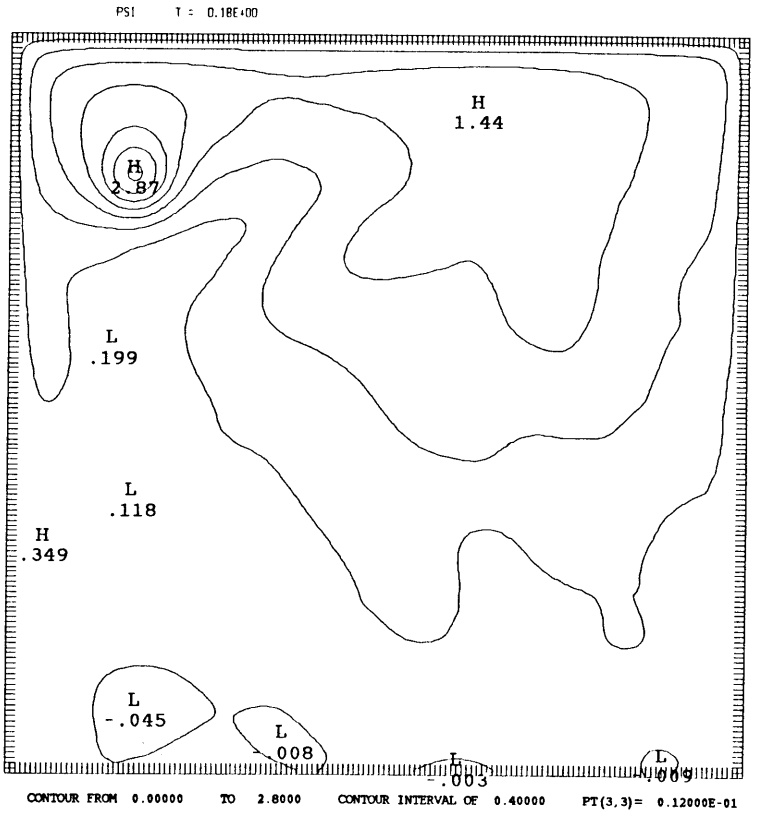
$$\int_0^1 \int_0^1 (\vec{\nabla} \times \vec{\tau})_z \, dxdy = \int_0^1 \int_0^1 (\zeta_0 + \zeta_p) \, dxdy$$

which gives $\tau_0 = 140$. The behavior of the vortex is essentially the same except that its westward motion is slower (it reached the western boundary after the time 0.22 (254 days)). By this time, its amplitude decreased by approximately 30% (lifetime of the vortex would be nearly 2 years). Decay was faster than before, because the forcing was weaker.

In another version of this experiment, the bottom friction was *not* turned on. The vortex started moving to the east but did not stop as in the previous experiments. Rather it proceeded to collide with the eastern boundary. This shows that it is indeed the friction which plays the dominant role in inducing the westward motion.

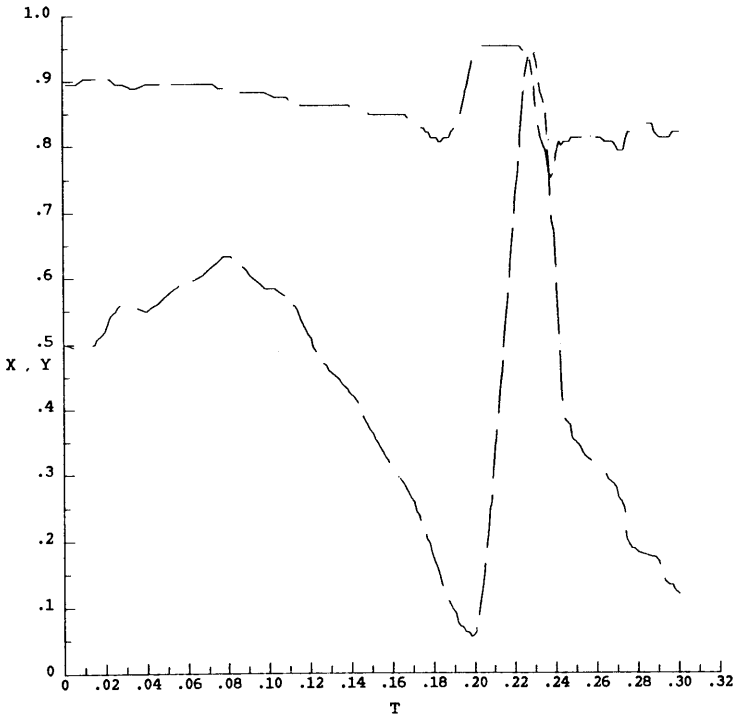


a) Initial condition; ML=1, MU=8, P=0.2, τ_0=200, r=1

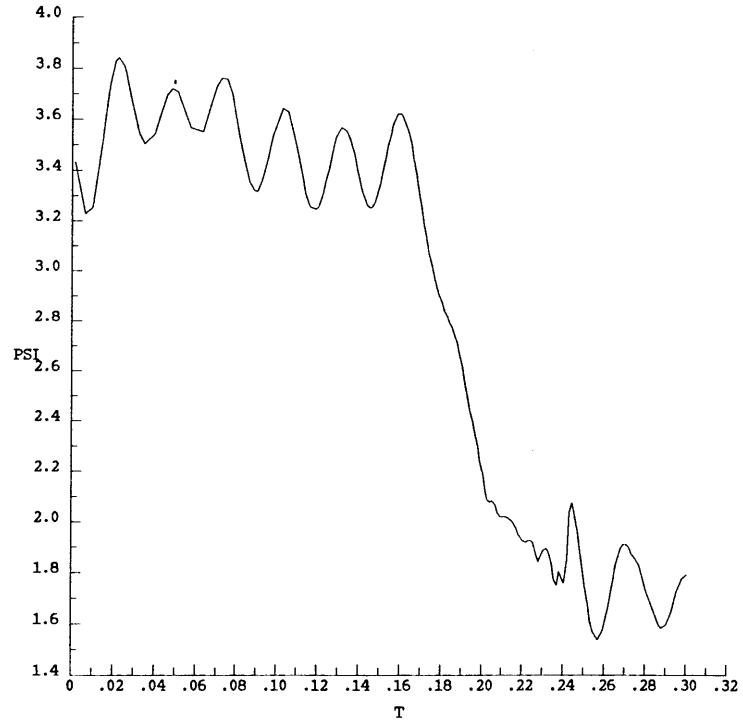


b) Streamfunction after t=0.18 (208 days).

Figure 25. EXPERIMENT II-13



c) Coordinates of the center of the vortex; x - lower curve; y - upper curve.



d) Magnitude of the streamfunction in the center of the vortex.

Figure 25. EXPERIMENT II-13

III TWO LAYER FLOWS

In this chapter we shall discuss three types of patterns of stratified steady large scale circulation. In the first section we shall briefly describe the numerical method. In the second two types of baroclinic flows with barotropic component will be described. They include a generalization of the vortex solution from the preceding chapter, and a generalization of Fofonoff's gyre, which has a potential vorticity distribution similar to the observed large scale flow (Keffer 1985). The robustness of vortices and their behavior in viscous forced flow will be discussed in the third section. In the fourth section we shall describe a "pure" baroclinic mode of general circulation.

Large scale oceanic flows in midlatitudes are governed by the quasi-geostrophic vorticity equation (Pedlosky (1979)):

$$\left[\frac{\partial}{\partial t} + \frac{\partial \psi}{\partial x} \frac{\partial}{\partial y} - \frac{\partial \psi}{\partial y} \frac{\partial}{\partial x} \right] \left[\nabla^2 \psi + \frac{\partial}{\partial z} \frac{1}{S} \frac{\partial \psi}{\partial z} + \beta y \right] = 0 \quad \text{(III-1)}$$

where ∇^2 is two dimensional Laplacian operator, S is the stratification defined by $S = (\frac{R}{L})^2$; L is the length scale and R is the Rossby deformation radius:

$$R = \frac{N_s(z)D}{f}$$

D is the depth of the ocean, $N_s(z)$ is Brunt-Väisälä frequency and f is Coriolis parameter. Since we shall consider large scale flow, a rigid lid approximation for the surface is appropriate.

The two layer equations are:

$$\frac{\partial}{\partial t}\left(\nabla^2\psi_1 + F_1\left(\psi_2 - \psi_1 \right)\right)$$

$$+ J\left(\psi_1 , \nabla^2\psi_1 + F_1\left(\psi_2 - \psi_1 \right) + \beta y \right) = \tag{III-2a}$$

$$= (\vec{\nabla}\times\vec{\tau})_k + \frac{1}{Re}\nabla^4\psi_1$$

$$\frac{\partial}{\partial t}\left(\nabla^2\psi_2 + F_2\left(\psi_1 - \psi_2 \right)\right) +$$

$$+ J\left(\psi_2 , \nabla^2\psi_2 + F_2\left(\psi_1 - \psi_2 \right) + \beta y \right) = \tag{III-2b}$$

$$= -\frac{r}{2}\nabla^2\psi_2 + \frac{1}{Re}\nabla^4\psi_2$$

where r is bottom friction coefficient, Re is Reynolds number, $\vec{\tau}$ is wind stress and F_1 and F_2 are coupling constants defined by

$$F_1 = \frac{f_0^2 L^2}{g\left(\Delta\rho/\rho \right) D_1} \tag{III-3b}$$

$$F_2 = \frac{f_0^2 L^2}{g\left(\Delta\rho/\rho \right) D_2} \tag{III-3b}$$

f_0 is Coriolis parameter, L is scale length and g gravitational constant. D_1 and D_2 are depths of upper and lower layer respectively, while $\Delta\rho$ is difference of densities.

For large scale flow in midlatitudes, typical values of these parameters are:

$$\frac{\Delta\rho}{\rho} = 2\ 10^{-3} \qquad f_0 = 10^{-4}\ s^{-1}$$

$$L = 2{\cdot}10^6\ m$$

$$D_1 = 1000 \text{ m}$$

$$D_2 = 4000 \text{ m}$$

so that $\beta = 2000$, $F_1 = 2000$ and $F_2 = 500$.

If friction and forcing are neglected, steady state equations are:

$$\begin{aligned} \nabla^2\psi_1 + F_1 (\psi_2 - \psi_1) + \beta (y - y_1) + f_1 (\psi_1) = 0 \\ \nabla^2\psi_2 + F_2 (\psi_1 - \psi_2) + \beta (y - y_2) + f_2 (\psi_2) = 0 \end{aligned} \qquad \text{(III-4)}$$

where $f_1 (\psi_1)$ and $f_2 (\psi_2)$ are arbitrary analytic functions, and y_1 and y_2 are constants which we shall choose from the interval [0,1].

The height of the interface is given by:

$$h_2 = \frac{D_2}{D} (1 + \epsilon F_2 (\psi_2 - \psi_1)) \qquad \text{(III-5)}$$

where D is total depth of the ocean and ϵ is Rossby number ($\epsilon = \frac{U}{f_0 L}$).

1 NUMERICAL METHOD

A discrete approximation of the equations (III-4) on the grid of mn points (in x and y direction respectively) can be written as the system of 2mn nonlinear equations:

$$G_i(\psi_i,y_i,\gamma) = 0 \qquad i = 1,...,2mn \qquad \text{(III-6)}$$

which is solved by Newton's iteration (we shall drop subscript i for simplicity):

1. For the initial guess ψ^0 we find the correction vector $\delta\psi^k$ from:

$$\frac{\partial G(\psi^k,y,\gamma)}{\partial \psi^k}\,\delta\psi^k = -\,G(\psi^k,y,\gamma)$$

2. We form the new approximation:

$$\psi^{k+1} = \psi^k + \delta\psi^k$$

This procedure is repeated for k = 1,2,3..., until the L_2 norms of the residual and correction satisfy given tolerances: $|G(\psi^k)| < \epsilon_1$; $|\delta\psi^k| < \epsilon_2$. In our computations we choose $\epsilon_1 = 10^{-5}$ and $\epsilon_2 = 10^{-3}$.

In this form, Newton's method is only locally convergent. To insure convergence and find all solutions of the system, some form of continuation in the parameter(s) must be used. The simplest and the most efficient form is a first-order predictor-corrector method, where the predictor is obtained by Euler extrapolation and Newton's iteration is used as the corrector. Let γ be the continuation parameter, then a guess for the solution ψ at $\gamma + \delta\gamma$ is obtained from:

$$\psi(\gamma+\delta\gamma) = \psi(\gamma) + \delta\gamma\frac{\partial\psi(\gamma)}{\partial\gamma} \qquad \text{(III-7)}$$

Since $G(\psi(\gamma+\delta\gamma),\gamma+\delta\gamma)$ must be zero, application of the chain rule immediately gives a linear equation for the "tangent vector" $\frac{\partial\psi}{\partial\gamma}$

$$\frac{\partial G}{\partial\psi}\frac{\partial\psi}{\partial\gamma} = -\frac{\partial G}{\partial\gamma} \qquad \text{(III-8)}$$

Euler's method (III-7) is only first order accurate in $\delta\gamma$, but it can be shown that it gives as good an initial guess for Newton's iteration as higher order methods while being simpler and computationally cheaper.

Such a simple continuation procedure works as long as the Jacobian $(\frac{\partial G}{\partial\psi})$ of the nonlinear system is not singular. If γ_0 is a singular point, the solution for $\gamma>\gamma_0$ may not exist and the procedure (III-7) will fail. Clearly, near the singular point γ must be regarded as a variable and not as an arbitrary parameter. Thus an equation for γ must be added to the system (III-4) in such a way as to make the Jacobian of the inflated system nonsingular. In order to skip over the singularity a new continuation parameter must be introduced.

In the pseudoarclength procedure (Keller (1977)), we consider γ and ψ as functions of the parameter s, and look for the solution of the inflated nonlinear system:

$$\begin{aligned} G(\psi,\gamma) &= 0 \\ N(\psi,\gamma,s) &= 0 \end{aligned} \qquad \text{(III-9)}$$

where $N(\psi,\gamma,s)$ is constructed to make the Jacobian of (III-9) nonsingular. To this purpose, we require that $\frac{\partial\psi}{\partial s}$ and $\frac{\partial\gamma}{\partial s}$ satisfy the arclength condition:

$$\bar{N}(\psi,\gamma,s) = \left|\frac{\partial\psi(s)}{\partial s}\right|^2 + \left|\frac{\partial\gamma(s)}{\partial s}\right|^2 - 1 = 0$$

However, in practical computation we shall know only ψ and γ and their derivatives with respect to s at the initial point s_0. To obtain the value of ψ and γ at a point $s > s_0$ we replace $\frac{\partial\psi}{\partial s}$ and $\frac{\partial\gamma}{\partial s}$ by their finite difference analogs to get:

$$N(\psi,\gamma,s) = \left(\frac{\partial\psi(s_0)}{\partial s}, \psi(s)-\psi(s_0)\right) + \left(\frac{\partial\gamma(s_0)}{\partial s}, \gamma(s)-\gamma(s_0)\right) + s - s_0 = 0 \qquad \text{(III-10)}$$

which is needed additional equation for (III-9); $(\cdot,\cdot)$ denotes an inner product.

The tangent vector $\begin{bmatrix} \frac{\partial\psi}{\partial s} \\ \frac{\partial\gamma}{\partial s} \end{bmatrix}$, can be obtained from the relation analogous to (III-8):

$$\frac{\partial G}{\partial\psi}\frac{\partial\psi}{\partial s}(s_0) = -\frac{\partial G}{\partial\gamma}\frac{\partial\gamma}{\partial s}(s_0) \qquad \text{(III-11)}$$

$\frac{\partial\gamma}{\partial s}$ can be treated as an arbitrary constant in (III-11) and determined from the arclength normalization condition:

$$\left|\frac{\partial\gamma}{\partial s}\right|^2 = 1 - \left|\frac{\partial\psi}{\partial s}\right|^2$$

while its sign is determined from

$$\left(\frac{\partial\psi(s_0)}{\partial s}, \frac{\partial\psi(s)}{\partial s}\right) + \left(\frac{\partial\gamma(s_0)}{\partial s}, \frac{\partial\gamma(s)}{\partial s}\right) > 0$$

which insures that the continuation is "forward". Thus, the initial guess for Newton's iteration is given by the analog of (III-7):

$$\psi(s) = \psi(s_0) + (s-s_0)\frac{\partial\psi(s_0)}{\partial s}$$

$$\gamma(s) = \gamma(s_0) + (s-s_0)\frac{\partial\gamma(s_0)}{\partial s}$$

The stepsize $\Delta s = s-s_0$ must be chosen sufficiently small to insure convergence, but large enough to make the computations economical. In a straightforward approach, one would choose large Δs and, if the procedure fails, keep reducing it by half until convergence is achieved. This is computationally expensive and a good estimate for stepsize can be obtained from the curvature of the continuation path and the error of the previous step as described by Rheinboldt (1978).

Partial differential operators in (III-4) are discretized with finite differences using a standard 5 point molecule. In each Newton's iteration during the continuation procedure one has to solve a linear system of the form:

$$Q \begin{bmatrix} x \\ y \end{bmatrix} = \begin{bmatrix} \overline{G} & \overline{dG} \\ \overline{N} & \overline{dN} \end{bmatrix} \begin{bmatrix} x \\ y \end{bmatrix} = \begin{bmatrix} a \\ b \end{bmatrix} \qquad \text{(III-12)}$$

$\overline{dG}$ and $\overline{N}$ are column and row matrices respectively and $\overline{dN}$ is a constant. Turning back to the system (III-4), we note that $\overline{G}$ corresponds to the Jacobian matrix $(\frac{\partial G}{\partial \psi})$ of the original system, $\overline{N} = \frac{\partial N}{\partial \psi}$ and $\overline{dG}$ and $\overline{dN}$ are derivatives of G and N with respect to γ. Figure 26 shows the structure of the matrix Q. Such bordered system can be solved by block gaussian elimination (see e.g. Keller (1977)), which requires one decomposition

of the matrix $\overline{G}$ and two back solves. The algorithm is:

1. Find u and v such that:

$$\overline{G}v=\overline{dG}$$

$$\overline{G}u=a$$

2. Form the solution:

$$y = \frac{b - (\overline{N}, u)}{\overline{dN} - (\overline{N}, v)}$$

$$x = u - y\, v$$

From the structure of the equations (III-4) it is clear that the matrix G (we shall drop bar for simplicity) can be written as:

$$G = \begin{bmatrix} A & C \\ D & B \end{bmatrix} \tag{III-13}$$

where C and D are diagonal matrices with elements given by (III-3) while matrices A and B are discrete analogs of the operators:

$$\overline{A} = \nabla^2 - F_1 + \frac{\partial f_1(\psi_1)}{\partial \psi_1}$$

$$\overline{B} = \nabla^2 - F_2 + \frac{\partial f_2(\psi_2)}{\partial \psi_2} \tag{III-14}$$

However the matrix G has bandwidth mn where m and n are number of grid points in x and y direction respectively. Consequently its inversion would require work and storage of the same order as the direct decomposition of the matrix Q. Noting that the C and D are diagonal with constant elements we can make an "inner" block elimination in the process of inverting Q. It is easy to show that the inverse of the matrix G is given by:

$$G^{-1} = \begin{bmatrix} X & Y \\ W & Z \end{bmatrix} \qquad \text{(III-15)}$$

where matrices X, Y, W, Z are defined by:

$$X = - [\, CD - BA \,]^{-1} B$$

$$Y = C [\, CD - BA \,]^{-1}$$

$$W = D [\, CD - AB \,]^{-1}$$

$$Z = - [\, CD - AB \,]^{-1} A$$

so that it is necessary to decompose two matrices, namely $F_1F_2 - BA$ and $F_1F_2 - AB$ which have bandwidth *2 min (m,n)* . It is clear that in the process of inversion of the matrix Q, $F_1F_2 - AB$ can be overwritten on the matrix $F_1F_2 - BA$. Note that because of the nonlinear terms, $\frac{\partial f_1(\psi_1)}{\partial \psi_1}$ and $\frac{\partial f_2(\psi_2)}{\partial \psi_2}$, A and B do not commute. The storage needed is only twice as large as for the barotropic equation, while the work is increased by a factor of eight.

The continuation calculations were done on the grid 31x31 (when dimension of Q is M = 1683) and at the desired points in the parameter space the solution was also found on the grid 47x47 (M = 4051). This allowed us to check whether the coarse grid solution was spurious, and if it was not, fourth order approximation was obtained from Richardson extrapolation. For selected functionals continuation was also made on the grid 37x37. By comparing solutions on the various grids and those obtained by extrapolation we found that the maximum error (after extrapolation) was less than 2%. Since computation of the determinant of the matrix G

would be too expensive, bifurcation points were not detected.

We have made two approaches to the solution of the system (III-2). In the first one continuation was started from the solution of the "linear" problem (two layer generalization of Fofonoff's result). This approach is fairly simple, since several natural parameters of the problem (β,F_1,F_2) were kept constant. Although flows with strong vertical shear were found, all solutions had significant barotropic component. To find a "pure" baroclinic mode, we considered an eigenvalue problem which arises from linearization of (III-4), and used natural parameters for continuation.

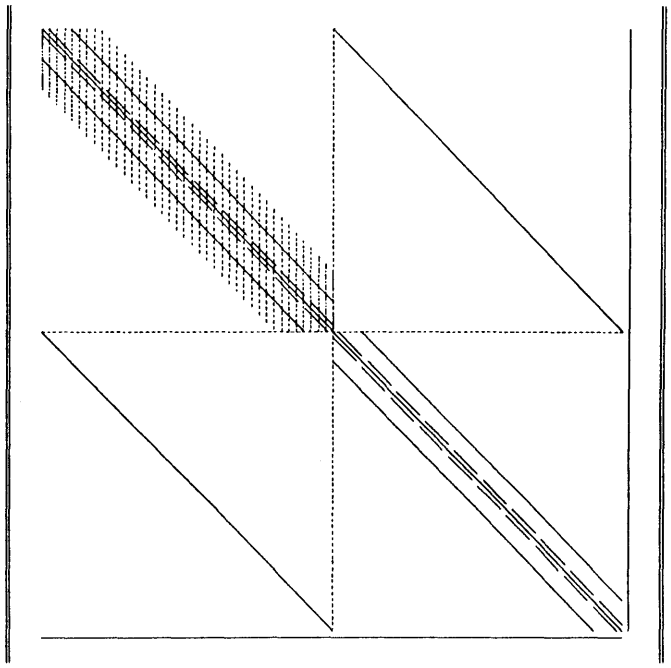


Figure 26. The structure of the matrix Q (III-12)
for the two layer equations (III-4).
Solid lines show nonzero elements. Dotted vertical and
horizontal line show the partition of the submatrix G.
Shaded area shows the storage needed for the
decomposition of the entire matrix.

2 MIXED MODES

In this section, we shall describe two classes of the steady state solutions which are "mixed" i.e. they are baroclinic but have a barotropic component. The first one will be a two-layer generalization of Fofonoff's gyre, and the second one will be a generalization of the vortex solution from the previous chapter.

A straightforward extension of the Fofonoff's result to the two layer model can be easily obtained by assuming that $f_1(\psi_1)$ and $f_2(\psi_2)$ are linear and solving (III-4). If it is further assumed that $y_1 = y_2$, one obtains just two inertial gyres stacked one upon another. If $y_1 \neq y_2$, one can obtain a strongly baroclinic flow. In particular when $y_1 = 0$ and $y_2 = 1$, the pattern consists of two gyres in each layer, of which the northern (anticyclonic) dominates in the upper layer and the southern (cyclonic) dominates in the lower. Two smaller gyres, cyclonic on the south side of the upper layer and anticyclonic on the northern side of the lower layer, are remaining weak barotropic components of the flow. However, such a pattern does not have a counterpart in the observed circulation and moreover may be baroclinically unstable. We shall describe a solution which is stable and has the potential vorticity field field similar to the observed one. As mentioned in the introduction, potential vorticity maps compiled by Keffer (1985) show that in the midthermocline (Keffer's layers B and C) the potential vorticity is nearly homogeneous in the interior of the oceanic basins. This is not the case in the deeper layer, where q is dominated by the planetary vorticity (e.g. North Atlantic). He described the q filed in

four layers; we have to choose two of them. The surface layer is under the strong influence of the atmospheric disturbances (it is essentially Ekman layer) and cannot be approximated by the inertial flow. The upper and mid-thermocline regions show homogenization (the depth is 200-500m) and one of them will be compared to the upper layer of our model. Layer D will be compared to our lower layer. In Keffer's study, the layers are relatively thin, but we shall take these two layers to represent the entire depth of the ocean. The main reason is technical. For large scale circulation with thin layers with small difference in density, the coupling constants F_1 and F_2 become very large giving very sharp boundary layers. Since our scheme is only second order accurate and the finest grid is 47x47, the effective upper limit for F_1 and F_2 is approximately 4000. However to make sure that the solution is not spurious, we have to solve the equations on at least one more grid (which must be coarser), so that F_1 and F_2 should be at most 2000.

We shall consider the basin with length, L = 2000km, scale velocity, U = 4cm/s, giving $\beta = 1000$ and $\epsilon = 2 \cdot 10^{-4}$. Layer depths will be D_1 = 1000m and D_2 = 4000m. If $\frac{\Delta\rho}{\rho} = 2 \cdot 10^{-3}$, we have $F_1 = 2000$ and $F_2 = 500$ (Rossby radii are 22.3km and 44.7 km respectively).

In (III-4), let

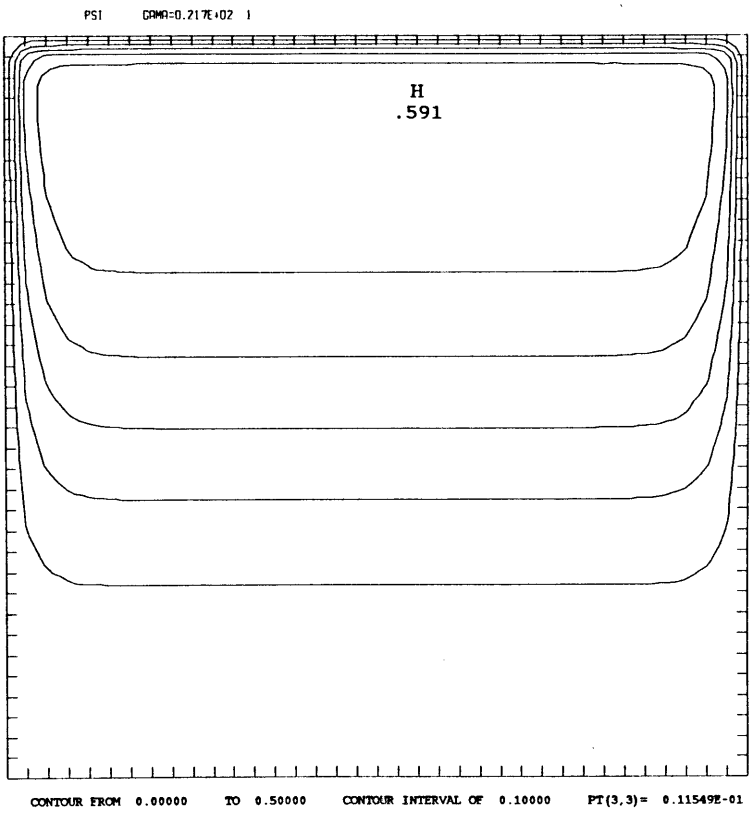
$$f_1(\gamma,\psi_1) = -\sinh(\gamma(\psi_1-\alpha)) - \sinh(\alpha\gamma)$$

$$f_2(\gamma,\psi_2) = -\delta\psi_2$$

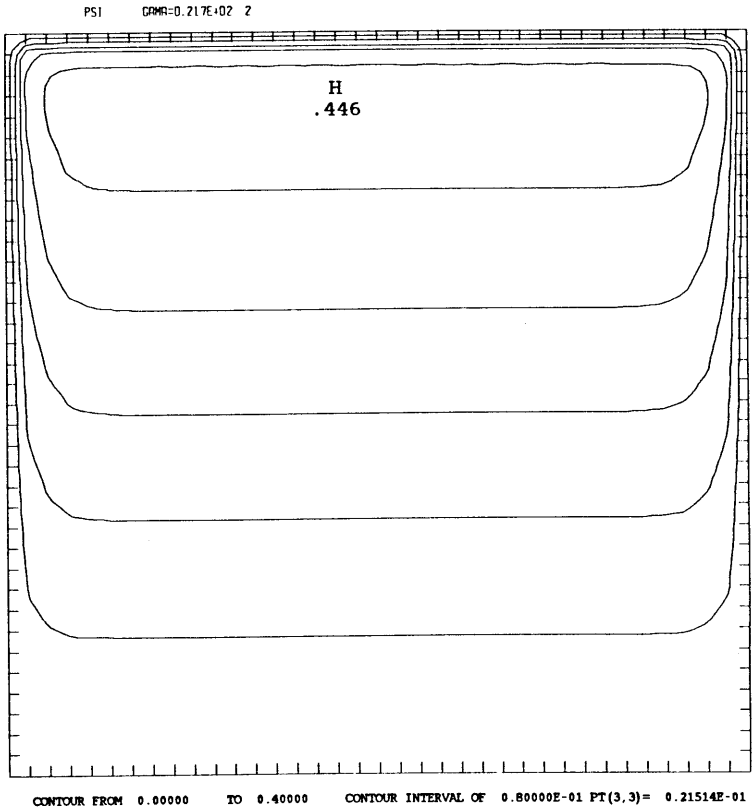
Recall that $f_1 = -q_1$ and $f_2 = -q_2$. For the solution which is only weakly

baroclinic, we expect that in the interior the streamfunction will be approximately proportional to y (compare the barotropic solutions). Then f_1 will, for large γ, have a "shoulder" around the latitude α. We shall set $\alpha = 0.3$. In the lower layer q is proportional to ψ_2 i.e. it is close to y. Figure 27 shows the potential vorticity distribution and the streamfunction of the flow with $\gamma = 21.68$ and $\delta = 1734.4$. Both the upper and lower layer consist of an anticyclonic gyre. The northern boundary current has a maximum speed of approximately 90 cm/s in the upper layer and 65 cm/s in the lower layer. The flow is only weakly baroclinic (maximum dimensional deviation from the mean height of the interface is approximately 65m). It is easy to show that this solution satisfies the generalized Arnold-Blumen condition and thus is stable under small but finite amplitude perturbations.

For comparison, we show in Figure 28, the potential vorticity field for the Atlantic Ocean (from Keffer 1985) for the midthermocline (layer C) and lower thermocline (D). Note the similarity of our solution to the North Atlantic Gyre.

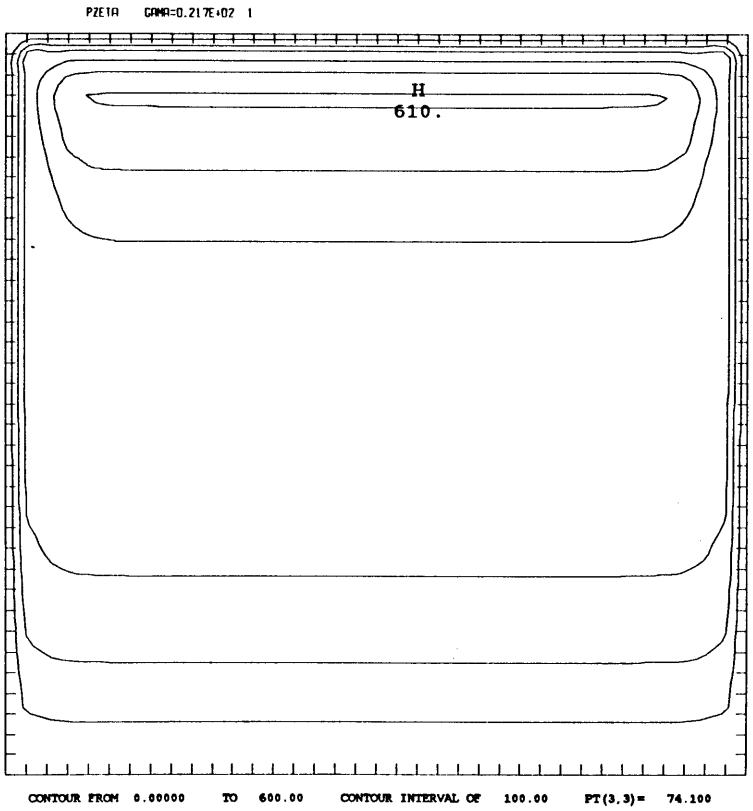


a) ψ_1

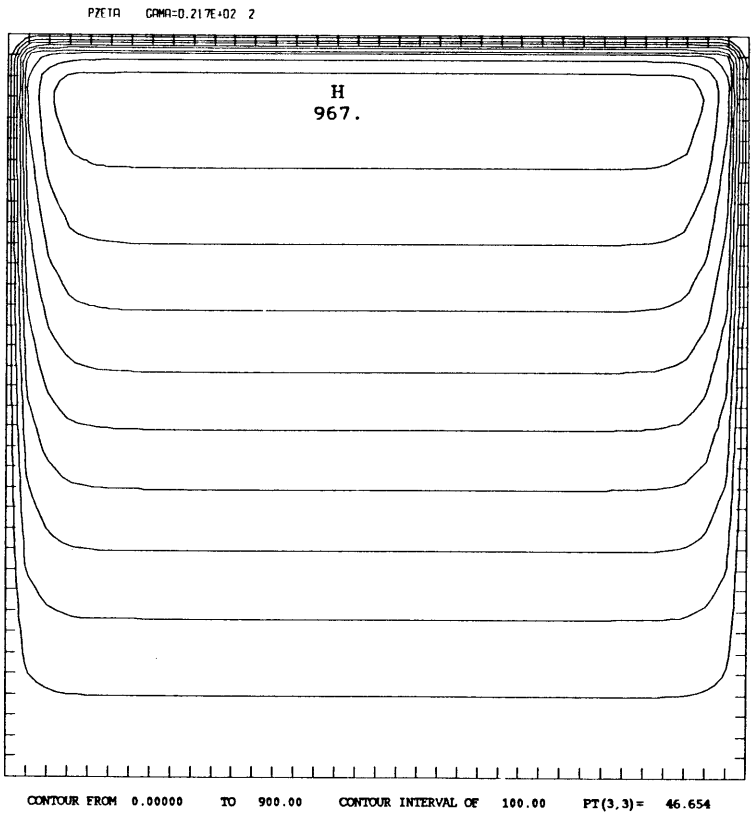


b) ψ_2

Figure 27. The streamfunction of the mixed mode;β=1000; F_1=2000; F_2=500; $f_1(\psi_1)$=–sinh(21.68(ψ_1–0.3))–sinh(6.504); $f_2(\psi_2)$=–1734.4ψ_2

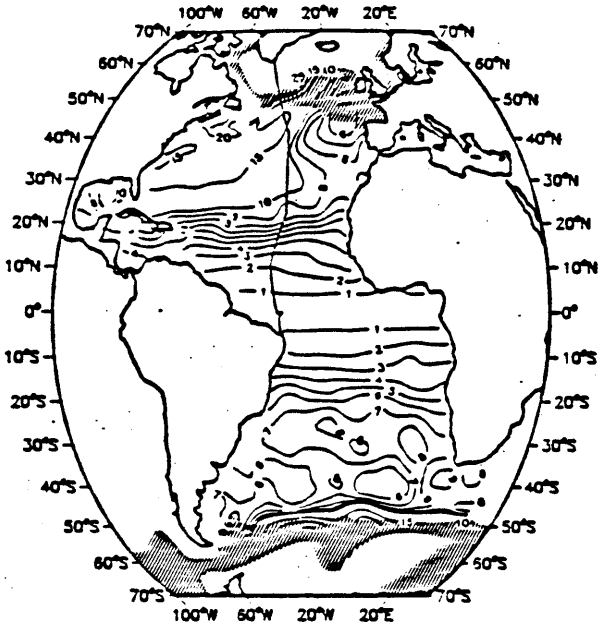


c) q_1

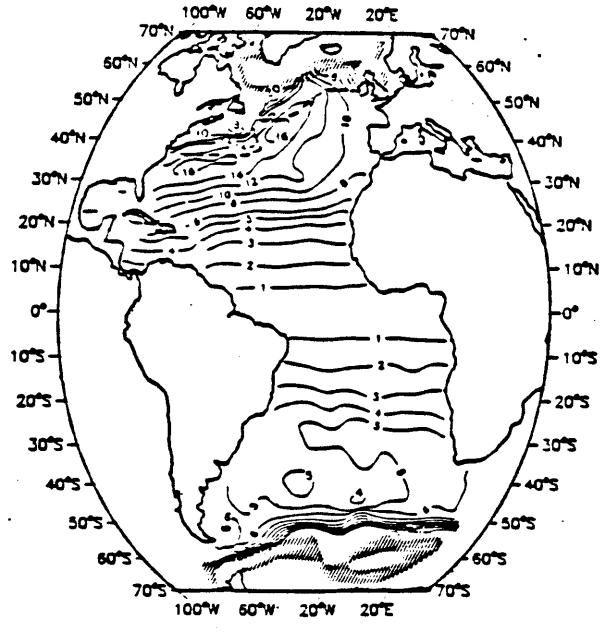


d) q_2

Figure 27. The potential vorticity of the mixed mode



a) midthermocline



b) lower thermocline

Figure 28. Potential vorticity field, Atlantic Ocean.
(Keffer, 1985)

In the second chapter, we showed that nearly radially symmetric vortices can exist in the homogeneous fluid in the basin. Here we shall show that similar vortices exist in the stratified fluid. Consider the flow with $\beta = 500$, (L= 1000km, U=2cm/s); depth of the upper layer 800m, and lower layer 4000m and $\frac{\delta\rho}{\rho} = 2 \cdot 10^{-3}$. Then the Rossby radius of the upper layer is $R_1 = 40$km and of the lower layer is $R_2 = 89.1$km. The constants F_1 and F_2 are 625 and 125, respectively.

Let:

$$f_1 (\gamma , \psi_1) = C_1 \psi_1 (1 + \gamma \psi_1^2)$$
$$f_2 (\gamma , \psi_2) = C_2 \psi_2 (1 - \gamma \psi_2^2) \qquad \text{(III-16)}$$

As in the barotropic case, constants C_1 and C_2 must be negative in order to obtain slow westward interior flow. Knowing the results for barotropic flow, we expect that polynomial-type functionals will have one solution similar to the linear one, and the other will have a small vortex near the boundary current. In the region where the particle velocity is large, nonlinear terms will dominate, and because of the form the functionals chosen, it is clear that they will produce strong vertical shear. We shall set $C_1 = C_2 (= - \beta)$ so that the interior flow will be almost barotropic even with large γ. The choice of y_1 and y_2 will determine whether there will be one or two gyres. We shall set $y_1 = y_2 = y_0 = 1$ so that the gyre will be cyclonic and a fast eastward current will appear at the southern boundary.

When $\gamma = 0$ (linear case), the flow is barotropic. For $-0.66 < \gamma < 0$ and $0 < \gamma < 0.32$ there are two solutions. From Figure 29 we infer that

on the lower part of both the left and right branches, the solution is still essentially barotropic (the solid curve representing maximum value of $|\psi_1(\gamma) - \psi_2(\gamma)|$ is nearly zero). Above the turning point (T') a strong cyclonic vortex appears in the upper layer (dashed curve), while in the lower layer (dotted curve) flow remains almost linear. For positive γ the layers reverse their roles. The curves are not symmetric with respect to the vertical axis because the layers have different depth. Figure 30 shows the solution at $\gamma = -0.406$ on the upper part of the left branch (this is the point V on the continuation curve). Maximum particle speed in the upper layer vortex is 55 cm/s which is about 10 times faster than the maximum velocity in the lower layer vortex. The dimensional diameter of the vortex is approximately 150km. A rough balance of the terms in the vorticity equation, near the center of the vortex, is given in the following table:

	upper layer	lower layer
ς^r	3400	170
ς^p	-450	-450
S	1350	-270
q	4300	-550

ς^r is the relative vorticity ς^p is the planetary vorticity, S is the stretching term and q is the potential vorticity.

In the figures 30ef, the normalized potential vorticity in the area of the vortex is shown ([0,40,0.60]x[0.01,0.21]), in the upper and lower layers. While the lower layer vortex is almost radially symmetric, the upper layer vortex has more complicated structure. We shall subtract the radially

symmetric part of the potential vorticity

$$q_1^i = \frac{\left(q^i - e^{-\left(\frac{r-r_0}{\alpha_1}\right)^2} \right)}{q^i_{max}}$$

for i=1,2, with $\alpha_1 = 0.037$ and $\alpha_2 = 0.17$ Figure 30g shows the underlying structure (q_1^1), which is an asymmetric quadrupole. q in the northern part is approximately 22% of q_{max}. In the lower layer, deviation from radial symmetry is less than 4%. The values of α_i show that the vortex in the upper layer is much more intense than in the lower layer.

Maximum (dimensional) displacement of the interface is 223 m, so that the eddy is not strong. The reason for choosing the solution with relatively weak eddy was to show that, when perturbed, it has about as long lifetime as stronger vortices. In the next section we shall examine its robustness and behavior under the influence of perturbations. The choice of the functionals (III-16) guarantees that the flow in the interior will be almost barotropic. In perturbation experiments we shall try to determine whether the vortex is baroclinically stable and we wanted to eliminate the possibility of the development of baroclinic instability in the interior of the basin.

The equation (III-4) was also solved for various other functionals. In general, functionals of polynomial type will give one solution which contains a small vortex. As in the barotropic fluid, such solutions do not satisfy sufficient condition for stability.

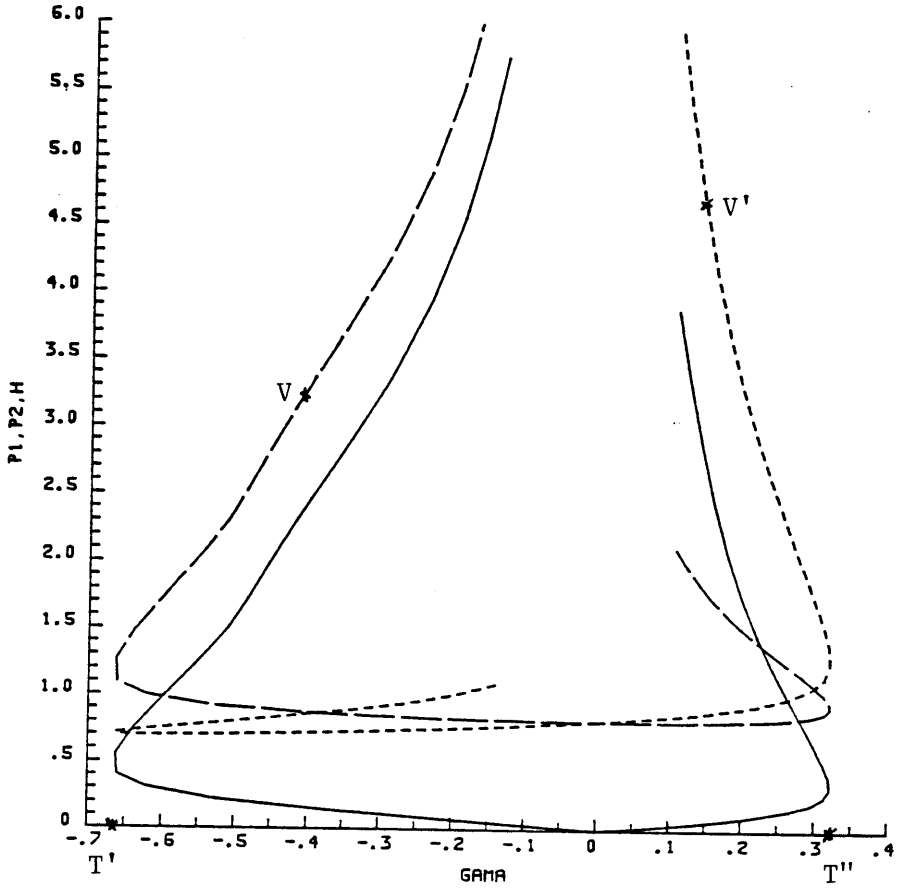
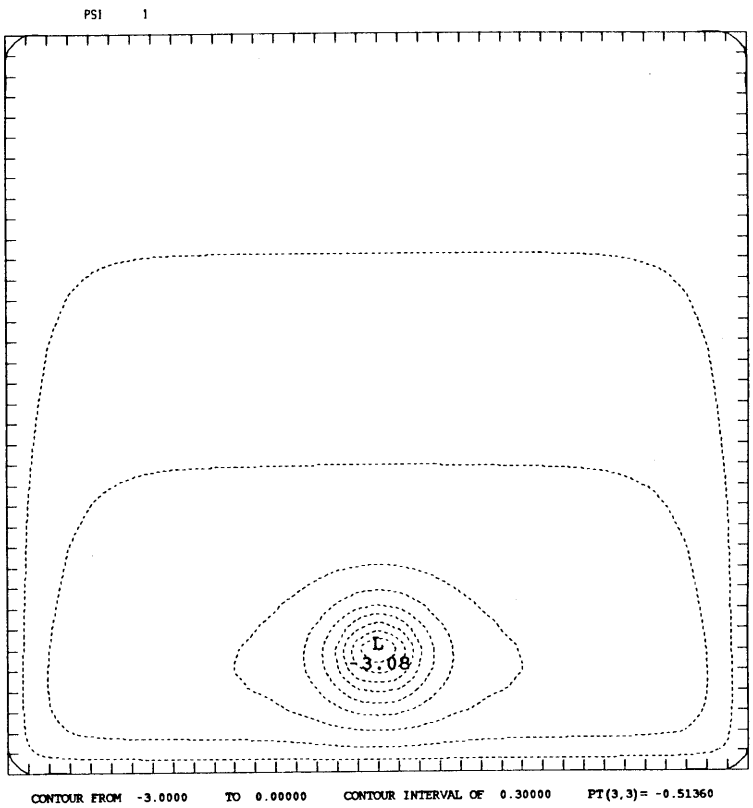
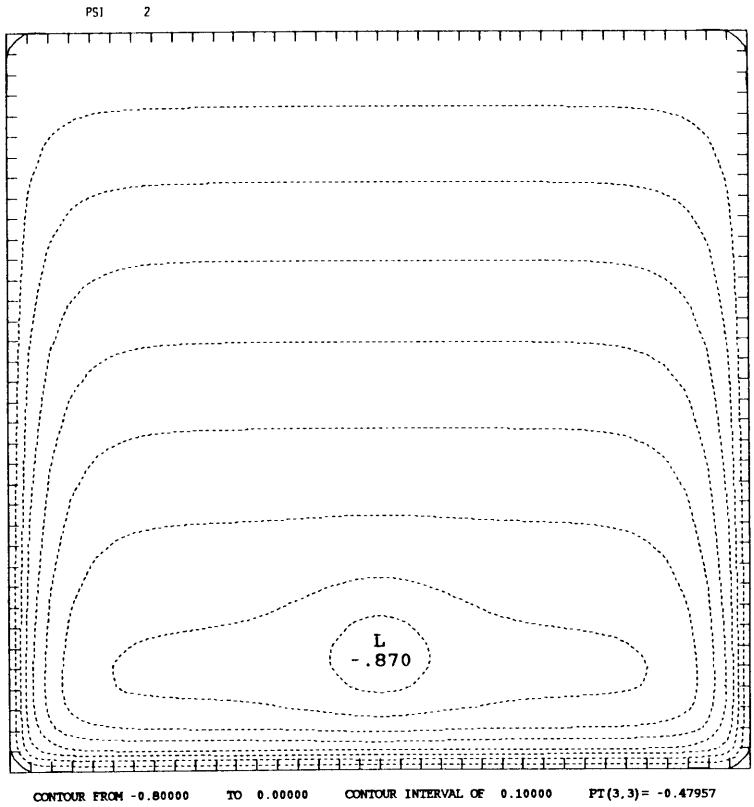


Figure 29. The continuation curves for the functionals (III-16). Dashed curve shows $|\psi_1(\gamma)|_{max}$; dotted curve is $|\psi_2(\gamma)|_{max}$; solid curve shows the maximum of the absolute value of the scaled deviation from the mean height of the interface ($|\psi_1(\gamma)-\psi_2(\gamma)|_{max}$). T' and T" are the turning points. Point V denotes the solution shown in the Figures 30, and V' the solution in the Figures 33ab.

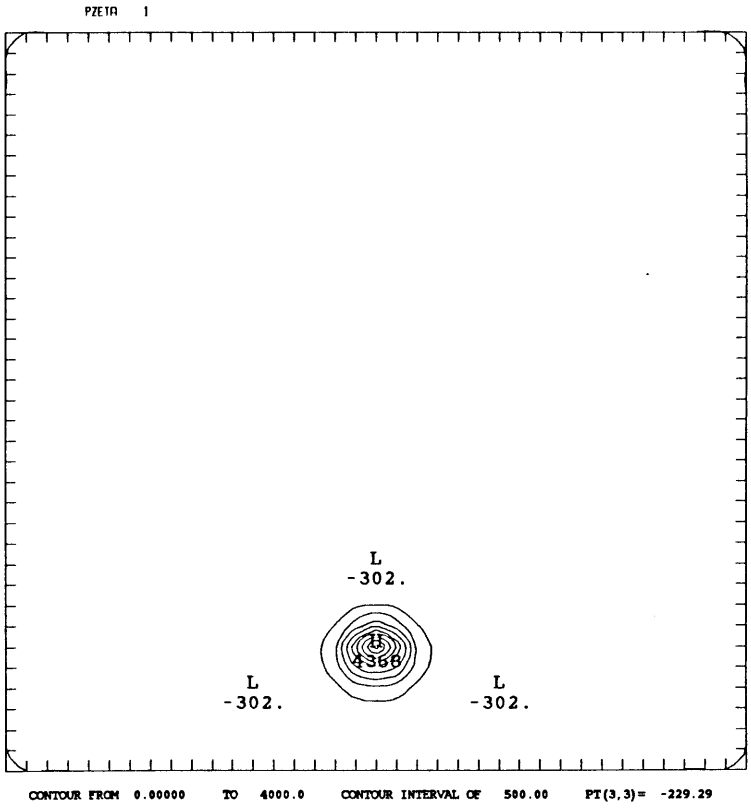


a) ψ_1

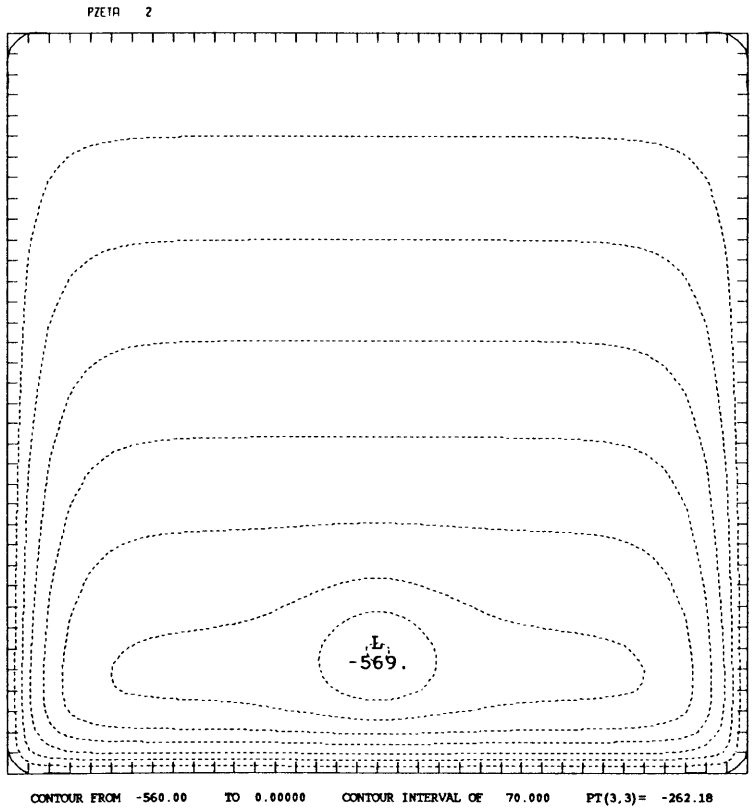


b) ψ_2

Figure 30. The streamfunction for the functional (III-16); β=500; γ=–0.406; C_1=C_2=–β; y_0=1. This solution is denoted by V in Fig. 29.

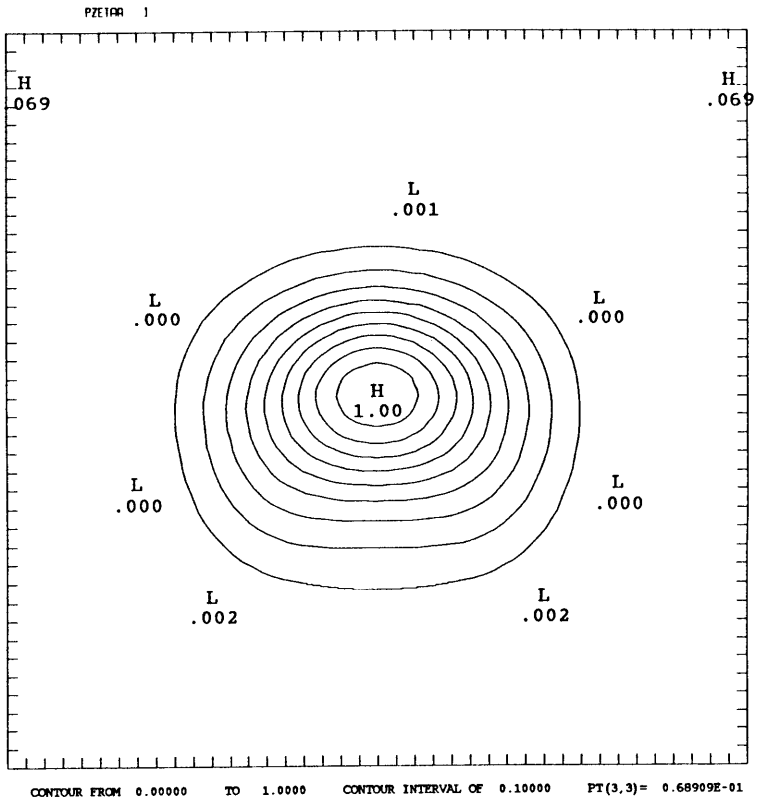


c) q_1

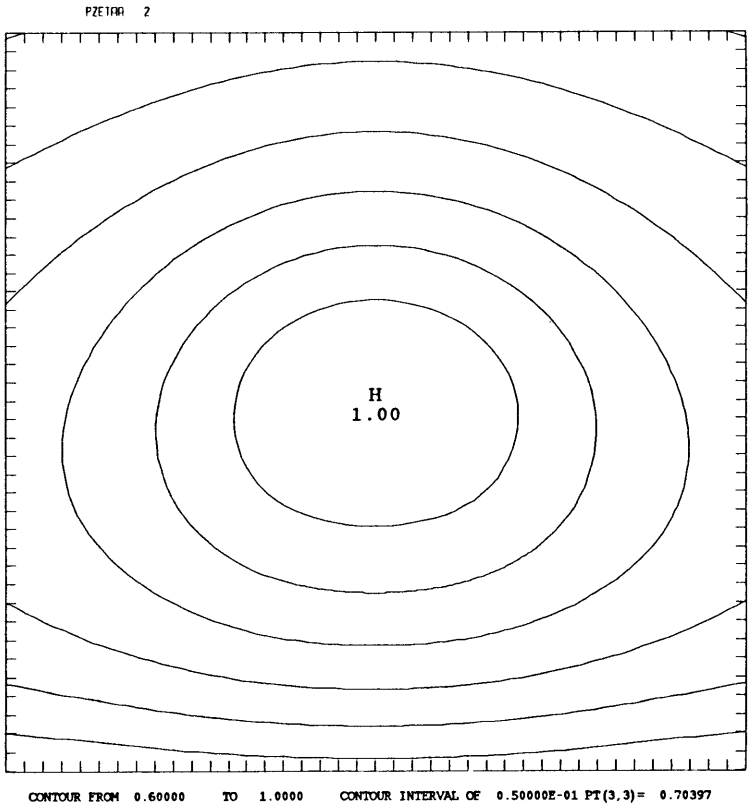


d) q_2

Figure 30. Potential vorticity

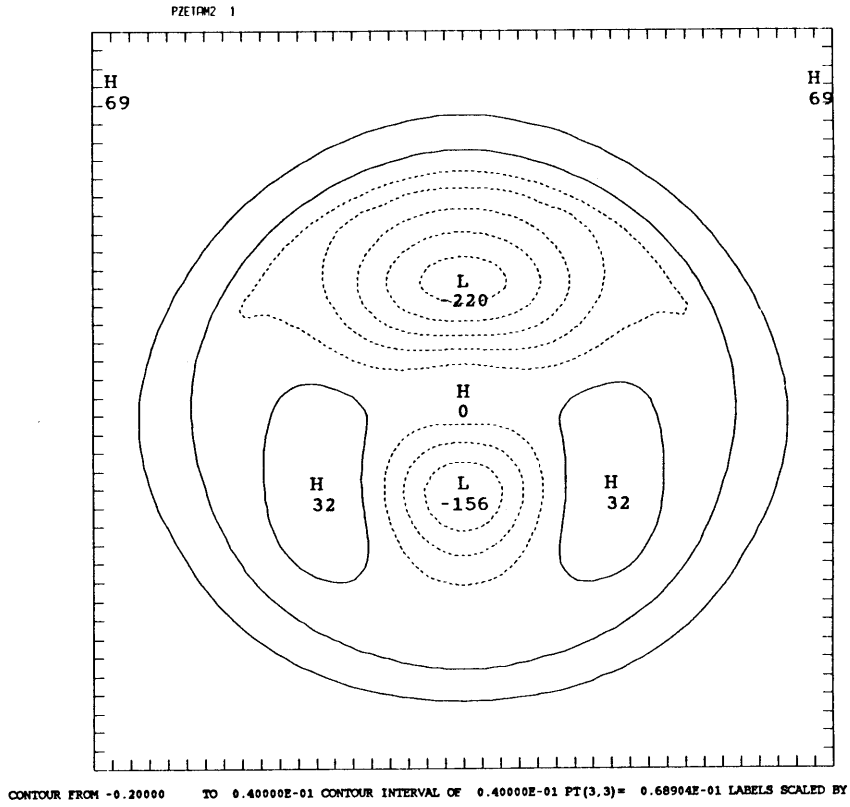


e) q_1

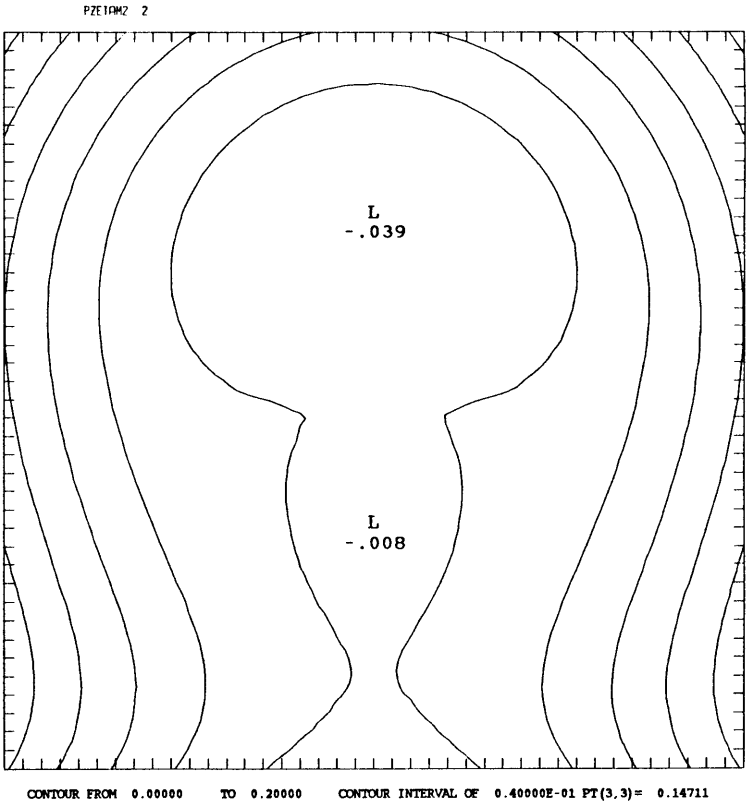


f) q_2

Figure 30. Enlarged area of the vortex [0.40,0.60]x[0.01,0.21] showing the potential vorticity.



g) $[q_1 - e^{-(\frac{r-r_0}{0.037})^2}]/q_{1max}$



h) $[q_2 - e^{-(\frac{r-r_0}{0.17})^2}]/q_{2max}$

Figure 30. The potential vorticity after subtracting radially symmetric part.

3 EVOLUTION EXPERIMENTS

In this section we shall examine evolution of the solutions with vortices under the influence of perturbations, friction and forcing. Such solutions do not satisfy the Arnol'd-Blumen condition and in the previous Chapter we showed that their analogs in homogeneous fluid are indeed unstable. In the first two experiments we shall observe the evolution of the perturbed flow without friction or forcing. In the third experiment we shall show the effect of bottom friction on the lower layer vortex, and in the fourth we shall see how the upper layer vortex behaves in perturbed, forced and viscous flow.

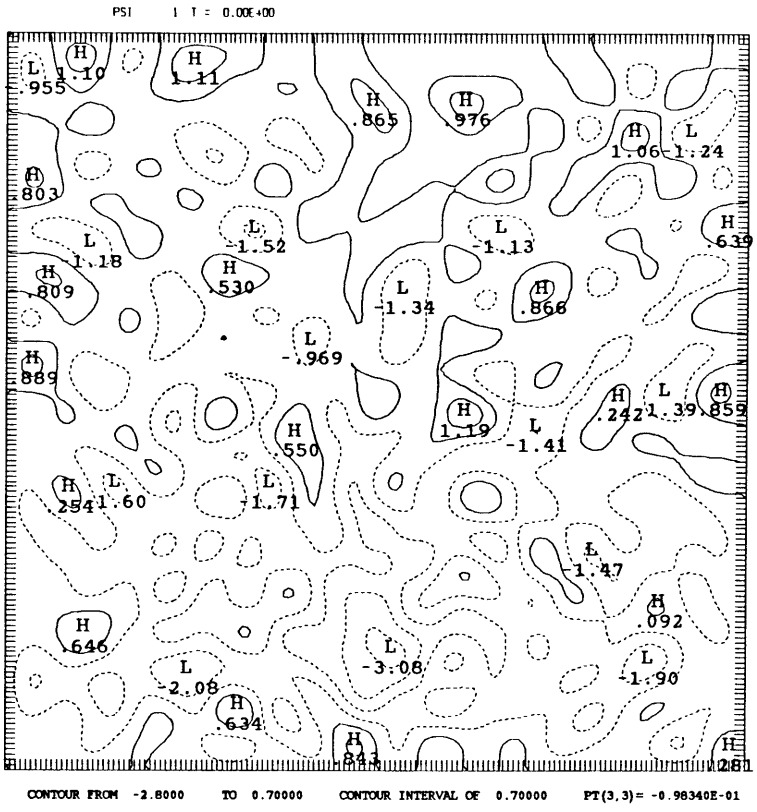
The equations (III-2) were solved numerically using the method described by Holland (1978) (see also the Appendix). The grid in the first, third and fourth experiments was 145x145, while in the second experiment it was 193x193.

EXPERIMENT III-1

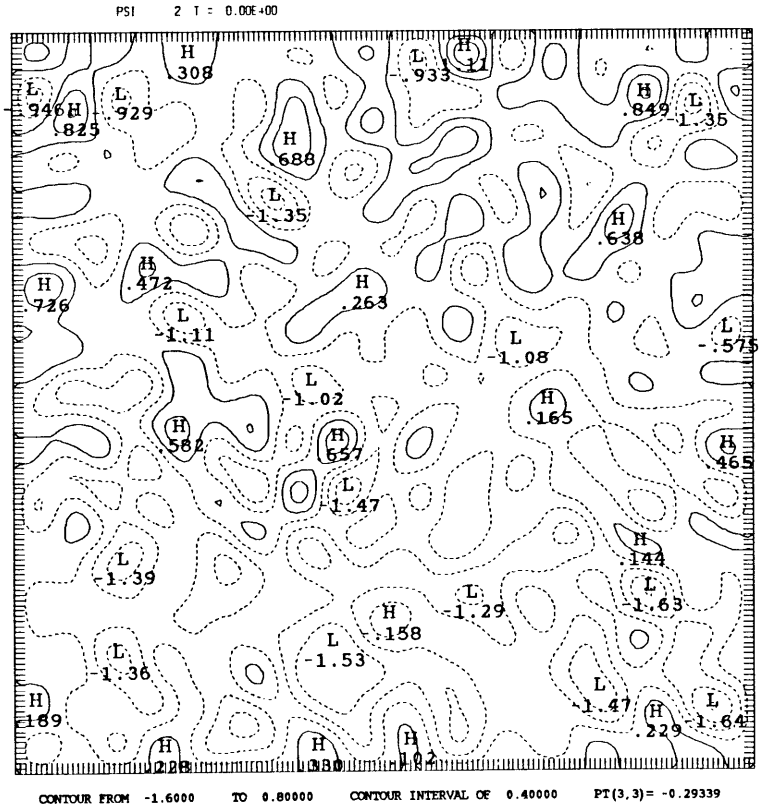
For this experiment we shall use a solution with a cyclonic vortex in the upper layer near the southern boundary current (Fig 30). Streamfunction of the perturbation in both layers was chosen in the form:

$$\psi_P = P \; | \psi_0 | \; \frac{\sum_{i=ML}^{i=MU} \sum_{j=ML}^{j=MU} \alpha_{i,j} \sin(i\pi x) \sin(j\pi y)}{\left| \sum_{i=ML}^{i=MU} \sum_{j=ML}^{j=MU} \alpha_{i,j} \sin(i\pi x) \sin(j\pi y) \right|}$$

where $\alpha_{i,j}$ are random numbers from the interval [-1/2,1/2].

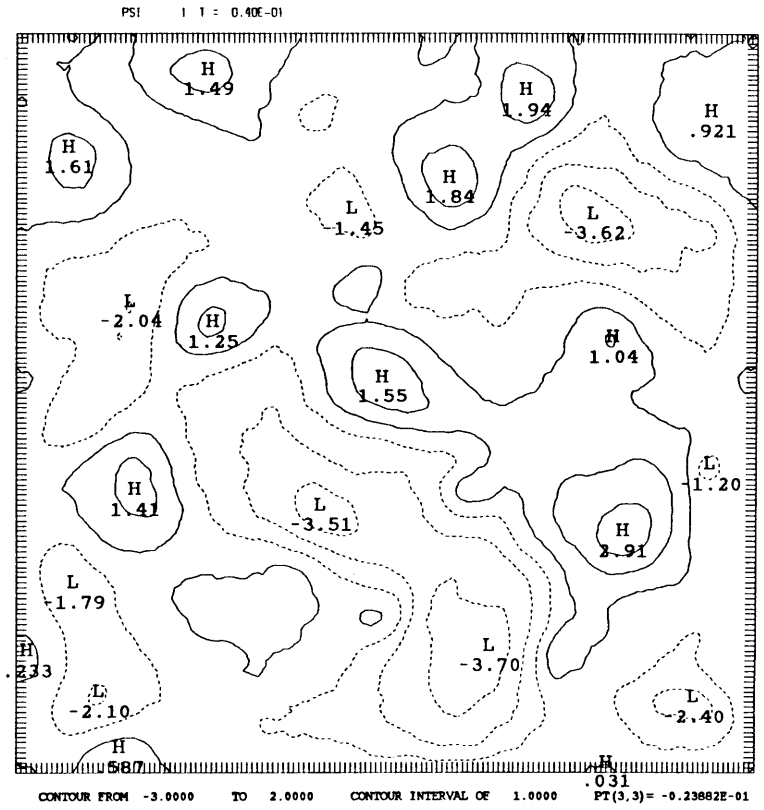


a) ψ_1; initial condition; ML=1, MU=20, P=0.75

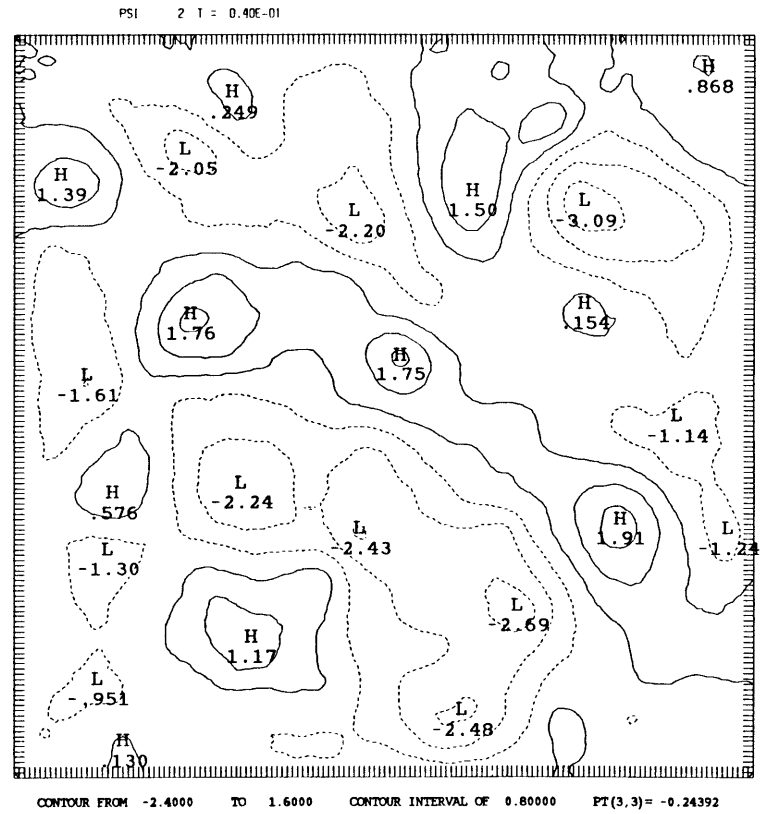


b) ψ_2; initial condition; ML=1, MU=20, P=0.75

Figure 31. EXPERIMENT III-1



c) ψ_1 after t=0.04 (23 days)



d) ψ_2 after t=0.04 (23 days)

Figure 31. EXPERIMENT III-1

We shall consider low frequency but relatively large amplitude perturbations: ML=1, MU=20, P=0.75. The shortest wavelength of the perturbations is approximately 2/3 of the diameter of the vortex. Figures 31 show the streamfunction of the initial condition and after the time 0.04 (23 days - characteristic time of the flow is $5 \cdot 10^7$ s). The vortex moved rapidly to the east and collided with the boundary. In the Figure 31c it can be seen in the lower right corner. Note that the perturbations were sufficiently large to destroy the boundary current, but up to this time did not destroy the vortex. After the collision, vortex decayed as in the barotropic case.

In the

EXPERIMENT III-2

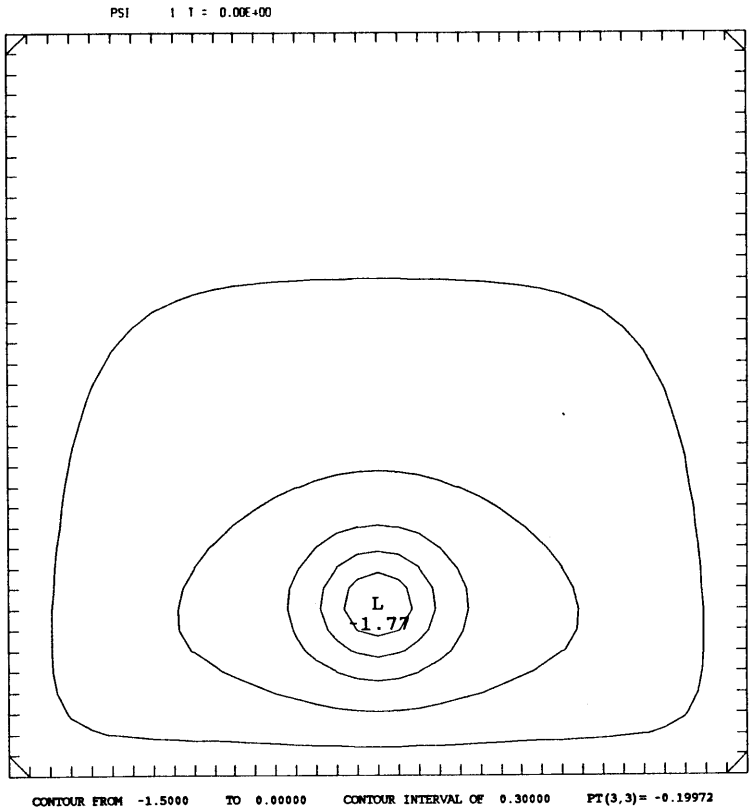
we examine the behavior of the vortex in flow with high frequency perturbations. In order to decrease relative wavelength of the perturbations we shall as in the homogeneous flow, consider low β vortex which is much larger relative to the size of the domain. Let L=1000km and U=10cm/s, then $\beta = 100$. Depths of the upper and lower layers will be 800 and 4000m, so that the Rossby radii are 40 and 89km, respectively. The Rossby number is 10^{-3}. The functional relationship between the potential vorticity and the streamfunction is still (III-16) with $C_1 = C_2 = -\beta$, and $\gamma = -2.617$.

Figure 32ab shows the streamfunction of the unperturbed vortex in both layers. The vortices are weaker than before and the barotropic component is relatively stronger. Note that outside the vortex, the flow is almost barotropic so that the entire available potential energy is in the

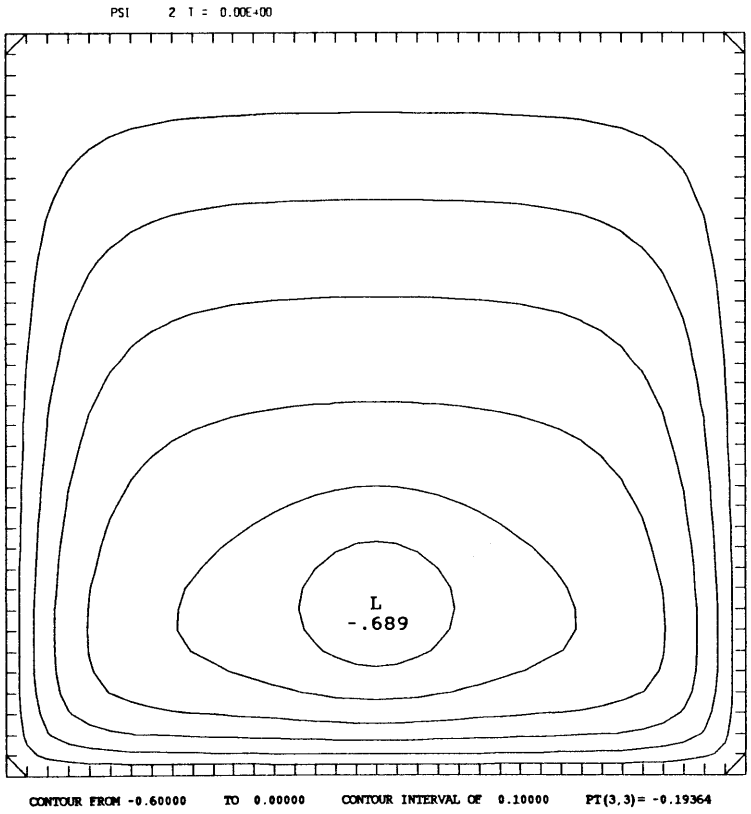
vortex itself.

Let P=0.1, ML=20 and MU=40 so that the smallest wavelength of perturbations is approximately 1/5 of the diameter of the vortex. Although the amplitude of ψ_p is small, the perturbation has large energy and enstrophy because of its high frequency. Energy is approximately 5 times larger and enstrophy 600 times larger than that of the basic flow. Figure 32cd shows the streamfunction of the initial condition. At the time 0.08 (approximately 10 days - characteristic time of the flow is 10^7 s) there is substantial decline of the amplitude in both upper and lower layer (Figure 32ef). It is interesting that while the amplitude of the upper layer vortex decreased by 45% the difference of the streamfunctions (i.e. height of the interface) decreased by only 25%. As the relative vorticity decreases, the vortex moves northward to conserve the potential vorticity (small westward drift is a consequence of the perturbations). After the time 0.08 the amplitude of the vortex started slowly increasing ("infrared cascade"), but this vortex cannot be identified with the original steady solution.

There was almost no change in the available potential energy during the integration and we conclude that the instability of the vortex is barotropic.

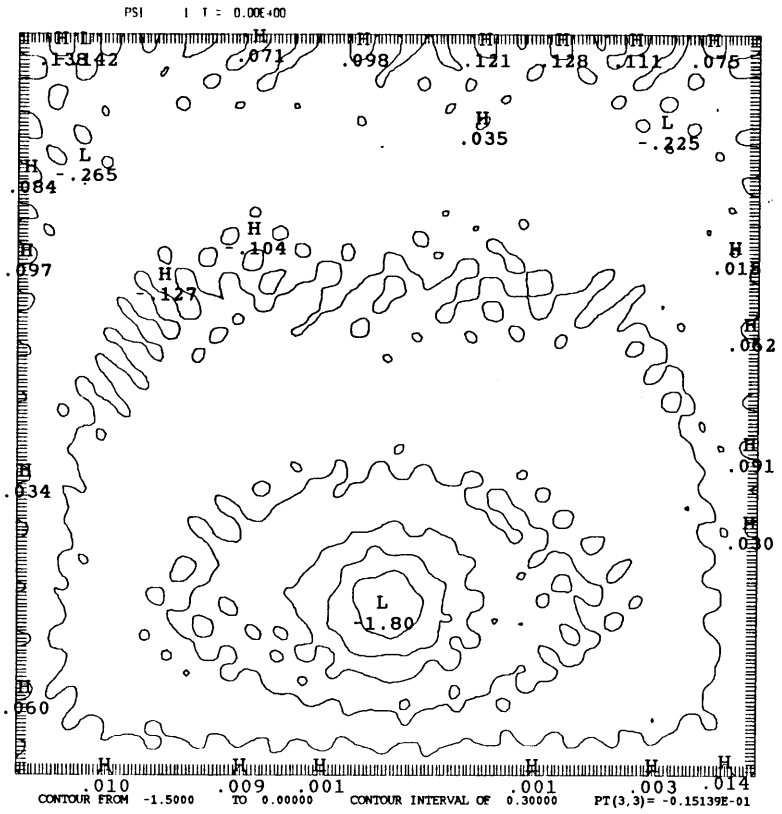


a) ψ_1 for the functional (III-16); $C_1 = C_2 = -\beta$; $\beta = 100$; $\gamma = -2.617$

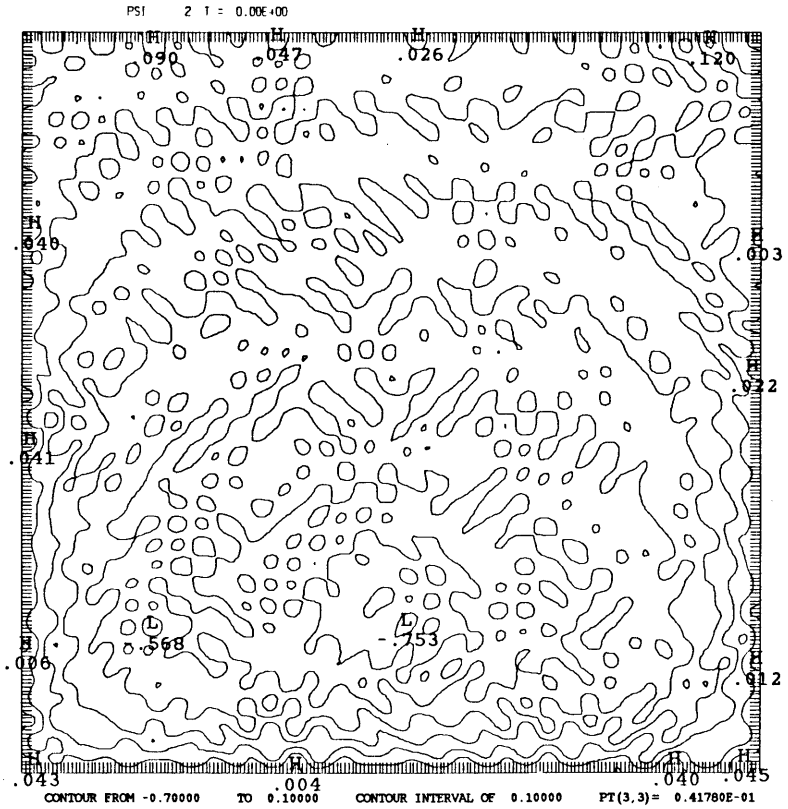


b) ψ_2

Figure 32. EXPERIMENT III-2

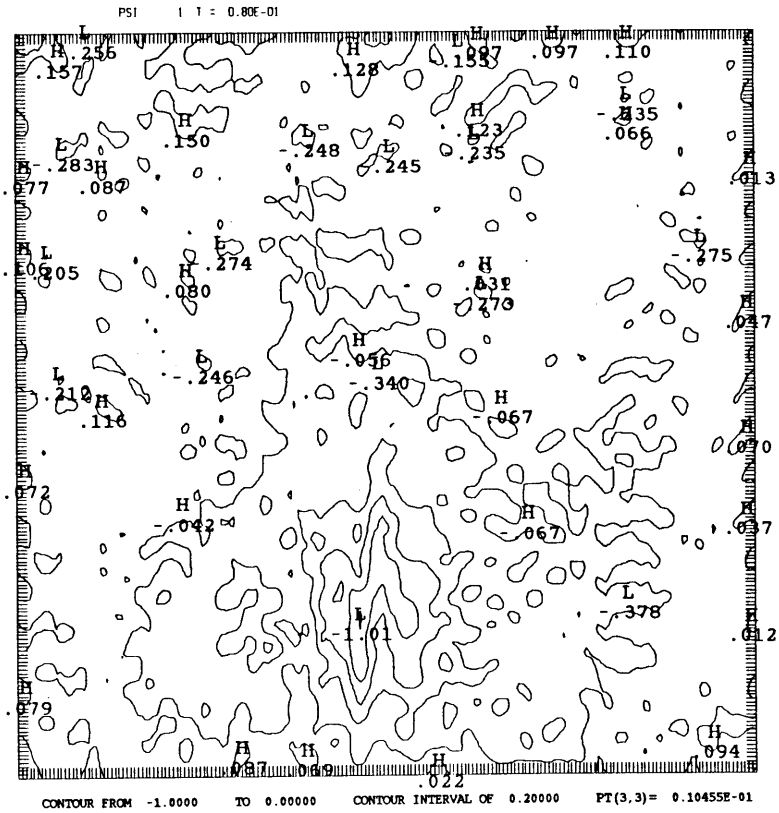


c) The initial condition: $\psi_1^0 + \psi_1^P$; ML=20, MU=40, P=0.1

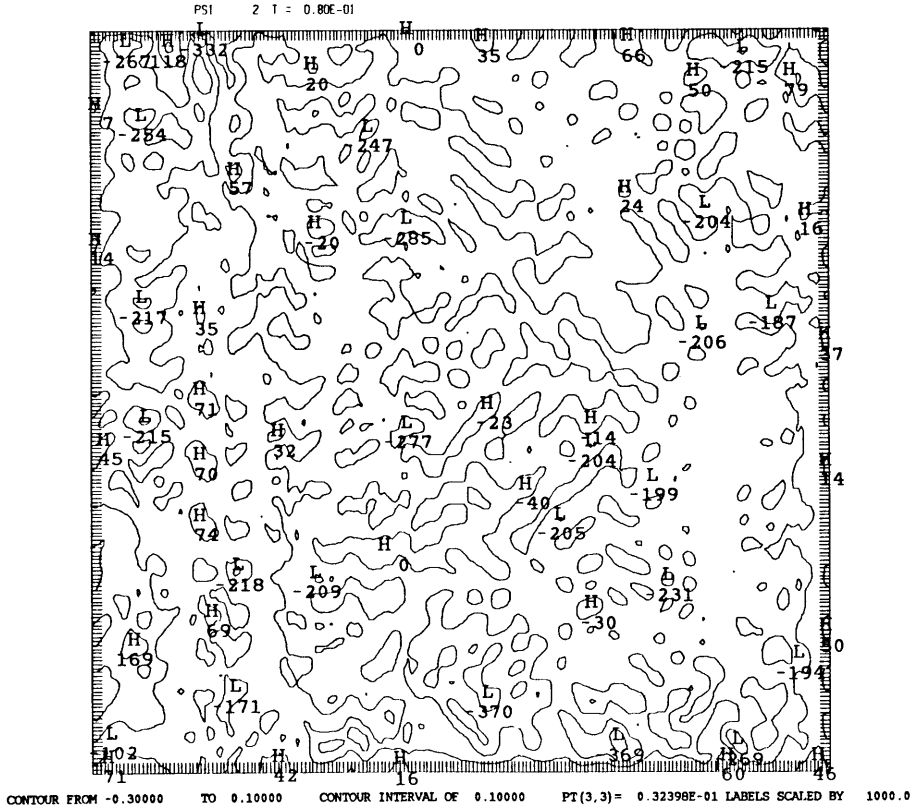


d) The initial condition: $\psi_2^0 + \psi_2^P$; ML=20, MU=40, P=0.1

Figure 32. EXPERIMENT III-2



e) ψ_1 after t=0.08



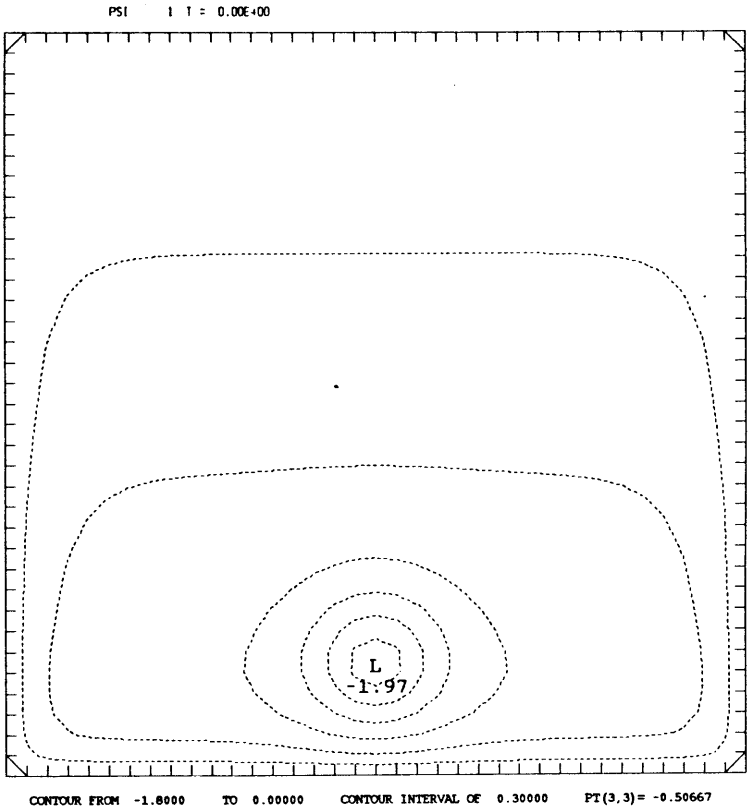
f) ψ_2 after t=0.08

Figure 32. EXPERIMENT III-2

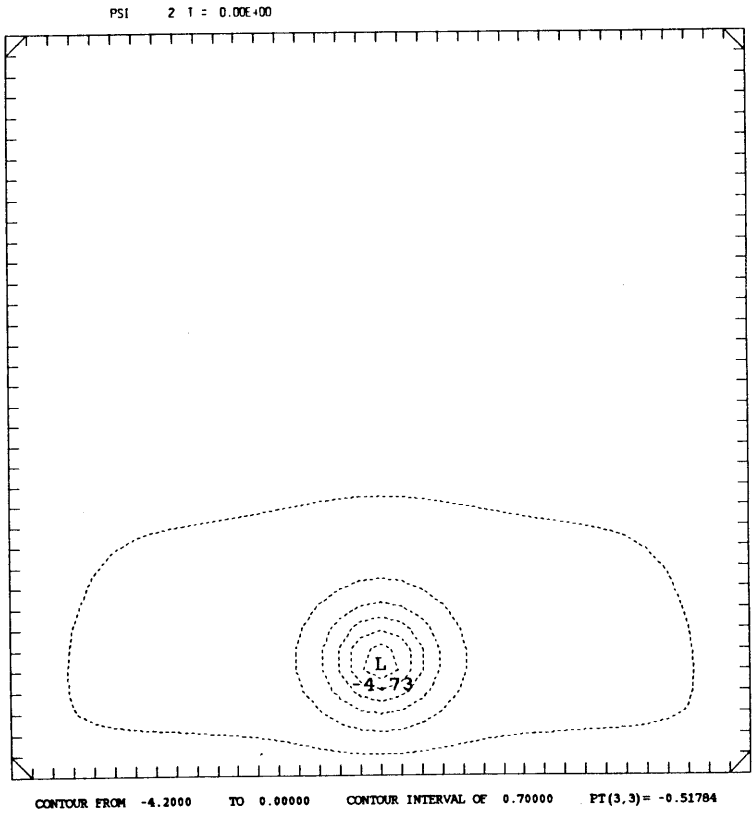
In the Chapter II we established the relations between the bottom friction or forcing and the motion of the vortex. In the two layer model situation is more complicated because of the interaction between the layers, and because the forcing and friction act on the different layers. In stratified fluid lateral friction may play a more important role than the bottom friction, but in demonstrating it we would again encounter difficulty with the discontinuity in the initial condition. Therefore, in the last two experiments only the bottom friction and the forcing will be included.

EXPERIMENT III-3

Consider the flow with the same parameters as for the vortex of Figure 30 and the same functional relationship only with $\gamma = 0.122$ (point V' in the Figure 29.). As can be seen from Figure 33ab, the vortex in the lower layer is stronger. We shall use this solution as an initial condition for the equations (III-2), without forcing or lateral friction, but with the bottom friction (r=10), which is turned on instantaneously. The vortex moves to the west, but with a much larger northward component than in the barotropic flow. Figure 33cd shows the streamfunction after the time 0.12 (70 days). In order to conserve the potential vorticity, the cyclonic vortex in the upper layer disappeared, and a weak anticyclonic vortex appeared above the weakened lower layer cyclonic vortex.

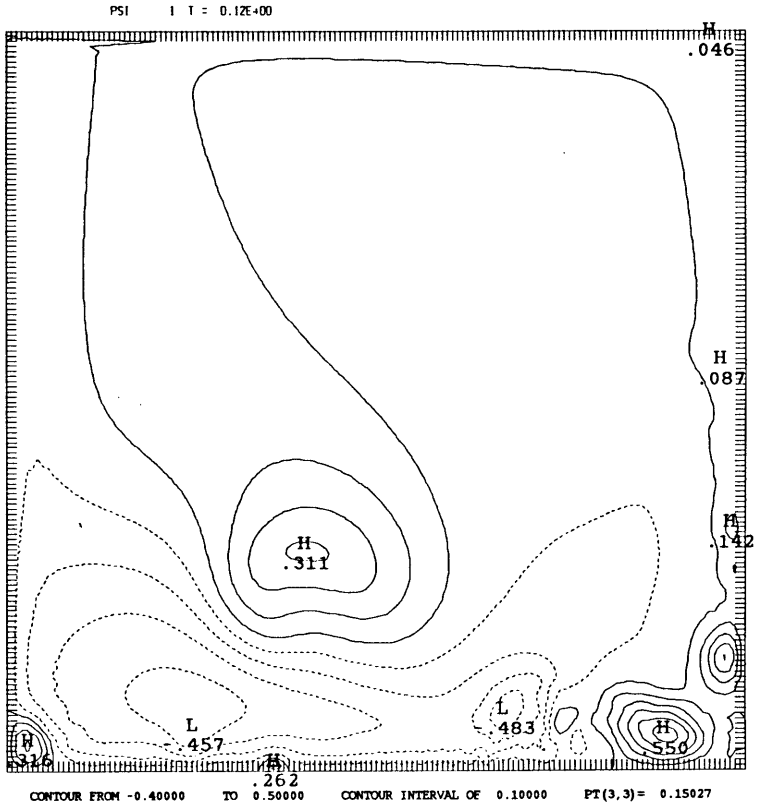


a) ψ_1

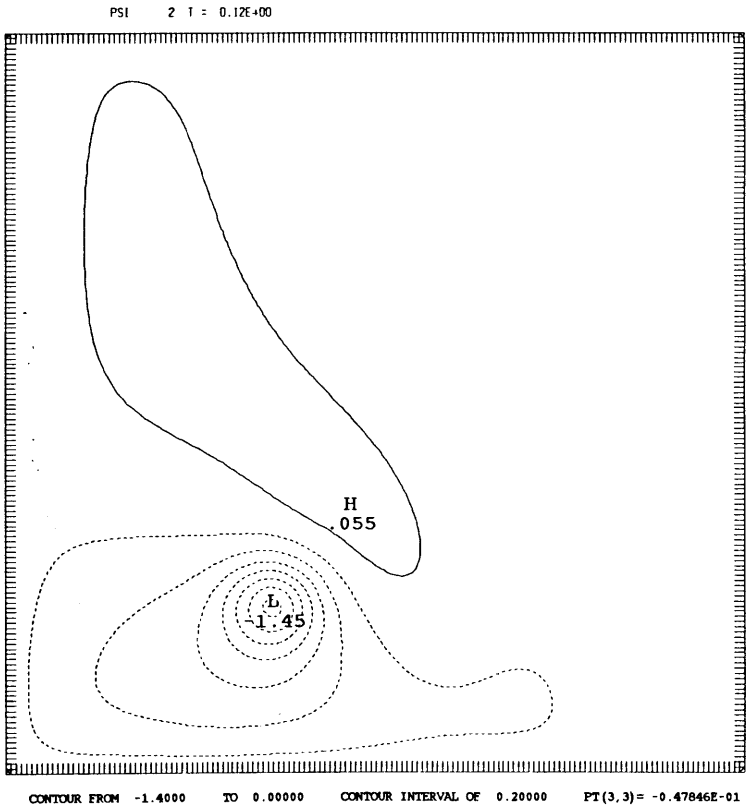


b) ψ_2

Figure 33. EXPERIMENT III-3. Initial condition. This solution is denoted by V' in Fig. 29.



c) ψ_1 after t=0.12 (70 days)



d) ψ_2 after t=0.12 (70 days)

Figure 33. EXPERIMENT III-3. P=0; r=10.

We have repeated the same experiment only with the vortex of Fig. 30. in the initial condition. When the bottom friction was turned on the vortex was drawn into the boundary current and immediately carried to the east. This is easy to explain through conservation of the potential vorticity. Friction caused a decrease of the amplitude of the lower layer vortex, which in turn increased the height of the interface (stretching term in the upper layer), so that the relative and planetary vorticity in the upper layer had to decrease, and the vortex moved southwards (i.e. into the current).

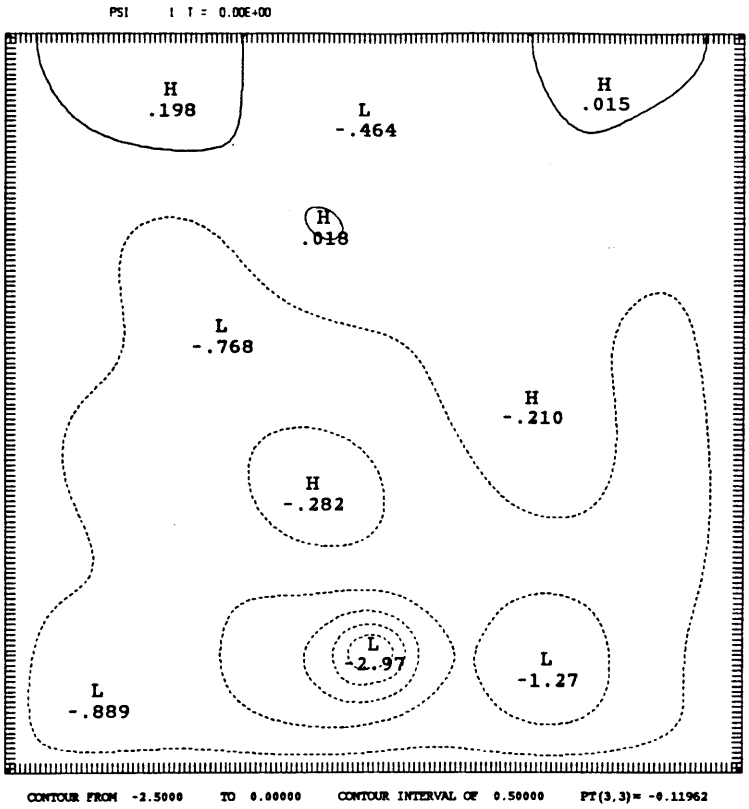
EXPERIMENT III-4

In the last experiment we shall consider the flow with the vortex (Fig. 30) in perturbed, viscous and forced flow. with r=4, P=0.25, ML=1 and MU=6.

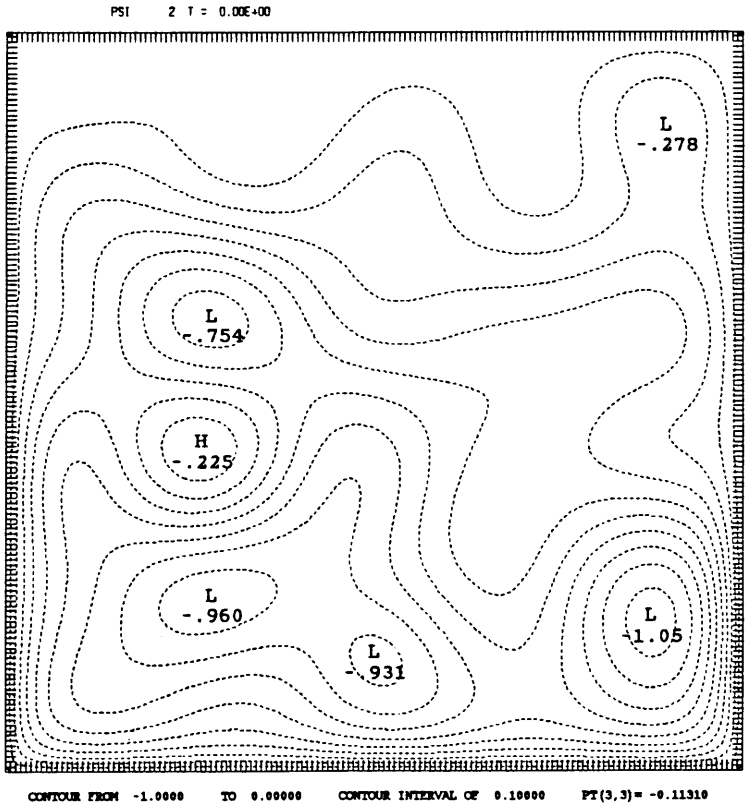
Figures 34ab show streamfunction of the initial condition. Perturbed vortex moves to the west with almost constant speed ($\approx$ 2.7 cm/s). This shows that the motion of the vortex is influenced primarily by the perturbations, while bottom friction plays a secondary role. After the time 0.30 (174 days) the vortex reaches the western boundary (Figures 34cd) and is subsequently absorbed into the southern boundary current and carried to the east. Kinetic energy of the upper layer increases due to the wind stress up to the time 0.33, when it levels off. In the lower layer, kinetic energy slowly decreases and after the time 0.25 remains nearly constant. Available potential energy of the flow is nearly constant for the time of integration. A strong vertical shear exists in the area of the vortex but

baroclinic instability was not observed.

We have performed several other perturbation experiments with vortices of various intensities and with different perturbations. In some instances, in the regions of strong vertical shear, baroclinic instability was observed, but never in the region of the vortex itself.

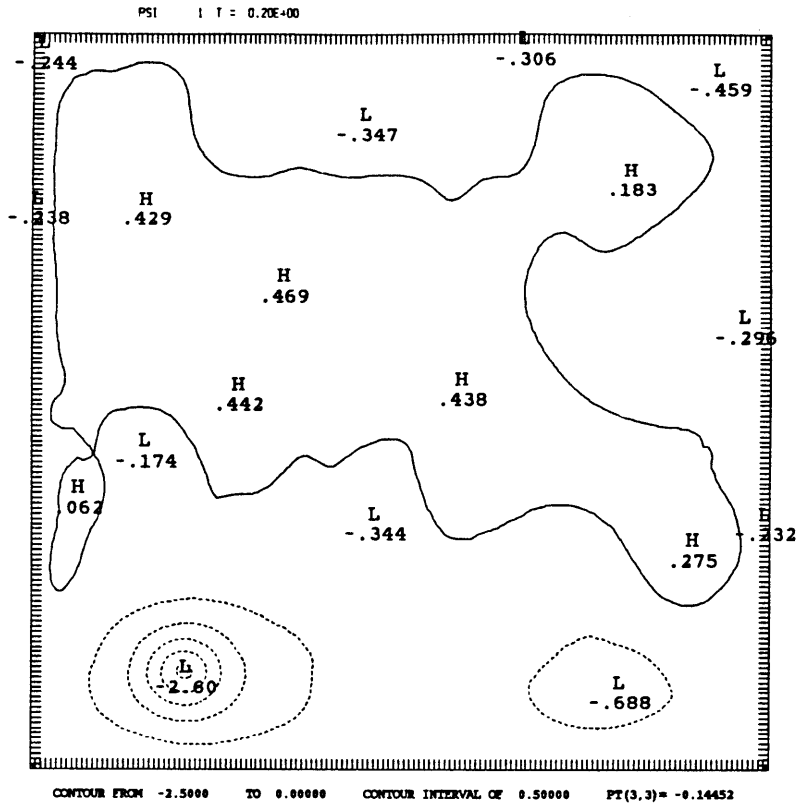


a) ψ_1; initial condition; ML=1, MU=6, P=0.25, r=4, τ_0=491

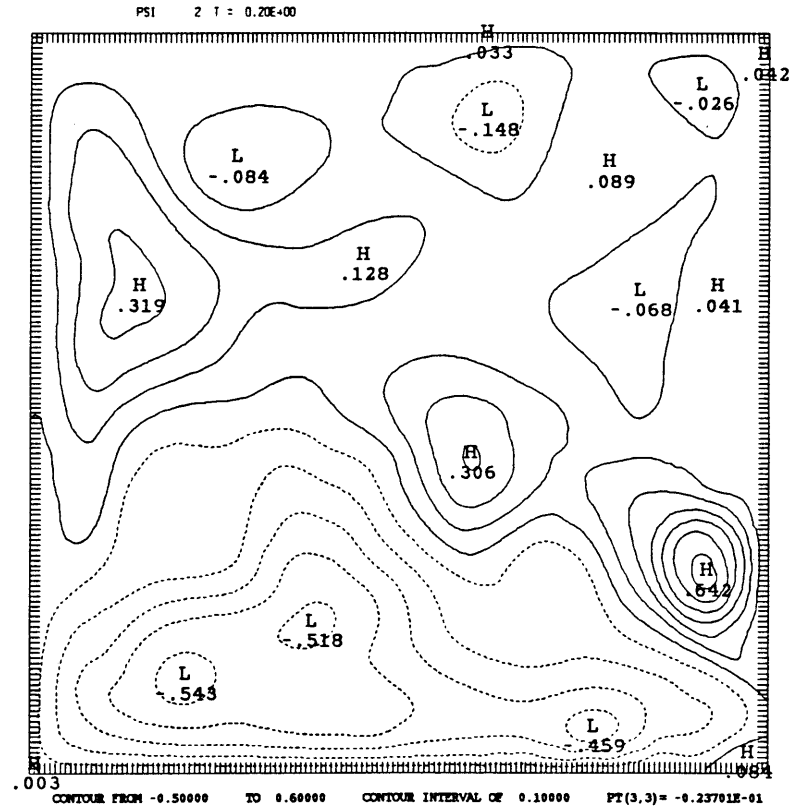


b) ψ_2; initial condition; ML=1, MU=6, P=0.25, r=4, τ_0=491

Figure 34. EXPERIMENT III-4

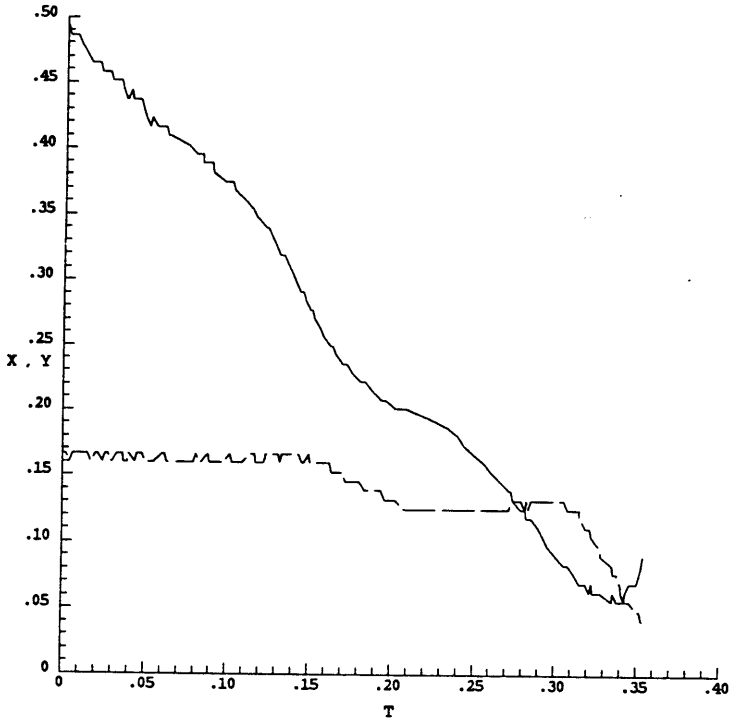


c) ψ_1 after t=0.20 (116 days)

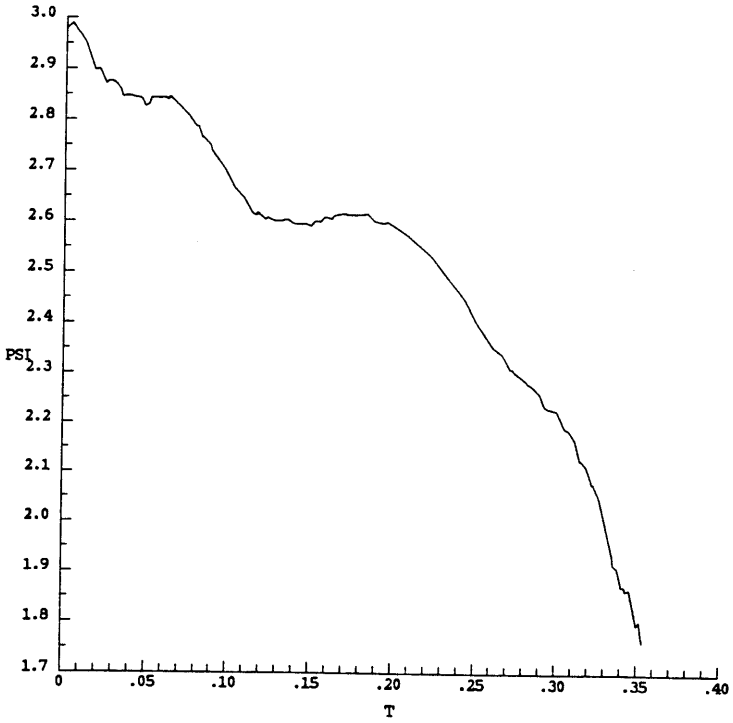


d) ψ_2 after t=0.20 (116 days)

Figure 34. EXPERIMENT III-4



e) Coordinates of the center of the vortex (x-solid curve; y-dashed)



f) Magnitude of the streamfunction in the center of the vortex

Figure 34. EXPERIMENT III-4

4 PURE BAROCLINIC MODE

The examples of steady stratified circulation shown in the second section had a barotropic component. Now we shall show that there exists a pure baroclinic mode of the steady general circulation.

Instead of taking "linear" flow on the β-plane as the initial point for the continuation, we consider the following eigenvalue problem:

$$\nabla^2\psi_1 + C\psi_1 + \delta_1 (\psi_2-\psi_1) = 0 \qquad \text{(III-17a)}$$

$$\nabla^2\psi_2 + C\psi_2 + \delta_2 (\psi_1-\psi_2) = 0 \qquad \text{(III-17b)}$$

where δ_1 , δ_2 and C are constants. Solution of this system exists for a special choice of parameters and we set:

$$\delta_2 = -\, 17\pi^2/5$$

$$\delta_1 = -\, 68\pi^2/5 = 4\delta_2$$

$$C = 0$$

when the solution is:

$$\psi_1(x,y) = \sin(\pi x)\, \sin(4\pi y) \qquad \text{(III-18)}$$

$$\psi_2(x,y) = -\, \frac{1}{4} \sin(\pi x)\, \sin(4\pi y)$$

Although (III-17) is a special case of the equation (III-4), it has no physical significance. The coupling coefficients $\delta_i = F_i$ are negative, implying that the Rossby radius is imaginary and the β-term is zero. This solution is needed for mathematical convenience only. We shall use it as a starting point in the continuation procedure described in the first section of this chapter.

Before we can start with the procedure, there appears a technical difficulty. Since we are using only a second order accurate finite difference scheme on a relatively coarse grid, the solution (III-18) is not sufficiently close to the true solution of the discrete problem which we need. By applying inverse iteration to the system (III-17) the constant C was determined (on the grid 31x31 $C \approx 2.30$). Now we consider the following problem (let $\delta_2 = \delta$):

$$\nabla^2\psi_1 - (2\alpha+1)C\psi_1 + 4\delta(\psi_2-\psi_1) - \gamma\,(\psi_1^3-6(y-y_0)) = 0 \qquad \text{(III-19a)}$$

$$\nabla^2\psi_2 - \alpha C\psi_2 + \delta(\psi_1-\psi_2) - \gamma\,(2\psi_2^3-6(y-y_0) = 0 \qquad \text{(III-19b)}$$

with $y_0 = 1/2$

For $\alpha = -1$, and $\gamma = 0$ (III-19) reduces to (III-17). Parameters, (α,δ,γ), in upper and lower layers need not be the same. We had to assume a special relationship among them in order to keep their number at a minimum for computational reasons. It appears that three is the smallest number of free parameters for which a new flow pattern can be found. At present, there are no systematic procedures for continuation in more than two parameters (Jepson and Spence (1985)). Usually the problem is solved by varying one parameter while keeping the other constant, then change the next parameter and repeat continuation in the first parameter. This procedure is very expensive and, since we know region in the (α,γ,δ) parameter space which is physically significant (note that $\delta = F_2$; $4\delta = F_1$ and $6\gamma = \beta$), we shall adopt another approach.

Basically, we shall reduce the continuation procedure in three parameters into three consecutive continuations in one parameter with the path

directed towards the physically relevant region of the parameter space ($\gamma >> 1$, $\delta >> 1$). It is clear that a solution exists only within certain surfaces in the (α,γ,δ) space. When the boundary of the domain of the existence of solutions is reached (it is a singular point in one of the parameters), continuation may proceed if the singularity is the turning point, or else it is switched to another parameter, always keeping in mind that the path must end with large positive values of γ and δ. The third parameter ,α, is unphysical and will be changed in such a way as to allow increase of the other two. The surface which separates regions in which the solutions exist from those where it does not will remain unknown. Determination of its shape would be computationally very expensive and in the present problem is not relevant, since we could choose some other functionals (e.g. with ψ^5) which are equally good for (III-4) but for which details of the surface may be very different.

We must start continuation (Figure 35) in γ, because it measures the size of the nonlinear terms, while α and δ are kept constant. At $\gamma = 80.3$ there was a turning point after which γ decreased to 13.4 when continuation was switched to α (with the first point being the last point of the previous continuation path). After twelve steps the prescribed maximum value of α ($\approx$ 400) was reached and continuation in δ was performed until another turning point was reached. This completed the first cycle of continuation paths. Since the desired value of γ was not reached the cycle was repeated.

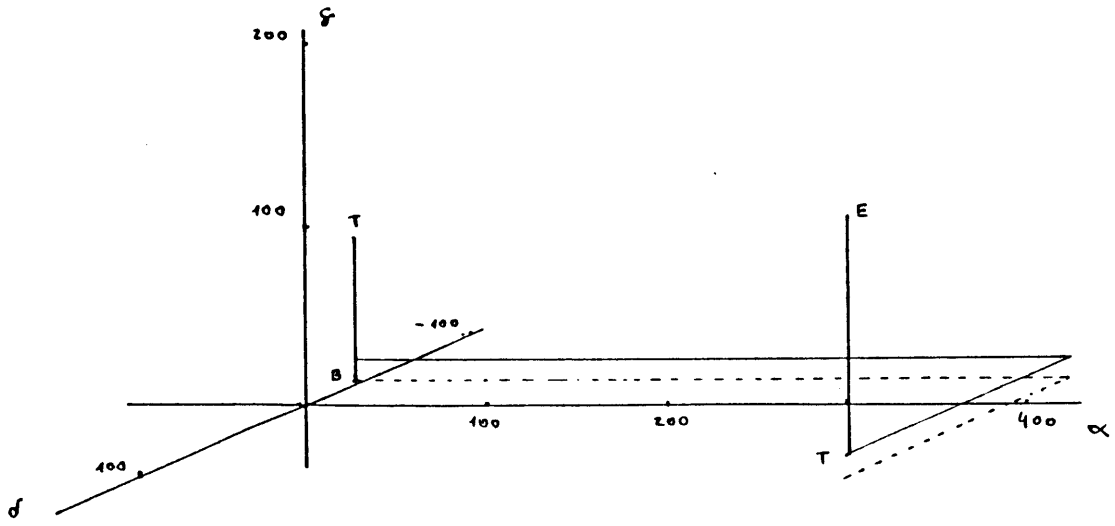


Figure 35. The continuation curve for a pure baroclinic mode in the (α,γ,δ) space. Point B is the beginning of the path, T are the turning points and E is the end point. Dashed curve is the projection of the path onto the (α,δ) plane.

The final point was $(\alpha,\gamma,\delta) = (402 , 136 , 102)$ which corresponds to the oceanic basin with scale length L = 1000 km, scale velocity $U_0 = 1.22$ cm/s (gradient of the Coriolis parameter $\beta = 815$); depths of upper and lower layers are 1000 and 4000 m respectively and $\Delta\rho/\rho_0 = 2.5 \cdot 10^{-3}$. F_1 and F_2 are 408 and 102 respectively, which correspond to the Rossby radii $R_1 = 50$km and $R_2 = 100$km. The Rossby number is $1.22 \cdot 10^{-4}$.

Although α is not a physical parameter, it cannot be chosen arbitrarily. When it is sufficiently small no solutions with large γ and δ were found. Whether the physically relevant values of γ and δ will be attained or not depends on the path taken. If continuation in γ is followed by continuation in δ instead of α, a limit point was reached at $\delta = 0$ beyond which no solutions could be found even as α is increased.

Figures 36ab show the streamfunction. Gyres in the upper and lower layers have opposite vorticity. They are separated by a narrow jet (eastward in the upper layer and westward in the lower). Northern and southern boundary currents in the upper layer flow to the west.

In the upper layer magnitude of the streamfunction decreases away from the jet, so that the circulation resembles two connected Fofonoff gyres (as was found recently by Marshall et al. (1985)). However, the similarity is only superficial, since the "linear" solution is not analytic (there is discontinuity at the latitude y_0 - center of the jet), while the nonlinear solution has continuous derivatives. From the convergence of the fourth

order Richardson extrapolation, it can be inferred that at least the first six derivatives of the streamfunction are continuous.

In the lower layer circulation is closer to a typical two gyre barotropic pattern, which can be expected since it is much thicker than the upper layer.

Figure 36g shows relative displacement of the interface. Its slope in the interior is small and the depression (elevation) from the mean height is largest near the center of the gyre (approximately 230 m). Interior flow is westward in both layers.

Rough balance of the terms in the vorticity equation and maximum east-west velocities are given in the following table (only values for the northern gyre are given):

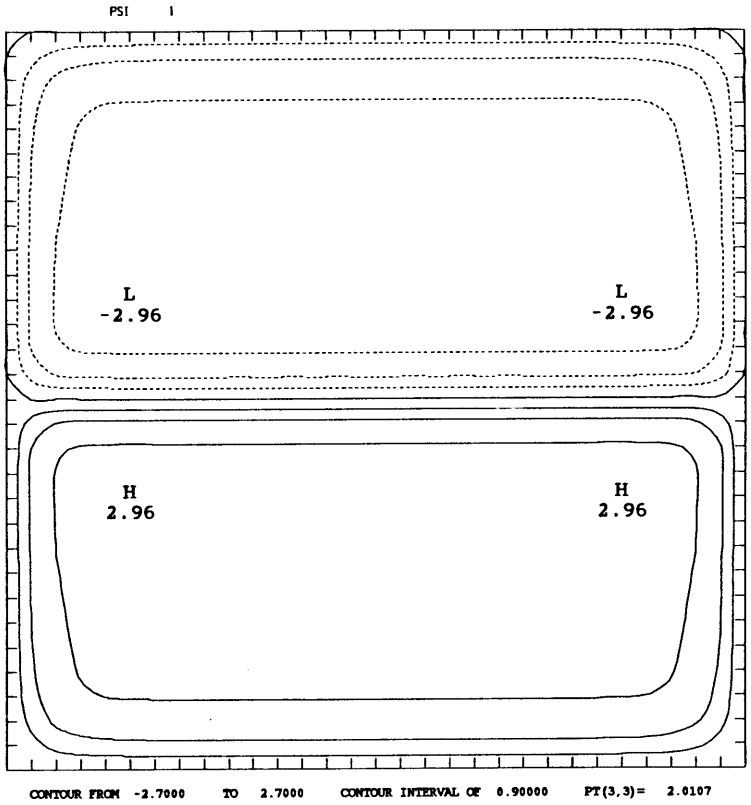
	boundary current	interior	northern part of the jet
ς_1^r	900	0	1400
ς^p	350	200	50
S_1	1150	1900	1150
q_1	2400	2100	2600
ς_2^r	-700	0	-300
ς^p	350	200	50
S_2	-300	-500	-300
q_2	-650	-300	-550
			center of the jet
U_1	-77	-0.7	+88
U_2	+60	-0.7	-32

ς_i^r is the relative vorticity in the i-th layer, ς^p is the planetary vorticity, S_i

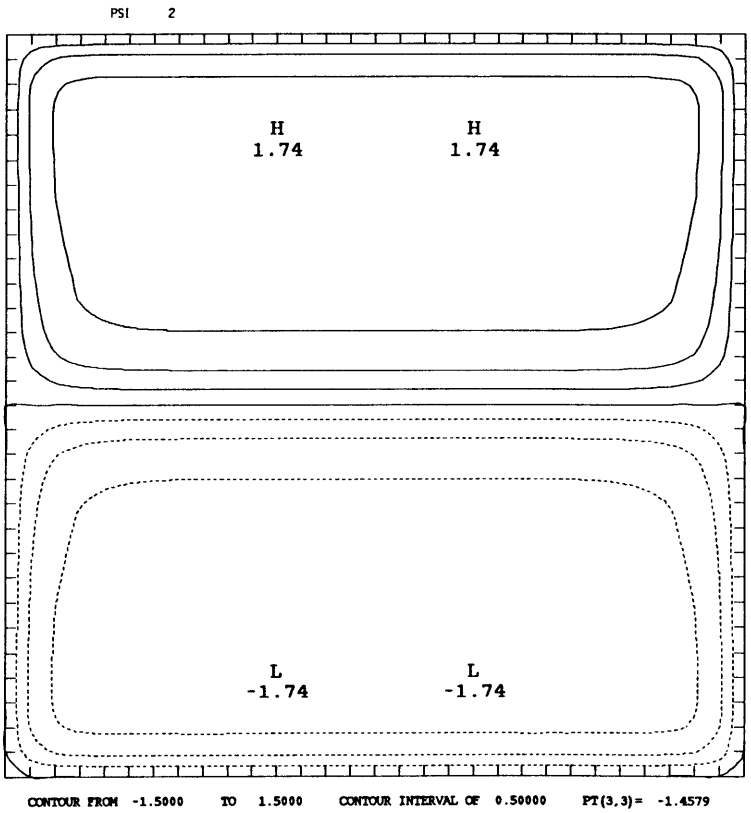
is the stretching term and q_i is the potential vorticity. Velocities U_i are in cm/s.

Note that the potential vorticity is nearly homogeneous in the interiors of the upper layer gyres (Fig. 36e).

Such a circulation pattern can be compared e.g. to the North Atlantic subtropical and subpolar gyres in the upper layer. The jet in the lower layer corresponds to the deep countercurrent observed along the coast of North America. Like observed free jets, this one is not stable (it can be shown that this solution does not satisfy generalized Arnol'd-Blumen condition).

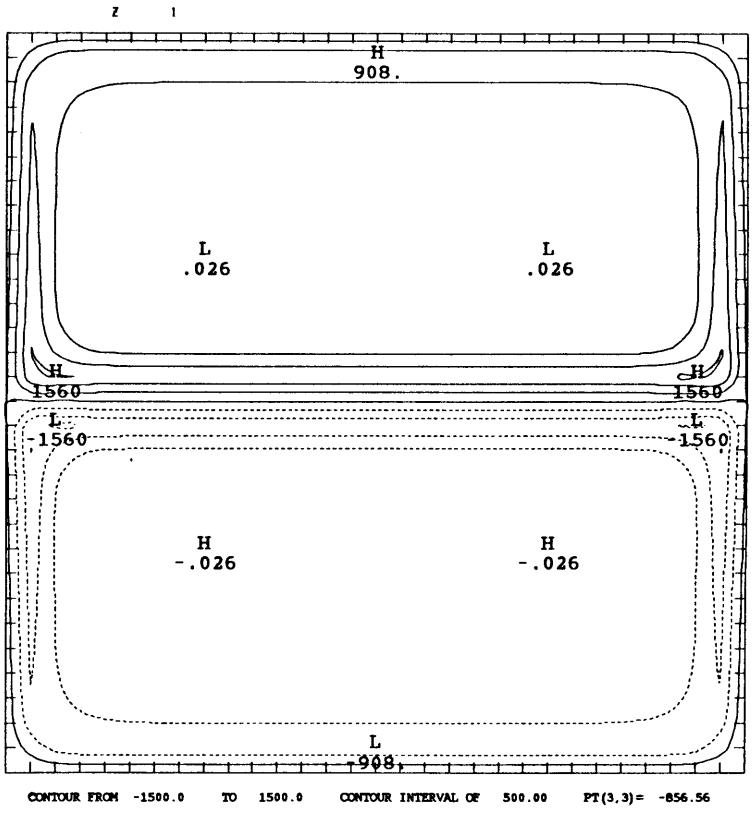


a) ψ_1

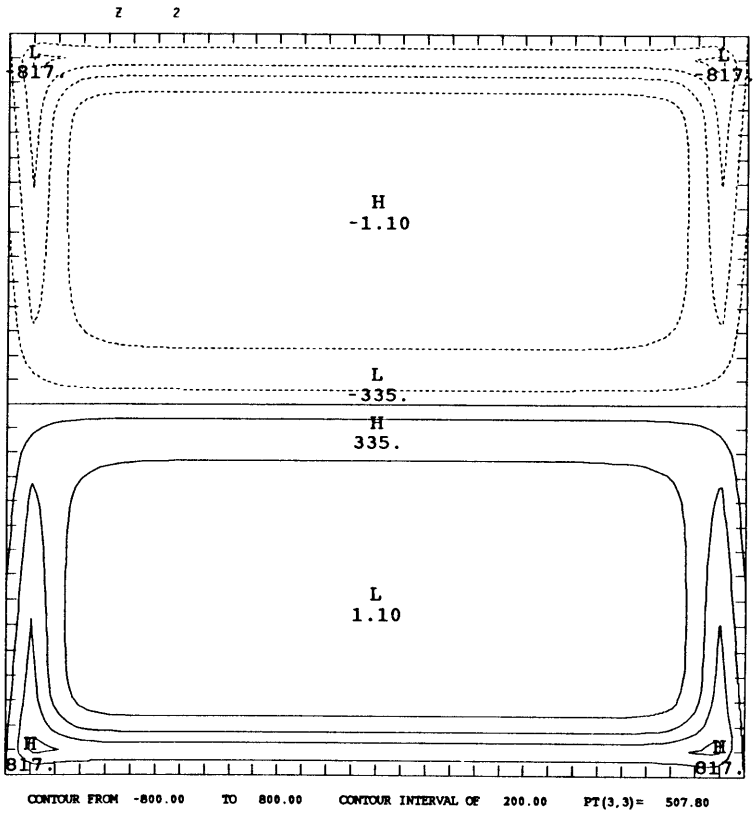


b) ψ_2

Figure 36. Pure baroclinic mode

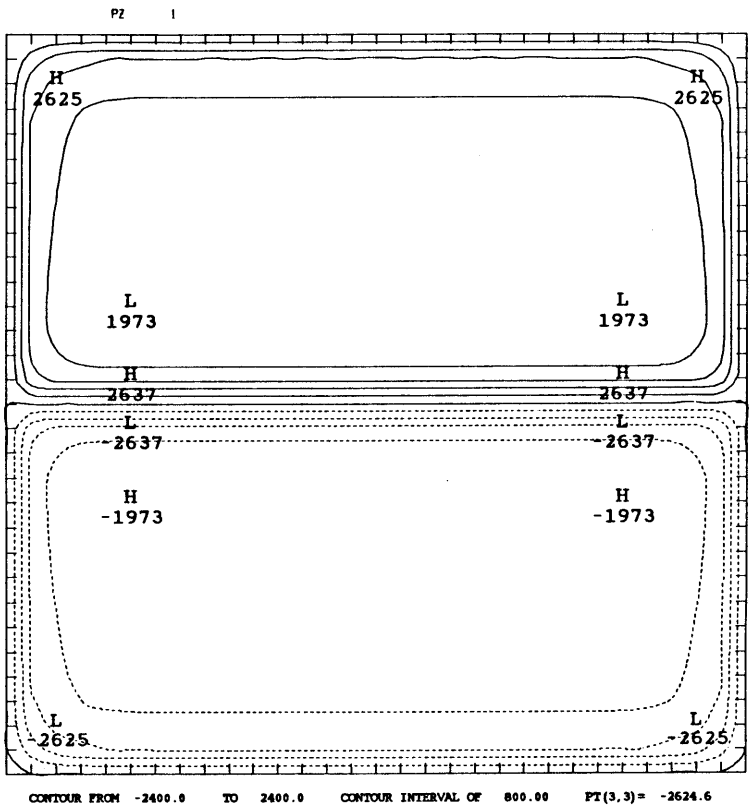


c) ς_1

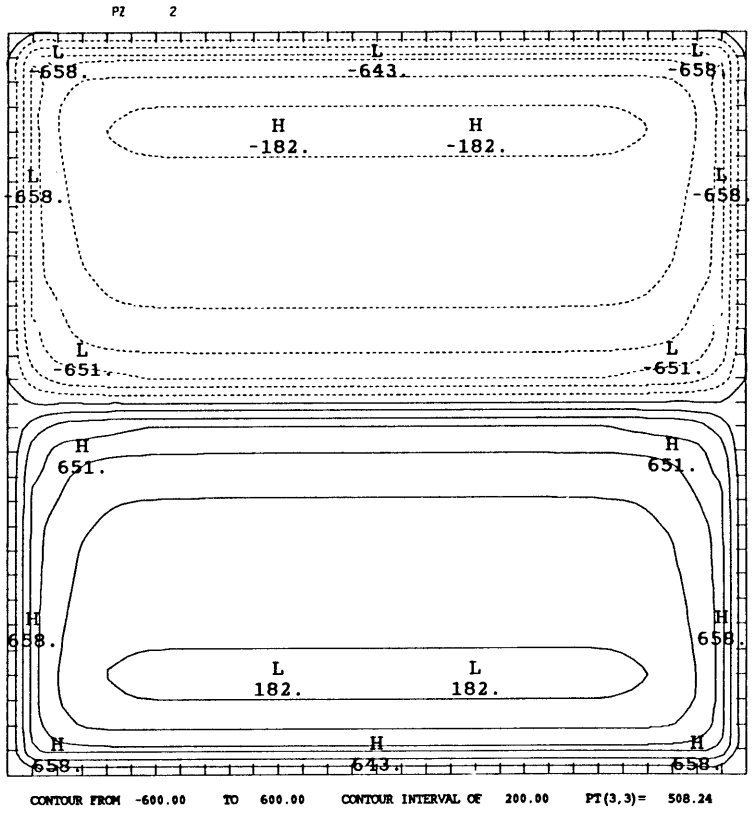


d) ς_2

Figure 36. Pure baroclinic mode

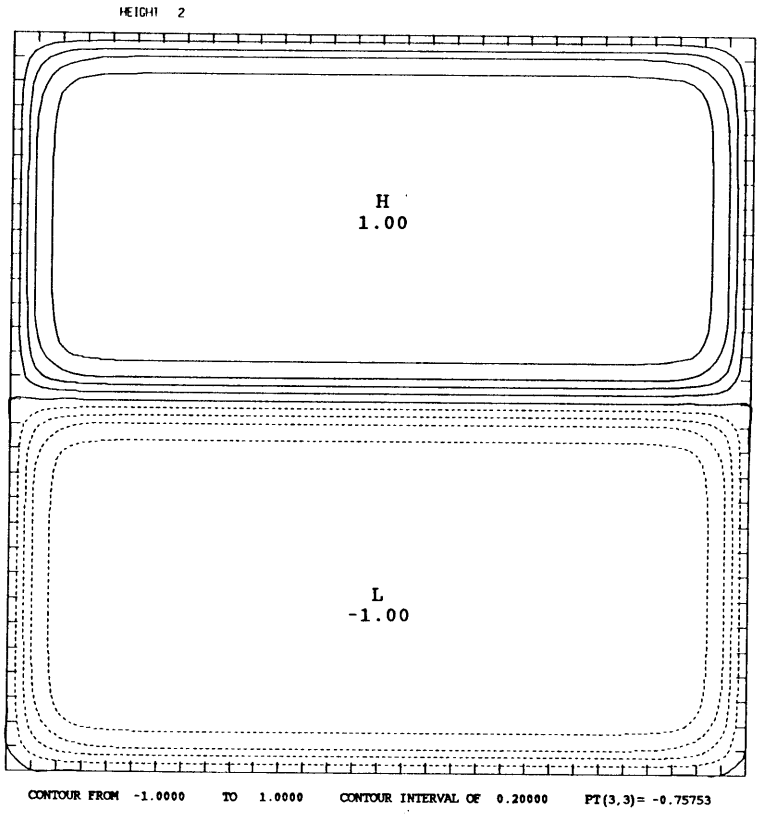


e) q_1



f) q_2

Figure 36. Pure baroclinic mode



g) The normalized displacement of the interface.
h=1 corresponds to the dimensional displacement of 230m.

Figure 36. Pure baroclinic mode

IV CONCLUSIONS

The results of the thesis can be summarized as follows:

1. The only steady solutions that we could find, which are both stable and have slow interior flow, are qualitatively of Fofonoff type. They have fast eastward boundary current at the northern and/or southern edge of the basin and a slow westward interior flow. Showing that this holds for a number of functional relationships between potential vorticity and the streamfunction, does not prove that it is true for *any* relationship, but it certainly indicates that its plausibility.

2. In the framework of quasigeostrophic dynamics, both bottom and lateral friction can act as a mechanism for conversion of kinetic energy of rotation into the energy of translation. Thus *friction can act as accelerating force* on vortices. Since in *all* of our experiments with barotropic flows, bottom friction caused westward motion of the vorticity extrema (at least for short time), it is possible that this would happen to *any* homogeneous rotating flow.[1]

---

[1] In the Part II we found that, when the bottom friction is turned on the vorticity extremum shifts to the west, with small southward shift if the extremum is negative, or northward if it is positive. More formally we make the following conjecture:

> Let ψ^0 be the solution of steady state inviscid barotropic vorticity equation ($\psi^0 = 0$) in finite or infinite domain D
>
> $$J (\psi^0 , \zeta^0 + \beta y) = 0 \qquad \text{with} \quad \zeta^0 = \nabla^2 \psi^0$$
>
> and boundary condition $\psi^0 = 0$ for finite D, or $\lim_{r \to \infty} \psi_0 = 0$ for D infinite.

3. Wind forcing not only provides energy for general circulation in which friction causes westward intensification, but may also play a direct role in intensification. Its influence in the establishing boundary current, though, is probably much smaller than that of friction. As with the friction, it affects not only the magnitude (intensity) of the vortices, but also the direction of their motion.

The dynamic interpretation of the westward intensification (Pedlosky (1965)) was a step forward from pure static models, but

---

If ψ^0 is the initial condition for barotropic vorticity equation without forcing, but with bottom friction:

$$\frac{\partial \varsigma}{\partial t} + J(\psi, \varsigma + \beta y) = -r(t)\,\varsigma$$

where $r(t) > 0$, and which has global vorticity extremum $|\varsigma|_{max}$. Then there exists $T > 0$ such that for any $t_1, t_2 \in [0,T]$ and $t_2 > t_1$, the following inequalities hold:

1. $|\varsigma(x_2,y_2,t_2)|_{max} < |\varsigma(x_1,y_1,t_1)|_{max}$
2. $x_2(t_2) \leq x_1(t_1)$
3. $y_2(t_2) \leq y_1(t_1)$ if $\varsigma^0_{max} < 0$
   $y_2(t_2) \geq y_1(t_1)$ if $\varsigma^0_{max} > 0$

The following comments apply:
- The coefficient of bottom friction is normally constant, but in order to turn viscosity on smoothly, there may be time dependent, at least initially.
- This conjecture may be too restrictive. E.g. although Fofonoff's inertial gyre shows westward intensification when friction is included, the conjecture does not apply since it does not have a vorticity extremum at a point (the extremum is $-\beta(1 - y_0)$ *along* the northern boundary, and $+\beta y_0$ *along* the southern boundary).
- If lateral friction is considered, the same inequalities will hold, provided that there are no discontinuities in the initial condition. For an inertial solution in a closed basin which has nonzero vorticity and parallel velocity on the boundary, application of no slip ($u_| = 0$) or free slip ($\varsigma = 0$) conditions leads to such a discontinuity. As shown in Part II, this will produce waves in the basin which will affect the position of the vorticity extremum.
- The time T may (and usually will be) very short, in particular for local vorticity extremum which will in evolving flow be influenced by other extrema and thus may quickly change direction of motion. However, the strong vortex will move to the west even in presence of perturbations (see page 81).

it falls short by being restricted to the small amplitude motions. In that interpretation friction plays only a passive role as a dissipative mechanism which traps Rossby waves in the western boundary layer. We have shown that the friction may play a direct role in intensification by forcing the energetic flows from the interior of the oceanic basin (e.g. mesoscale eddies) towards the western boundary. Our examples show that the wind forcing may have a similar effect, but we must keep in mind that the direction of the forcing depends on the wind profile. In realistic situation, the wind stress is highly variable on the scale of Gulf Stream Rings and smaller, and its magnitude is much smaller than in our experiments, so that its direct influence on the motion of eddies will be small.

The vortices (Fig 4) are among very few examples of the solutions of the barotropic vorticity equation with nonzero net angular momentum, which are similar to the mesoscale eddies. Compared with the previous models, they have an advantage for they exist for several functional relationships between the potential vorticity and the streamfunction, and the parameters do not have to satisfy any dispersion relation. Unlike the Gulf Stream Rings, they have the same sign of the vorticity as the large scale gyre in which they are embedded. But, we note that other steady models of the mesoscale eddies, do not take into account the general circulation at all.

It is likely that there are no similar solutions with the "correct" sign of the vorticity in *homogeneous* flow. However they

may exist in stratified flow and the investigation of solutions of the steady two-layer equations should be continued. Another topic for further research may be study of a local analytical solution describing the vortex. For barotropic flow with $|\gamma| \ll 1$ (on the upper branch), the local approximation is possible. In this case, the rest of the flow is essentially linear so that the analytical solution is known, and the two could be matched along the edge of the vortex.

Perturbation experiments have shown that such a large scale flow is unstable under the finite amplitude perturbations, both in homogeneous and in stratified fluid. The primary manifestation of the instability is the drift of the vortex. If the perturbations have sufficiently small amplitude and a high frequency, the vortex not only survives but its amplitude may increase. A large amplitude perturbation or the collision with the boundary cause its rapid dispersion. The experiments with two layer vortices show that this instability is barotropic.

Our solutions were obtained by considering the steady state problem and cannot show how they come about. One of our experiments showed that the wind stress can generate small, though unsteady, vortices near the boundary.

We have shown two generalizations of the Fofonoff's pattern to the two layer model.

- The pure baroclinic mode containing a jet unsupported by the boundary is unstable. The free jet in the ocean (Gulf

Stream or Kuroshio after separation from the coast) is unstable as well, but it may be regarded as steady in statistical sense. The inertial model should be compared with such *statistically steady* states of the general circulation.

- The stable, single gyre, mixed mode is more important. Unlike the model of Marshall et al. (1985) which has constant potential vorticity on upper layer, q in our solution has wide shoulder in the middle of the basin and rapidly varies near the northern and southern edge, showing much better agreement with the observations.

We hope that this thesis has pointed out some problems in oceanography which were either unnoticed before or thought to be solved, and indicated an approach to their solution.

V APPENDIX

NUMERICAL SOLUTION OF THE QUASIGEOSTROPHIC VORTICITY EQUATION IN TWO LAYER MODEL

System of equations (III-2) can be rewritten as:

$$\begin{aligned} &\frac{\partial}{\partial t}\left(\left(\nabla^2 - F_1 - F_2\right)\left(\psi_1 - \psi_2\right)\right) = \\ &= -J\left(\psi_1, \nabla^2\psi_1 + F_1\psi_2 + \beta y\right) + \\ &+ J\left(\psi_2, \nabla^2\psi_2 + F_2\psi_1 + \beta y\right) + \\ &+ \left(\vec{\nabla}\times\vec{\tau}\right)_k + \frac{1}{Re}\nabla^4\left(\psi_1 - \psi_2\right) + \frac{r}{2}\nabla^2\psi_2 \end{aligned} \tag{V-1a}$$

$$\begin{aligned} &\frac{\partial}{\partial t}\nabla^2\left(F_2\psi_1 + F_1\psi_2\right) = \\ &= -F_2 J\left(\psi_1, \nabla^2\psi_1 + F_1\psi_2 + \beta y\right) - \\ &- F_1 J\left(\psi_2, \nabla^2\psi_2 + F_2\psi_1 + \beta y\right) + \\ &+ F_2\left(\vec{\nabla}\times\vec{\tau}\right)_k + \frac{1}{Re}\nabla^4\left(F_2\psi_1 + F_1\psi_2\right) - \frac{F_1 r}{2}\nabla^2\psi_2 \end{aligned} \tag{V-1b}$$

The method for solving the above system was described by Holland (1978).

Let:

$$\Phi = \frac{\partial}{\partial t}\left(\psi_1 - \psi_2\right)$$

then Φ satisfies equation:

$$\begin{aligned} &\left(\nabla^2 - F_1 - F_2\right)\Phi = \\ &= -J\left(\psi_1, \nabla^2\psi_1 + F_1\psi_2 + \beta y\right) + \\ &+ J\left(\psi_2, \nabla^2\psi_2 + F_2\psi_1 + \beta y\right) + \end{aligned} \tag{V-2}$$

$$+ (\vec{\nabla}\times\vec{\tau})_k + \frac{1}{Re}\nabla^4(\psi_1 - \psi_2) + \frac{r}{2}\nabla^2\psi_2$$

Since the height of the interface is proportional to $\psi_1 - \psi_2$, we have, because of conservation of the volume, the following condition:

$$\int_D \int \Phi \, dx \, dy = 0 \qquad \text{(V-3)}$$

$\psi_1 - \psi_2$ must be constant along the boundary (no normal flow), but dependent on time in order to satisfy (V-3).

We write solution of (V-2) as:

$$\Phi = \Phi_t + c(t)\,\Phi_c$$

where Φ_t is time dependent function, satisfying equation (V-2) with homogeneous boundary conditions, and Φ_c is constant in time and satisfies equation:

$$(\nabla^2 - F_1 - F_2)\,\Phi_c = 0$$

$$\text{with} \quad \Phi = 1 \qquad \text{on} \quad \partial D \qquad\qquad i=1,2$$

Then, from (V-3) there follows that

$$c(t) = -\frac{\int \Phi_t \, dx \, dy}{\int \Phi_c \, dx \, dy}$$

Let $\Psi = \frac{\partial}{\partial t}(F_2\,\psi_1 + F_1\,\psi_2)$, then it satisfies the equation:

$$\begin{aligned}\nabla^2\Psi = &- F_2\,J(\psi_1, \nabla^2\psi_1 + F_1\,\psi_2 + \beta y) - \\ &- F_1\,J(\psi_2, \nabla^2\psi_2 + F_2\,\psi_1 + \beta y) + F_2(\vec{\nabla}\times\vec{\tau})_k + \\ &+ \frac{1}{Re}\nabla^4(F_2\,\psi_1 + F_1\,\psi_2) - \frac{F_1\,r}{2}\nabla^2\psi_2\end{aligned} \qquad \text{(V-4)}$$

which is solved with homogeneous boundary conditions.

Finally, timestepping scheme reads:

$$(\psi_1 - \psi_2)^{k+1} = (\psi_1 - \psi_2)^{k-1} + 2 \Delta t \, \Phi^k$$

$$(F_2 \psi_1 + F_1 \psi_2)^{k+1} = (F_2 \psi_1 + F_1 \psi_2)^{k-1} + 2 \Delta t \, \Psi^k$$

After each 200 steps it was restarted using Euler's scheme to avoid splitting instability. The scheme is leapfrog for advection terms (error is $O((\Delta t)^2,(\Delta x)^2))$, and explicit Euler in friction terms. These terms are lagged by one time step to avoid linear instability. Error is $O((\Delta t,(\Delta x)^2))$, but since the time step must be very small because β term is large, this does not affect overall accuracy of the scheme.

Lateral friction terms in (V-1a) and (V-1b) require additional boundary condition which may be either free slip:

$$\frac{\partial}{\partial n} \zeta_i = 0 \quad \text{on } \partial D \qquad\qquad i = 1,2$$

or no slip:

$$u^i = 0 \quad \text{on } \partial D \qquad\qquad i = 1,2$$

We used free slip condition since, for experiments with solutions of the *inviscid* vorticity equation, it is physically more appropriate.

For space discretization, we used second order centered finite differences. The Jacobians were evaluated using Arakawa's scheme. Helmholtz and Poisson equations (V-2) and (V-4), were solved by the modification of the fast Poisson solver, originally developed by Dr. Julianna Chow.

REFERENCES:

Arnol′ d, V.I. , 1965: Conditions for nonlinear stability of stationary plane curvilinear flows of an ideal fluid. Sov. Math. Dokl. 6, 773-776.

Benzi, R. , S. Pierini, A. Vulpiani and E. Salusti, 1982: On nonlinear hydrodynamic stability of planetary vortices. Geophys. Astrophys. Fluid Dyn. 20, 293-306.

Berestov, A. ,1979: Solitary Rossby waves. Izvestya, Atmos. and Oceanic Phys. 15, 443-447.

Blumen, W. , 1968: On the stability of quasi-geostrophic flow. J. Atmos. Sci. 25, 929-931.

Charney, J.G. and J. DeVore, 1979: Multiple flow equilibria in the atmosphere and blocking. J. Atmos. Sci. 35, 1205-1216.

Cheney, R. and P. Richardson, 1977: POLYMODE News, 31

Davey, M.K. and P.D. Killworth, 1984: Isolated waves and eddies in a shallow water model. J. Phys. Oceanogr. 14, 1047-1063.

Flierl, G. , 1979: Baroclinic solitary waves with radial symmetry. Dyn.Atmos.and Oceans 3, 15-38.

Flierl, G. , V. Larichev, J. McWilliams and G.Reznik, 1980: The dynamics of barotropic and baroclinic solitary eddies. Dyn.Atmos.and Oceans 5, 1-41.

Flierl, G. , M.E. Stern and J.A. Whitehead, 1983: The physical significance of modons: laboratory experiments and general integral constraints.

Dyn.Atmos.and Oceans 7, 233-263.

Fofonoff, N.P. , 1954: Steady flow in a frictionless homogeneous ocean. J. Mar. Res. 13, 254-262.

Fuglister, F. and V. Worthington, 1951: Some results of a multiple ship survey of the Gulf Stream. Tellus 3, 1-14.

Hall, M.M. , and H. Bryden, 1982: Direct estimates and mechanisms of ocean-heat transport. Deep-Sea Res., 29A , 339 -360.

Holland, W.R. , 1978: The role of mesoscale eddies in the general circulation of the ocean - numerical experiments using a wind-driven quasi-geostrophic model. J. Phys. Oceanogr., 8, 363-392.

Jepson, A.D. , and A. Spence, 1985: Folds in solutions of two parameter systems and their calculation, Part 1. SIAM J.Num.Anal., 22 , 347 -368.

Keffer, T. , 1985: The ventilation of world's oceans: Maps of the potential vorticity field. J. Phys. Oceanogr. 15, 509-523.

Keller, H.B. , 1977: Numerical solutions of bifurcation and nonlinear eigenvalue problems. In: P.Rabinowitz (ed.), Applications of Bifurcation Theory, Academic Press, New York, pp 359-384.

Lai, D. and P. Richardson, 1977: Distribution and movement of Gulf Stream rings. J. Phys. Oceanogr. 7, 670-683.

Larichev, V. and G. Reznik, 1976: Two-dimensional solitary Rossby waves. Doklady Akad. Nauk SSSR 231, 1077-1079.

Larsen, L.H., 1965: Comments on "Solitary waves in the westerlies". J. Atmos. Sci. 22, 222-224.

Long, R.R., 1964: Solitary waves in the westerlies. J. Atmos. Sci. 21, 197-200.

Lumley, J.L., 1964: Drag reduction by additives. Ann. Rev. Fluid Mech., 1, 367-384.

Malguzzi, P. and P. Malanotte-Rizzoli, 1984: Nonlinear stationary Rossby waves on nonuniform zonal winds and atmospheric blocking. Part 1: The analytical theory. J. Atmos. Sci. 41, 2620-2628.

Marshall, J.C., G. Nurser and R. Greatbatch, 1985: Steady, free circulation in a stratified quasi-geostrophic ocean. To be published.

Maxworthy, T. and L. Redekopp, 1976: A solitary wave theory of the Great Red Spot and other observed features in the Iovian atmosphere. Icarus 29, 261-271.

McWilliams, J. , G. Flierl, V. Larichev and G. Reznik, 1981: Numerical studies of barotropic modons. Dyn.Atmos.and Oceans 5, 219-238.

Merkine, L., K.C. Mo and E. Kalnay, 1985: On Fofonoff's mode. Geophys. Astrophys. Fluid Dynamics, 32, 175-196.

Pierini, S. , 1985: On the stability of equivalent modons. Dyn.Atmos. and Oceans 9, 273-280.

Pedlosky, J. , 1964: The stability of currents in the atmosphere and ocean: Part 1. J. Atmos. Sci. 21, 201-219.

Pedlosky, J. , 1965: A note on the western intensification of the oceanic circulation. J. Mar. Res. 23, 207-209.

Pedlosky, J. , 1979: Geophysical Fluid Dynamics. Springer-Verlag, New York, 624pp.

Pedlosky, J. and H.P. Greenspan, 1967: A simple laboratory model for the oceanic circulation. J. Fluid Mech. 27, 291-304.

Pierrehumbert,R.and P. Malguzzi, 1984: Forced coherent structures and local multiple equilibria in a barotropic atmosphere. J. Atmos. Sci. 41, 246-257.

Rheinboldt W. , 1982: Computation of critical boundaries on equilibrium manifolds. SIAM J.Num.Anal., 19, 653-669.

Robinson A.R. , D.E. Harrison, Y. Mintz and A. Semtner, 1977: Eddies and the general circulation of an idealized oceanic gyre: A wind and thermally driven primitive equation numerical experiment. J. Phys. Oceanogr. 7, 182-207.

Stern M. , 1975: Minimal properties of planetary eddies. J.Mar.Res. 33, 1-13.

Stommel H. , 1960: The Gulf Stream. University of California Press.

Veronis, G. , 1966: Wind driven ocean circulation-Part 2. Numerical solutions of the nonlinear problem. Deep-Sea Res. 13, 31-55.

Warren, B.A. , 1963: Topographic influences on the path of the Gulf Stream. Tellus 15, 167-173.

APPENDIX II

We observed change in time of various quantities: $\varsigma, \psi, \frac{\partial \psi}{\partial x}, \frac{\partial \psi}{\partial y}, \frac{\partial \varsigma}{\partial x}, \frac{\partial \varsigma}{\partial y}$ and their combinations as they occur in the vorticity equation.

Figure A1a shows change of profile of the streamfunction through the center of the vortex. Solid line shows $\psi(0.5,y,0.0)$, dashed lines show $\psi(x_0,y,t_0)$ where x_0 is the abscissa of the center of the vortex at the time t_0 which is taken in the intervals of 0.01. The last dashed line (farthest from the solid line) is taken at the time 0.08 when $x_0 \approx 0.375$. (vortex drifted 250 km to the west). Bottom friction coefficient r=2.

Other figures from the first set are:

A1b $u(x_0,y,t_0)$

A1c $\varsigma(x_0,y,t_0)$

A1d $\frac{\partial \varsigma}{\partial y}(x_0,y,t_0)$

A1e $q(x_0,y,t_0)$

Figures A2,A3 and A4.

Plots of the terms in the vorticity equation. Only area of the vortex is plotted. Center of the plot moves with the center of the vortex. Bottom friction coefficient r=1.

Legend:

PSI	ψ
FRICT	$r\varsigma$
BETA	$\beta\frac{\partial\psi}{\partial x}$
PSIX	$\frac{\partial\psi}{\partial x}$
PSIZ	$\frac{\partial\psi}{\partial y}$
ZETAX	$\frac{\partial\varsigma}{\partial x}$
ZETAZ	$\frac{\partial\varsigma}{\partial y}$
PXZZ	$\frac{\partial\psi}{\partial x}\frac{\partial\varsigma}{\partial y}$
PZZX	$\frac{\partial\psi}{\partial y}\frac{\partial\varsigma}{\partial x}$
JAC	$J(\psi,\varsigma)$
JB	$J(\psi,q)$

S denotes the scaling factor (values plotted must be multiplied by 1/S). At the time t=0.00005, the full Jacobian term ,JB, should be approximately zero. The plot of JB here is dominated by numerical errors.

Time when the plot is made is in the lower left corner.

Figure A2. After the time 0.00005

Figure A3. After t=0.08

Figure A4. After t=0.10

Figures A5, A6 and A7 are similar to the previous set, only they were taken in a shorter period and friction was turned on smoothly as $r(t) = 10^4\ t^2$
Plots of the potential vorticity are included. The center of the vortex is the same point for all three sets of figures.

Symbols are the same as in the previous set of figures except:

ZX	$\frac{\partial \varsigma}{\partial x}$
ZZ	$\frac{\partial \varsigma}{\partial y}$
PXQZ	$\frac{\partial \psi}{\partial x}\frac{\partial q}{\partial y}$
PZQX	$\frac{\partial \psi}{\partial y}\frac{\partial q}{\partial x}$
QX	$\frac{\partial q}{\partial x}$
QZ	$\frac{\partial q}{\partial y}$
JACB	$J(\psi,q)$

Figure A5. After the time 0.00005; bottom friction coefficient r=0

Figure A6. After t=0.01; r=1

Figure A7. After t=0.02; r=4

Clearly, the friction causes larger decrease of the magnitude of the vorticity on the northern side of the vortex. This results in a small southward shift of the vortex. Similarly, the east-west velocity is substantially more reduced on the northern side, which yields net westward transport.

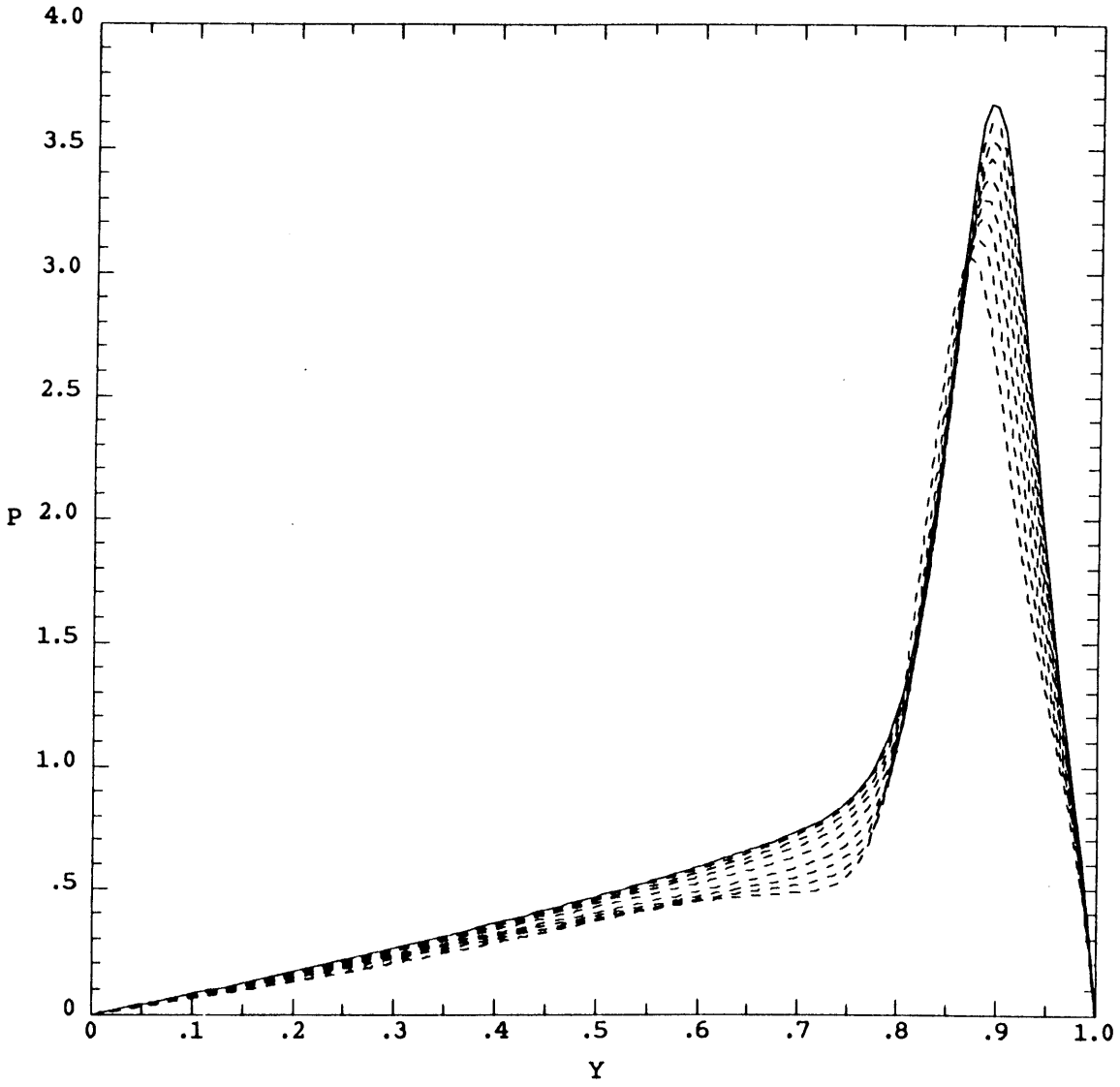


Fig A1a $\Psi(x_0, y, t_0)$

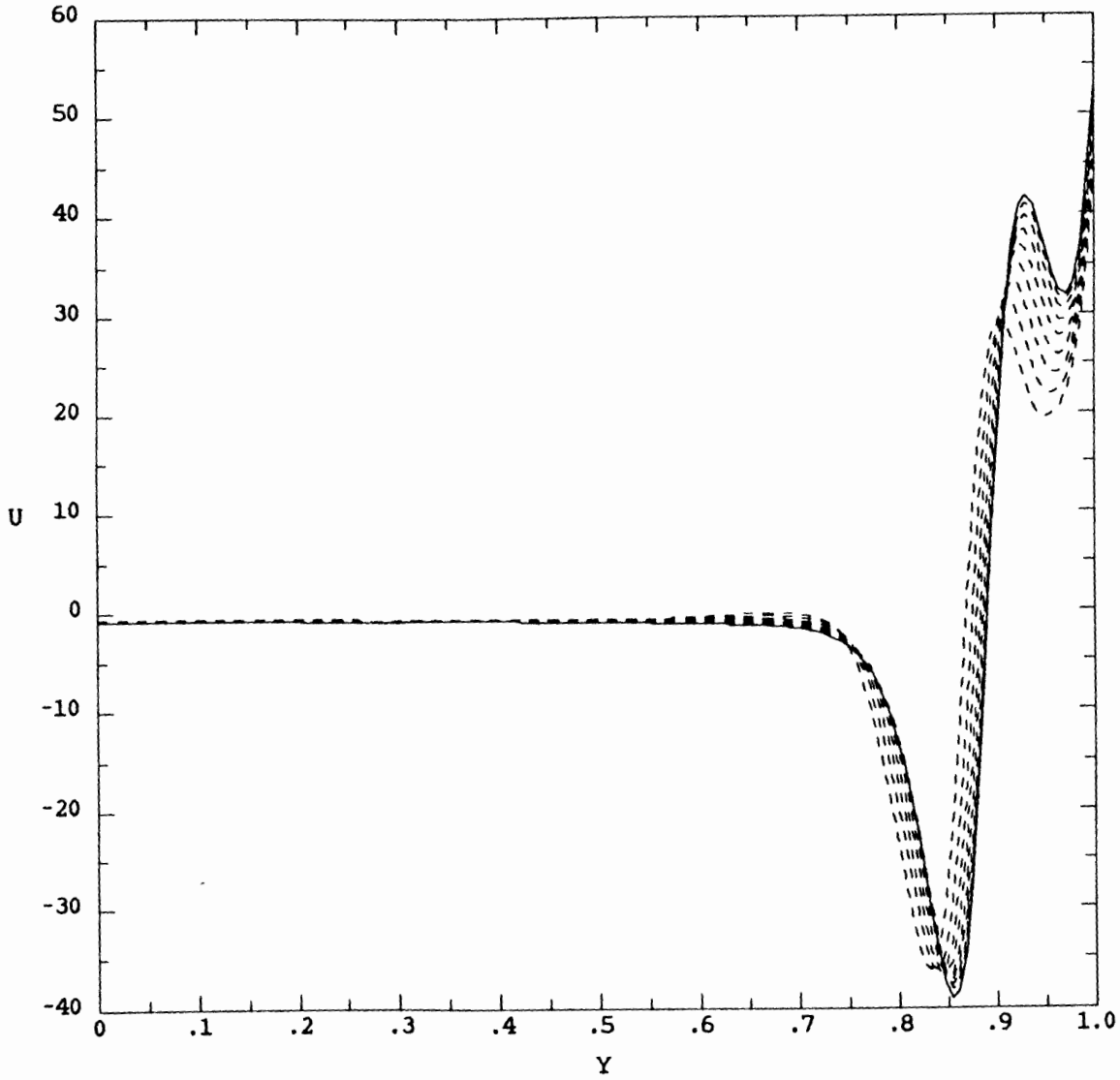


Fig A1.2 $u(x_0, y, t_0)$

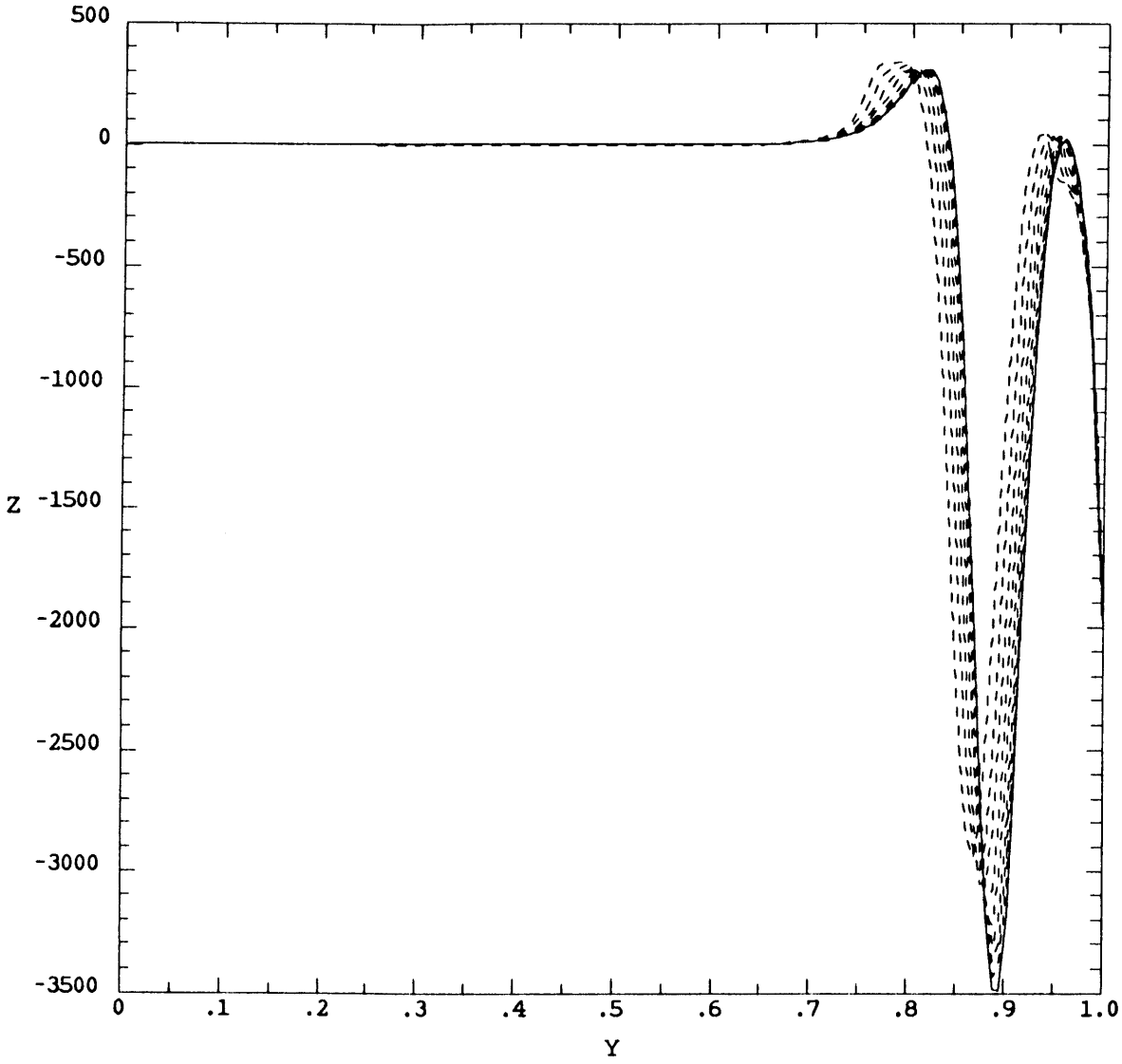


Fig A1c $\zeta(x_0, y_1, t_0)$

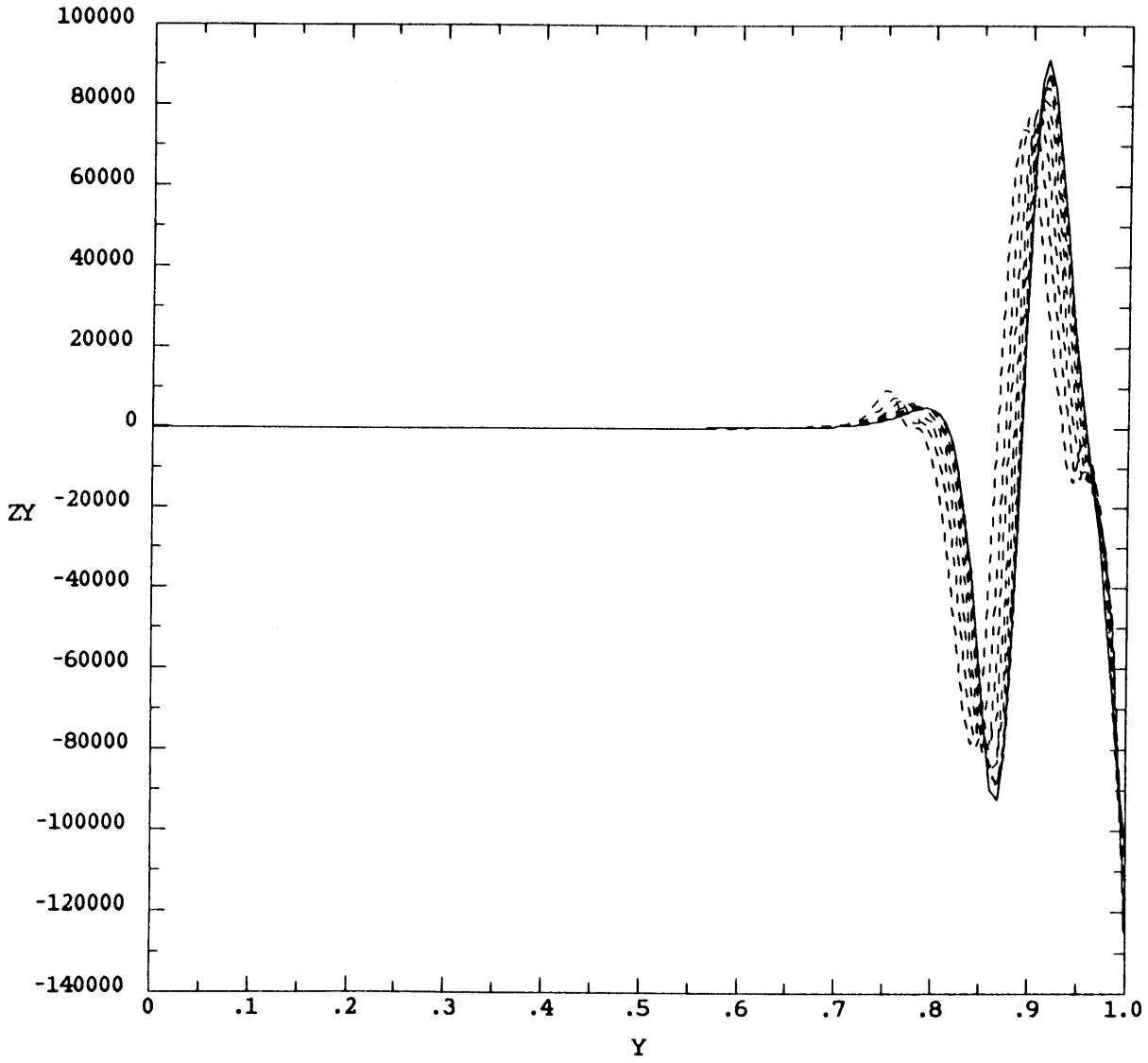


Fig A1d $\frac{\partial \rho}{\partial y}$

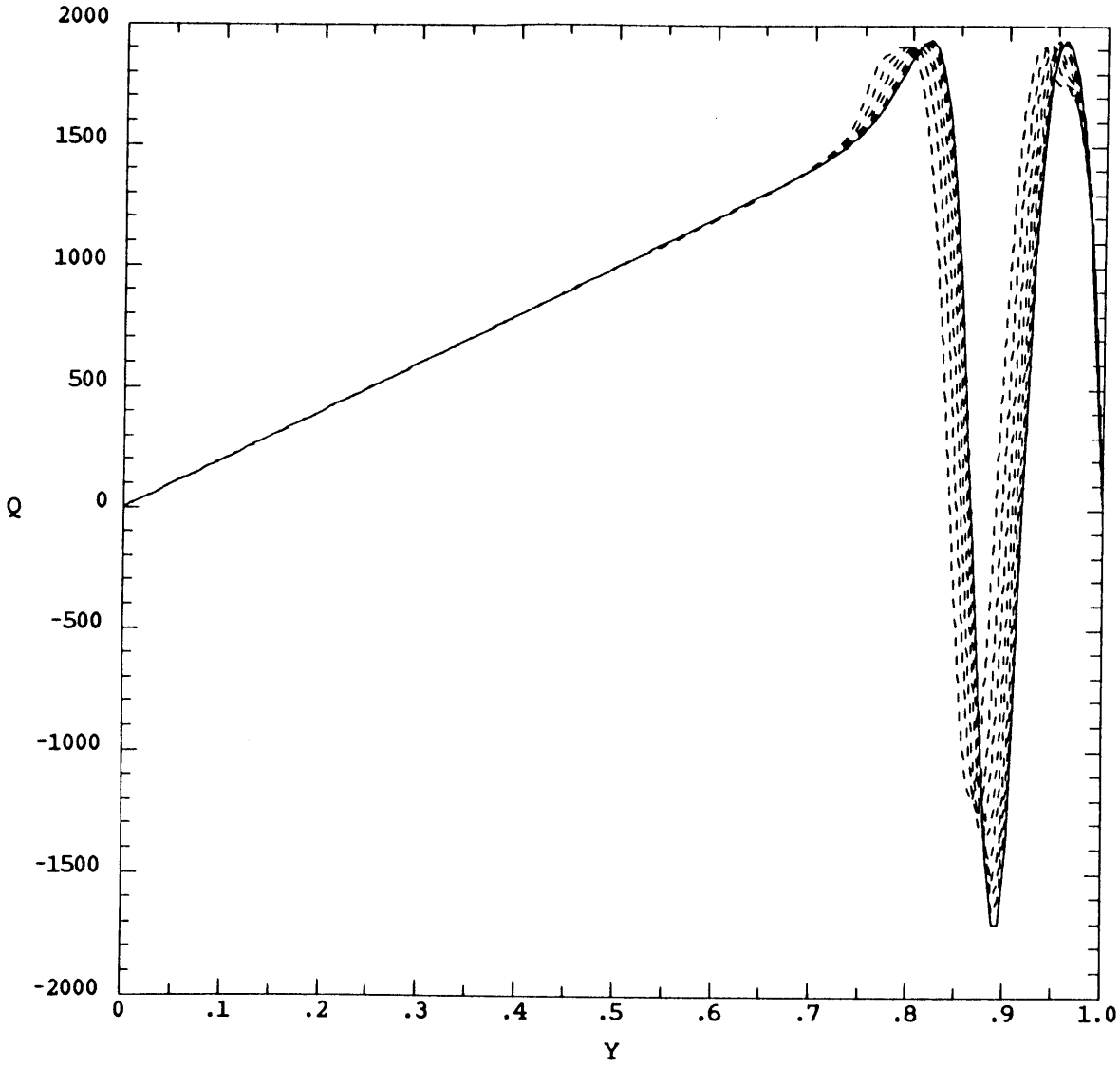
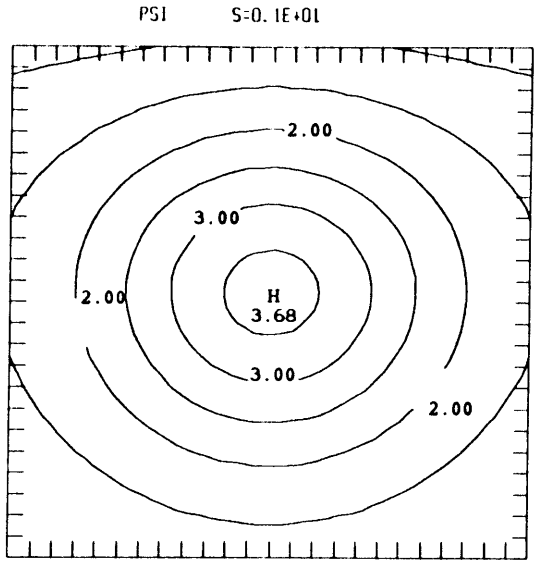
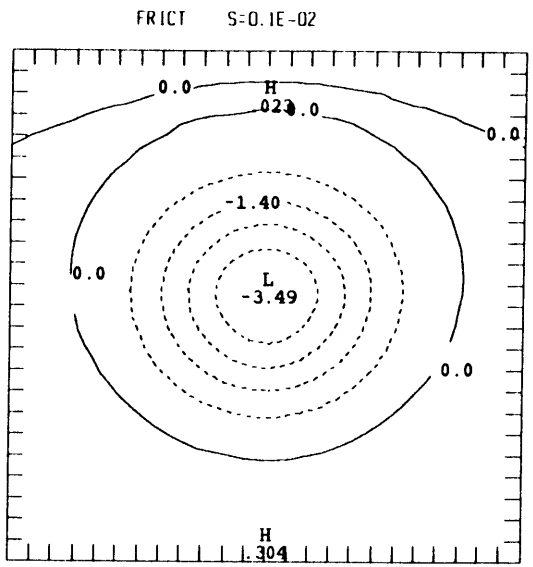


Fig A1e) $q(x_0, y, t_0)$


PSI S=0.1E+01
2.00
3.00
2.00
H
3.68
3.00
2.00


FRICT S=0.1E-02
0.0
H
0.0
0.0
-1.40
0.0
L
-3.49
0.0
H

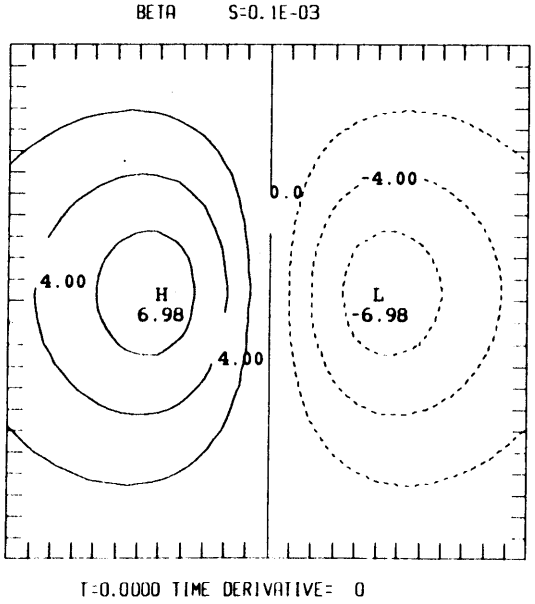

BETA S=0.1E-03
0.0
-4.00
4.00
H
6.98
L
-6.98
4.00
T=0.0000 TIME DERIVATIVE= 0

Fig A2a

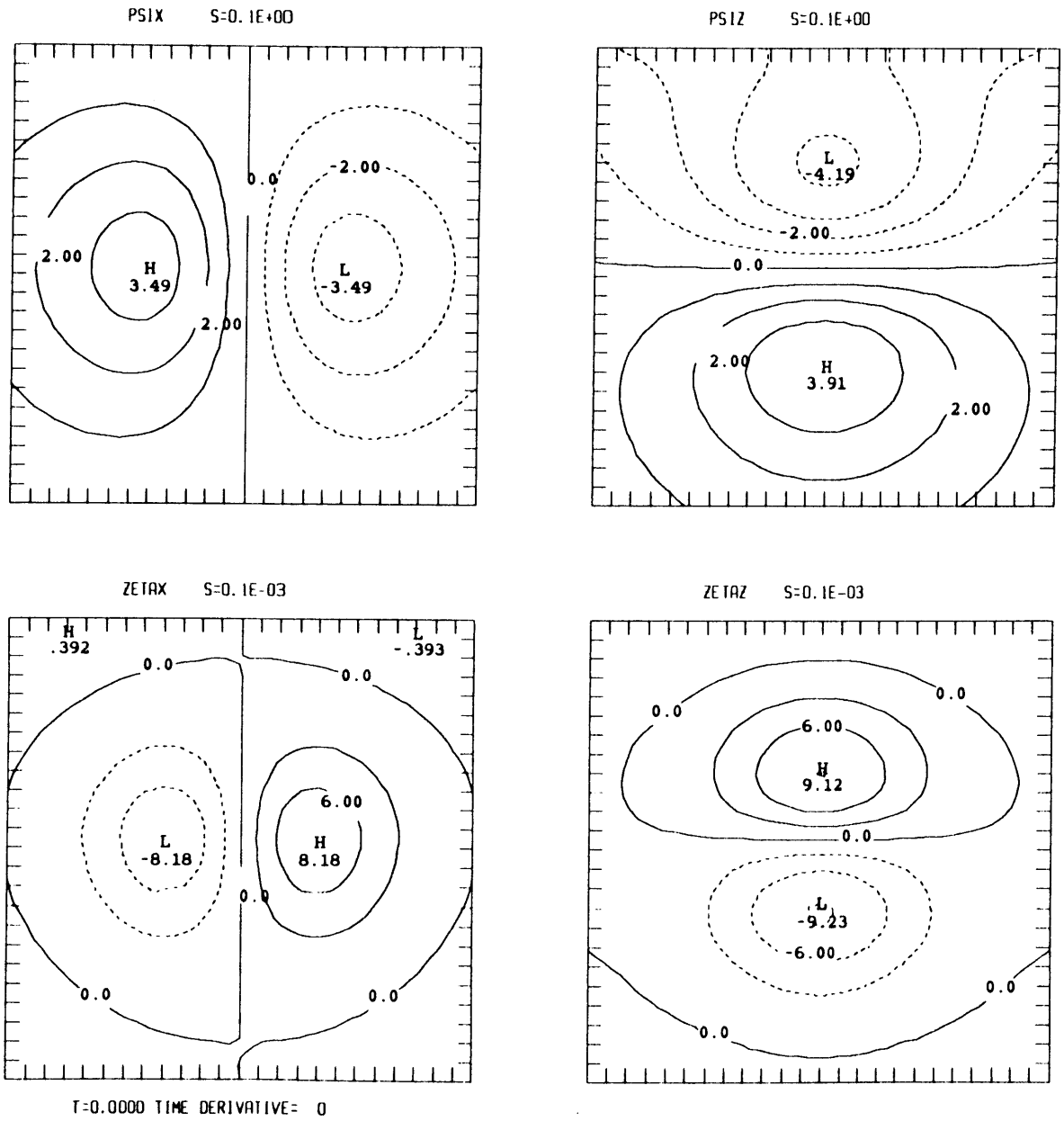

PSIX S=0.1E+00
0.0
-2.00
2.00
H
3.49
L
-3.49
2.00
PSIZ S=0.1E+00
L
-4.19
-2.00
0.0
2.00
H
3.91
2.00
ZETAX S=0.1E-03
H
.392
L
-.393
0.0
0.0
6.00
L
-8.18
H
8.18
0.0
0.0
0.0
ZETAZ S=0.1E-03
0.0
0.0
6.00
H
9.12
0.0
L
-9.23
-6.00
0.0
0.0
T=0.0000 TIME DERIVATIVE= 0

Fig A2c

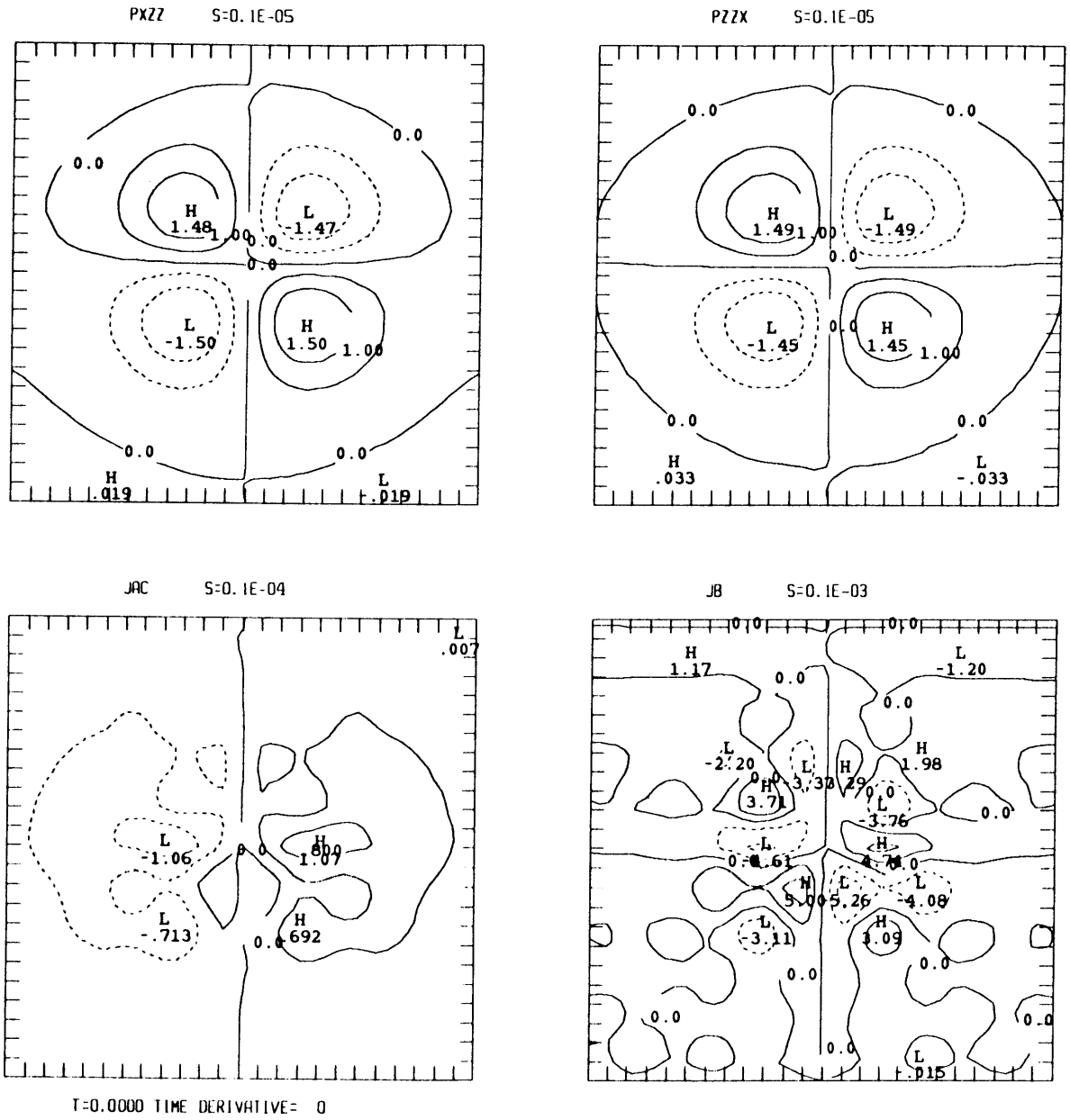

PXZZ S=0.1E-05
PZZX S=0.1E-05
JAC S=0.1E-04
JB S=0.1E-03
T=0.0000 TIME DERIVATIVE= 0

Fig A2c

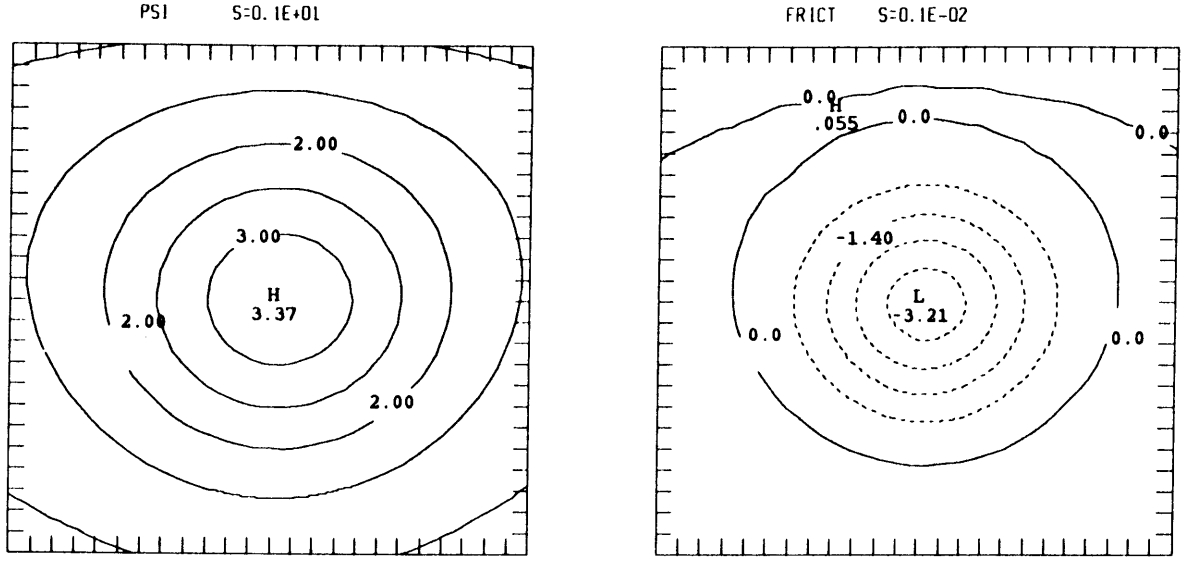

PSI S=0.1E+01
2.00
3.00
H
3.37
2.00
2.00
FRICT S=0.1E-02
0.0
H
.055
0.0
0.0
-1.40
L
-3.21
0.0
0.0
BETA S=0.1E-03
0.0
-4.00
4.00
H
6.42
L
-6.53
4.00
T=0.0802 TIME DERIVATIVE= 0

Fig A3e

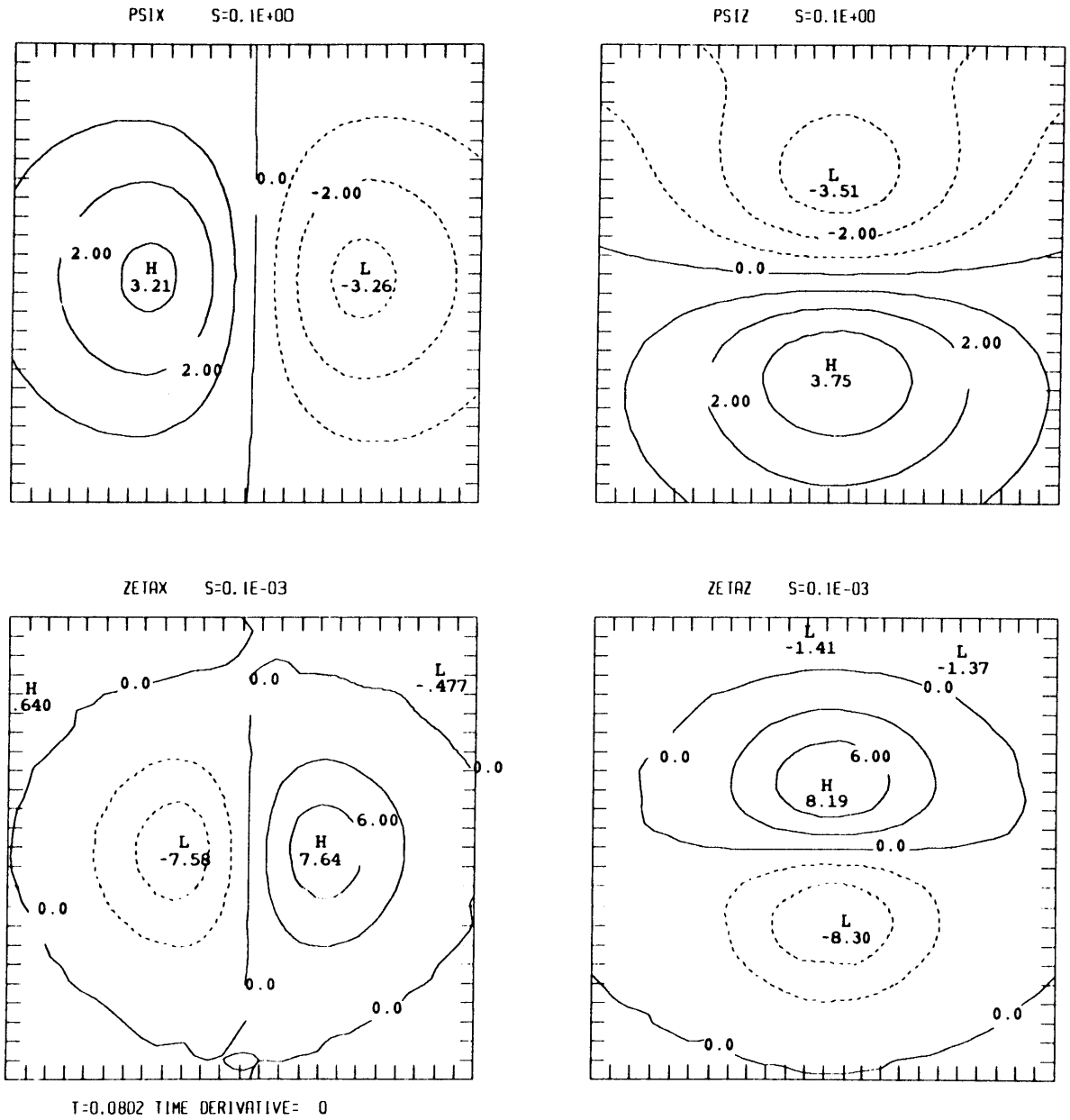

PSIX S=0.1E+00
0.0
-2.00
2.00
H
3.21
L
-3.26
2.00
PSIZ S=0.1E+00
L
-3.51
-2.00
0.0
2.00
H
3.75
2.00
ZETAX S=0.1E-03
H
.640
0.0
0.0
L
-.477
0.0
6.00
L
-7.58
H
7.64
0.0
0.0
0.0
ZETAZ S=0.1E-03
L
-1.41
L
-1.37
0.0
0.0
6.00
H
8.19
0.0
L
-8.30
0.0
0.0
T=0.0802 TIME DERIVATIVE= 0

Fig A 3l

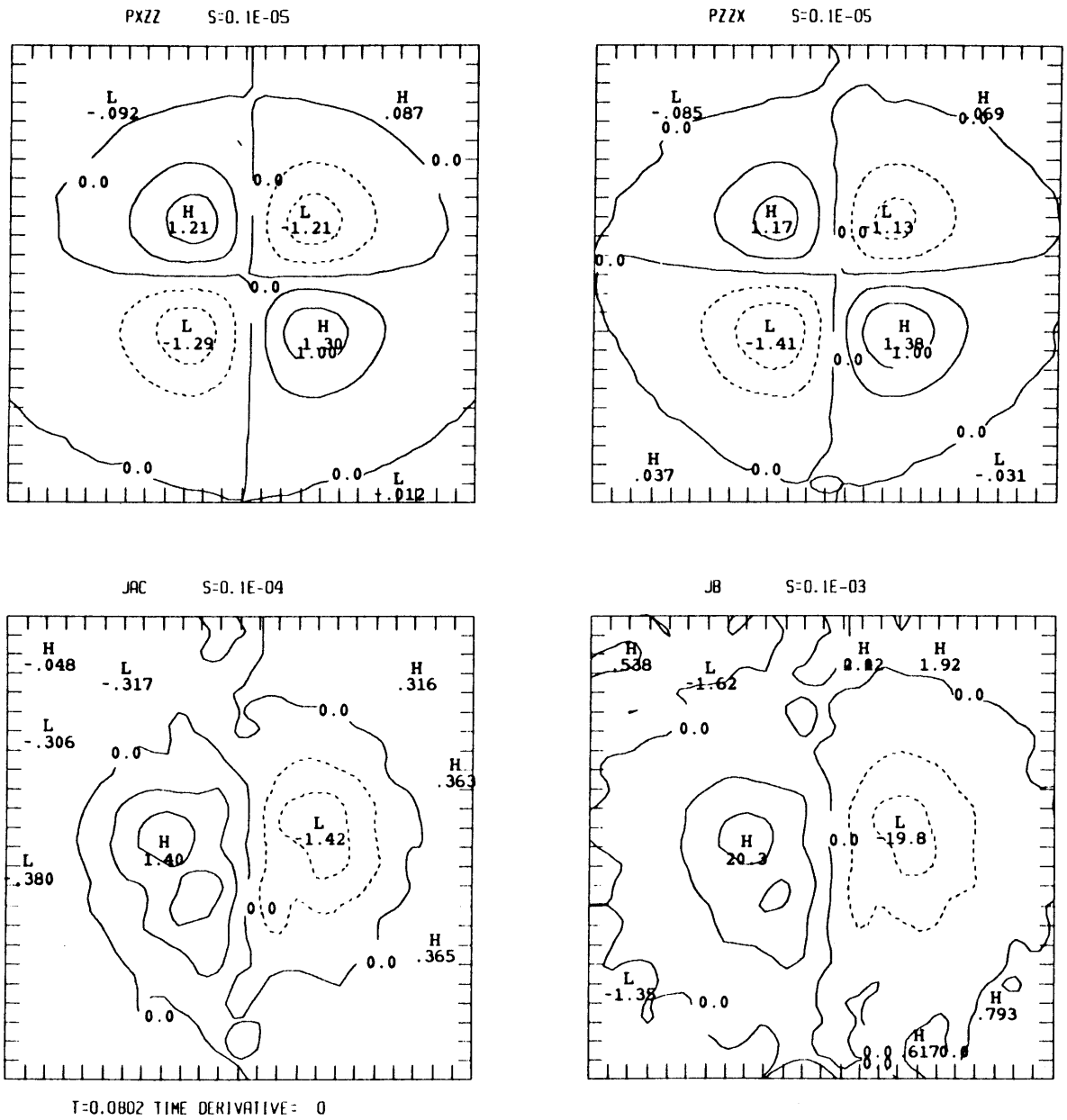

PXZZ S=0.1E-05
L -.092
H .087
0.0
0.0
0.0
H 1.21
L -1.21
0.0
L -1.29
H 1.30
1.00
0.0
0.0
L -.012
PZZX S=0.1E-05
L -.085
0.0
H 0.069
H 1.17
0.0
L 1.13
0.0
L -1.41
H 1.38
1.00
0.0
0.0
H .037
0.0
L -.031
JAC S=0.1E-04
H -.048
L -.317
H .316
0.0
L -.306
0.0
H .363
L 1.42
H 1.40
L .380
0.0
H .365
0.0
0.0
JB S=0.1E-03
H .538
L -1.62
H 1.92
0.0
0.0
L 19.8
H 20.3
0.0
L -1.38
0.0
H .793
H 6170.
0.0
T=0.0802 TIME DERIVATIVE= 0

Fig A3c

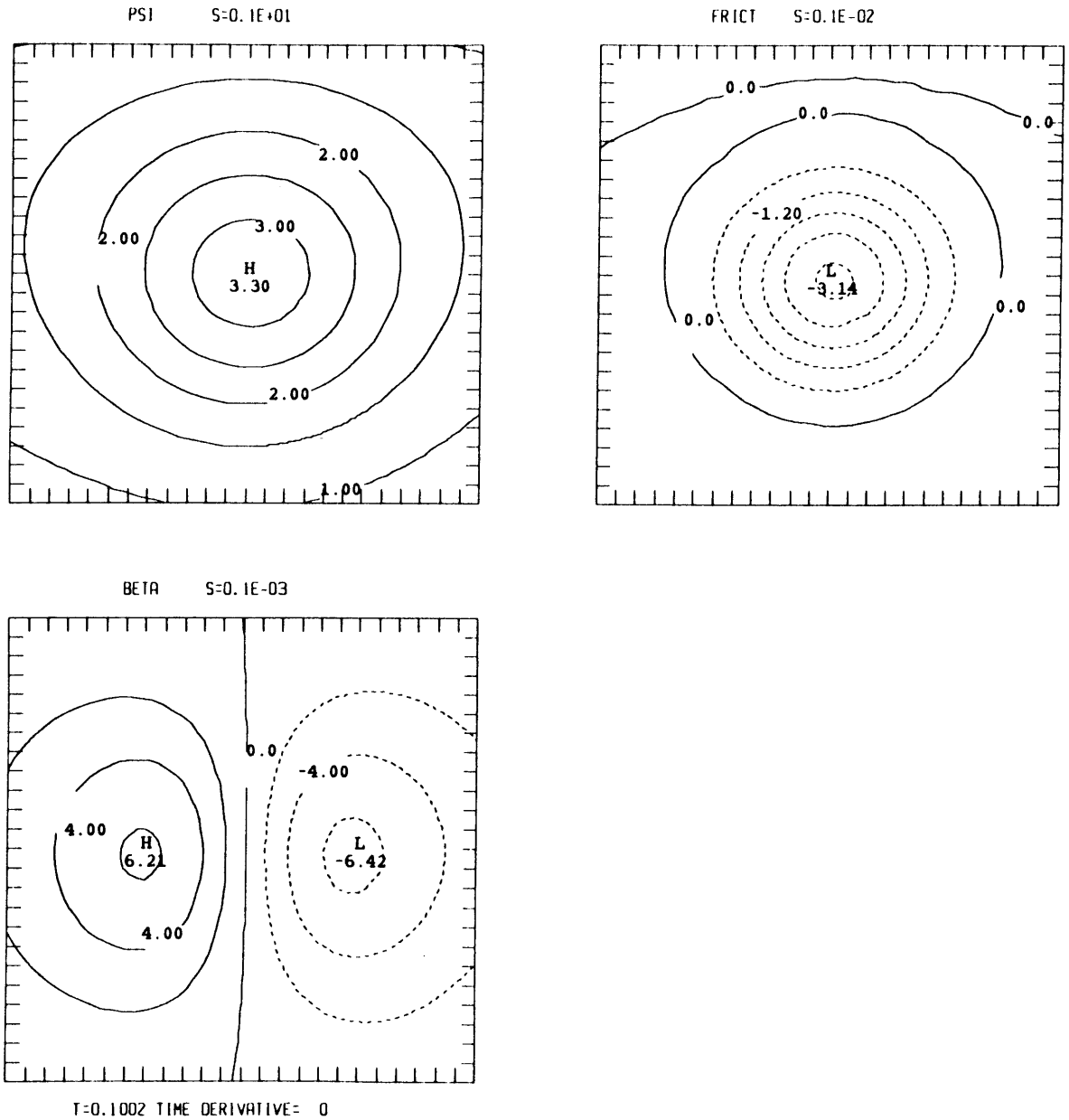

PSI S=0.1E+01
2.00
3.00
H
3.30
2.00
2.00
1.00
FRICT S=0.1E-02
0.0
0.0
0.0
-1.20
L
-3.14
0.0
0.0
BETA S=0.1E-03
0.0
-4.00
4.00
H
6.21
L
-6.42
4.00
T=0.1002 TIME DERIVATIVE= 0

Fig A4e

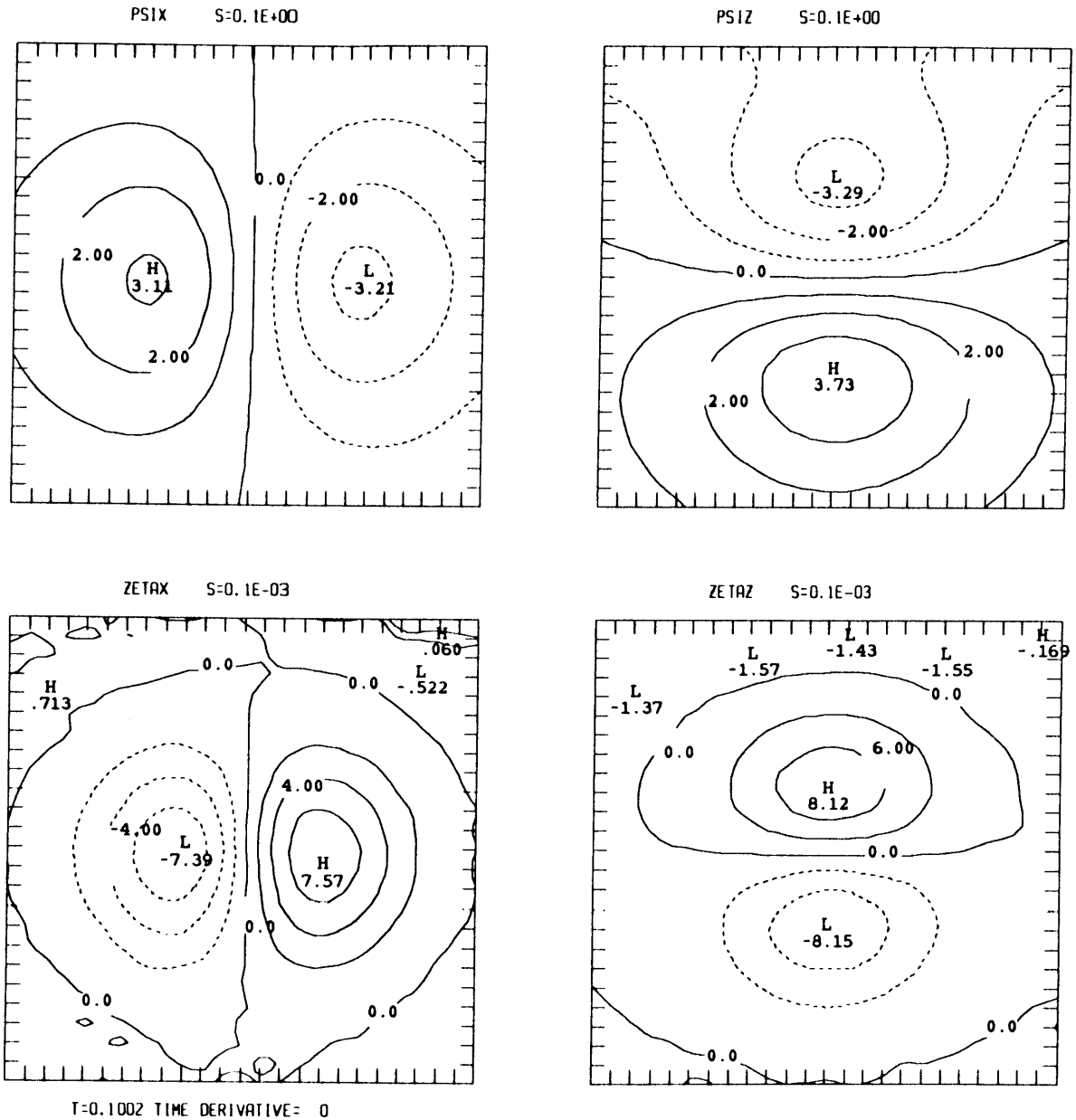

PSIX S=0.1E+00
0.0
-2.00
2.00
H
3.11
L
-3.21
2.00
PSIZ S=0.1E+00
L
-3.29
-2.00
0.0
2.00
H
3.73
2.00
ZETAX S=0.1E-03
H
.060
0.0
0.0
L
-.522
H
.713
4.00
-4.00
L
-7.39
H
7.57
0.0
0.0
0.0
ZETAZ S=0.1E-03
L
-1.43
L
-1.57
L
-1.55
H
-.169
L
-1.37
0.0
0.0
6.00
H
8.12
0.0
L
-8.15
0.0
0.0
T=0.1002 TIME DERIVATIVE= 0

Fig A4b

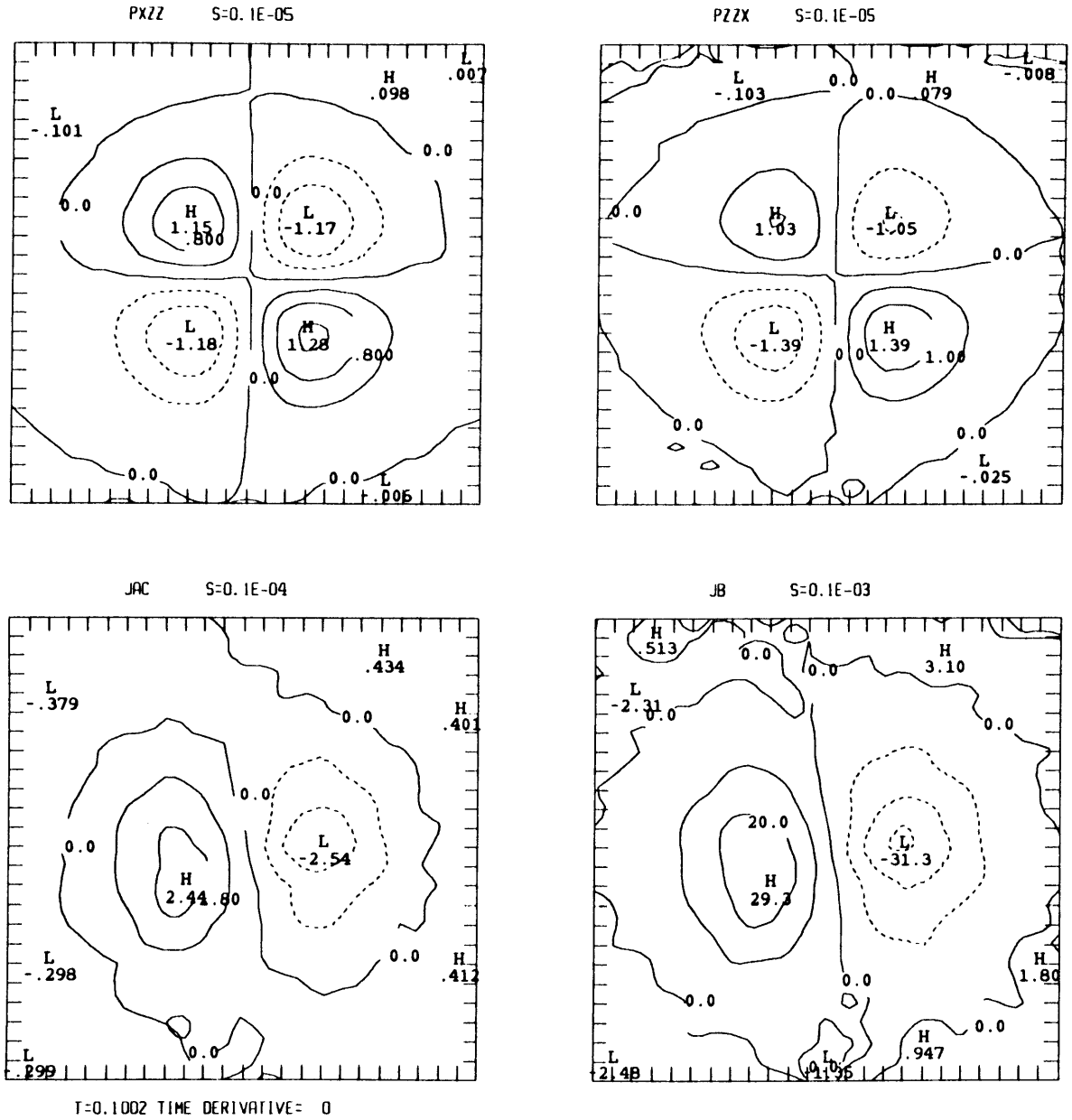

PXZZ S=0.1E-05
L -.101
H .098
L .007
0.0
H 1.15
.800
L -1.17
L -1.18
H 1.28
.800
L .006
PZZX S=0.1E-05
L -.103
0.0
H .079
L -.008
H 1.03
L -1.05
L -1.39
H 1.39
1.08
L -.025
JAC S=0.1E-04
H .434
L -.379
H .401
L -2.54
H 2.44.80
L -.298
H .412
L .299
JB S=0.1E-03
H .513
H 3.10
L -2.31
20.0
L -31.3
H 29.3
H 1.80
H .947
L 2.48
T=0.1002 TIME DERIVATIVE= 0

Fig A4C

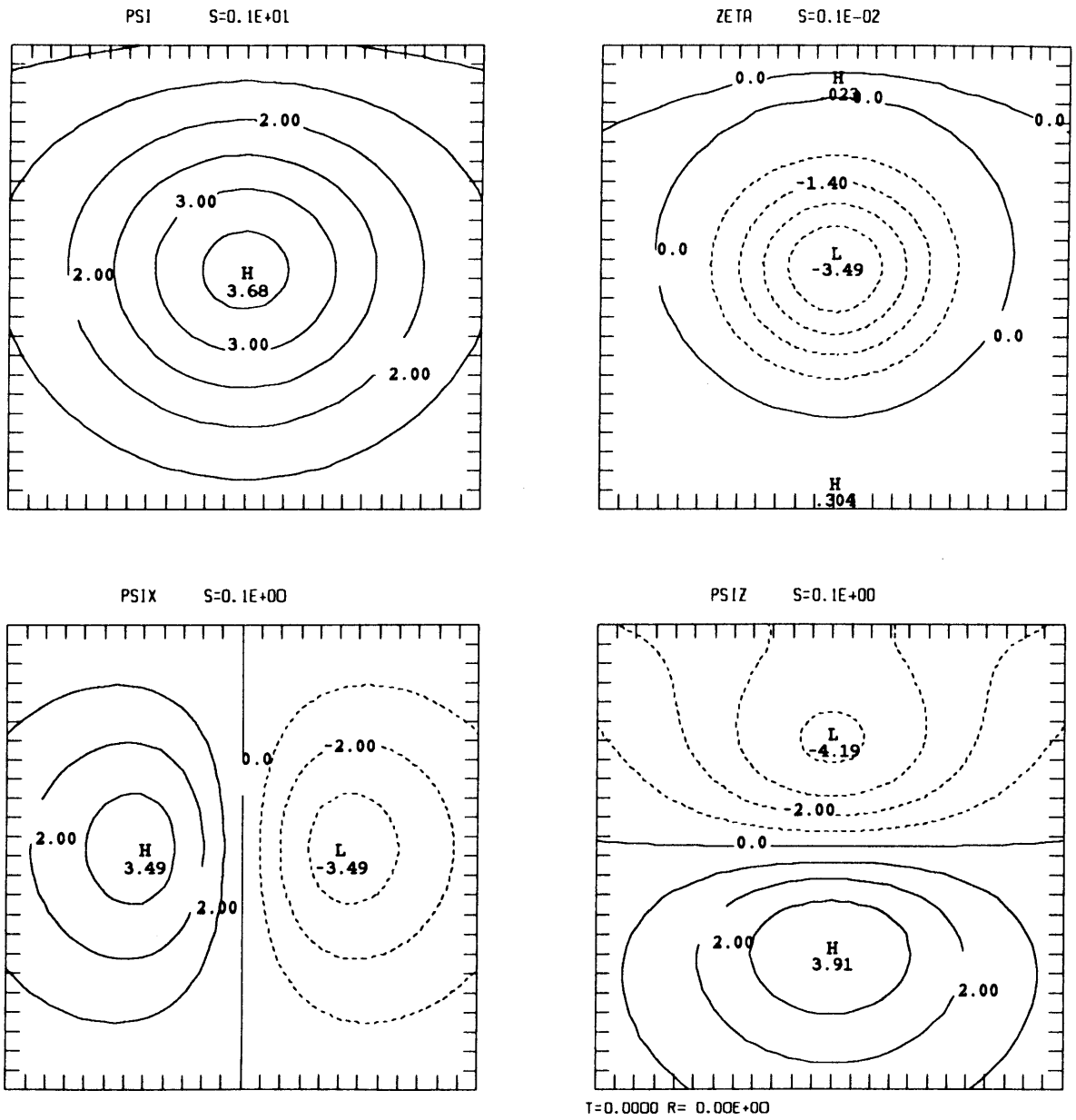

PSI S=0.1E+01
2.00
3.00
H
3.68
3.00
2.00
2.00
ZETA S=0.1E-02
0.0
H
0.0
0.0
-1.40
0.0
L
-3.49
0.0
H
1.304
PSIX S=0.1E+00
2.00
H
3.49
2.00
0.0
-2.00
L
-3.49
PSIZ S=0.1E+00
L
-4.19
-2.00
0.0
2.00
H
3.91
2.00
T=0.0000 R= 0.00E+00

Fig A5a

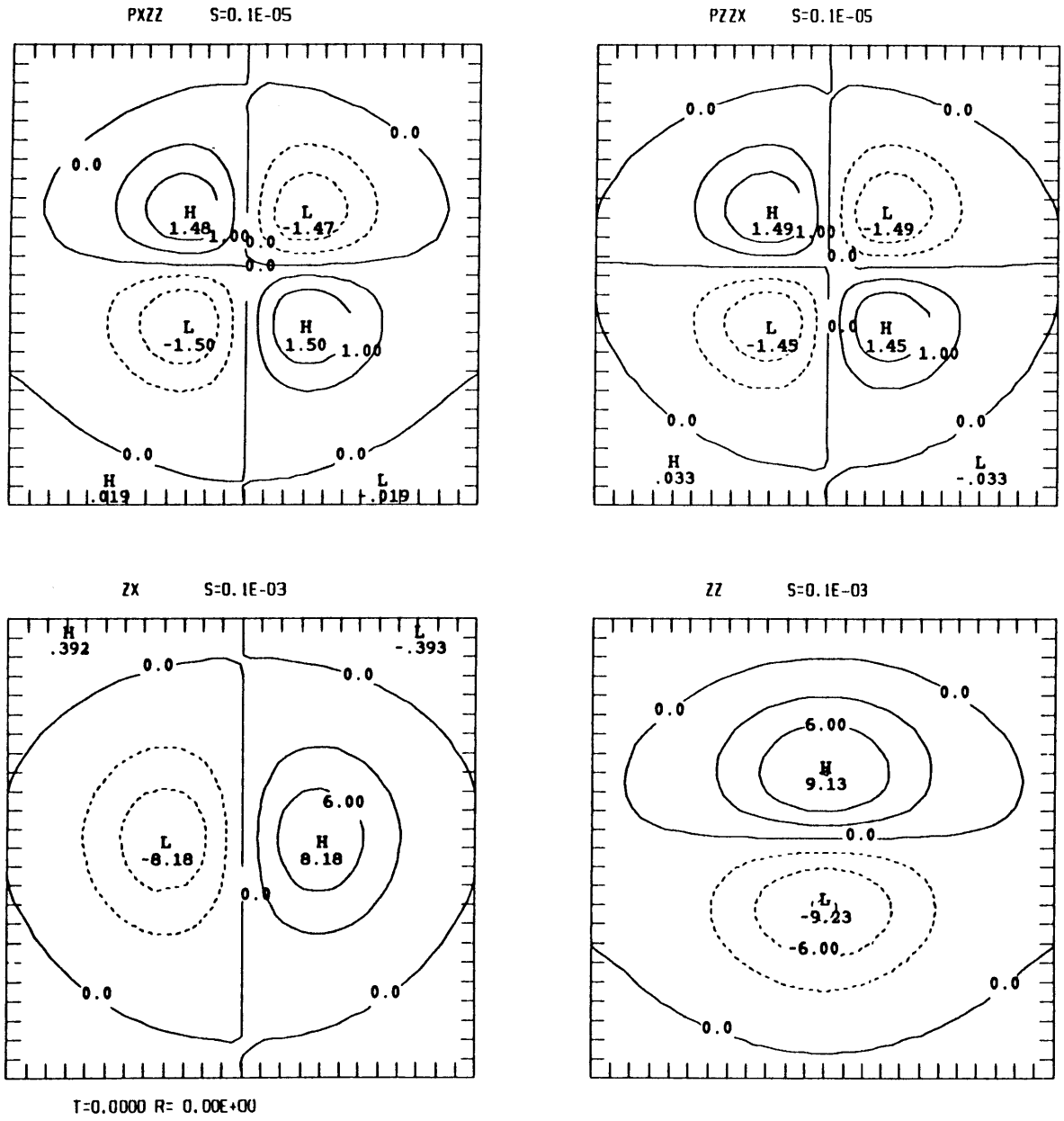

PXZZ S=0.1E-05
H 1.48
L -1.47
L -1.50
H 1.50
1.00
0.0
H .019
L -.019
PZZX S=0.1E-05
H 1.49
L -1.49
L -1.45
H 1.45
H .033
L -.033
ZX S=0.1E-03
H .392
L -.393
L -8.18
6.00
H 8.18
ZZ S=0.1E-03
6.00
H 9.13
L -9.23
-6.00
T=0.0000 R= 0.00E+00

Fig A5h

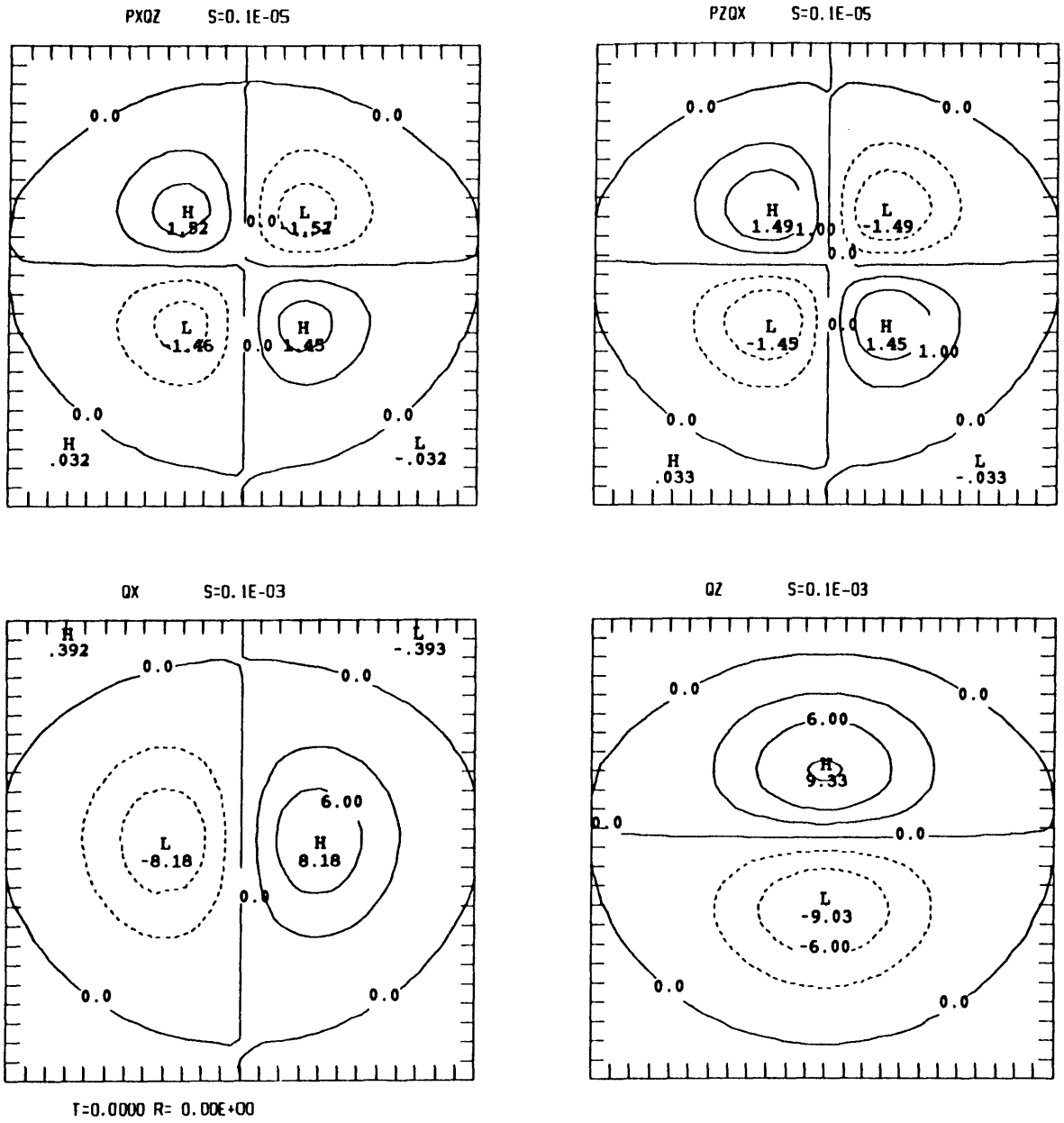
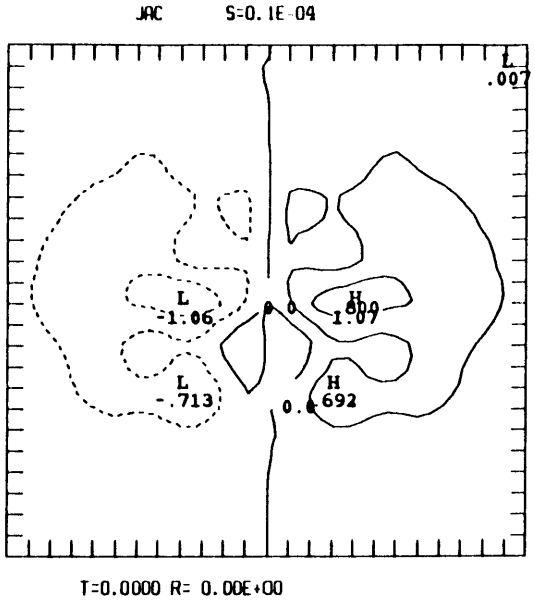
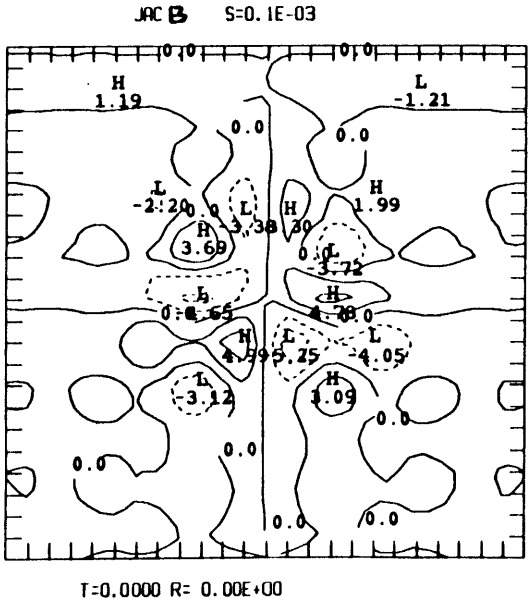

PXQZ S=0.1E-05
0.0
H
1.52
L
-1.52
L
-1.46
H
1.46
H
.032
L
-.032
PZQX S=0.1E-05
H
1.49
L
-1.49
L
-1.49
H
1.45
H
.033
L
-.033
QX S=0.1E-03
H
.392
L
-.393
L
-8.18
6.00
H
8.18
QZ S=0.1E-03
6.00
H
9.33
L
-9.03
-6.00
T=0.0000 R= 0.00E+00

Fig A5c


JAC S=0.1E-04
L .007
L -1.06
H 1.07
L -.713
H .692
T=0.0000 R= 0.00E+00


JAC B S=0.1E-03
H 1.19
L -1.21
L -2.20
H 1.99
H 3.69
L -3.72
L -4.05
L -3.12
H 1.09
T=0.0000 R= 0.00E+00

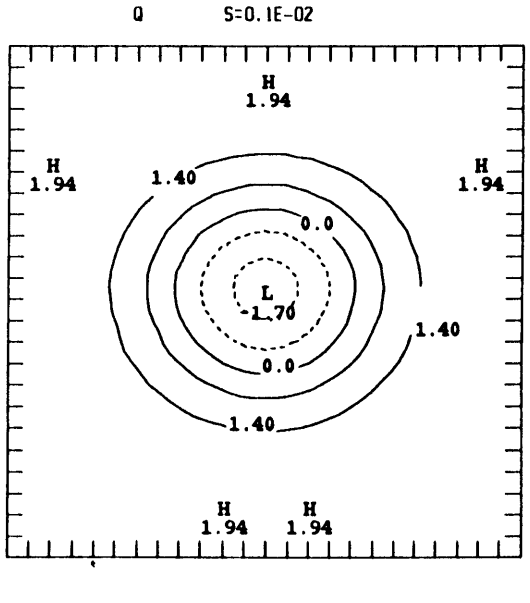

Q S=0.1E-02
H 1.94
H 1.94
H 1.94
1.40
L -1.70
1.40
1.40
H 1.94
H 1.94

Fig A5d

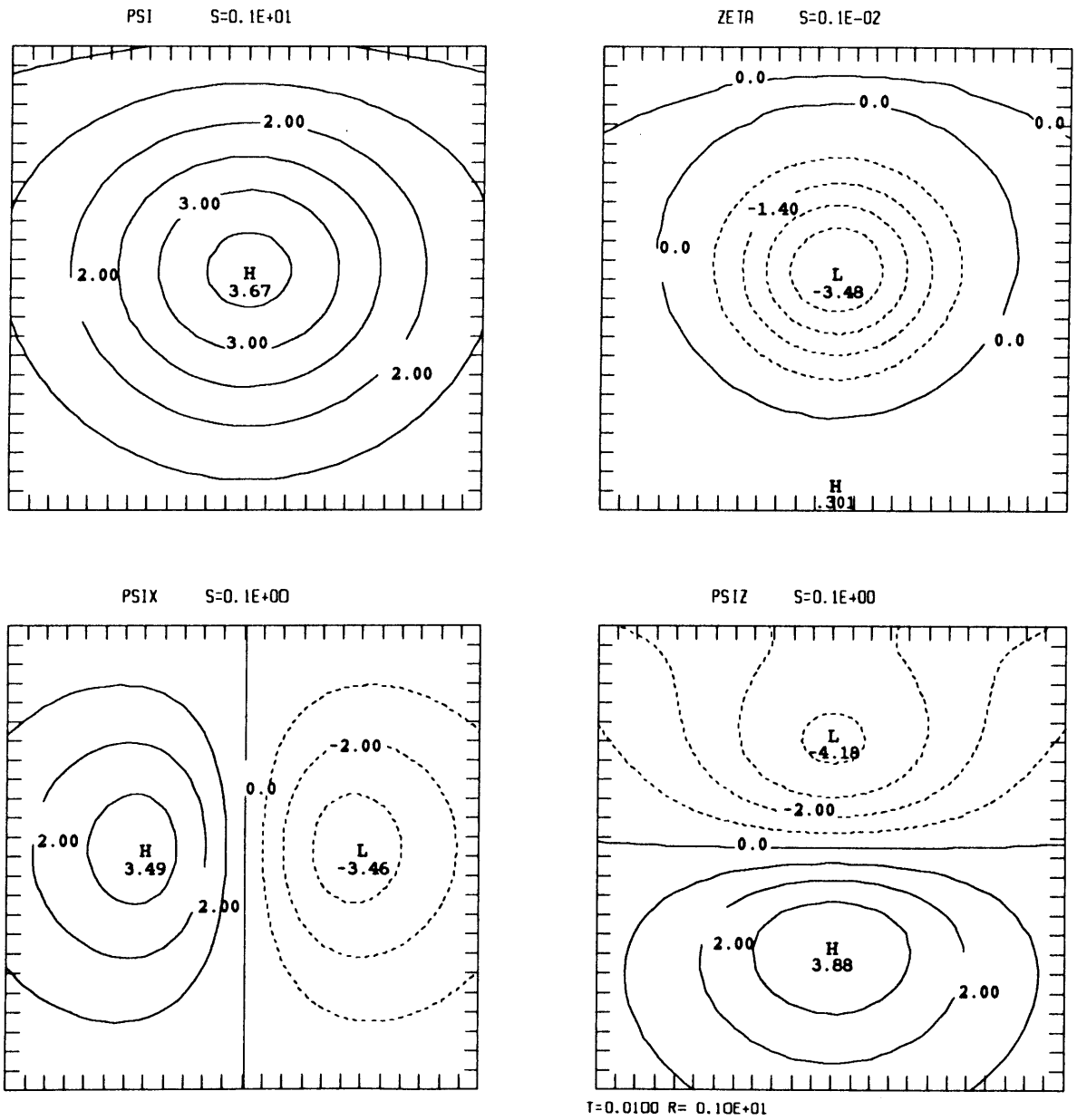

PSI S=0.1E+01
2.00
3.00
H
3.67
2.00
3.00
2.00
ZETA S=0.1E-02
0.0
0.0
0.0
-1.40
0.0
L
-3.48
0.0
H
.301
PSIX S=0.1E+00
-2.00
0.0
2.00
H
3.49
L
-3.46
2.00
PSIZ S=0.1E+00
L
-4.18
-2.00
0.0
2.00
H
3.88
2.00
T=0.0100 R= 0.10E+01

Fig A6a

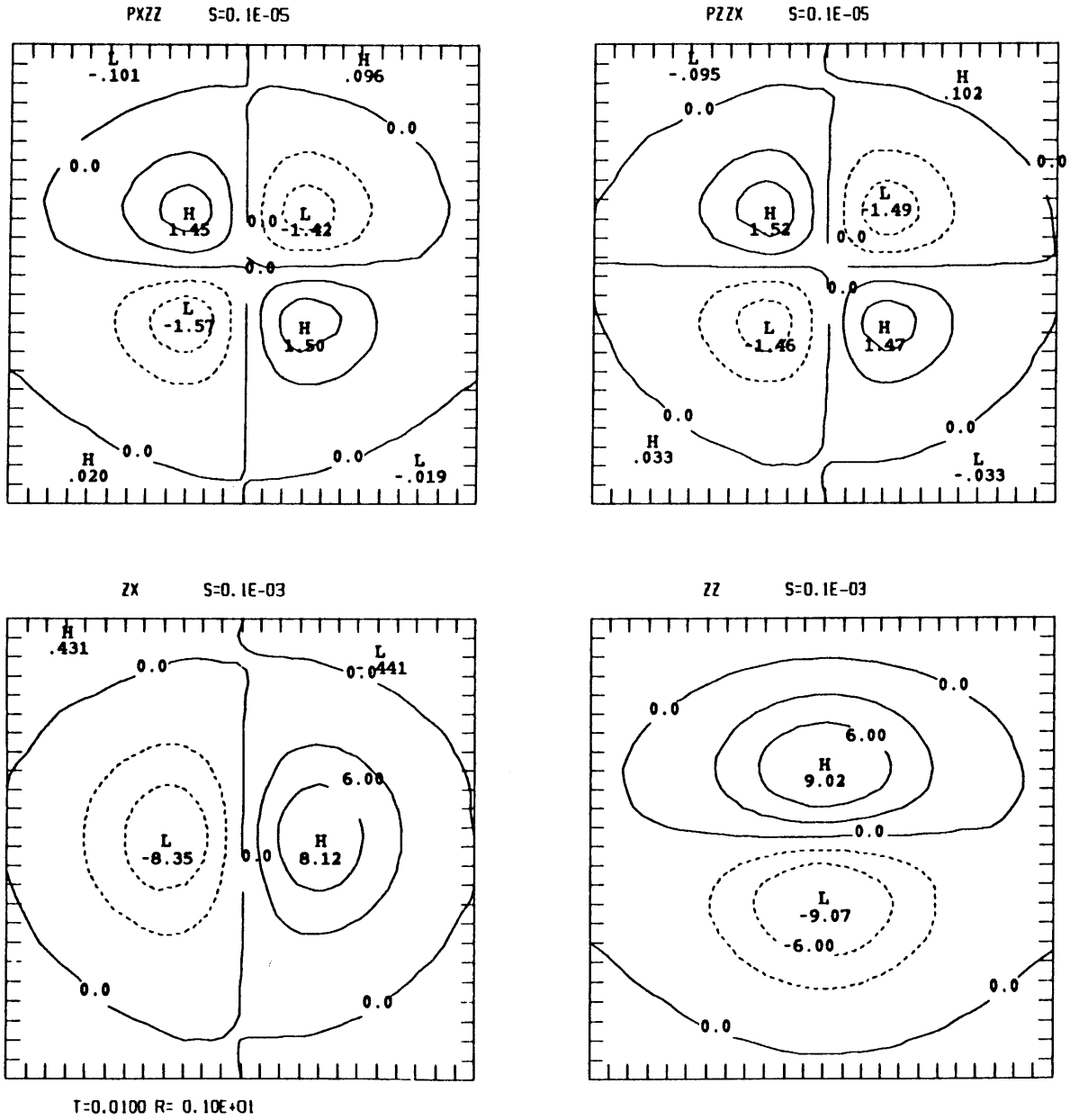

PXZZ S=0.1E-05
L -.101
H .096
0.0
0.0
H 1.45
L -1.42
0.0
0.0
L -1.57
H 1.50
H .020
0.0
0.0
L -.019
PZZX S=0.1E-05
L -.095
H .102
0.0
0.0
H 1.52
L -1.49
0.0
0.0
L -1.46
H 1.47
0.0
H .033
0.0
L -.033
ZX S=0.1E-03
H .431
0.0
L -.441
0.0
6.00
L -8.35
0.0
H 8.12
0.0
0.0
ZZ S=0.1E-03
0.0
0.0
6.00
H 9.02
0.0
L -9.07
-6.00
0.0
0.0
T=0.0100 R= 0.10E+01

Fig A 6b

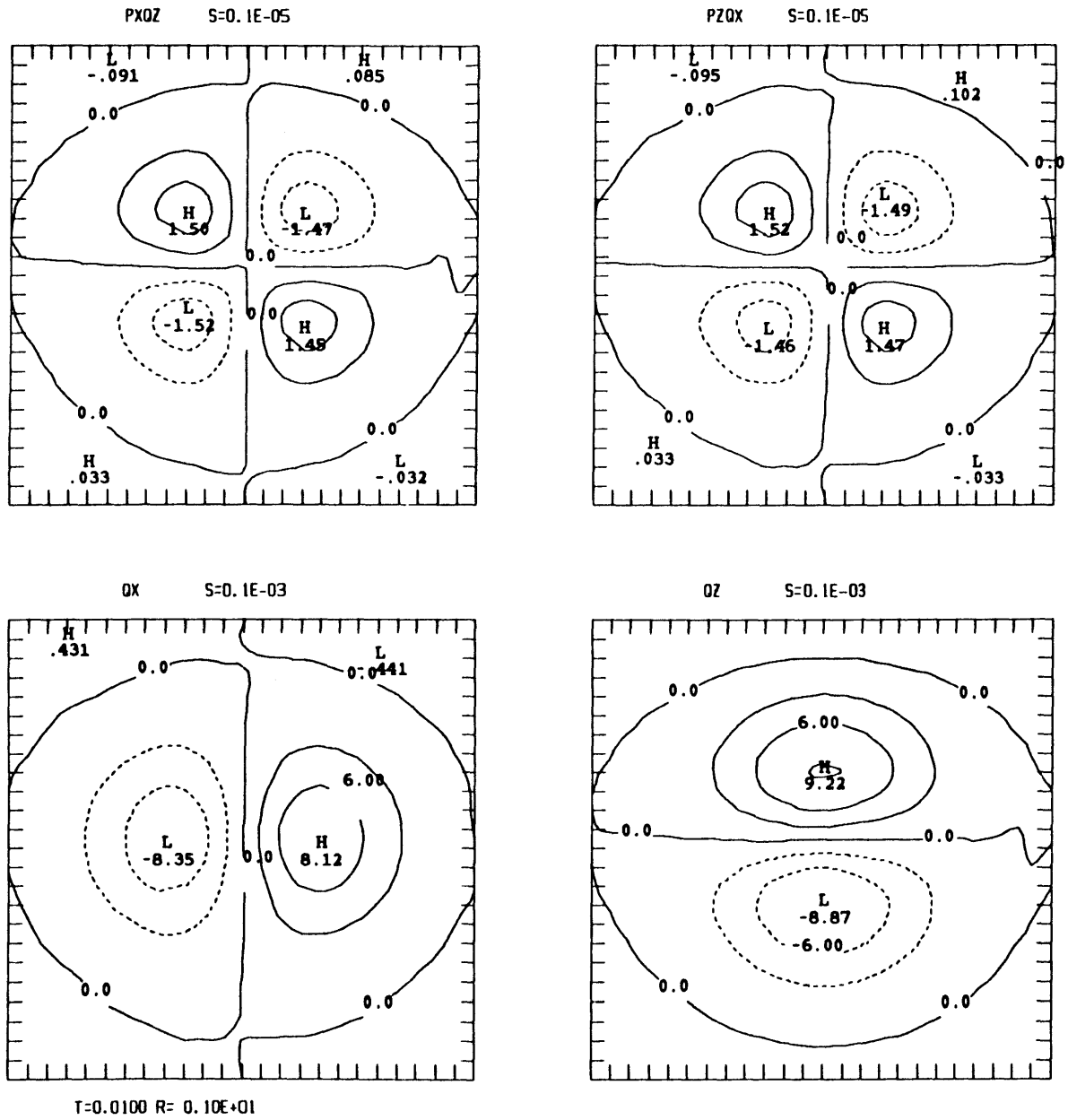
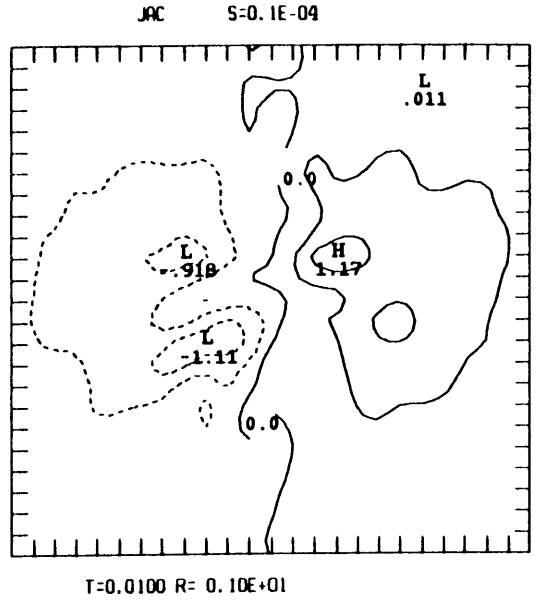
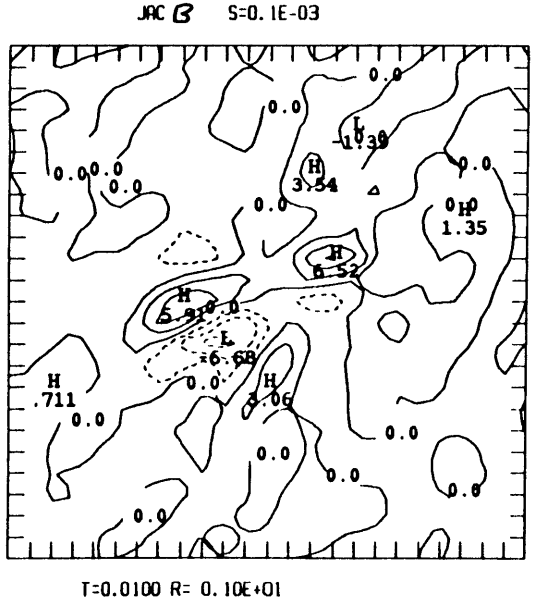

PXQZ S=0.1E-05
L -.091
H .085
0.0
H 1.56
L -1.47
L -1.52
H 1.48
H .033
L -.032
PZQX S=0.1E-05
L -.095
H .102
H 1.52
L -1.49
L -1.46
H 1.47
H .033
L -.033
QX S=0.1E-03
H .431
L -.441
6.00
L -8.35
H 8.12
QZ S=0.1E-03
6.00
H 9.22
L -8.87
-6.00
T=0.0100 R= 0.10E+01

Fig A6c


JAC S=0.1E-04
L
.011
0.0
L
.918
H
1.17
L
1.11
0.0
T=0.0100 R= 0.10E+01


JAC B S=0.1E-03
0.0
0.0
L
1.39
0.0
0.0
0.0
0.0
H
3.54
H
1.35
H
6.52
H
6.91
0.0
L
6.68
H
.711
0.0
H
3.06
0.0
0.0
0.0
0.0
0.0
T=0.0100 R= 0.10E+01

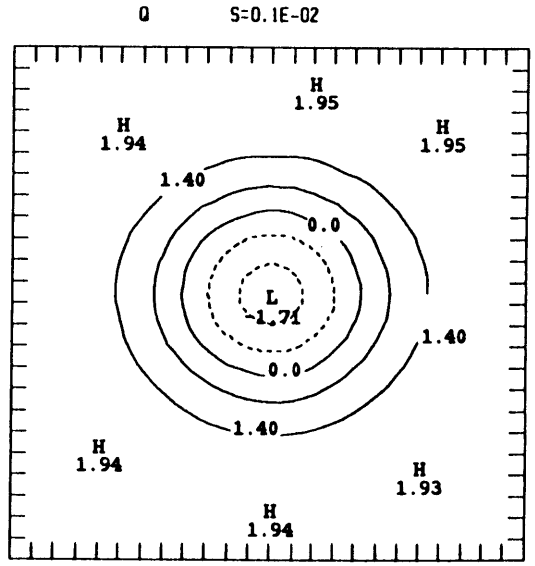

Q S=0.1E-02
H
1.95
H
1.94
H
1.95
1.40
0.0
L
1.71
1.40
0.0
1.40
H
1.94
H
1.93
H
1.94

Fig A6 d

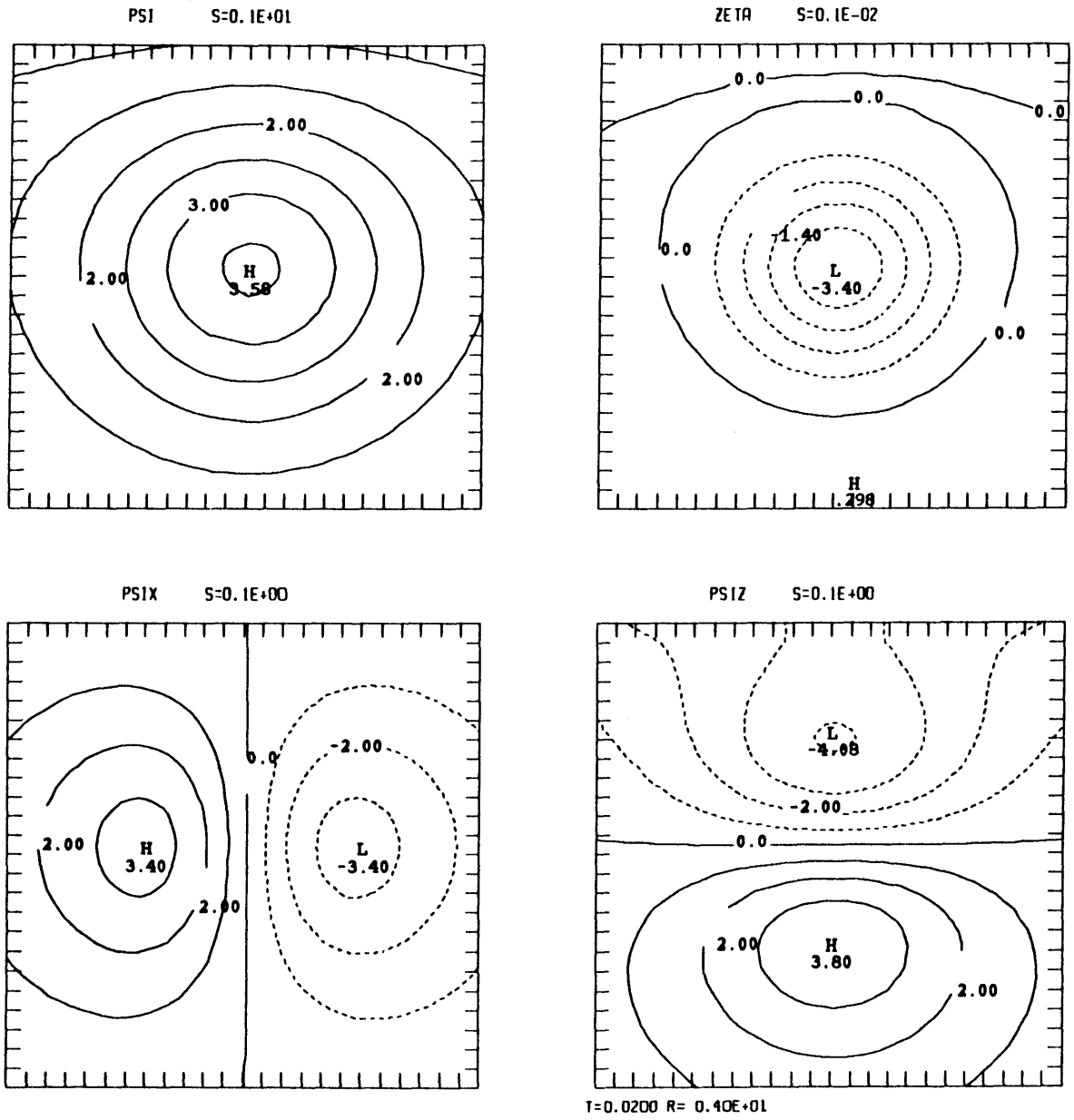

PSI S=0.1E+01
2.00
3.00
H
3.50
2.00
2.00
ZETA S=0.1E-02
0.0
0.0
0.0
0.0
-1.40
L
-3.40
0.0
H
PSIX S=0.1E+00
0.0
-2.00
2.00
H
3.40
L
-3.40
2.00
PSIZ S=0.1E+00
L
-2.00
0.0
2.00
H
3.80
2.00
T=0.0200 R= 0.40E+01

Fig A7e

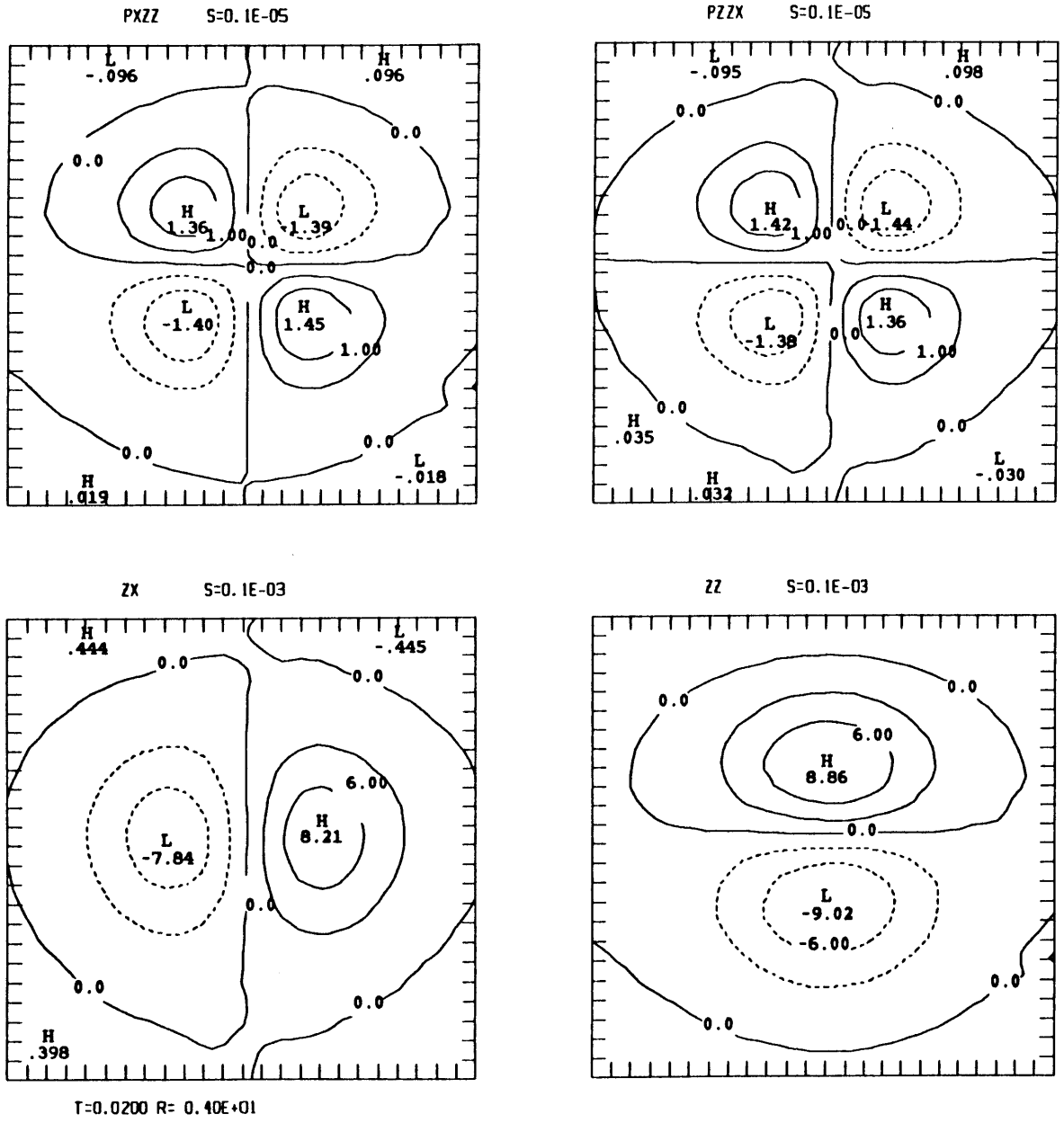

PXZZ S=0.1E-05
L -.096
H .096
0.0
H 1.36
1.00
L -1.39
L -1.40
H 1.45
1.00
H .019
L -.018
PZZX S=0.1E-05
L -.095
H .098
H 1.42
L -1.44
L -1.38
H 1.36
H .035
L -.030
ZX S=0.1E-03
H .444
L -.445
6.00
H 8.21
L -7.84
H .398
ZZ S=0.1E-03
6.00
H 8.86
L -9.02
-6.00
T=0.0200 R= 0.40E+01

Fig A7b

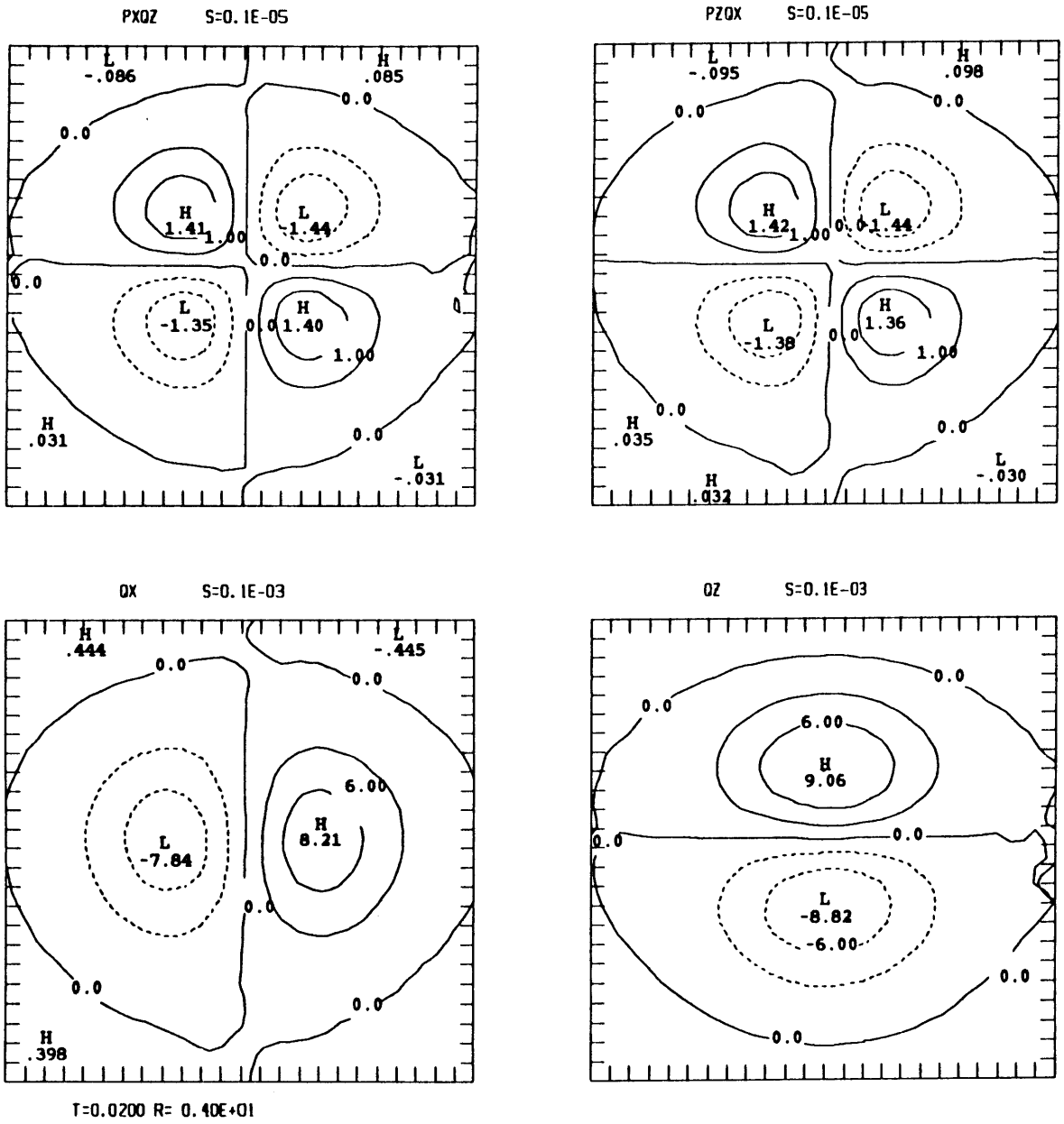
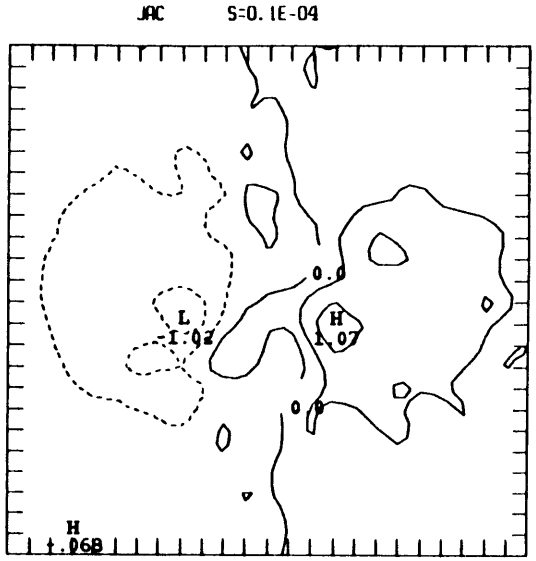
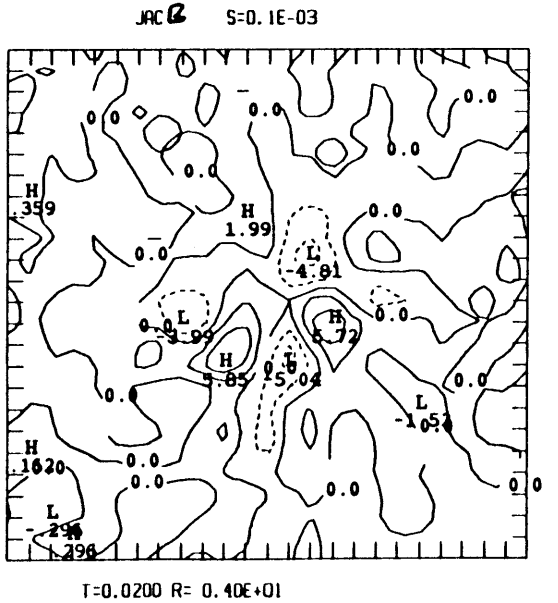

PXQZ S=0.1E-05
L -.086
H .085
0.0
0.0
H 1.41
1.00
L -1.44
0.0
0.0
L -1.35
H 1.40
1.00
H .031
0.0
L -.031
PZQX S=0.1E-05
L -.095
H .098
0.0
0.0
H 1.42
1.00
L -1.44
L -1.38
H 1.36
1.00
H .035
0.0
0.0
H .032
L -.030
QX S=0.1E-03
H .444
L -.445
0.0
0.0
6.00
H 8.21
L -7.84
0.0
0.0
0.0
H .398
QZ S=0.1E-03
0.0
0.0
6.00
H 9.06
0.0
0.0
L -8.82
-6.00
0.0
0.0
T=0.0200 R= 0.40E+01

Fig A7c





T=0.0200 R= 0.40E+01

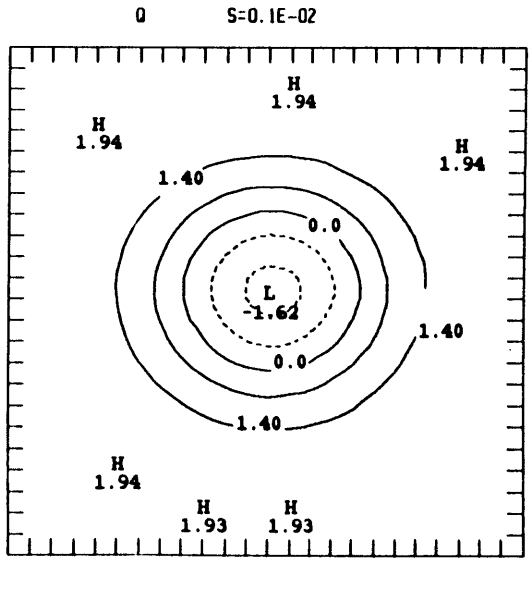


Fig A7d